CHARACTERISTICS OF FAULTS IN NONWELDED IGNIMBRITES FROM THE PAJARITO PLATEAU AND IMPLICATIONS FOR FLUID FLOW

by

Jennifer E. Wilson

Submitted in Partial Fulfillment
of the Requirements for the

Doctorate of Philosophy in Geology

New Mexico Institute of Mining and Technology
Department of Earth and Environmental Science

Socorro, New Mexico

December, 2004

ACKNOWLEDGMENTS

I would like to thank all of my committee members Drs. Nelia Dunbar, Laurel Goodwin, Claudia Lewis, Harold Tobin, and John Wilson for their support, guidance, and useful discussions during my Ph.D. program. I especially appreciate the extra efforts of Drs. Laurel Goodwin and Claudia Lewis. Thanks also to Alexis Lavine, Jamie Gardner, and Schön Levy of Los Alamos National Laboratory (LANL), who helped both in the field and through valuable discussion. Thanks to LANL field assistants Amy Jones, Danielle Katcher, Emily Schultz, and Teryn Ebert. I sincerely appreciate the accommodation and help of Steve Chipera at LANL's XRD lab, and Nelia Dunbar and Lynn Heizler at New Mexico Tech's electron microprobe lab. Special thanks to J. Matt Davis for allowing his minipermeameter to be replicated by New Mexico Tech's machine shop. Thanks to Floyd Hewitt for constructing the minipermeameter, and to Ed Wood at the New Mexico Firefighter Training Academy for the use of air tanks. Thanks also to Geoff Rawling, John Sigda, Dave Boutt, Glen Gettemy, B.J. Lechler, Christina Calvin, Justin Prien, Mark Cal, and Dr. Robert Bowman for their assistance in various labs at New Mexico Tech. I also thank Dr. Andrew Campbell, Dr. Dana Ulmer-Scholle, Dr. Peter Mozley, Dr. James Boles, and Dr. Philip Kyle for useful discussions that helped me to refine and interpret portions of the geochemical data collected in this dissertation.

Extra special thanks to my husband, Dave Wilson, for his endless support and patience.

TABLE OF CONTENTS

LIST OF FIGURES

LIST OF TABLES

ABSTRACT

Faults can impact groundwater flow as well as vadose-zone processes of recharge and transport. The impact of a given fault on fluid flow and transport depends in part on geologic products of fault-zone processes. For example, the presence of fractures versus deformation bands (narrow cataclastic shear zones) and degree and nature of diagenetic alteration directly influence the hydrologic properties of a given fault. Both fractures and deformation bands occur in ignimbrite sequences at Los Alamos, New Mexico, and Busted Butte, Nevada. The primary controls on mode of failure in these ash-dominated ignimbrites are grain-contact area and strength, which are directly related to degree of welding and crystallization and inversely proportional to porosity. Low-porosity welded units deform by transgranular fracture; high-porosity, glassy, nonwelded units deform by cataclasis within deformation bands. Moderately high-porosity, nonwelded units that have undergone devitrification and/or vapor-phase crystallization form either deformation bands or fractures, depending on local variations in the degree and nature of crystallization (qualitatively indexed by relative amounts of glass, cristobalite, and tridymite).

Grain- and pore-size reduction in deformation bands commonly produces indurated, tabular zones of clay-sized fault material. Unlike fractures, which increase saturated permeability through welded ignimbrites by at least two orders of magnitude, preliminary data suggest that deformation-band permeability can be up to an order of

magnitude less than adjacent protolith. This decrease in permeability within deformation bands may introduce permeability heterogeneity into nonwelded ignimbrites, which were previously considered to accommodate fluid flow by slow, matrix diffusion. If sufficiently continuous and numerous, deformation bands may cause permeability anisotropy at the scale of perched aquifers. This could affect water recovery rates in shallow wells, where short production time scales are coupled with subvertical zones of small reductions in permeability.

Although this reduction may have minimal impact on saturated flow, preferential water retention and geochemical modification within these deformation bands in unsaturated, near-surface ignimbrite deposits suggest that they do affect fluid flow and solute transport in the vadose zone. More than two-thirds of the deformation bands identified in this study are locally rich in smectite and/or cemented by calcite. Stable isotope analyses indicate that these diagenetic minerals result from low-temperature meteoric fluid-fault interaction. The microstructural character, REE signatures, and chemical compositions of smectite in the deformation bands suggest that it is added to fault zones by a combination of localized *in situ* alteration of fault gouge and translocation from the surface. *In situ* alteration of ignimbrite to form smectite indicates preferential water retention in the presence of unstable mafic minerals and volcanic glass. Colloidal transport of smectite into the deformation bands requires preferential fluid flow in these zones. Rod-shaped microcrystallites of calcite and increased spatial density of plant roots in deformation bands suggest pedogenic precipitation associated with repeated desiccation events and microbial activity. Since roots in this semiarid climate seek moisture, it is inferred that preferential root growth and associated calcite are indicators

of episodic preferential wetting of deformation bands, which facilitates fluid flow in semiarid vadose zones. Presence of smectite and calcite increases the surface area of fault material available for contact with fluids. This is interpreted to facilitate the addition and subtraction of some trace elements and oxides in these fault zones (e.g., TiO_2, Cr, Cu, and V).

Collectively, these observations indicate that these faults have served as, and may still be, zones of preferential vadose-zone fluid flow. Therefore, numerous, vertically continuous deformation-band faults in nonwelded ignimbrites in the vadose zone may serve as relatively fast pathways for fluids to reach the water table from the surface. Preferential fluid flow and transport lead to alteration and mineralization, further modifying fault-zone permeability (by closing pore throats) and the mechanical properties of the fault zone (through the development of relatively weak, clay-rich gouge or relatively strong calcite-cemented zones).

CHAPTER 1

INTRODUCTION

Background

My dissertation research addresses fault-zone deformation of ignimbrite deposits and the impact of resulting structures on fluid flow and transport above and permeability below the water table. Numerous previous workers have documented fault-zone impacts on fluid flow (e.g., Kastning, 1977; Antonellini and Aydin, 1994; Caine et al., 1996; Rawling et al., 2001). These studies show that faults may behave as conduits, barriers, or complex barrier-conduit systems depending on the types of structures present and their spatial distribution (e.g., Bruhn and Yonkee, 1988, Forster and Evans, 1991; Caine et al., 1996; Fig. 1.1). None of these studies have addressed faults in ignimbrite deposits, which are physically and mechanically heterogeneous materials. My research therefore was designed to 1) evaluate petrophysical controls on the type and spatial distribution of structures in faulted ignimbrite sequences, 2) explore the microstructural and diagenetic record of fault-zone fluid flow in the vadose zone, and 3) document changes in saturated permeability produced by fault-zone deformation and diagenesis.

The fundamental fault-zone structure in low porosity sedimentary and crystalline rocks is the fracture (e.g., Flinn, 1977; Chester and Logan, 1986; Lloyd and Knipe, 1992; Reches and Lockner, 1994). Fractures are the result of opening or shearing across a

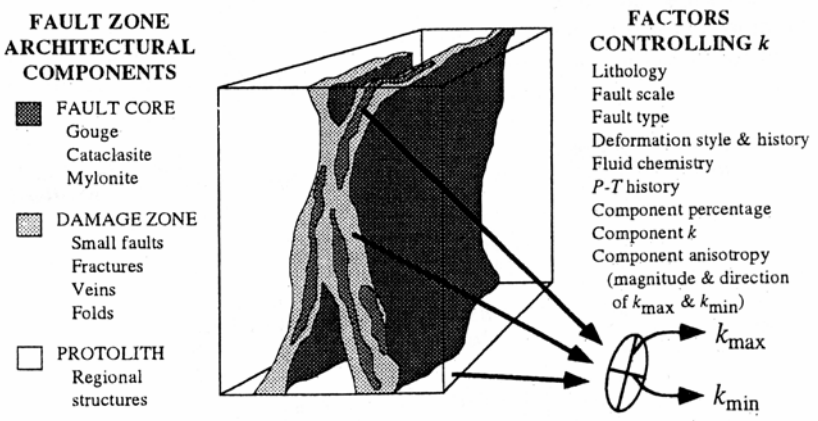

Figure 1.1. Conceptual model of fault zone with protolith removed. Ellipse represents relative magnitude and orientation of the bulk two-dimensional permeability (k) tensor that might be associated with each distinct architectural component of fault zone. From Caine et al. (1996).

discrete surface and are found in a volume, called the damage zone, surrounding the primary fault or slip surface; fractures increase in spatial density toward the fault core (Chester and Logan, 1986; Chester et al., 1993; Wilson et al., 2003a). The fault core may consist of an open shear fracture, a zone of shear fractures, a zone of variably cemented slip surfaces or breccia, or cataclastic gouge. In small-displacement faults that are unaffected by gouge development or diagenesis, fractures remain open, and fault-zone permeability is greatly enhanced (e.g., Chester and Logan, 1986; Caine et al., 1996). Similarly, fracture-rich damage zones enhance permeability. However, well-developed fault cores that contain diagenetic clays or cement have decreased permeability relative to protolith.

The above studies have greatly enhanced our understanding of how fault-zone deformation of low porosity rocks affects fault-zone permeability structure. However, ignimbrite sequences consist of materials with variable porosity and degree of

lithification. To provide context for this study of fault-zone impacts on fluid flow through ignimbrite sequences, it is useful to consider the results of detailed field, experimental deformation, and hydrologic studies of other materials that exhibit variations in degree of lithification, namely sand and sandstone. As clastic sedimentary materials, they share important characteristics with ignimbrites. Both consist of collections of clasts of variable size, strength, and roundness, and both exhibit varying amounts of porosity and lithification (the result of processes such as consolidation, cementation, and welding). In both materials, the strength of grain contacts varies: in sandstone, with amount and type of cement; in ignimbrites, with degree of welding and postdepositional crystallization. Investigations of deformation in high porosity sandstones (Aydin and Johnson, 1978; Antonellini and Aydin, 1994) and poorly consolidated sands (Cashman and Cashman, 2000; Rawling et al., 2001) reveal that the basic fault-zone structure in these materials is the deformation band rather than the fracture. Deformation bands are narrow zones in which grain-size reduction through microcracking, frictional grain-boundary sliding, and pore collapse accommodate mm-cm displacements. Transgranular fractures are not found in deformation bands.

Essentially, the controls on fault type in sand and sandstone can be divided into two categories: extrinsic controls, namely confining pressure, temperature, and strain rate; and intrinsic controls, here referred to as petrophysical controls, such as porosity and grain size (e.g., Wong et al., 1997). Experimental work on both extrinsic and intrinsic controls on deformation in rock with variable petrophysical properties shows that, in the absence of variable confining pressure, fluid pressure, etc., porosity is the dominant petrophysical control on mode of deformation (Dunn et al., 1973; Wong et al., 1997; Fig.

1.2). Rather than enhancing permeability, as fractures do, deformation bands can reduce porosity and saturated permeability by as much as four orders of magnitude with respect to protolith (e.g., Antonellini and Aydin, 1994; Hong, 1999; Sigda et al., 1999; Wong and Zhu, 1999; Rawling et al., 2001). In the vadose zone of dry desert environments, deformation bands can be up to six orders of magnitude more permeable than protolith because smaller pores can retain more water under unsaturated zone capillary pressures (cf. Stephens, 1996; Sigda et al., 1999; Sigda and Wilson, 2003).

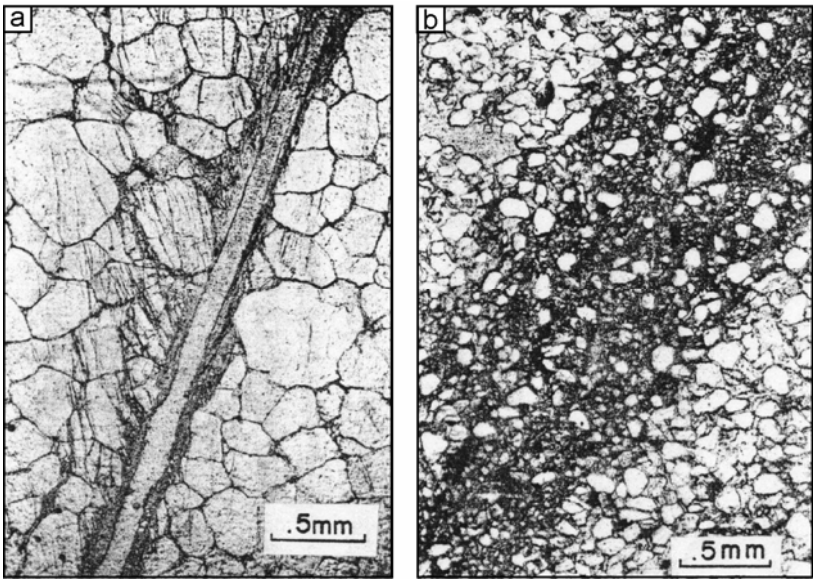

Figure 1.2. Photomicrographs of faults through sandstone of (a) low porosity (4%) and (b) high porosity (24%), resulting in formation of fractures and a deformation band, respectively. From Dunn et al. (1973).

The work presented here expands on these earlier studies of faults in sands and sandstones through a systematic investigation of small-displacement faults in ignimbrites. The Bandelier Tuff of northern New Mexico offers a unique natural lab in which to investigate petrophysical controls on fault-zone deformation (Figs. 1.3 and 1.4). In the vicinity of Los Alamos, New Mexico, ignimbrite units within the Bandelier Tuff have

variable petrophysical properties (porosity, grain size, mineralogy, etc.). All units have been faulted under relatively constant, near-surface conditions (i.e., low temperature and confining pressure) in response to Rio Grande rift extension. By systematically recording the type(s) of fault present in units with different petrophysical properties, I have been able to evaluate relationships between fault-zone deformation characteristics and these properties. A similar, though much more limited, investigation of a few faults in ignimbrite deposits in Busted Butte, Nevada, have so far confirmed the results of the larger study. Field observations at this additional site therefore suggest that the results of work in the Bandelier Tuff are not site specific, but are generally applicable to ash-dominated ignimbrite sequences.

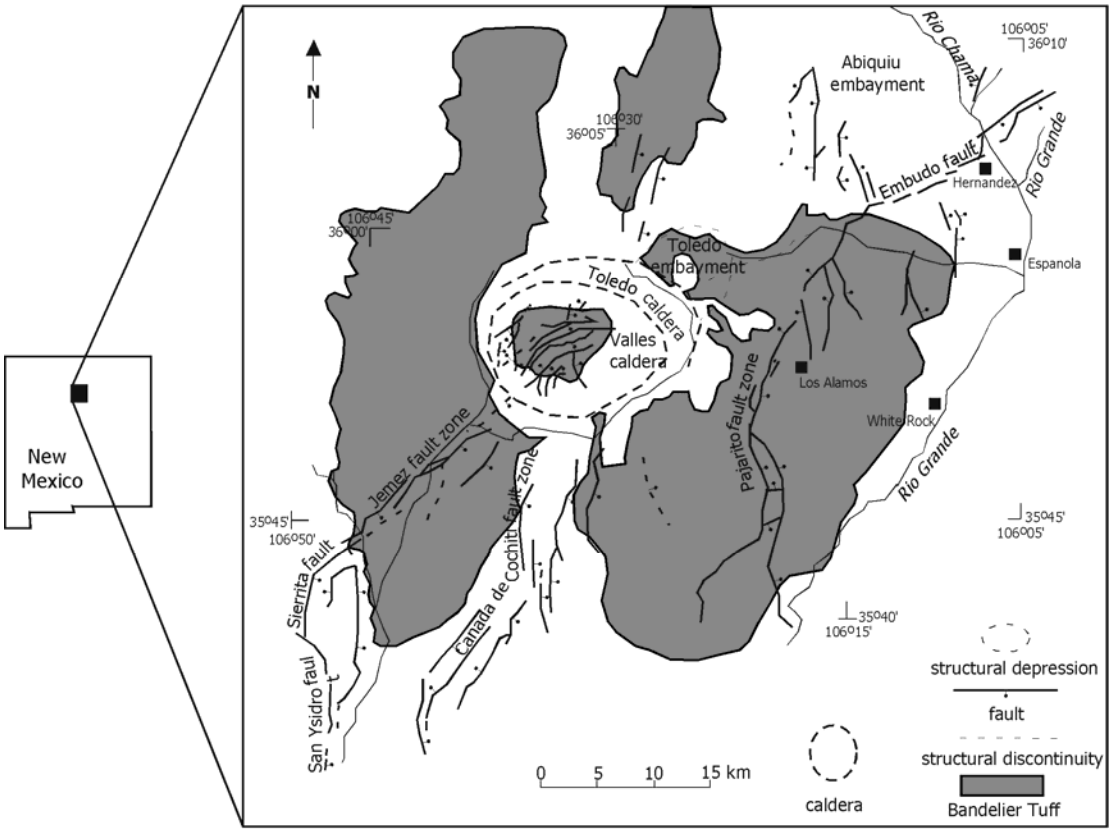

Figure 1.3. Location and simplified structural map of the Jemez Mountains showing the extent of Bandelier Tuff deposition. After Heiken et al. (1990) and Purtymun (1995).

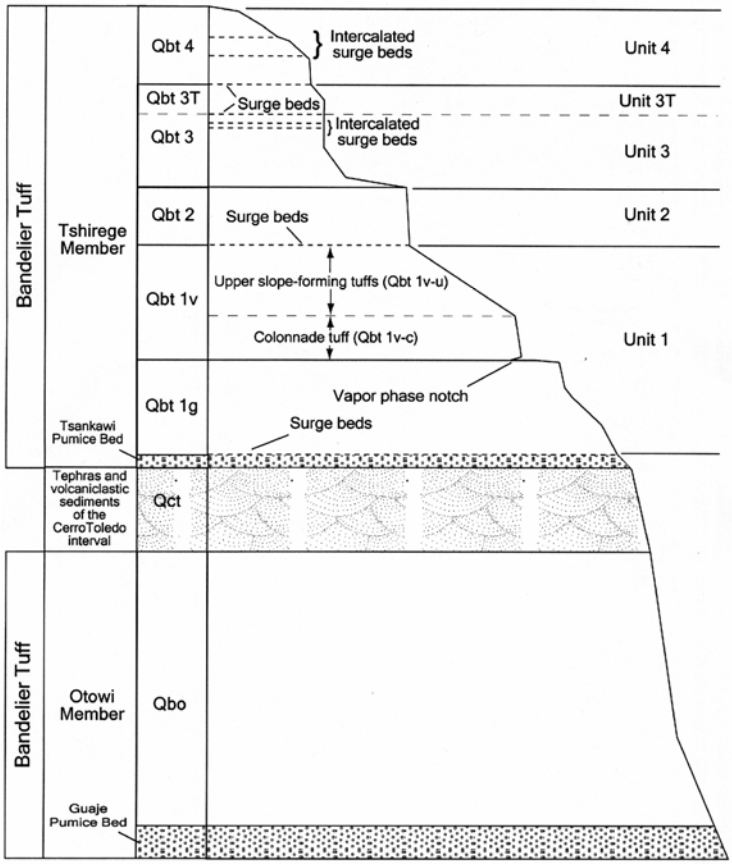

Figure 1.4. Bandelier Tuff stratigraphy. From Lewis et al. (2002; modified from Broxton and Reneau, 1995).

The investigation I have conducted can be broadly divided into three parts:

1. *Detailed meso- to micro-structural characterization of small-displacement faults and consideration of the relationship between protolith petrophysical characteristics and fault type*. Protolith petrophysical characteristics include degree of welding, nature of postdepositional crystallization (mineralogy and grain size), and modal composition (i.e., % pumice, phenocrysts, matrix ash, lithic clasts, and porosity). To identify the mode of deformation in each unit, the following structures were noted for each sample of fault-zone material: transgranular microfractures, foliations or lineations, and zones of grain crushing and/or pore collapse.

2. *Mineralogical and geochemical analysis of faults and surrounding protolith to document differences (if any) between the diagenetic history of faults and protolith ignimbrites*. Because diagenesis includes water-rock interactions, this is fundamentally an investigation of the record of paleoflow through faults relative to protolith. Because the units studied have been above the water table since deposition, I have essentially documented the impact of the faults on vadose-zone hydrologic processes.

3. *Measurement of porosity and saturated permeability for fault-zone material and adjacent protolith.* Although full characterization of hydrologic properties is beyond the scope of this dissertation, I have considered how faulting affects porosity and saturated permeability of units of the Bandelier Tuff and Calico Hills Tuff. The preliminary results of this work are reported here, along with a road map for future studies.

Organization of Dissertation

The structure of this dissertation generally follows the three-part division of topics given above, prefaced by this and a second introductory chapter. Chapter 2 is a brief overview of previous work defining the petrophysical and mechanical characteristics of ignimbrites. Chapter 3 is an overview of petrophysical controls on fault-zone deformation in variably welded and crystallized ash-dominated ignimbrites, emphasizing the occurrence of deformation bands in glassy and crystallized nonwelded ignimbrite at Los Alamos, New Mexico, and Busted Butte, Nevada. Evidence of preferential fluid flow through these faults is documented by differences between protolith and

deformation-band mineralogies. A modified version of this chapter was published in Geology (volume 31, no. 10, p. 837-840) with co-authors Laurel B. Goodwin and Claudia J. Lewis.

Chapter 4 details the geochemical evidence of preferential vadose-zone flow and transport as indicated by diagenetic modification of deformation bands in the nonwelded units of the Bandelier Tuff. Mineralogical controls on propagation of deformation bands in nonwelded units of the Bandelier Tuff are also explored in this chapter. A modified version of this chapter is intended for submission to the Journal of Geophysical Research with co-authors Laurel B. Goodwin and Claudia J. Lewis.

Chapter 5 is an overview of the effect that deformation bands may have on saturated permeability structure within faulted ignimbrite sequences that have undergone variable welding and postdepositional crystallization. Pending the results of permeability data corrections, a modified version of this chapter is intended for submission to Water Resources Research with co-authors Laurel B. Goodwin, Claudia J. Lewis, and John L. Wilson. Chapter 6 provides conclusions from the research presented in Chapters 3-5 and suggestions for future work.

CHAPTER 2

PETROPHYSICAL AND MECHANICAL CHARACTERISTICS OF IGNIMBRITES

Ignimbrites, also known as ash-flow tuffs, are pyroclastic flow deposits that consist of a poorly sorted assemblage of ash (volcanic glass shards less than 4 mm in size), pumice, phenocrysts, and lithic fragments (Fig. 2.1; Ross and Smith, 1961; Wilson and Walker, 1982; Freundt et al., 2000). The poor sorting of this rock type is inherently related to the mode of deposition of a pyroclastic flow deposit. Glass shards, phenocrysts, pumice, and lithic fragments are typically very angular when deposited, and come to rest touching one another only at points (Ross and Smith, 1961). This creates a large amount of interstitial pore space. These interstitial spaces may be preserved in the absence of welding (Fig. 2.1a). Welding is the flattening and/or fusion of ash and pumice during compaction under sufficiently high eruption temperature (> 650^{o}C) and load induced by overlying deposits (Fig. 2.2). The process of welding usually occurs within days of initial deposition (Ross and Smith, 1961), during which time volcanic glass is sufficiently hot to plastically compact around more competent phenocrysts and lithic fragments (Fig. 2.1b). Degree of welding can be quantified by pumice aspect ratio (e.g., Broxton et al., 1995; Freundt et al., 2000). Welding results in a loss of porosity; the reduction in pore space can be drastic. For example, previous work documents a decrease from 70% to 24% in Battleship Rock Tuff, New Mexico (Ross and Smith,

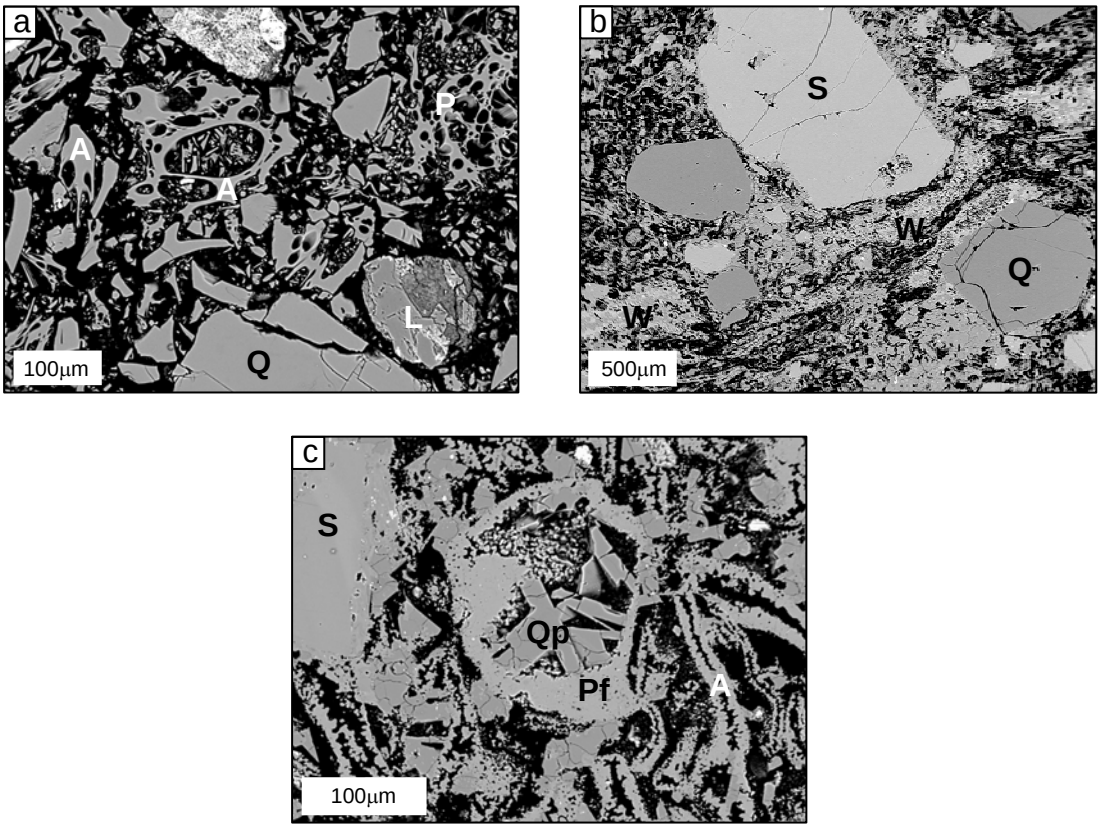

Figure 2.1. Backscattered-electron (BSE) microprobe images of (a) glassy nonwelded, (b) crystallized welded, and (c) nonwelded crystallized Bandelier Tuff. Black = porosity, gray particles = grains (S = sanidine phenocrysts, Q = quartz phenocrysts, L = lithic clasts, P = pumice, Qp = quartz polymorphs, Pf = postdepositional alkali feldspar) and matrix (A = nonwelded ash and shards, W = welded ash, shards, and pumice).

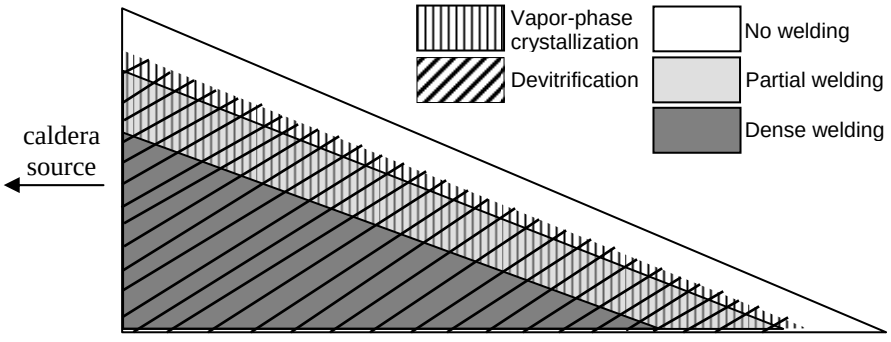

Figure 2.2. Welding and crystallization zones in a schematic, vertically exaggerated section through an ignimbrite unit. After Freundt et al. (2000).

1961). The compaction, fusion along contacts, and decrease in porosity significantly indurate the ignimbrite (Ross and Smith, 1961).

Postdepositional crystallization (devitrification and vapor-phase crystallization) may also occur in an ignimbrite deposit. Devitrification is the process by which amorphous glass (ash and pumice) is crystallized to alkali feldspar and quartz polymorphs (usually cristobalite and tridymite; Fig. 2.1c; Ross and Smith, 1961). The process of vapor-phase crystallization involves the alteration of glass and precipitation of crystals in open pore spaces (interstices between glass shards and vesicles in pumice) from a vapor phase (Fig. 2.1c; Stimac et al., 1996). The degree and nature of postdepositional crystallization are functions of the chemical composition of a given ignimbrite, the rate of cooling, the presence and composition of volatiles, and the initial temperature of the material (Ross and Smith, 1961; Smith and Bailey, 1966). Crystallization tends to be more prevalent in higher temperature welded units, but nonwelded ignimbrites may also experience devitrification or vapor-phase crystallization (Fig. 2.2; Ross and Smith, 1961; Freundt et al., 2000). The process of crystallization commonly, but does not always, hardens or indurates the ignimbrite (Ross and Smith, 1961).

Although variably welded and crystallized—and thus variably indurated—ignimbrites underlie environmentally sensitive and tectonically active areas (e.g., Yucca Mountain, NV, and Los Alamos, NM), few investigations of deformed ignimbrites have been published. Two investigations of experimental deformation of variably welded ignimbrites from New Zealand (Moon, 1993a; 1993b) and Nevada (Schultz and Li, 1995) are most applicable to the work presented here. Moon (1993a) identified the relationship

between mechanical behavior and petrophysical properties, such as porosity (a proxy for degree of welding and closeness of packing of groundmass shards), phenocryst versus pumice content, and size of clasts. Of these petrophysical properties, porosity exerts the dominant control on mechanical behavior of the ignimbrite (Fig. 2.3; Moon, 1993b; Schultz and Li, 1995). Ignimbrites with low porosity (welded contacts and close shard packing) and smaller but more numerous phenocrysts and lithic clasts have higher compressive strength. Although Moon (1993a; 1993b) identified these stronger, low porosity ignimbrites as being more likely to allow propagation of microfractures, the microstructures resulting from deformation in weaker, high porosity ignimbrite were not investigated or documented in detail. My field-based investigation therefore takes over where these experimental studies left off, with an investigation that compares deformation processes in welded ignimbrite with those in nonwelded ignimbrite.

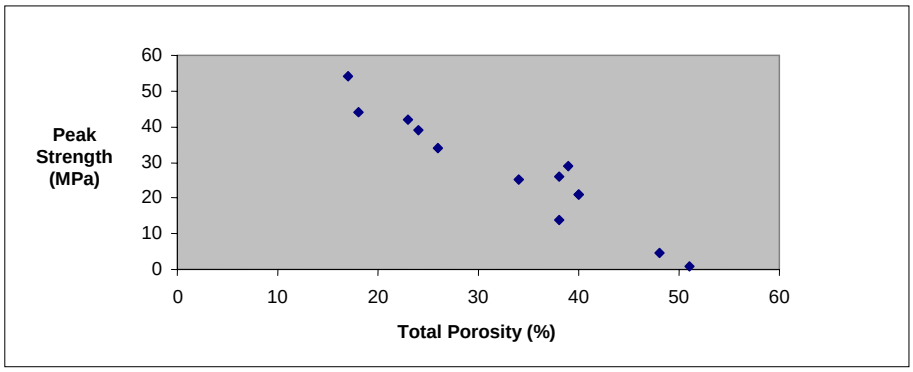

Figure 2.3. Relationship between peak uniaxial compressive strength (i.e., stress level at which failure occurs under atmospheric pressure and ambient temperature) and total porosity for ignimbrites. Data from Moon (1993b) and Schultz and Li (1995).

CHAPTER 3

DEFORMATION BANDS IN NONWELDED IGNIMBRITES: PETROPHYSICAL CONTROLS ON FAULT-ZONE DEFORMATION AND EVIDENCE OF PREFERENTIAL FLUID FLOW[1]

Abstract

The impact of faults on fluid flow and transport through thick vadose zones depends in part on the nature of fault-zone deformation. Both fractures and deformation bands occur in ignimbrite sequences at Los Alamos, New Mexico, and Busted Butte, Nevada. The primary controls on mode of failure are grain-contact area and strength, which are directly related to degree of welding and crystallization and inversely proportional to porosity. Low-porosity welded units deform by transgranular fracture; high-porosity, glassy, nonwelded units deform by cataclasis within deformation bands. Moderately high-porosity, nonwelded units that have undergone devitrification and/or vapor-phase crystallization form either deformation bands or fractures, depending on local variations in the degree and nature of crystallization.

Grain- and pore-size reduction in deformation bands commonly produces indurated, tabular zones of clay-sized fault material. Many of these bands are locally rich in smectite and/or cemented by calcite. Preferential wetting of deformation bands is

---

[1] A modified version of this chapter has been published in Geology, v. 31, no. 10, p. 837-840.

inferred to promote alteration and cementation. We therefore interpret variably altered fault-zone material as evidence of preferential fluid flow in the vadose zone, which we infer to result from enhanced unsaturated permeability due to pore-size reduction in deformation bands.

Introduction

Faults can impact fluid flow through the juxtaposition of hydrologically distinct lithologic units and by changes in fault-zone permeability through deformation, alteration, and cementation (e.g., Knipe, 1993; Caine et al., 1996; Rawling et al., 2001). Where fault displacement is less than bed thickness, flow is impacted only by structural and diagenetic modification of the fault zone. Fault-zone structures have been described in geologic materials ranging in strength from crystalline rock (e.g., Chester and Logan, 1986; Reches and Lockner, 1994) to high-porosity sandstones (e.g., Aydin and Johnson, 1978; Antonellini and Aydin, 1994) and poorly lithified sands (e.g., Mozley and Goodwin, 1995; Sigda et al., 1999; Cashman and Cashman, 2000). These studies demonstrate that fractures are the fundamental fault-zone structure in crystalline and low-porosity sedimentary rock, whereas deformation bands are dominant in high-porosity sandstones and poorly lithified sands. Deformation bands are narrow zones in which grain-size reduction through cataclasis, grain-boundary sliding, and pore collapse accommodate millimeter- to centimeter-scale displacements. In contrast to fractures, deformation bands reduce porosity and saturated permeability with respect to the protolith (e.g., Antonellini and Aydin, 1994; Sigda et al., 1999). Under unsaturated conditions, permeability is a function of water content and pore size. In semi-arid to arid climates, where small pores retain water more effectively than large pores, low-porosity

deformation bands can be up to six orders of magnitude more permeable than protolith sands in the vadose zone (Sigda and Wilson, 2003).

These field-based studies suggest that the primary controls on mode of failure of a given rock include the petrophysical properties of the protolith. Deformation experiments have isolated specific properties, such as grain size and porosity, that affect whether a rock fails by fracture or cataclastic flow (e.g., Wong et al., 1997). These experimental studies also emphasize the importance of extrinsic variables, such as effective pressure.

Ignimbrites are spatially heterogeneous pyroclastic flow deposits consisting of poorly sorted assemblages of phenocrysts, pumice, and lithic clasts in an ashy matrix. Ignimbrite units show a range in degree of welding (compaction and fusion of matrix glass and pumice) and postdepositional crystallization (e.g., devitrification and vapor-phase crystallization, by which secondary minerals replace glass and grow in pore spaces, respectively). These processes are dependent on such factors as eruption temperature and melt composition (Ross and Smith, 1961; Smith and Bailey, 1966). Welding decreases porosity and increases grain-contact area and strength: compaction enlarges contact area, and fusion of contacts increases their strength. This increase in area and strength of grain contacts provides a rigid framework through which fractures may propagate, thereby increasing the rock's mechanical strength (e.g., Moon, 1993). Postdepositional crystallization also reduces porosity and can increase grain-contact area and strength where interlocking crystals replace glass and grow across grain margins.

In this paper, we document deformation bands in ash-dominated ignimbrites near Los Alamos, New Mexico, and at Busted Butte, Nevada. Deformation bands have

previously been described only in sedimentary materials, such as high-porosity sandstone, poorly lithified sand, and mudstone. Because their impact on fluid flow is quite different from that of fractures, we have evaluated what controls whether a given ignimbrite unit fails by fracture or by cataclasis within a deformation band. Confining pressure is low in these near-surface deposits, and variations in extrinsic properties within the study areas are negligible; this allows us to isolate the effect of petrophysical properties on deformation. This is the first systematic study of physical controls on fault-zone structure in a natural laboratory setting. We have found that welded units fail by fracture, whereas failure by cataclasis within deformation bands occurs only in nonwelded units; thus, degree of welding is the primary control on mode of failure. Spatially variable postdepositional crystallization exerts a secondary control on mode of failure, inferred from the observation that crystallized nonwelded ignimbrites exhibit both shear fractures and deformation bands.

Widespread alteration and cementation of deformation bands provides evidence that they have served as preferential fluid flow paths in the vadose zone. Pore-size reduction may therefore enhance the unsaturated permeability of deformation bands in ignimbrites. Although rarely mapped because of their size, small-displacement faults like these are common in tectonically active areas (e.g., Carter and Winter, 1995), and their character and spatial distribution are important to consider when evaluating fault-zone impacts on fluid flow (cf. Sigda and Wilson, 2003).

Study Sites

Bandelier Tuff, Los Alamos, New Mexico

The Bandelier Tuff of northern New Mexico includes the 1.6 Ma Otowi Member and the 1.2 Ma Tshirege Member (Fig. 3.1a; Smith and Bailey, 1966; Izett and Obradovich, 1994). Both are dominated by silicic ash with subordinate amounts of pumice, lithic clasts, and phenocrysts of quartz, sanidine, and plagioclase feldspar (Broxton and Reneau, 1995). The Otowi Member is a single, nonwelded, glassy ignimbrite unit. The Tshirege Member comprises a sequence of ignimbrite units that vary in degree of welding and postdepositional crystallization.

In the vicinity of Los Alamos, the Bandelier Tuff is cut by the 41-km-long, rift-related, Pajarito normal-fault system, comprising four large fault traces, each dipping steeply west or east and striking approximately north (Fig. 3.1a). Displacement is typically dip slip, as much as 180 m on the Pajarito fault, with local evidence of strike slip (Carter and Gardner, 1995). Numerous small-displacement faults (millimeter- to meter-scale throw) are the focus of this study (Fig. A1, Table A1, Appendix A).

Calico Hills & Topopah Spring Tuffs, Busted Butte, Nevada

Normal faults also cut ash-dominated ignimbrite strata in Busted Butte, Nevada (Fig. 3.1b). These 13 Ma silicic ignimbrites include the Topopah Spring member of the Paintbrush Tuff and the Calico Hills Formation (Broxton et al., 1987), which are stratigraphically correlative and mineralogically similar to unsaturated units between the potential high-level nuclear waste repository at Yucca Mountain and the underlying water table (Turin et al., 2002). Major faults associated with Basin and Range extension dip

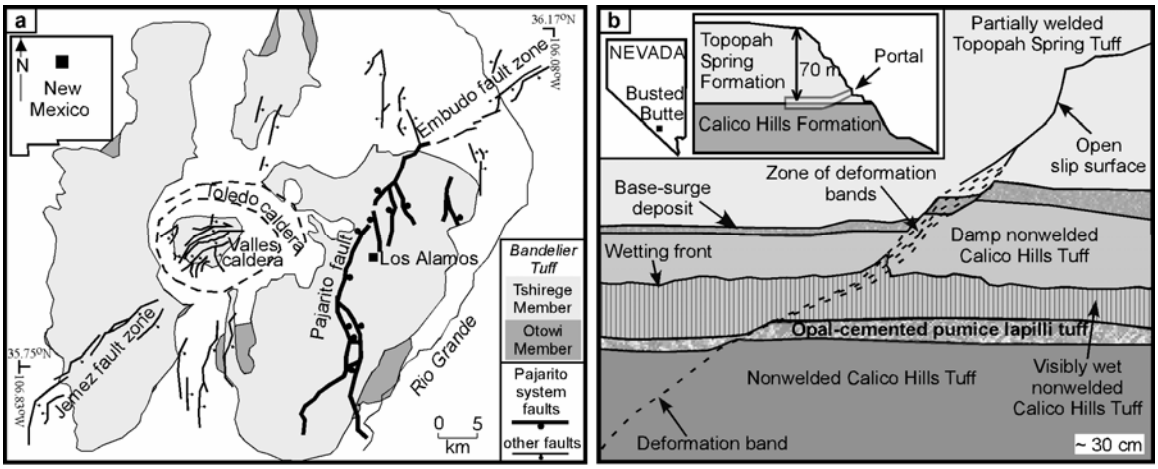

Figure 3.1. (a) Location and simplified structure map of Jemez Mountains, modified from Aldrich (1986), Heiken et al. (1990), and Purtymun (1995). Study area includes Bandelier Tuff east of Pajarito fault system. (b) Normal-fault exposure in Unsaturated Zone Transport Test final mine-back face at Busted Butte, Nevada. Inset gives location, schematic cross section of stratigraphy, and location of portal that leads to face illustrated in larger diagram. Fault-zone character changes from a slip surface in partially welded Topopah Spring Tuff to a zone of deformation bands in nonwelded Calico Hills Tuff. Striped pattern denotes extent of preferential wetting.

steeply, strike approximately north, and juxtapose ignimbrite units by hundreds of meters of dip slip and left-lateral strike slip. Smaller displacement faults occur between these major faults; we studied one of these at the Busted Butte Unsaturated Zone Transport Test facility (Fig. A2, Appendix A; Turin et al., 2002). Tracer migration in the test facility was monitored and analyzed at mine-back faces, the last of which exposed the fault on which we focused (Fig. A3, Appendix A). Tracers did not reach the portion of the fault investigated.

Methods

In addition to study of the fault at Busted Butte, field characterization of more than 100 small-displacement fault zones was conducted in the Bandelier Tuff (Tables A1

and A5, Appendix A). Petrographic analysis of oriented samples of faults and corresponding protolith was followed by backscattered-electron (BSE) imaging and quantitative chemical analysis of clays and alteration phases, performed on a Cameca SX-100 electron microprobe operated at 15 keV and 20 nA beam current. Pixel counts of black (porosity) versus gray (grains) in 100 BSE images per protolith thin section (three sections per sample) were used to quantify porosity (Fig. B2, Appendix B).

Bulk mineral contents of fault-zone material and corresponding protolith were determined by quantitative X-ray diffraction (XRD) analysis using the FULLPAT QXRD method (Chipera and Bish, 2001). Diffraction patterns were obtained on a Siemens D500 X-ray powder diffractometer using Cu$K\alpha$ radiation, incident- and diffracted-beam Soller slits, and a Kevex Si(Li) solid-state detector from 2° to 70° 2θ, using 0.02° steps, and counting for at least 2 s per step.

Fault-Zone Structures in Ignimbrites

Fractures vs. Deformation Bands

The ignimbrites display spatially variable welding, porosity, postdepositional crystallization and matrix ash, pumice, phenocryst, and lithic clast content (Fig. 3.2; Table B1, Appendix B). Poorly lithified, nonwelded units (pumice aspect ratio < 6:1) have high porosity and exhibit variable amounts of crystallization (0–24 wt% cristobalite $\pm$ tridymite). Welded units (pumice aspect ratio > 6:1) are crystallized, have higher phenocryst and ash contents per unit volume, and have considerably lower porosity (Fig. 3.2).

Fractures are the only fault-zone structures observed in welded units. In contrast,

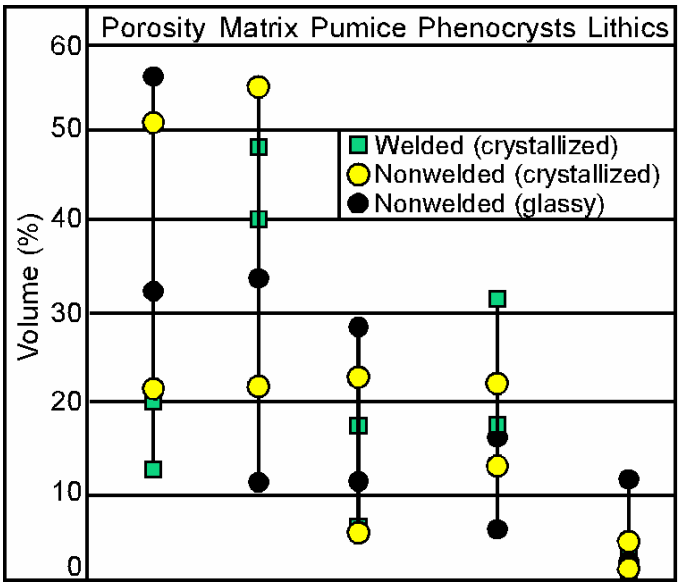

Figure 3.2. Porosity and grain types in undeformed Bandelier and Calico Hills tuffs. Porosities determined from pixel counts of BSE images; relative abundance of grain types determined from point counts on a petrographic microscope. Matrix includes intact glass shards, ash, and crushed pumice (glassy or crystallized). Data from three samples of welded units, six samples of crystallized nonwelded units, and six glassy nonwelded units.

deformation bands are the only structures found in high-porosity, glassy, nonwelded units. Moderately high-porosity units that are not welded but have undergone postdepositional crystallization exhibit both deformation bands and fractures, commonly in the same outcrop. In the latter cases, deformation bands and fractures have similar orientations, but rarely intersect, instead occurring in spatially distinct zones. In one outcrop, fractures crosscut a zone of deformation bands. In nonwelded but variably crystallized units of the Bandelier Tuff, deformation bands are least prevalent where postdepositional crystallization results in higher cristobalite versus tridymite and glass contents (Fig. 3.3).

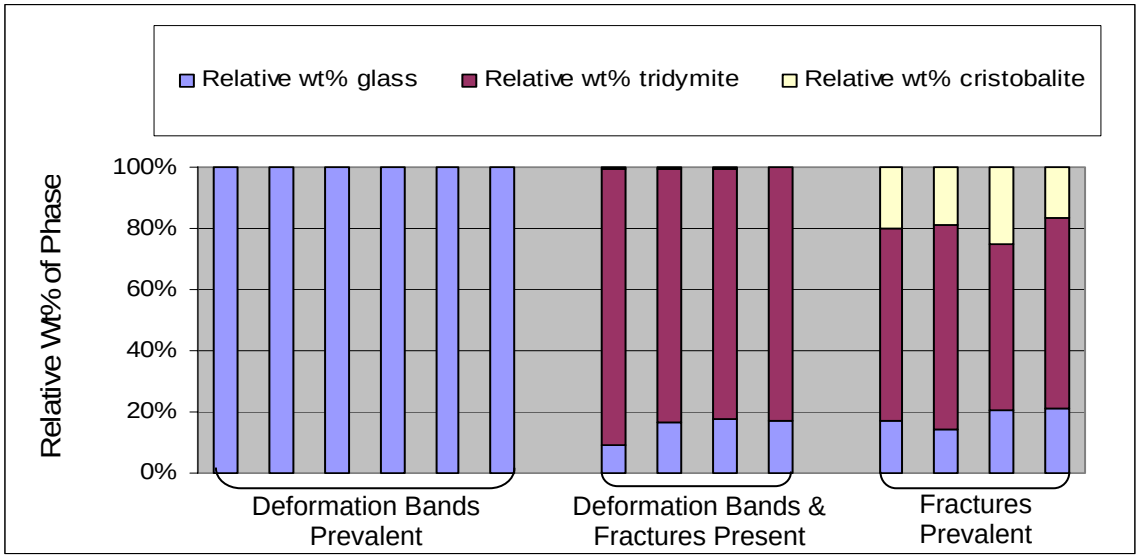

Figure 3.3. Variation in glass, tridymite, and cristobalite content of nonwelded Bandelier Tuff exhibiting various deformation mechanisms. Only these three phases were considered for mechanical influence on fault-zone deformation, and were therefore normalized to 100 wt%. Mode-of-failure categories are based on the predominant fault type found in each outcrop location (vertical bars). Thus, 6 outcrops are dominated by deformation bands, 4 outcrops have both deformation bands and fractures, and 4 outcrops are dominated by fractures. Only outcrop locations for which mineralogic data were obtained are considered in this comparison.

Deformation-band fault zones are 0.1–15 cm wide and vary in complexity from a single deformation band to a zone of anastomosing bands (Fig. 3.4). At the microscopic scale, they exhibit diffuse, nonplanar boundaries, which locally weave around large phenocrysts and lithic clasts. Deformation bands exhibit lower porosity and smaller pore and grain sizes than protolith. Grain crushing has destroyed the walls of pumice vesicles, connecting previously isolated pore space even though porosity is reduced. Elongate grains are typically aligned and pores are elongate parallel to aligned grains, recording dip, oblique, or strike slip for a given fault, consistent with the variety of sense-of-slip indicators on larger faults in the area (Carter and Gardner, 1995). Pore throat size was reduced by this grain alignment, which may have altered the tortuosity of flow pathways. Clay- and silt-sized grains are common; large grains are locally preserved. XRD analyses

confirm petrographic observations that fine-grained fault material consists mostly of ignimbrite fragments with variable amounts of alteration minerals and/or cement (Table 3.1, also see Chapter 4).

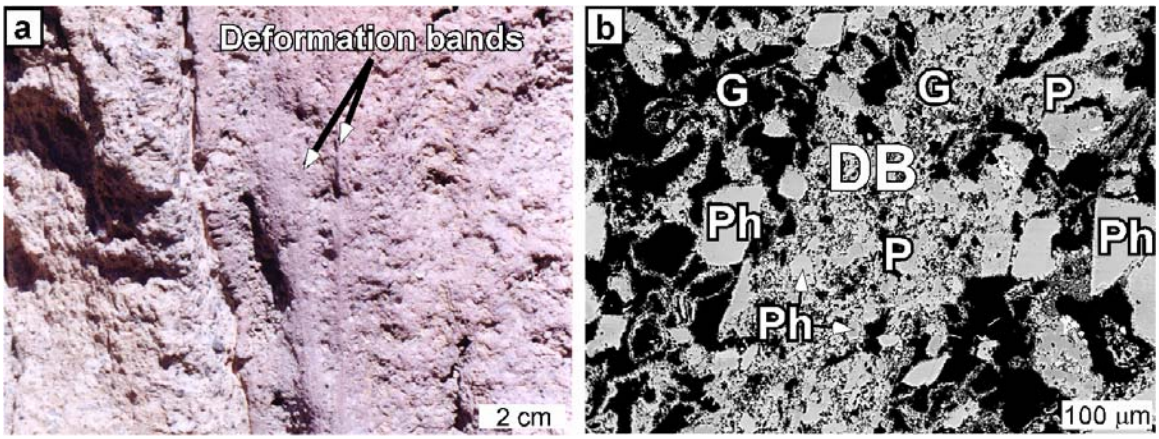

Figure 3.4. (a) Deformation bands in crystallized nonwelded Bandelier Tuff. (b) BSE image of a deformation band (DB) in sample from (a). Note reduction in both porosity (black) and size of phenocrysts (Ph), crystallized glass shards (G), and pumice fragments (P) in deformation band.

Table 3.1. Porosity and mineral contents for selected protolith-deformation band pairs

Deformation-band (DB) and protolith* type	Porosity (%)	Glass (wt%)	Quartz (wt%)	Feldspar (wt%)	Cristobalite (wt%)	Tridymite (wt%)	Smectite (wt%)	Calcite (wt%)	Other† (wt%)	Total§ (wt%)
Unaltered DB (BB5)	10.7	73.1	2.3	8.7	0.0	0.0	14.4	0.0	1.5	100.0
Glassy protolith (BB2)	41.0#	76.0	3.0	8.0	1.0	0.0	11.0	0.0	1.0	100.0
Unaltered DB (bt1)	25.9	11.7	3.8	58.6	7.3	13.5	0.0	0.0	5.3	100.2
Crystallized protolith (bt37)	46.9	5.8	16.8	52.4	4.5	17.2	0.0	0.0	2.9	99.6
DB with smectite (bt7)	2.0#	21.2	2.0	6.6	0.0	0.0	70.2	0.0	0.0	100.0
Glassy protolith (bt7c)	48.6#	71.9	10.7	13.0	0.0	0.0	1.5	0.0	2.0	99.1
DB with smectite (bt119)	14.4	0.0	1.4	4.8	0.2	0.0	93.5	0.0	0.0	99.9
Crystallized protolith (bt120)	42.4	4.2	6.3	65.9	5.2	11.2	0.0	0.0	6.1	98.9
DB with smectite & calcite (bt111b)	21.7	16.0	10.9	24.1	1.7	6.3	36.5	2.8	1.2	99.9
Crystallized protolith (bt68)	40.6#	4.0	17.6	55.1	4.8	14.9	0.0	0.0	3.5	99.9

*All protoliths are nonwelded ignimbrites, and sample numbers correspond to those given in Appendix A.

†Other minerals include magnetite, augite, mica, and hematite.

§Total weight percentages exclude trace amounts of dolomite, halite, and fluorite found in some samples.

#Porosity determined from nearby sample (different from the sample analyzed for bulk mineral contents).

Alteration and Mineralization

More than two-thirds of the deformation bands contain some smectite (1.4–93.5 wt%) and/or calcite cement (2.8–42.4 wt%; Table 3.1). These minerals line or fill pore space and, in faults reactivated subsequent to alteration and/or cementation, help define a compositional-banding foliation with cataclastic ignimbrite material (Fig. 3.5).

Deformation bands containing clay (0.1–3 cm wide) are characterized by bands of foliated smectite that anastomose around fragments of ash, pumice, phenocrysts, and lithic clasts (Fig. 3.5a). Multiple episodes of deformation and clay enrichment are evidenced by crosscutting relationships between clay-rich bands that contain variable amounts of cataclastic ignimbrite fragments.

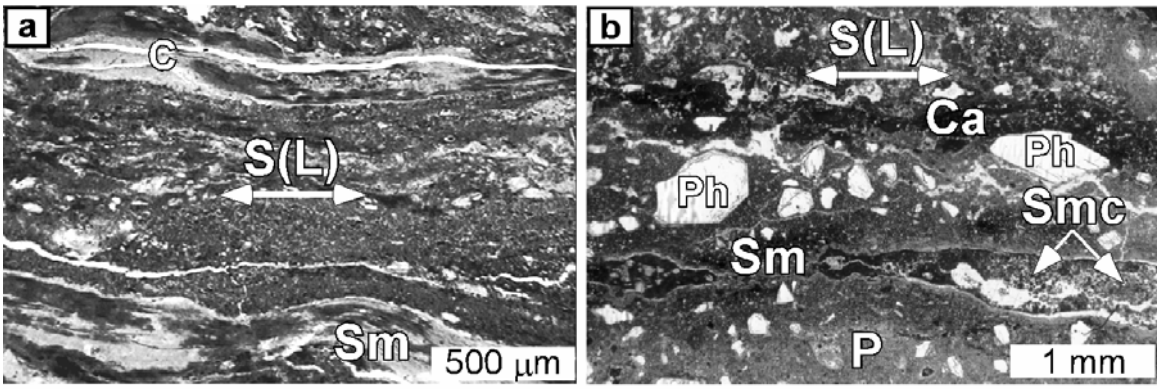

Figure 3.5. (a) Plane-light photomicrograph of a deformation-band fault zone containing 70.2 wt% smectite. Foliated smectite (Sm) and bands of smectite with ignimbrite fragments (S) are parallel to fault plane (arrow). Elongate clasts define a slip-parallel lineation (L). Desiccation cracks (C) in pure smectite bands formed during sample preparation. (b) Scanned thin-section image of a deformation-band fault zone with foliation (S) defined by bands of smectite (e.g., Sm) and calcite (Ca, black) containing clasts of smectite (Smc), crushed phenocrysts, glass, and pumice. Some phenocrysts (Ph) were rotated into alignment with slip direction (L) without crushing. Boundary between deformation band and protolith (P) is irregular.

Some of these deformation bands are also variably cemented by microcrystalline calcite. Grain-size reduction and fault-parallel alignment of elongate grains and pores

are evident in these 0.5–5-cm-wide fault zones. Episodic fault movement, alteration, and cementation are recorded by aligned pores and bands of calcite that typically contain clasts of both ignimbrite and smectite and anastomose around foliated smectite bands (Fig. 3.5b).

Mode-of-Failure Transition

A range in structures was observed in a single, continuous fault zone at Busted Butte (Fig. 3.1b). The 0.5 to 10 cm-wide fault zone shows 10 cm of apparent throw. Where it cuts partially welded Topopah Spring Tuff, the fault zone consists of fractures. In the nonwelded base-surge deposit of the Topopah Spring Tuff and the nonwelded Calico Hills Tuff, it consists of deformation bands, indicating that mode of failure is directly dependent on degree of welding of the protolith. Part of the Calico Hills Tuff is preferentially wet with water injected into an opal-cemented lapilli tuff layer during the Unsaturated Zone Transport Test (Turin et al., 2002; Fig. 3.1b). The wetting front extends farther into the fault zone than into the surrounding material, suggesting that it has different hydrologic properties than the protolith.

In addition to this spatial mode-of-failure transition across a boundary between partially welded and nonwelded ignimbrite layers, evidence of a temporal mode-of-failure transition is observed in one outcrop of crystallized nonwelded Bandelier Tuff. At this location (Location 2 in Fig. A1 and Table A1, Appendix A), a 15-cm wide fault zone contains deformation bands in its center and fractures at its boundaries (Fig. 3.6a). The bounding fractures truncate and deform the zone of deformation bands, indicating that the fractures are younger (Fig. 3.6b). This is similar to observations of zones of deformation

bands bounded by slip surfaces in high porosity sandstone (e.g., Aydin and Johnson, 1978; 1983). Evidence of fluid-fault interaction is seen in the post-faulting Fe- and Sn-oxide mineralization extending from the zone of deformation bands into the open slip surface (Fig. 3.6c).

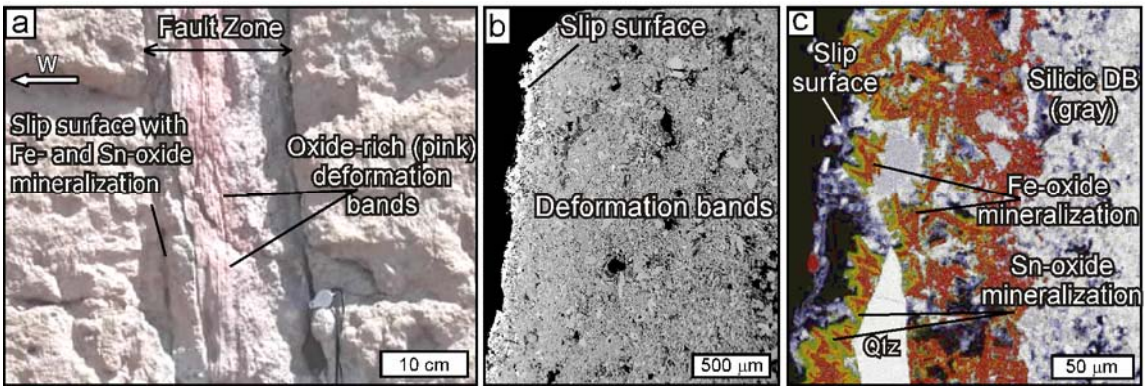

Figure 3.6. Temporal mode-of-failure transition in crystallized nonwelded Bandelier Tuff. (a) Outcrop photo of a deformation-band fault zone in which unaltered and oxide-mineralized (pink) deformation bands are truncated by an open, mineralized slip surface. (b) BSE image of open slip surface that cuts adjacent zone of deformation bands. (c) X-ray map showing iron- (red) and tin-oxide (green) mineralization on slip surface. Note the undeformed nature of individual oxide minerals, and the apparent outward growth from the deformation band margin.

Discussion

Controls on Fault-Zone Structure in Ignimbrites

Deformation bands are observed in glassy, nonwelded units in the Bandelier Tuff and at Busted Butte; fractures are observed in welded units. Welding increases the mechanical strength of the rock (Moon, 1993) by decreasing porosity and increasing the strength and area of grain contacts. We therefore infer that welding influences mode of failure.

Postdepositional crystallization can decrease porosity and increase grain-contact area and strength in nonwelded units via occlusion of porosity and production of a fine-grained, crystalline rock. This strengthening effect appears to be secondary to welding,

as both fractures and deformation bands are found in crystallized, nonwelded units. Where present in the same outcrop, fractures and deformation bands generally occur in spatially distinct zones. This suggests spatial variations in the strength of crystallized, nonwelded units, consistent with variations in degree and nature of postdepositional crystallization. Degree of postdepositional crystallization is indicated in this study by wt% glass versus tridymite and cristobalite, in which higher degrees of crystallization result in embrittlement of the ignimbrite and preferential development of fractures over deformation bands (Fig. 3.3). Nature of postdepositional crystallization refers to a combination of quantitative and qualitative characteristics of an ignimbrite, such as wt% cristobalite vs. tridymite and connectivity of postdepositional crystals, respectively. Relative abundances of cristobalite and tridymite in protolith suggest that the presence of cristobalite is either the cause (i.e., the mineral itself imparts strength to the rock via its finer grain size and stronger crystal lattice configuration) or an indicator (i.e., indicates higher eruption temperature, causing incipient welding and more extensive crystallization) of embrittlement of the ignimbrite, resulting in development of fractures instead of deformation bands (Fig. 3.3). Observations of incipient welding, finer grain size, and more extensive grain connectivity for protolith containing higher wt% cristobalite confirm that cristobalite is both a cause and indicator for the development of fractures over deformation bands. Accordingly, the spatial mode-of-failure transition from cataclasis within deformation bands to fracturing in crystallized nonwelded ignimbrites may be qualitatively described in terms of relative contents of glass, tridymite, and cristobalite in protolith (Fig. 3.3). A quantitative relationship between the relative contents of these phases and deformation behavior has not been investigated.

In one location, where fractures and deformation bands occur together, a temporal mode-of-failure transition is documented by deformation bands that are truncated by bounding fractures (Fig. 3.6). It is hypothesized that the reduction in pore and grain size within the central zone of deformation bands (Fig. 3.6b) resulted in a strain or strain-rate hardening and development of a through-going fracture surface (Goodwin et al., 2001), a process similar to that inferred from structures in faults in porous sandstone (cf. Aydin and Johnson, 1983; Antonellini and Aydin, 1994; Shipton and Cowie, 2001).

Within the ranges considered (Fig. 3.2), relative amounts of ash, pumice, phenocrysts, and lithic clasts in protolith ignimbrite do not affect mode of failure. However, these ash-dominated units may be mechanically distinct from more pumice- or lithic-rich ignimbrites (e.g., Evans and Bradbury, 2004).

Implications for Fluid Flow

The effect of deformation bands on nonwelded ignimbrite permeability has not been previously considered, as the structures were not previously recognized. Our observations allow us to make qualitative statements about the impact of these deformation bands on fluid flow.

The variability of pore-throat geometry and pore connectivity in nonwelded ignimbrites causes highly variable saturated permeability (e.g., Rogers and Gallaher, 1995). Within deformation bands, cataclasis also can reduce porosity by up to 30% (Table 3.1) and saturated permeability by up to one order of magnitude relative to protolith (see Chapter 5). Future corrections to this dataset that isolate the permeability of the deformation band from the surrounding protolith may reveal larger reductions in

saturated permeability caused by fault-zone deformation. These data and an understanding of the continuity and spatial density of deformation bands in nonwelded ignimbrites must be integrated in order to evaluate the impact of these structures on groundwater flow.

Pore-size reduction in deformation bands in nonwelded ignimbrites enhances unsaturated permeability because capillarity and water retention are inversely related to pore radius (Stephens, 1996). In the vadose zone of dry desert environments, this inverse relationship causes the smaller pores in deformation bands in sand to preferentially retain water (cf. Sigda and Wilson, 2003). Preferential wetting of the zone of deformation bands observed at Busted Butte supports an interpretation of increased unsaturated fault-zone permeability (Fig. 3.1b). Our hypothesis is also supported by the presence of at least small amounts of smectite and calcite in most deformation bands in the Los Alamos area. At most of these locations, the Bandelier Tuff has been above the water table since deposition (Purtymun and Johansen, 1974); therefore, preferential alteration and cementation of these fault zones is evidence of localized vadose-zone fluid transport.

Conclusions

Degree of welding and degree and type of postdepositional crystallization determine whether a given ash-dominated ignimbrite unit deforms by formation of fractures or deformation bands. These characteristics are inversely proportional to porosity and directly related to grain-contact area and strength. These relationships between fault-zone structure and protolith petrophysical properties provide a basis for predicting fault-zone character from rock type, which is useful for fluid flow and

transport models. Widespread fault-zone diagenesis records preferential vadose-zone fluid transport, suggesting that deformation bands in nonwelded ignimbrites enhance unsaturated fault-zone permeability. The magnitude of this increase and the density of deformation bands necessary to create significant flow paths for recharge and contaminant transport have not yet been determined. However, our work illustrates the importance of considering near-surface deformation of porous materials in understanding fault-zone impacts on flow and transport.

Acknowledgments

This research was funded by a grant from the Institute of Geophysics and Planetary Physics (IGPP Proposal #1121R) at Los Alamos National Laboratory, with additional funding from the Wyoming Geological Association, the New Mexico Tech Graduate Student Association, and the New Mexico Geological Society. We thank Nelia Dunbar and Lynn Heizler for assistance on the electron microprobe, Steve Chipera for XRD analyses, Schön Levy for access and assistance at Busted Butte, and members of the Faults and Fluids Group at New Mexico Tech for useful discussions. This is Los Alamos National Laboratory publication number LA-UR-03-1701.

References Cited

Aldrich, M., 1986, Tectonics of the Jemez lineament in the Jemez Mountains and Rio Grande Rift: Journal of Geophysical Research, v. 91, p. 1753–1762.

Antonellini, M., and Aydin, A., 1994, Effect of faulting on fluid flow in porous sandstones: Petrophysical properties: American Association of Petroleum Geologists Bulletin, v. 78, p. 355–377.

Aydin, A., and Johnson, A., 1983, Analysis of faulting in porous sandstones: Journal of Structural Geology, v. 5, no. 1, p. 19-31.

Aydin, A., and Johnson, A., 1978, Development of faults as zones of deformation bands and as slip surfaces in sandstones: Pure and Applied Geophysics, v. 116, p. 931–942.

Broxton, D., and Reneau, S., 1995, Stratigraphic nomenclature of the Bandelier Tuff for the Environmental Restoration Project at Los Alamos National Laboratory: Los Alamos National Laboratory Report LA-13010-MS, 20 p.

Broxton, D., Bish, D., and Warren, R., 1987, Distribution and chemistry of diagenetic minerals at Yucca Mountain, Nye County, Nevada: Clays and Clay Minerals, v. 35, p. 89–110.

Caine, J.S., Evans, J.P., and Forster, C.B., 1996, Fault zone architecture and permeability structure: Geology, v. 24, p. 1025–1028.

Carter, K.E., and Gardner, J.N., 1995, Quaternary fault kinematics in the northwestern Espanola Basin, Rio Grande rift, New Mexico, *in* Bauer, P.W., Kues, B.S., Dunbar, N.W., Karlstrom, K.E., Harrison, B., eds., Geology of the Santa Fe region: New Mexico Geological Society Guidebook, 46th Field Conference, p. 97–103.

Carter, K.E., and Winter, C.L., 1995, Fractal nature and scaling of normal faults in the Espanola Basin, Rio Grande rift, New Mexico: implications for fault growth and brittle strain: Journal of Structural Geology, v. 17, no. 6, p. 863-873.

Cashman, S., and Cashman, K., 2000, Cataclasis and deformation-band formation in unconsolidated marine terrace sand, Humboldt County, California: Geology, v. 28, p. 111–114.

Chester, F., and Logan, J., 1986, Implications for mechanical properties of brittle faults from observations of the Punchbowl fault zone, California: Pure and Applied Geophysics, v. 124, p. 79–106.

Chipera, S.J., and Bish, D.L., 2001, FULLPAT: An improved full-pattern quantitative X-ray diffraction method: Madison, Wisconsin, Clay Minerals Society, Proceedings of the 38th Annual Meeting, p. 105.

Evans, J.P., and Bradbury, K.K., 2004, Faulting and Fracturing of Nonwelded Bishop Tuff, Eastern California: Deformation mechanisms in very porous materials in the vadose zone, Vadose Zone Journal, v. 3, p. 602-623.

Goodwin, L.B., Rawling, G.C., Wilson, J.E., and Tobin, H.J., 2001, Mode-of-failure transitions in high porosity sedimentary and ignimbrite deposits, and implications for fault-zone structure and architecture: Eos Trans. AGU, v. 82, no. 47, Fall Meet. Suppl., Abstract S41A-0581.

Heiken, G., Goff, F., Gardner, J., Baldridge, W., Hulen, J., Nielson, D., and Vaniman, D., 1990, The Valles/Toledo caldera complex, Jemez volcanic field, New Mexico: Annual Review of Earth and Planetary Sciences, v. 18, p. 27–53.

Izett, G.A., and Obradovich, J.D., 1994, $^{40}Ar/^{39}Ar$ age constraints on the Jaramillo Normal Subchron and the Matuyama-Brunhes geomagnetic boundary: Journal of Geophysical Research, v. 99, p. 2925–2934.

Knipe, R.J., 1993, The influence of fault zone processes and diagenesis on fluid flow, *in* Horbury, A.D., and Robinson, A.G., eds., Diagenesis and basin development: American Association of Petroleum Geologists Studies in Geology no. 36, p. 135–148.

Moon, V., 1993, Microstructural controls on the geomechanical behavior of ignimbrite: Engineering Geology, v. 35, p. 19–31.

Mozley, P.S., and Goodwin, L.B., 1995, Patterns of cementation along a Cenozoic normal fault: A record of paleoflow orientations: Geology, v. 23, p. 539–542.

Purtymun, W., 1995, Geologic and hydrologic records of observation wells, test holes, test wells, supply wells, springs, and surface water stations in the Los Alamos area: Los Alamos National Laboratory Report LA-12883-MS, 339 p.

Purtymun, W.D., and Johansen, S., 1974, General geohydrology of the Pajarito Plateau, *in* Ghost Ranch: New Mexico Geological Society Guidebook, 25th Field Conference, p. 347–349.

Rawling, G., Goodwin, L., and Wilson, J., 2001, Internal architecture, permeability structure, and hydrologic significance of contrasting fault zone types: Geology, v. 29, p. 43–46.

Reches, Z., and Lockner, D.A., 1994, Nucleation and growth of faults in brittle rock: Journal of Geophysical Research, v. 99, p. 18,159–18,173.

Rogers, D., and Gallaher, B., 1995, The unsaturated hydraulic characteristics of the Bandelier Tuff: Los Alamos National Laboratory Report LA-12968-MS, 76 p.

Ross, C.S., Smith, R.L., 1961. Ash-flow tuffs: their origin, geologic relations, and identification. U.S. Geological Survey Professional Paper 366, 81 p.

Shipton, Z.K., and Cowie, P.A., 2001, Damage zone and slip surface evolution over μm to km scales in high-porosity Navajo sandstone, Utah, Journal of Structural Geology, v. 23, p. 1825-1844.

Sigda, J., Goodwin, L., Mozley, P., and Wilson, J., 1999, Permeability Alteration in Small-Displacement Faults in Poorly Lithified Sediments: Rio Grande Rift,

Central New Mexico, *in* Haneberg, W., Mozley, P., Moore, J., and Goodwin, L., eds., Faults and Subsurface Fluid Flow in the Shallow Crust: American Geophysical Union Monograph, v. 113, p. 51-68.

Sigda, J., and Wilson, J.L., 2003, Are faults preferential flow paths through semi-arid and arid vadose zones?: Water Resources Research v. 39, doi:10.1029/2002WR001406.

Stephens, D.B., 1996, Vadose Zone Hydrology: Boca Raton, Florida, CRC Press, Inc., 347 p.

Turin, J.H., Groffman, A.R., Wolfsberg, L.E., Roach, J.L., and Strietelmeier, B.A., 2002, Tracer and radionuclide sorption to vitric tuffs of Busted Butte, Nevada: Applied Geochemistry, v. 17, no. 6, p. 825–836.

Smith, R.L., and Bailey, R.A., 1966, The Bandelier Tuff—A study of ash-flow eruption cycles from zoned magma chambers: Bulletin of Volcanology, v. 29, p. 83–104.

Wong, T.-F., David, C., and Zhu, W., 1997, The transition from brittle faulting to cataclastic flow in porous sandstones: Mechanical deformation: Journal of Geophysical Research, v. 102, p. 3009–3025.

CHAPTER 4

DIAGENETIC ALTERATION AND MINERALIZATION OF DEFORMATION-BAND FAULTS IN THE BANDELIER TUFF, LOS ALAMOS, NM: A RECORD OF VADOSE-ZONE FLOW AND TRANSPORT[1]

Abstract

The character of a given fault zone (presence of fractures versus deformation bands, degree and nature of diagenetic alteration, etc.) directly influences the effect it will have on fluid flow and transport. This study focuses on the microstructural and geochemical record of unsaturated fluid flow and transport within deformation-band faults in nonwelded ignimbrites of the Bandelier Tuff. More than two-thirds of these faults display preferential alteration and mineralization compared to adjacent protolith. Stable isotope analyses indicate that smectite alteration and calcite cementation in deformation bands result from low-temperature meteoric fluid-fault interaction. The microstructural character, rare earth element (REE) signatures, and chemical compositions of smectite in the deformation bands suggest that it is introduced to fault zones by a combination of translocation from the surface and localized *in situ* alteration of fault gouge. Translocation of smectite in deformation bands requires preferential fluid flow. Rod-shaped calcite microcrystallites and the close association of calcite with plant roots suggest a combination of pedogenic, biologically mediated and physicochemical

[1]To be submitted to the Journal of Geophysical Research.

(desiccation through cyclic wetting/drying) precipitation. Since roots in this semiarid climate seek moisture, we infer that associated calcite indicates preferential wetting of deformation bands, which facilitates fluid flow in semiarid vadose zones. Enrichment in smectite and calcite associated with this preferential fluid flow is accompanied by changes in oxide and trace element contents (e.g., CaO, MgO, Fe_2O_3, TiO_2, Na_2O, K_2O, V, Cr, Cu, and Sr) of deformation bands with respect to protolith. Collectively, these observations indicate that these faults have served as, and may still be, zones of preferential vadose-zone fluid flow and transport. Continued alteration, infiltration, and mineralization can further modify fault-rock permeability, change the mechanical properties of the fault zone, and affect the transport of solutes via hydrogeochemical processes such as dissolution, precipitation, and adsorption.

Introduction

The interaction between fluid flow and faulting is complex and involves an incompletely understood combination of processes. One approach to understanding these processes is to measure the hydrologic properties (e.g., porosity and permeability) of fault rock with respect to protolith [e.g., Antonellini and Aydin, 1994; Sigda et al., 1999; Rawling et al., 2001; Dinwiddie et al., 2002]. This approach usually requires sophisticated equipment, large amounts of data, and time-consuming data reduction and correction algorithms [e.g., Aronson, 1999; Tidwell and Wilson, 2000]. Another useful way to evaluate the interaction between faulting and fluid flow is to integrate microstructural characterization with the diagenetic record of flow found in fault rock [e.g., Knipe, 1993; Evans and Chester, 1995; Mozley and Goodwin, 1995]. In this

approach, microstructural analysis of fault-zone material characterizes the pores and pathways through which fluids move through fault rock and geochemical analyses of variably altered fault material can identify fault zones as conduits, barriers, or complex conduit-barrier systems [e.g., Caine et al., 1996; Tobin et al., 2001].

Faults occur in a variety of classes, including large- (> cm-scale) versus small-displacement faults and those that are dominated by fractures versus deformation bands. Larger displacement faults affect fluid flow by both the juxtaposition of lithologies with different hydrologic properties and the structural and diagenetic modification of fluid pathways within the fault zone. Small-displacement faults, which are typically not mapped but are common in tectonically active areas [e.g., Carter and Winter, 1995], impact fluid flow only by the latter process. These faults are the focus of this paper, in which we report on the inferred effects of deformation bands on vadose-zone flow and transport in ignimbrites.

Deformation bands are narrow zones in which grain-size reduction, grain-boundary sliding, and pore collapse accommodate mm-cm displacements (Fig. 4.1). These structures have been described in high porosity sandstones [e.g., Aydin and Johnson, 1978; Antonellini and Aydin, 1994], poorly lithified sands [e.g. Mozley and Goodwin, 1995; Cashman and Cashman, 2000], and nonwelded, ash-dominated ignimbrites [Wilson et al., 2003]. In contrast to fractures, which increase porosity and saturated permeability with respect to protolith, deformation bands reduce these properties [e.g., Antonellini and Aydin, 1994; Sigda et al., 1999]. Under unsaturated conditions, permeability is a function of water content and pore size [Stephens, 1996]. In the vadose zone of semiarid to arid climates, where small pores retain water more

effectively than large pores, low-porosity deformation bands in sand can be up to six orders of magnitude more permeable than surrounding protolith [Sigda and Wilson, 2003]. This can have significant effects on fluid flow and diagenesis since these processes are more likely to occur in zones of pore collapse and grain crushing due to increased capillarity and surface area for chemical reaction.

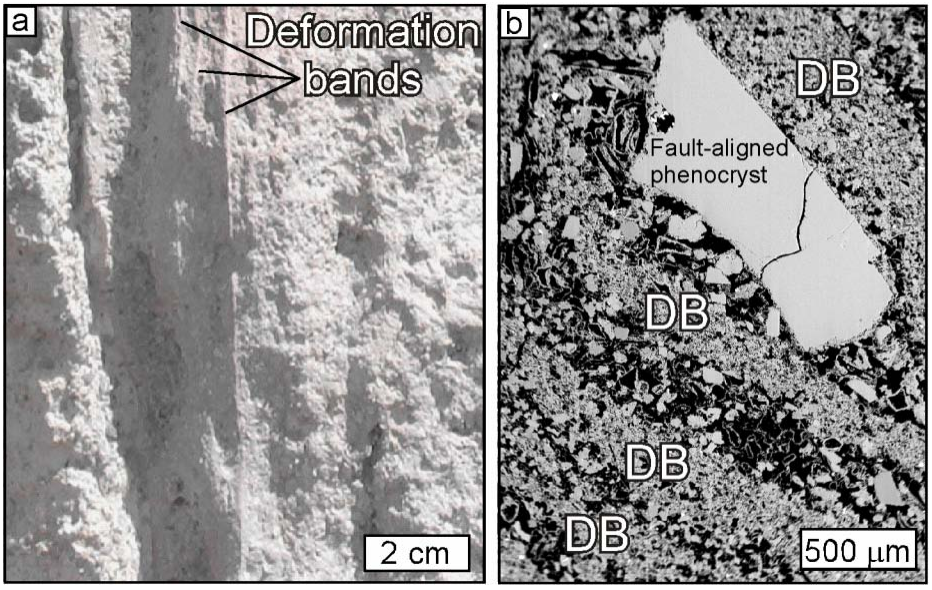

Figure 4.1. (a) Deformation bands in nonwelded crystallized Bandelier Tuff. (b) BSE image of deformation bands (DBs) in sample from (a). DBs are characterized by crushed and/or aligned grains (gray) and collapsed pores (black).

The Bandelier Tuff is a sequence of ignimbrite deposits located in northern New Mexico that, for the most part, has been above the water table since deposition [Purtymun and Johansen, 1974; Fig. 4.2a]. Wilson et al. [2003] documented deformation bands in more than half of the stratigraphic thickness of the ignimbrite deposit that defines the Pajarito Plateau (Fig. 4.2a, b). Through outcrop characterization, petrographic observations, and mineralogic data, they showed that these fault zones are found only in nonwelded units of the Bandelier Tuff (Fig. 4.2b). As small-displacement faults, deformation bands are common features of the Pajarito Plateau [cf., Carter and Winter,

1995; Wilson et al., 2003]. However, because these structures were only recently recognized in the area, little is known about the influence of the deformation bands on vadose-zone fluid flow and transport. Wilson et al. [2003] do, however, note that these faults have experienced a different diagenetic history than surrounding protolith. In this paper, we use detailed geochemical analyses (major oxide abundances and trace element concentrations compared to bulk and trace mineralogy) to evaluate whether this diagenesis records preferential flow within these faults in the vadose zone. Stable isotope analyses are used to constrain the sources of fluids that caused preferential diagenesis of deformation bands. Additionally, abundances of Fe-bearing minerals and major oxides, as well as REE signatures are used to constrain the source of diagenetic minerals (i.e.,

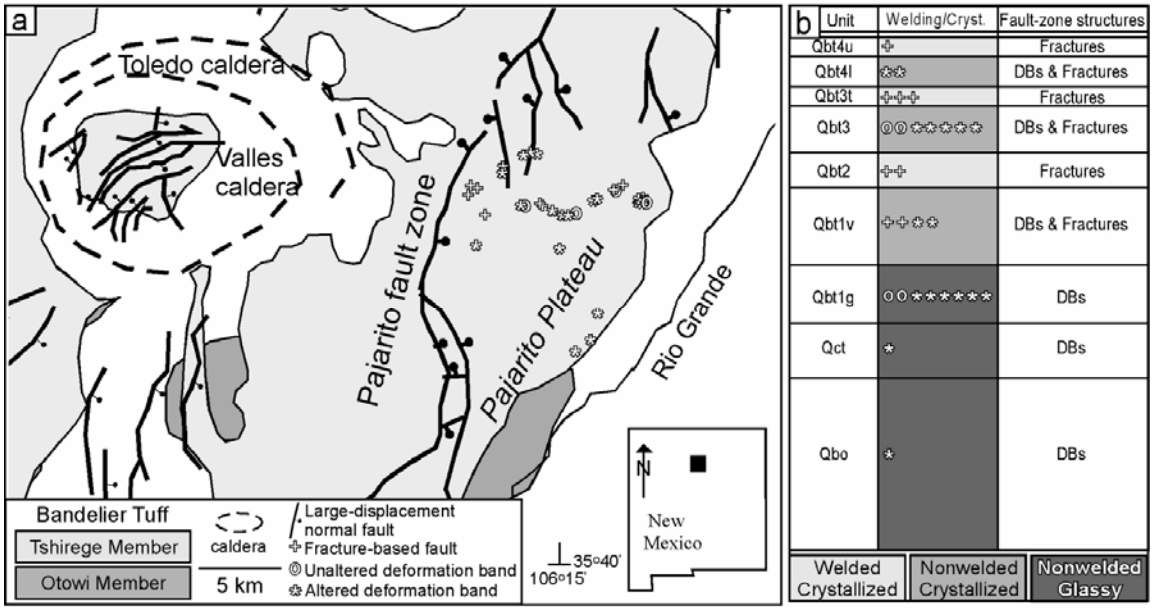

Figure 4.2. (a) Location map and simplified structure map of the Jemez Mountains modified from Aldrich [1986], Heiken et al. [1990], and Purtymun [1995]. Study area covers the Pajarito Plateau, the region of Bandelier Tuff exposure east of the Pajarito fault zone. (b) Mechanical stratigraphy of the Bandelier Tuff. Cooling unit stratigraphy modified from Lewis et al. [2002]. Symbols each represent a single location at which outcrop characterization of at least one fault zone was conducted; the dominant type of fault zone is indicated (see legend). DB = deformation band. Qbo = Otowi Member, Qbt = Tshirege Member.

translocation versus *in situ* alteration) in deformation bands [cf. Vaniman et al., 2002].

Diagenetic modification of deformation bands includes preferential smectite enrichment and calcite cementation. We identify and explore two potential explanations for these processes: (1) Fault zones preferentially retain water, which would be recorded by *in situ* alteration of fault-zone material to hydrous phases and a stable isotope signature indicating that this alteration occurred at near-surface temperatures (i.e., through interaction of ignimbrite and meteoric water). (2) Fault zones experienced higher fluid flux than protolith, which would be recorded by the addition or subtraction of elements from fault rock, indicating transport through deformation bands.

The microstructural and geochemical analyses presented here provide evidence of enhanced fluid flow rather than simply preferential water retention within deformation-band fault zones. If sufficiently closely spaced, such faults might therefore accelerate both recharge and contaminant transport through the vadose zone. This study thus enhances our understanding of the record of preferential paleoflow in the Bandelier Tuff and represents a first step toward understanding how deformation bands might affect present-day vadose-zone fluid flow and solute transport**.**

Geologic Setting

Bandelier Tuff ignimbrite deposits are located on the flanks of the Jemez Mountains of northern New Mexico (Fig. 4.2). The ignimbrite sequence consists of the 1.6 Ma Otowi Member (Qbo) and the 1.2 Ma Tshirege Member (Qbt), which were deposited from pyroclastic eruptions of the Valles/Toledo caldera complex [Smith and Bailey, 1966; Izett and Obradovich, 1994]. Both members are dominated by silicic ash,

with subordinate pumice, lithic clasts, and phenocrysts of quartz, sanidine, and plagioclase feldspar [Broxton et al., 1995; Stimac et al., 1996; Wilson et al., 2003].

Common compositions for silicic glass of the Bandelier Tuff are given in Table 4.1 [Stimac et al., 1996]. Where this silicic glass has undergone postdepositional devitrification, it is replaced by fine-grained cristobalite and potassium feldspar (Table 4.1: Qbt1v feldspar and Qbt1v matrix). During subsequent vapor-phase crystallization, silicic glass and vapor-filled pores are replaced by coarser-grained tridymite, potassium feldspar, minor amounts of cristobalite, and a variety of trace minerals (Table 4.1: Qbt3 matrix and Qbt3 exsolved Fe oxides). The latter include micron-scale mineral coatings of magnetite, zircon, titanite (sphene), monazite, apatite, sylvite, barite, chevkinite, and other minerals rich in Ba, Nb, Y, Pb, Bi, Fe, Ag, Cu, Zn, V, Ni, W, and Sn [Stimac et al., 1996].

The Otowi Member of the Bandelier Tuff is a single, glassy, nonwelded cooling unit. The Tshirege Member comprises a sequence of cooling units, which vary in degree of welding and postdepositional crystallization (Fig. 4.2b). This variation in postdepositional processes leads to a trace-element geochemical stratigraphy [Stimac et al., 1996] as well as a mechanical stratigraphy in which welded units deform by fracture, glassy nonwelded units deform by cataclasis within deformation bands, and crystallized nonwelded units deform by either of these processes (Fig. 4.2b) [Wilson et al., 2003].

On the Pajarito Plateau, the focus of our study, the Bandelier Tuff is cut by the Pajarito fault system, a 41-km long, rift-related, normal fault system consisting of four large faults, each dipping steeply west or east and striking approximately north (Fig. 4.2a). Displacement is characteristically dip-slip, up to 180 m on the Pajarito fault, with

Table 4.1. Chemical Compositions for Glass and Vapor-Phase Replacement Minerals in the Bandelier Tuff*

	Qbt1g glass	Qbt1g glass	Qbt1v feldspar	Qbt1v matrix	Qbt3 matrix	Qbt3 exsolved Fe Oxides
SiO2 (wt%)	74.02	74.51	67.14	78.97	66.74	0.05
TiO2	0.05	0.1	0	0.03	0	9.59
Al2O3	11.55	11.87	17.52	7.38	17.15	0.28
FeO	1.48	1.5	0.16	0.34	0.48	80.65
MnO	0.08	0.1	0	0.02	0	0.24
MgO	<0.01	0.01	0	<0.01	0	0.02
CaO	0.22	0.24	0.01	0.03	0.01	0.01
Na2O	4.09	4.118	4.09	2.2	4.32	NA
K2O	4.22	4.57	10.24	3.63	9.74	NA
Total	95.71	97.08	99.16	92.6	98.44	90.84
Fe (ppm)	11426	11660	1244	2643	3731	626900
Cu	36	ND	ND	5	ND	ND
Zn	169	164	11	20	24	1623
Ga	40	33	5	9	4	72
Ge	10	5	ND	2	ND	ND
Rb	329	356	51	140	12	ND
Sr	ND	ND	ND	ND	4	31
Y	94	111	3	41	14	926
Zr	322	300	18	105	50	3371
Nb	172	162	7	75	3	111
Pb	43	63	4	14	3	86
Th	37	59	4	19	ND	ND
U	ND	14	ND	ND	ND	ND

* Electron microprobe and PIXE data from Stimac et al. [1996]. ND = not detected, NA = not analyzed.

local evidence of strike-slip [Carter and Gardner, 1995]. Many small-displacement faults (mm-m throw) are also present. Although rarely mapped because of their size, the spatial distribution and character of these faults are important to understanding regional deformation [e.g., Carter and Winter, 1995] and subsurface fluid flow [cf. Sigda et al., 1999]. We have focused on these small-displacement faults, particularly deformation bands in nonwelded ignimbrite units, which exhibit variable, apparently diagenetic, alteration and mineralization.

Methods

Outcrop Characterization, Petrography, and Microprobe Analyses

Field characterization of more than 100 small-displacement fault zones in the Bandelier Tuff was conducted over an area covering much of the Pajarito Plateau (Fig. 4.2; Fig. A1, Appendix A). Small-displacement faults were identified as either fracture-

based faults or deformation bands (Table A1, Appendix A). Since fractures have been studied extensively on the Pajarito Plateau [e.g., Wohletz, 1996; Vaniman et al., 2002], we focus here on deformation-band faults. More than two-thirds of the identified deformation-band faults contain >1 wt% smectite and/or calcite—minerals that are present only in trace amounts in the protolith. A representative subset of 10 deformation-band faults was chosen for detailed petrographic and microprobe analyses (Table 4.2). This subset includes five classes of deformation bands, found in both glassy and crystallized nonwelded ignimbrites: (1) unaltered, (2) low smectite content (<10 wt%), (3) high smectite content (>10 wt%), (4) smectite with variable amounts of calcite, and (5) oxide mineralized. Thin sections were prepared from oriented samples of fault-zone material and corresponding protolith. Mineralogy, protolith textures, and fault-zone microstructures were analyzed with a petrographic microscope (Table B1, Appendix B). Calcite cathodoluminescence was observed with a MAAS/Nuclide Luminiscope, ELM-3R Series at <100 millitorr vacuum, 0.3-0.5 mA beam current, and 5-10kV. Backscattered-electron (BSE) imaging and quantitative chemical analysis of protolith matrix and mafic minerals as well as fault-zone clay and other diagenetic phases were performed at the New Mexico Bureau of Geology and Mineral Resources on a Cameca SX-100 electron microprobe operated at 15 keV and 20 nA beam current. Pixel counts (1024 x 768 resolution) of black (porosity) versus gray (mineral grain) area in 100 BSE images per protolith thin section (three thin sections per sample) were used to quantify two-dimensional porosity (Appendix B). Secondary electron microscopy (SEM) of freshly broken fault-zone and protolith samples was used to document the three-

dimensional character of pore spaces and to define the morphology of key diagenetic minerals (Table B5, Appendix B).

Table 4.2. Protolith-deformation band sets from nonwelded units of the Bandelier Tuff, classified by sample number and analyses performed.

Sample Number	Fault	Protolith	Protolith Description	Diagenetic Minerals	Analyses Performed					
					Outcrop	Petrography	XRD	XRF	INAA	Stable Isotope
bt66	x			carbonate, illite	x	x				
bt67		x	nonwelded glassy (Qbt1g)		x	x				
bt45a	x			smectite (2.7 wt%)	x	x	x	x		
bt46		x	nonwelded glassy (Qbt1g)		x	x	x	x		
bt8	x			smectite (7.8 wt%)	x	x	x	x		x
bt9	x			smectite (17.4 wt%)	x	x	x	x		x
bt63		x	nonwelded glassy (Qbt1g)		x	x				x
bt8/9a		x	nonwelded glassy (Qbt1g)		x		x	x		x
bt8/9b		x	nonwelded glassy (Qbt1g)		x		x	x		x
bt7	x			smectite (70.2 wt%)	x	x	x	x	x	
bt7b	x			smectite (18.1 wt%) carbonate (21.7 wt%)	x	x	x	x		
bt63		x	nonwelded glassy (Qbt1g)		x	x				
bt7c		x	nonwelded glassy (Qbt1g)		x		x	x		
bt7d		x	nonwelded glassy (Qbt1g)		x		x	x		
bt115	x*			n/a	x	x	x	x		
bt29		x	nonwelded crystallized (Qbt3)		x	x	x	x		
bt115FW		x	nonwelded crystallized (Qbt3)		x		x	x		
bt115HW		x	nonwelded crystallized (Qbt3)		x		x	x		
bt1	x			n/a	x	x	x	x		x
bt2a	x			oxide minerals	x	x	x	x		x
bt2b	x				x	x	x	x		x
bt37		x	nonwelded crystallized (Qbt3)		x	x	x	x		x
bt116	x			smectite (1.4 wt%)	x	x	x	x		x
bt29		x	nonwelded crystallized (Qbt3)		x	x	x	x		x
bt116b		x	nonwelded crystallized (Qbt3)		x		x	x		x
bt116c		x	nonwelded crystallized (Qbt3)		x		x	x		x
bt111a	x			smectite (24.6 wt%) carbonate (42.4 wt%)	x	x	x	x		x
bt111b	x			smectite (36.5 wt%) carbonate (2.8 wt%)	x	x	x	x	x	
bt68		x	nonwelded crystallized (Qbt3)				x	x		x
bt69		x	nonwelded crystallized (Qbt3)			x	x	x		x
bt73		x	nonwelded crystallized (Qbt3)							x
bt119	x			smectite (93.5 wt%)	x	x	x	x	x	
bt120		x	nonwelded crystallized (Qbt4)		x	x	x	x		
ch71A	x			smectite	x	x				
ch102	x			smectite	x	x				
ch70	x			smectite	x	x				
ch3		x	nonwelded glassy (Qbt1g)		x	x				
ch5		x	nonwelded crystallized (Qbt1v)		x	x				

bt=Bandelier Tuff, DB=deformation band, ch=chupaderos canyon (Guaje Mountain fault)
*Structure may be an elutriation pipe rather than a deformation band. See discussion for details.

Bulk Mineralogy (XRD)

The bulk mineralogy of fault-zone material and corresponding unaltered protolith was determined by quantitative X-ray diffraction (XRD) analysis. Determining the bulk

mineralogy for a deformation band and surrounding protolith allows us to evaluate (1) the presence of clay minerals versus clay-sized particles; (2) bulk quantities of trace minerals that are difficult to detect in point counts by optical petrography, and (3) whether fault-zone material is composed of ground-up ignimbrite fragments or is a combination of ignimbrite, minerals formed *in situ* through alteration and/or mineralization, and/or material transported from the surface.

Eight of the ten previously mentioned protolith-fault sets were selected for mineralogic analysis (Table 4.2). Each sample was prepared by crushing in a tungsten carbide shatterbox for approximately 15 minutes. A small portion of each sample (~0.8 g) was mixed with 1.0-mg corundum (Al_2O_3) internal standard in the ratio of 80% sample to 20% corundum by weight. Each sample was then ground with acetone in an automatic Retsch Micro-Rapid mill (fitted with an agate mortar and pestle) for at least 10 minutes. This produced a sample with an average particle size of less than 5 microns and ensured thorough mixing of sample and internal standard. All diffraction patterns were obtained at Los Alamos National Laboratory on a Siemens D500 X-ray powder diffractometer using CuK (alpha) radiation, incident- and diffracted-beam Soller slits, and a Kevex Si (Li) solid-state detector from 2-70 degrees two-theta, using 0.02 steps, and counting for at least 2s/step. Quantitative analysis of each sample was conducted using FULLPAT QXRD software [Chipera and Bish, 2001]. FULLPAT is based on a quantitative X-ray diffraction methodology that merges the advantages of existing full-pattern fitting methods with the traditional reference intensity ratio (RIR) method.

Whole rock geochemistry (XRF & INAA)

Chemical data were collected from portions of the same samples prepared for XRD analyses (Table 4.2). After crushing, samples were prepared for x-ray fluorescence (XRF) analyses following the methods described by Hallet and Kyle [1993]. The samples were analyzed on a Phillips Panalytical PW2400 wavelength dispersive, sequential x-ray fluorescence spectrometer at the New Mexico Bureau of Geology and Mineral Resources. An end window Rh-tube was used to excite the sample, and fluorescent x-rays were detected using a variety of analyzing crystals. All major element data were collected using a tube voltage of 35kV and 75mA and all trace element concentrations were obtained using an x-ray tube setting of 60kV and 45mA. Phillips software was used to control the spectrometer and reduce the raw data.

Of the eight protolith-fault sets analyzed for mineralogy, major oxides, and trace elements, three relatively clay-rich (>10 wt% smectite) fault samples were selected for determination of rare-earth element (REE) concentrations by instrumental neutron activation analysis (INAA; Table 4.2). Rare-earth element distributions are commonly used as indicators of geological processes in clastic materials [e.g., Gotze and Lewis, 1994; Aubert et al., 2001]. In these kinds of studies, the abundance of a given element in detrital sediment reflects the source-rock characteristics, chemical weathering, processes of sorting during transport, and diagenesis [e.g., McLennan, 1989]. Likewise, REE distributions can provide useful information about the geochemical processes responsible for formation of diagenetic minerals (such as clays) in variably altered ignimbrite deposits, especially when compared to unweathered material. REE distributions of fault smectites are used to determine if the clay formed through *in situ* alteration of ignimbrite

matrix (fault gouge) and/or was introduced by translocation from the surface [cf. Vaniman et al., 2002].

Samples were prepared for INAA by sample disruption with a sonic probe, sequential sedimentation in deionized water, and centrifugation at 8000 rpm for 40 minutes to 1 hour to obtain a 0.5 to 0.1 micron size fraction [Chipera et al., 1993]. Clay separates were then allowed to dry in order to evaporate the centrifuged supernatant to obtain purified clay as a <0.1-micron size fraction. These clay separates were analyzed in the trace-element geochemistry laboratory at Washington University (St. Louis) using methods described by Korotev [1991].

Stable Isotope Characterization

Stable isotope analyses of samples from four deformation-band fault zones were conducted to evaluate both the extent of fluid-rock interaction and potential fluid sources. Sample sets were chosen from the eight protolith-fault sets for which outcrop, petrographic, microprobe, XRD, and XRF analyses were performed (Table 4.2). The four sample sets include the full variety of deformation-band fault types mentioned previously.

The stable oxygen isotope ratio ($\delta^{18}O$) of a rock depends mainly on the isotopic composition, salinity, and temperature of the fluids with which the rock interacted during and subsequent to its formation. The stable carbon isotope ratio ($\delta^{13}C$) reflects the source of CO_2 for precipitation or rock formation, such as magmatic fluids, meteoric water, or microbial oxidation of organic matter and methane [Nelson and Smith, 1996]. Therefore, the stable isotopic signatures of fault zones will be different from protolith if

the faults have acted as preferential pathways for water distinct from formation fluids. Sampling and analysis of fault-zone wall rock also allows evaluation of whether or not fluids 'leaked' from the faults into the surrounding host rock, and if they did leak, how far into the host rock fault-related fluid was transported.

Samples of fault material, footwall- and hanging wall-rock material <5 mm from fault boundary, and corresponding protolith (>50 cm from fault boundary) were prepared for isotope analysis by manual grinding using a mortar and pestle and subsequently sieved to <1 mm grain size. Silicate samples were reacted with chlorine trifluoride (ClF_3) reagent at elevated temperature to liberate molecular oxygen [Campbell and Larsen, 1998]. A subsequent reaction with a hot carbon rod converted the evolved oxygen to CO_2 gas, which was then analyzed with a Finnigan MAT Delta E isotope ratio mass spectrometer. One calcite-cemented fault sample was reacted with 100% phosphoric acid [McCrea, 1950], and the evolved CO_2 gas analyzed for carbon and oxygen isotopic composition on the mass spectrometer. All samples were analyzed at New Mexico Tech in the Stable Isotope Mass Spectrometry Laboratory.

Results

Outcrop Character and Petrography of Protolith-Deformation Band Sets

The ash-dominated nonwelded ignimbrites of the Bandelier Tuff range in color from white to lavender to orange. This, and variable induration, are due to spatially variable postdepositional crystallization. Each unit is dominated by silicic ash (2 micron to 2 mm grains) with subordinate pumice, lithic clasts, and phenocrysts (cm-scale). Thus, the undeformed ignimbrite units have a wide grain-size distribution, ranging from clay-

sized particles to cm-scale grains. Based on qualitative observations in thin section, there are roughly equal volumes of large (cm-scale) and small (mm-scale) fragments in the undeformed Bandelier Tuff.

Unaltered deformation bands are composed of grain-size-reduced ignimbrite fragments, including glass shards, pumice fragments, lithic clasts, and phenocrysts (Fig. 4.1) [Wilson et al., 2003]. Deformation bands also have a wide grain-size distribution, but smaller components generally make up the majority of grains. Commonly, glass and pumice fragments make up the smallest grains, and the fewer, larger grains are the mechanically stronger phenocrysts and lithic clasts. These stronger grains are typically aligned with long axes subparallel to deformation band boundaries and are commonly bypassed completely by individual deformation bands (Fig. 4.1b). The stronger grains are not typically crushed, but do contain microfractures that are probably the result of thermal contraction upon rapid cooling during deposition rather than fault-zone deformation [N. Dunbar, personal communication, 2002]. Transgranular fractures are not found in deformation bands.

We have described one other type of unaltered feature in the Bandelier tuff: a tabular structure of undetermined origin, which may be either primary or secondary. This type of structure, observed in only three locations, is dominated by phenocrysts and lithic clasts. These structures (sample bt115, Table 4.2) do not show evidence of grain crushing, but pore collapse between phenocrysts is observed. We later explore both primary and secondary (i.e., deformation band, compaction band) explanations for the formation of these features.

The majority of alteration and mineralization products are located at the margins of and in the interstices between ignimbrite fragments in diagenetically modified deformation bands. They are particularly common along glass and mafic grain boundaries, as well as within some pumice vesicles (Figs. 4.3-4.6). These alteration and mineralization products include smectite, calcite, and (rarely) Fe-oxides.

Smectite within deformation bands is orange to brown (Figs. 4.3a and 4.4a) in outcrop and typically exhibits desiccation cracks. In thin section, two distinct morphologies of smectite are evident, depending on its abundance within the fault. In deformation bands with <10 wt% smectite, smectite is mostly clay-sized (Fig. 4.3b) and shows little or no birefringence or color. In deformation bands with >10 wt% smectite, larger grains and books of smectite exhibit an orange to brown color with plane-polarized light, and display mottled birds-eye extinction with cross-polarized light. The distortion and desiccation cracking evident in these clay accumulations may be associated with wetting and drying cycles [cf. Vaniman et al., 2002]. Books of smectite commonly define a compositional banding foliation within the fault zone (see Fig. 3.5a, Chapter 3).

The texture of smectite in many of the deformation bands with little or no evidence of shear displacement subsequent to introduction of smectite is similar to that of clay found in Bt (clay-rich) horizons of desert soils (Figs. 4.4b and 4.5a) [Gile et al., 1995]. Soil clay, which is transported from the surface in colloidal form, has a texture that is marked by the lining of grains and filling of matrix porosity [cf. Davenport et al., 1995; Vaniman and Chipera, 1995]. Another texture of smectite that is less common (or

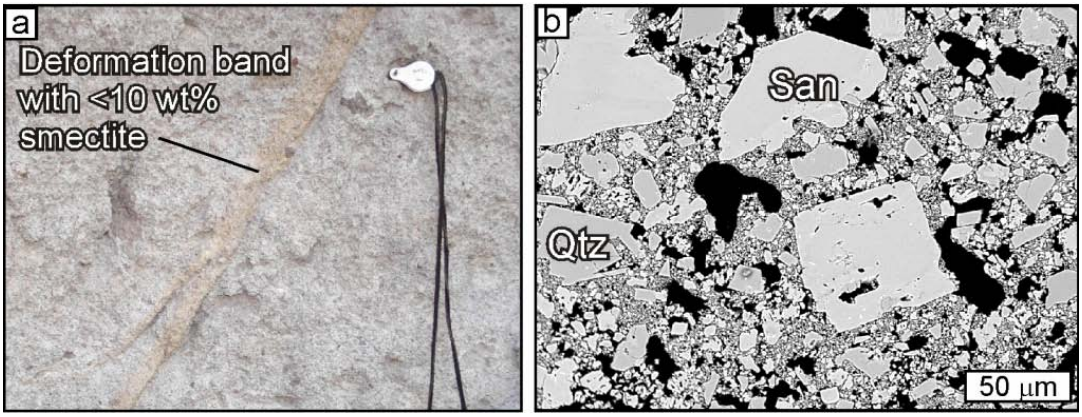

Figure 4.3. Outcrop photo (a) and BSE image (b) of a deformation band with <10 wt% smectite showing quartz (Qtz) and sanidine (San) phenocrysts and phenocryst fragments in a silt- to clay-sized matrix of ignimbrite fragments and smectite.

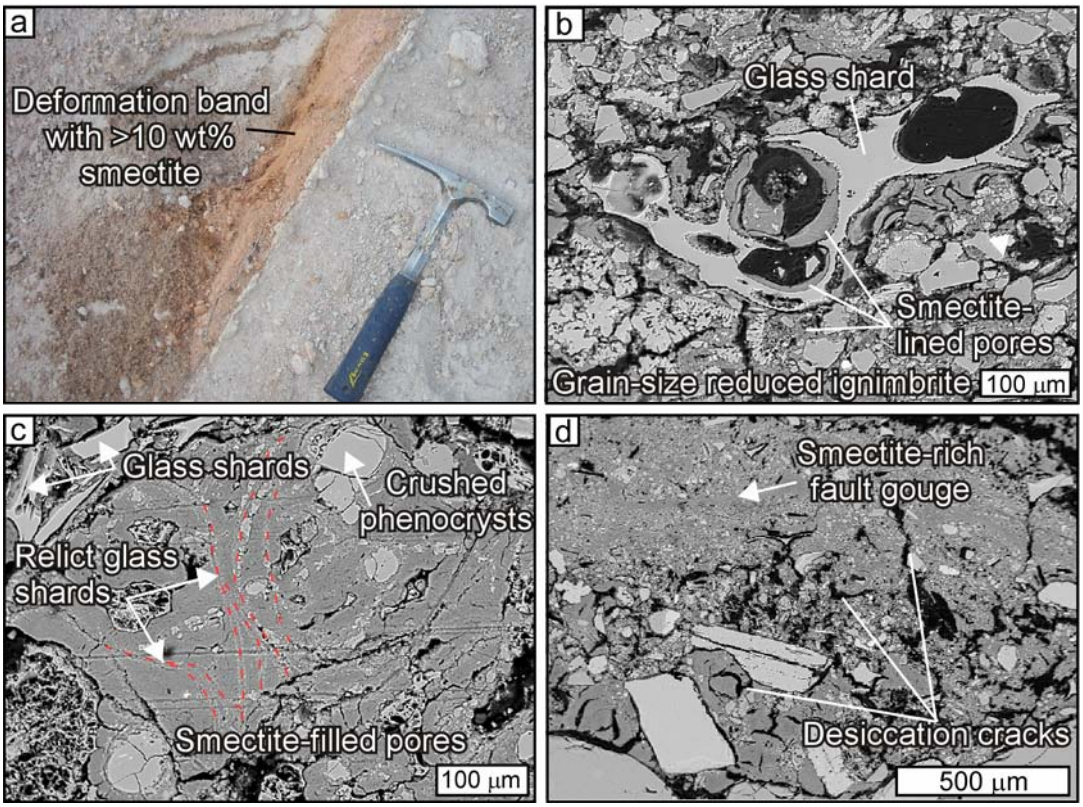

Figure 4.4. Outcrop photo (a) and BSE images (b, c, and d) of deformation bands with >10 wt% smectite. BSE images are from deformation bands other than that shown in (a). (b) Microstructural evidence of smectite accumulation that is similar to the morphology of translocated (eluviated) smectite seen in soils. Also note the diffuse boundary between glass and smectite, suggesting post-translocation, *in situ* alteration. (c) Microstructural evidence of glass shards (margins outlined with red dashed lines for clarity) that have altered to smectite. (d) Smectite-rich fault gouge developed by shear in a smectite-rich deformation band.

less commonly preserved) is one in which glass shards appear to have altered to smectite (Fig. 4.4b, c). For deformation bands in which post-diagenetic shear is evident from either grain alignment or compositional foliation, these diagenetic microstructures are transformed into a gouge-like compositional-banding foliation (Figs. 4.4d and 4.5b). Compositional bands are composed of variable amounts of foliated smectite and fragments of ignimbrite and smectite.

Calcite in deformation bands is distinguished as white, cohesive layers commonly defining a compositional banding foliation with smectite (Fig. 4.6a). Smectite is consistently found in association with calcite-cemented deformation bands in which the calcite is either situated in the middle of the fault (Fig. 4.6a), at the fault boundary, or as anastomosing lenses with the smectite. Ignimbrite and smectite fragments are commonly found within the calcite (Fig. 4.6b). Also, many of these deformation bands contain plant roots that extend several meters into the subsurface. In some cases, calcite is concentrated along these roots [cf. Lavine et al., 2003].

Calcite found in deformation bands of the Bandelier Tuff is not a pure, crystalline, void-filling mineral. Instead, scanning electron microscopy (SEM) reveals that this calcite consists of rod-shaped (needle-fiber) [cf. Verrecchia and Verrecchia, 1994] microcrystallites (Fig. 4.5a, c). Common crystallite morphologies in these deformation-band faults fall into two main categories: (1) single or coupled smooth rods 1-2 μm wide and 5-20 μm long; and (2) serrate rods 5 μm wide and 100 μm long. These two morphological categories are characteristic of calcite precipitation associated with microbial activity in the presence of decaying plant roots and with physicochemical

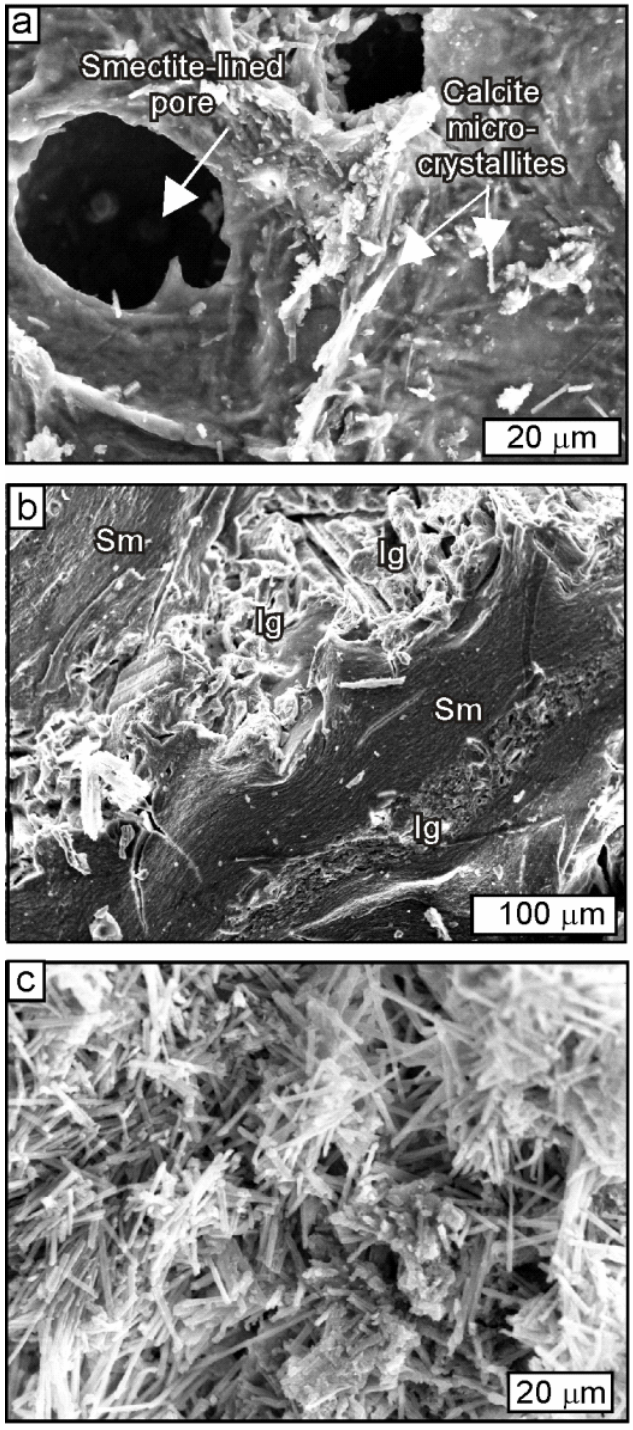

Figure 4.5. SEM images of (a) smectite-lined pores in a deformation band (bt111b) containing 36 wt% smectite and 3 wt% calcite, (b) compositional-banding foliation of smectite and ignimbrite material in a deformation band (bt7) containing 70 wt% smectite, and (c) calcite microcrystallites within a calcite-cemented deformation band (bt66). Sm = smectite, Ig = ignimbrite fragments.

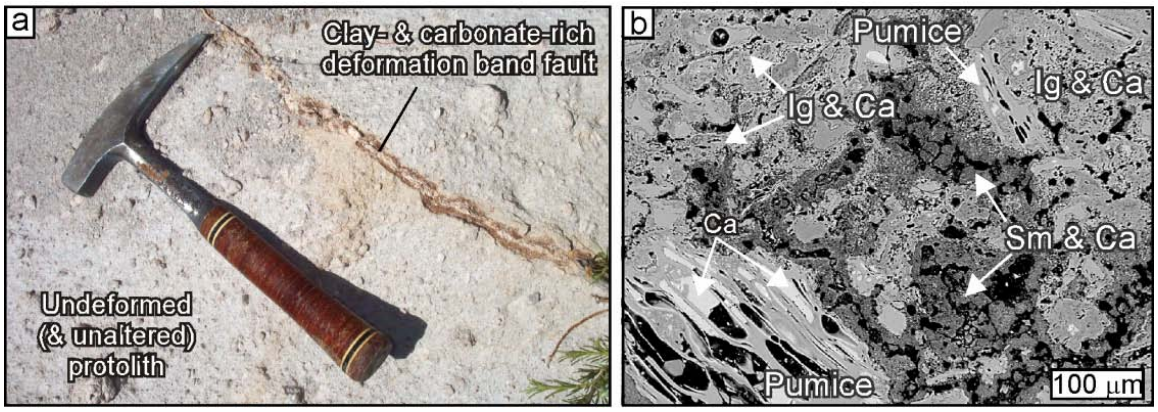

Figure 4.6. Outcrop photo (a) and BSE image (b) of a deformation band enriched in smectite [orange in (a), darker material in (b)] and calcite [white in (a), brighter material in (b)]. Ca = calcite, Sm = smectite, Ig = ignimbrite fragments. Purest calcite fills pumice vesicles; black = pores; calcite rich in fine-grained ignimbrite inclusions (Ig) lines micropores in deformation band.

desiccation, respectively, in a pedogenic environment [Verrecchia and Verrecchia, 1994]. Such pedogenic sources for the calcite are consistent with the observed non-luminescence of this mineral. Also, outcrop characterization of calcite-cemented deformation bands on the Pajarito Plateau reveals the widespread occurrence of desiccated smectite and/or plant roots in these faults, consistent with both processes of precipitation.

Fe-oxides (dominantly magnetite and ilmenite) are locally found along glass and lithic grain boundaries, as well as within smectite accumulations, in some deformation bands. The affinity of clays to adsorb these oxide minerals is documented by Vaniman et al. [2002]. One deformation-band fault zone identified in this study (Fig. 4.7), however, has larger than typical amounts of oxide minerals in the absence of other diagenetic phases (i.e., smectite and calcite). This fault exhibits internal zoning, with a discrete, open slip surface that separates a zone of closely spaced deformation bands from undeformed protolith (Fig. 4.7a). The deformation bands form gray, unaltered zones on the east side of the fault zone, which grade into distinctly pink zones on the west side of

the fault. The pink color corresponds to oxide mineralization that is observed at the microscale within, and within 1 cm of, the deformation bands. These oxide minerals are distinguished as opaque with a petrographic microscope, and are bright (high atomic number) in BSE images (Fig. 4.7b). Chemical analysis of these phases on the electron microprobe reveals that they are magnetite and ilmenite. The minerals have a

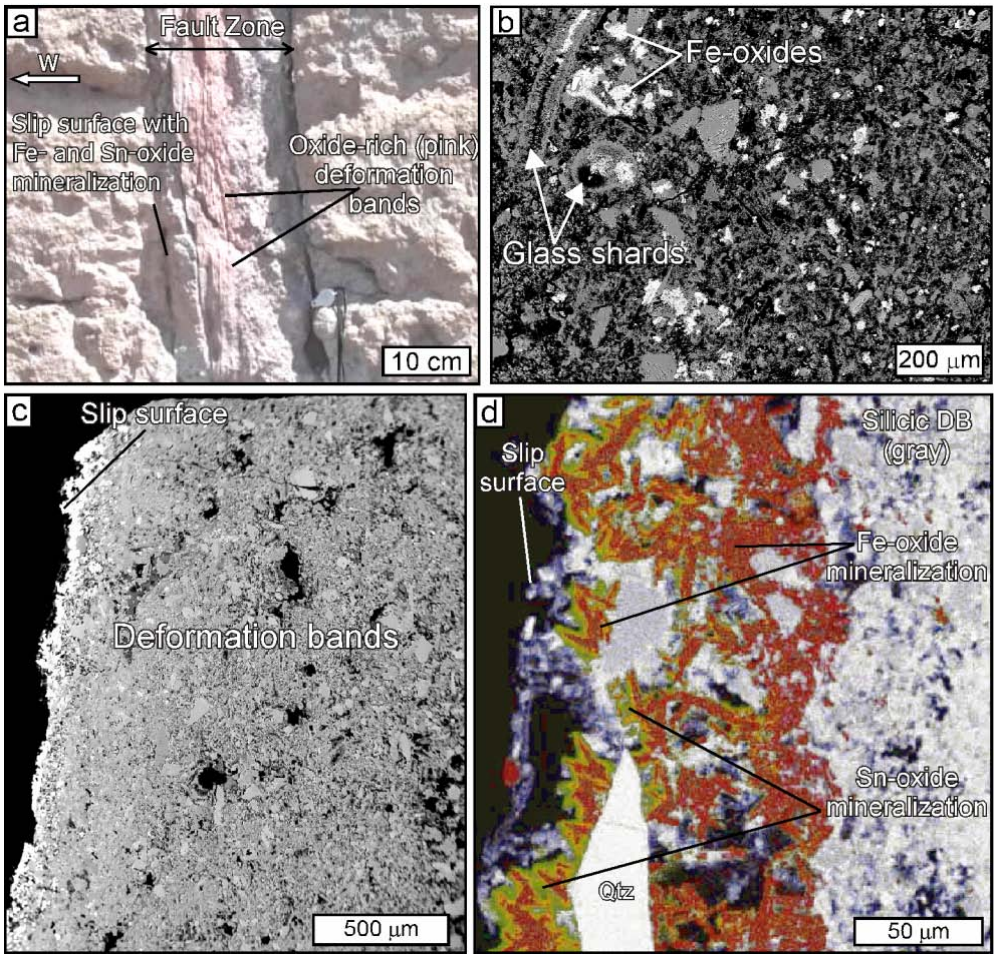

Figure 4.7. Outcrop photo (a) of a deformation-band fault zone in which unaltered and oxide-mineralized (pink) deformation bands are truncated by an open, mineralized slip surface. Arrow with "W" points toward the west. (b) BSE image of an oxide-mineralized deformation band shown in (a). Fe-oxide minerals line some pore spaces and postdepositionally crystallized glass shards. (c) BSE image of open slip surface adjacent to the zone of deformation bands. (d) X-ray map showing iron- (red) and tin-oxide (green) mineralization on slip surface. Note the undeformed nature of individual oxide minerals.

roughly even distribution throughout the fault material (Fig. 4.7b). Where the open slip surface truncates the zone of deformation bands (Fig. 4.7a, c), white Fe- and Sn-oxide minerals are present. The euhedral morphology and undeformed character of the latter suggest they have grown outward from the deformation-band fault zone into the fracture opening after the last period of faulting (Fig. 4.7d).

Mineralogy and Whole Rock Geochemistry of Protolith-Deformation Band Sets

Bulk mineralogy, major oxide, and trace element geochemical data for eight protolith-fault sets are given in Tables 4.3 (glassy nonwelded Qbt1g protolith) and 4.4 (crystallized nonwelded Qbt3 and Qbt4 protolith). Ignimbrite deposits are inherently heterogeneous. This heterogeneity is evident in the variability in mineralogy and chemistry of protolith illustrated in Figures 4.8 (Qbt1g protolith), 4.9 (Qbt3 protolith), and 4.10 (Qbt4 protolith). In this section and later discussion, we focus on bulk differences between deformation band and protolith mineralogy and chemical signatures that are greater than detection limits, analytical errors, estimated precision, and the variation exhibited by protolith alone. Detection limits, analytical errors, and precision estimates are given in Tables 4.3 and 4.4. Variation exhibited by protolith is shown in Figs. 4.8, 4.9, and 4.10, where protolith data from across the Pajarito Plateau are plotted along with protolith data from this study.

Each protolith unit contains significant quartz, alkali feldspar, and plagioclase feldspar with minor (commonly less than analytical error of 2 wt%) smectite, hematite, magnetite, augite, and biotite (Figs. 4.8a, 4.9a, and 4.10a). Glassy units are dominated by silicic glass, whereas crystallized units contain higher amounts of cristobalite and tridymite than glass. Deformation bands show variable differences in bulk mineralogy

Table 4.3. Mineralogy, major oxides, and trace elements for Qbt1g protolith-deformation band sets.

	Protolith (bt45c)	DB with <10 wt% Sm (bt45a)	Protolith (bt8/9b)	DB with <10 wt% Sm (bt8)	DB with >10 wt% Sm (bt9)	Protolith (bt7c)	DB with >10 wt% Sm (bt7)	DB with >10 wt% Sm & Ca (bt7b)
Quartz (wt%)	11	16	13	10	14	11	2	1
Alkali Feldspar	5	5	5	4	7	5	3	0
Plag Feldspar	12	11	8	7	10	8	4	1
Glass	70	64	69	70	51	72	21	55
Smectite	0	3	2	8	17	2	70	18
Cristobalite	0	0	0	0	0	0	0	0
Tridymite	0	0	0	0	0	0	0	0
Hematite	0	0	0	0	0	0	0	0
Magnetite	0	0	0	0	0	0	0	0
Augite	2	1	2	1	1	2	0	0
Calcite	0	0	0	0	0	0	0	22
Other^	1	1	1	1	1	0	0	3
Total	100	100	100	100	100	100	100	100
SiO_2 (wt%)	76.53 *(0.54)*	74.39 *(0.52)*	76.61 *(0.54)*	74.78 *(0.52)*	74.03 *(0.52)*	76.22 *(0.53)*	67.11 *(0.47)*	57.88 *(0.41)*
TiO_2	0.08 *(0.00)*	0.26 *(0.00)*	0.09 *(0.00)*	0.11 *(0.00)*	0.14 *(0.00)*	0.09 *(0.00)*	0.28 *(0.00)*	0.06 *(0.00)*
Al_2O_3	11.73 *(0.02)*	14.06 *(0.03)*	12.70 *(0.03)*	14.76 *(0.03)*	14.27 *(0.03)*	12.95 *(0.03)*	19.29 *(0.04)*	3.86 *(0.01)*
Fe_2O_3	1.53 *(0.01)*	2.57 *(0.01)*	1.65 *(0.01)*	2.03 *(0.01)*	2.58 *(0.01)*	1.75 *(0.01)*	5.15 *(0.02)*	0.92 *(0.00)*
MnO	0.07 *(0.00)*	0.05 *(0.00)*	0.07 *(0.00)*	0.06 *(0.00)*	0.05 *(0.00)*	0.08 *(0.00)*	0.08 *(0.00)*	0.07 *(0.00)*
MgO	0.07 *(0.00)*	0.56 *(0.00)*	0.08 *(0.00)*	0.17 *(0.00)*	0.48 *(0.00)*	0.12 *(0.00)*	1.81 *(0.01)*	0.71 *(0.00)*
CaO	0.38 *(0.00)*	0.83 *(0.00)*	0.34 *(0.00)*	0.48 *(0.00)*	0.34 *(0.00)*	0.43 *(0.00)*	1.2 *(0.00)*	34.89 *(0.07)*
Na_2O	5.26 *(0.07)*	3.63 *(0.05)*	3.86 *(0.05)*	3.55 *(0.05)*	3.99 *(0.05)*	3.88 *(0.05)*	2.38 *(0.03)*	0.93 *(0.01)*
K_2O	4.33 *(0.03)*	3.59 *(0.02)*	4.57 *(0.03)*	4.03 *(0.02)*	4.09 *(0.03)*	4.45 *(0.03)*	2.66 *(0.02)*	0.57 *(0.00)*
P_2O_5	0.02 *(0.00)*	0.05 *(0.00)*	0.03 *(0.00)*	0.04 *(0.00)*	0.036 *(0.00)*	0.02 *(0.00)*	0.05 *(0.00)*	0.11 *(0.00)*
Total~	100.00	100.00	100.00	100.00	100.00	100.00	100.00	100.00
LOI	3.61	5.37	2.80	4.59	5.01	3.28	11.41	24.56
V (ppm)	10	22	nd	nd	11	4	40	14
Cr	4	25	11	15	12	11	37	10
Ni	3	8	4	7	6	6	18	7
Zn	89	105	99	101	134	106	158	34
Rb	210	177	209	195	185	223	166	30
Sr	19	72	20	42	41	23	90	280
Y	80	106	79	86	87	84	74	52
Zr	201	236	225	269	222	233	207	40
Nb	96	82	104	121	90	109	69	17
Ba	49	178	71	86	108	72	145	164
Th	29	27	34	34	29	33	27	3
U	9	8	9	8	7	10	6	31
Pb	35	45	45	43	33	45	33	9
Cu	3	14	nd	5	6	nd	14	5
La*	-	-	-	-	-	-	87.7 *(0.9)*	-
Ce*	-	-	-	-	-	-	149.4 *(1.5)*	-
Nd*	-	-	-	-	-	-	84 *(4)*	-
Sm*	-	-	-	-	-	-	20.1 *(0.2)*	-
Eu*	-	-	-	-	-	-	1.16 *(0.02)*	-
Tb*	-	-	-	-	-	-	3.42 *(0.05)*	-
Yb*	-	-	-	-	-	-	10.44 *(0.10)*	-
Lu*	-	-	-	-	-	-	1.454 *(0.016)*	-
Hf*	-	-	-	-	-	-	10.26 *(0.10)*	-
Ta*	-	-	-	-	-	-	6.68 *(0.12)*	-
Sc*	-	-	-	-	-	-	11.97 *(0.12)*	-
Co*	-	-	-	-	-	-	15.78 *(0.16)*	-
As	3	4	nd	2	1	1	3	8
Sb*	-	-	-	-	-	-	0.82 *(0.03)*	-

DB = deformation band, Sm = smectite, Ca = calcite, Plag = plagioclase, - = not analyzed, nd = below detection limits.

^Other minerals include biotite, halite, dolomite, and fluorite. ~Major oxide wt% normalized to 0 wt% LOI. *INAA data uncertainties given in parantheses are one-standard-deviation estimates of analytical precision. Mineralogic data analytical error = 2 wt%. Major oxide analytical error from XRF analyses given in parantheses are calculated according to Hallet and Kyle (1993). Precision (in %) for trace elements determined by XRF are 5 (V), 5 (Cr), 3 (Ni), 2 (Zn), 1 (Rb), 1 (Sr), 1 (Y), 2 (Zr), 1 (Nb), 5 (Ba), 2 (Th), 3 (U), 2 (Pb), 3 (Cu), and 3 (As). Detection limits (in ppm) for XRF analyses are 3 (V), 4 (Cr), 3 (Ni), 2 (Zn), 2 (Rb), 2 (Sr), 1 (Y), 2 (Zr), 2 (Nb), 15 (Ba), 2 (Th), 2 (U), 2 (Pb), 3 (Cu), and 2 (As).

Table 4.4. Mineralogy, major oxides, and trace elements for Qbt3 and Qbt4 protolith-deformation band sets.

	Protolith (Qbt3) (bt115FW)	Unaltered DB (bt115[#])	Protolith (Qbt3) (bt37)	Unaltered DB (bt1)	Oxide-mineralized DB (bt2a)	Protolith (Qbt3) (bt116b)	DB with <10 wt% Sm (bt116)	Protolith (Qbt3) (bt68)	DB with >10 wt% Sm & Ca (bt111b)	Protolith (Qbt4) (bt120)	DB with >10 wt% Sm (bt119/bt117)[#]
Quartz (wt%)	16	35	17	4	2	13	17	18	11	6	1
Alkali Feldspar	26	20	25	23	23	23	23	26	13	26	1
Plag Feldspar	27	25	27	36	29	30	22	29	11	40	4
Glass	2	3	6	12	14	5	10	4	16	4	0
Smectite	0	0	0	0	0	0	1	0	37	0	94
Cristobalite	0	0	5	7	12	0	2	5	2	5	0
Tridymite	24	13	17	14	13	22	15	15	6	11	0
Hematite	0	0	1	2	2	0	0	0	0	1	0
Magnetite	2	2	0	1	1	0	0	2	0	3	0
Augite	3	3	2	2	4	6	10	1	1	2	0
Calcite	0	0	0	0	0	0	0	0	3	0	0
Other[^]	0	0	0	1	0	0	0	0	1	1	0
Total	100	100	100	100	100	100	100	100	100	100	100
SiO_2 (wt%)	78.02 *(0.55)*	79.95 *(0.56)*	76.89 *(0.54)*	74.13 *(0.52)*	74.24 *(0.52)*	78.03 *(0.55)*	77.97 *(0.55)*	77.83 *(0.55)*	73.10 *(0.51)*	71.99 *(0.50)*	67.88 *(0.48)*
TiO_2	0.11 *(0.00)*	0.09 *(0.00)*	0.11 *(0.00)*	0.22 *(0.00)*	0.21 *(0.00)*	0.11 *(0.00)*	0.11 *(0.00)*	0.10 *(0.00)*	0.27 *(0.00)*	0.36 *(0.00)*	0.41 *(0.00)*
Al_2O_3	11.76 *(0.02)*	10.77 *(0.02)*	11.69 *(0.02)*	13.29 *(0.03)*	13.85 *(0.03)*	11.73 *(0.02)*	11.81 *(0.02)*	11.76 *(0.02)*	14.00 *(0.03)*	14.34 *(0.03)*	17.89 *(0.04)*
Fe_2O_3	1.35 *(0.00)*	1.05 *(0.00)*	1.39 *(0.00)*	1.79 *(0.01)*	2.29 *(0.01)*	1.40 *(0.00)*	1.47 *(0.00)*	1.38 *(0.00)*	3.80 *(0.01)*	2.68 *(0.01)*	5.88 *(0.02)*
MnO	0.05 *(0.00)*	0.03 *(0.00)*	0.05 *(0.00)*	0.07 *(0.00)*	0.02 *(0.00)*	0.05 *(0.00)*	0.05 *(0.00)*	0.05 *(0.00)*	0.03 *(0.00)*	0.07 *(0.00)*	0.04 *(0.00)*
MgO	0.06 *(0.00)*	0.08 *(0.00)*	0.09 *(0.00)*	0.35 *(0.00)*	0.15 *(0.00)*	0.07 *(0.00)*	0.08 *(0.00)*	0.11 *(0.00)*	1.93 *(0.01)*	0.30 *(0.00)*	1.69 *(0.01)*
CaO	0.21 *(0.00)*	0.28 *(0.00)*	0.39 *(0.00)*	1.05 *(0.00)*	0.46 *(0.00)*	0.20 *(0.00)*	0.19 *(0.00)*	0.32 *(0.00)*	2.31 *(0.01)*	1.02 *(0.00)*	1.70 *(0.00)*
Na_2O	4.01 *(0.05)*	3.72 *(0.05)*	5.02 *(0.07)*	4.52 *(0.06)*	4.04 *(0.05)*	3.99 *(0.05)*	3.95 *(0.05)*	4.01 *(0.05)*	1.83 *(0.02)*	4.66 *(0.06)*	1.91 *(0.03)*
K_2O	4.42 *(0.03)*	4.00 *(0.02)*	4.33 *(0.03)*	4.52 *(0.03)*	4.68 *(0.03)*	4.40 *(0.03)*	4.35 *(0.03)*	4.42 *(0.03)*	2.67 *(0.02)*	4.47 *(0.03)*	2.52 *(0.02)*
P_2O_5	0.02 *(0.00)*	0.02 *(0.00)*	0.03 *(0.00)*	0.07 *(0.00)*	0.06 *(0.00)*	0.03 *(0.00)*	0.03 *(0.00)*	0.02 *(0.00)*	0.05 *(0.00)*	0.10 *(0.00)*	0.08 *(0.00)*
Total[~]	100.00	100.00	100.00	100.00	100.00	100.00	100.00	100.00	100.00	100.00	100.00
LOI	0.14	0.26	1.70	0.85	1.41	0.27	0.38	0.26	9.09	0.59	14.48
V (ppm)	3	nd	7	5	7	3	nd	6	49	16	54
Cr	7	7	15	7	17	11	17	8	39	10	40
Ni	3	4	4	5	7	4	4	4	21	7	25
Zn	48	37	47	124	934	50	54	56	69	63	91
Rb	106	73	105	124	140	110	116	121	92	74	72
Sr	24	32	25	86	69	26	27	20	84	130	113
Y	39	27	39	43	41	60	70	46	118	31	247
Zr	203	134	188	283	308	196	218	196	160	360	270
Nb	49	33	45	46	67	50	53	55	33	37	23
Ba	128	159	100	328	365	124	139	96	263	575	347
Th	12	9	13	14	nd	14	17	15	12	10	16
U	5	2	5	5	nd	5	5	5	5	4	6
Pb	18	18	24	144	6100	20	20	24	20	26	18
Cu	nd	5	nd	11	16	5	6	4	12	6	16
La*	-	-	-	-	-	-	-	-	180.4 *(1.8)*	-	317 *(3)*
Ce*	-	-	-	-	-	-	-	-	144.5 *(1.4)*	-	95.5 *(1.0)*
Nd*	-	-	-	-	-	-	-	-	217 *(8)*	-	377 *(14)*
Sm*	-	-	-	-	-	-	-	-	52.7 *(0.5)*	-	95.3 *(1.0)*
Eu*	-	-	-	-	-	-	-	-	2.68 *(0.03)*	-	6.69 *(0.08)*
Tb*	-	-	-	-	-	-	-	-	7.28 *(0.08)*	-	15.41 *(0.15)*
Yb*	-	-	-	-	-	-	-	-	16.56 *(0.17)*	-	31.1 *(0.3)*
Lu*	-	-	-	-	-	-	-	-	2.43 *(0.03)*	-	4.10 *(0.04)*
Hf*	-	-	-	-	-	-	-	-	7.11 *(0.08)*	-	7.43 *(0.14)*
Ta*	-	-	-	-	-	-	-	-	3.23 *(0.07)*	-	1.80 *(0.08)*
Sc*	-	-	-	-	-	-	-	-	6.32 *(0.06)*	-	28.4 *(0.3)*
Co*	-	-	-	-	-	-	-	-	4.58 *(0.05)*	-	5.80 *(0.09)*
As	nd	nd	5	26	460	nd	nd	nd	4	nd	4
Sb*	-	-	-	-	-	-	-	-	1.19 *(0.04)*	-	1.37 *(0.07)*

DB = deformation band, Sm = smectite, Ca = calcite, Plag = plagioclase, - = not analyzed, nd = below detection limits. [#]Structure may be an elutriation pipe rather than a deformation band; see discussion for details. [^]Other minerals include biotite, halite, dolomite, and fluorite. ~Major oxide wt% normalized to 0 wt% LOI. *INAA data uncertainties given in parantheses are one-standard-deviation estimates of analytical precision. Mineralogic data analytical error = 2 wt%. Major oxide analytical error from XRF analyses given in parantheses are calculated according to Hallet and Kyle (1993). Precision (in %) for trace elements determined by XRF are 5 (V), 5 (Cr), 3 (Ni), 2 (Zn), 1 (Rb), 1 (Sr), 1 (Y), 2 (Zr), 1 (Nb), 5 (Ba), 2 (Th), 3 (U), 2 (Pb), 3 (Cu), and 3 (As). Detection limits (in ppm) for XRF analyses are 3 (V), 4 (Cr), 3 (Ni), 2 (Zn), 2 (Rb), 2 (Sr), 1 (Y), 2 (Zr), 2 (Nb), 15 (Ba), 2 (Th), 2 (U), 2 (Pb), 3 (Cu), and 2 (As).

and abundances of major and trace elements relative to adjacent protolith (Table 4.5; Figs. 4.8, 4.9, and 4.10). In general, faults with higher amounts of diagenetic minerals exhibit greater differences in chemistry relative to protolith. These differences are summarized in Table 4.5 and the following paragraphs.

Unaltered structures contain no smectite, calcite, or Fe-oxide mineralization. These features, sampled at only two locations within crystallized nonwelded unit Qbt3, are rare, and fall into two categories. Unaltered deformation bands, (represented by sample bt1; Table 4.5) show measurable geochemical variation relative to protolith, with higher glass and lower quartz contents (Fig. 4.9a). In addition, the deformation band analyzed is higher in TiO_2, MgO, CaO, P_2O_5, Sr, Ba, Pb, and As than protolith (Fig. 4.9c

Table 4.5. Geochemical differences between deformation-band types and adjacent protolith.

Deformation Band (DB) Type	Mineralogy	Major Oxides	Trace Elements
Unaltered Structures			
Crystallized protolith (Qbt3) 1 protolith-fault set analyzed *(bt1/bt37)*	+ Glass, - Qtz	+TiO_2, +MgO, +CaO, +P_2O_5	+Sr, +Ba, +Pb, +As
Crystallized protolith (Qbt3) *1 protolith-structure set analyzed* *(bt115*/bt115FW)*	+ Qtz, - Trid	none	none
DB with <10 wt% smectite			
Crystallized protolith (Qbt3) *1 protolith-fault set analyzed* *(bt116/bt116b)*	+Glass, +Smect, +Aug	none	none
Glassy protolith (Qbt1g) *2 protolith-fault sets analyzed* *(bt45a/bt45c, bt8/bt8/9b)*	+Smect	+TiO_2, +MgO	+V, +Cr, +Cu
DB with >10 wt% smectite			
Crystallized protolith (Qbt4) *1 protolith-fault set analyzed* *(bt119/bt120)*	+Smect, -Mag, -Aug -Qtz, -Feld, -Crist, -Trid	+Fe_2O_3, +MgO, -SiO_2, -MnO, -Na_2O, -K_2O	+V, +Cr, +Ni, +Y, +As, +Th, +U, +Cu, +Sc, +Sb, -Nb, -Ta, -Co
Glassy protolith (Qbt1g) *2 protolith-fault sets analyzed* *(bt9/bt8/9b, bt7/bt7c)*	+Smect,±Qtz, ±Feld	+TiO_2, +Al_2O_3, +Fe_2O_3, +MgO +CaO, -SiO_2, -Na_2O, -K_2O	+V, +Cr, +Sr, +Ni, +Ta, +Cu, +Sb, +Sc, -Co, -U
DB with >10 wt% smectite + calcite			
Crystallized protolith (Qbt3) *1 protolith-fault set analyzed* *(bt111b/bt68)*	+Glass, +Smect, +Calc -Feld, -Trid	+TiO_2, +Fe_2O_3, +MgO, +CaO, +P_2O_5 -SiO_2, -Na_2O, -K_2O	+V, +Cr, +Ni, +Sr, +Y, +Ba, +Cu, +Sc, +Sb, -Ta, -Co
Glassy protolith (Qbt1g) *1 protoilth-fault set analyzed* *(bt7b/bt7c)*	+Smect, +Calc -Qtz, -Feld	+MgO, +CaO, -Al_2O_3, -Fe_2O_3, -SiO_2, -Na_2O, -K_2O	+Sr, +U, +Cu, +As, -Rb, -Zr, -Nb, -Th, -Pb
Oxide-mineralized DB			
Crystallized protolith (Qbt3) *1 protolith-fault set analyzed* *(bt2a/bt37)*	+Glass, + Crist, -Qtz	+Al_2O_3, +TiO_2, +Fe_2O_3, +P_2O_5 -MnO	+Zn, +Ba, +Sr, +Zr, +Cu, +As, +Pb

*Structure may be an elutriation pipe rather than a deformation; see discussion for details. Qtz = quartz, Smect = smectite, Aug = augite, Feld = alkali and plagioclase feldspar, Crist = cristobalite, Calc = calcite, + indicates minerals or elements in which deformation band is relatively high relative to protolith, - shows where these minerals or elements are relatively low. Sample numbers are given as (fault/protolith) and correspond to those given in Table 4.2 and A1.

and d).

The other category of unaltered structure (sample bt115; Table 4.5) may be either a deformation band or an elutriation pipe - a primary volcanic feature (e.g., Freundt et al., 2000). It is higher in quartz and lower in tridymite than protolith. There are no differences in major oxides or trace elements in this structure relative to protolith (Fig. 4.9). The minimal mineralogical contrasts reflect a higher number of phenocrysts relative to protolith. The possible cause of this greater phenocryst abundance is explored further in the discussion.

A deformation band with <10 wt% smectite in crystallized nonwelded unit Qbt3 is higher in glass, smectite, and augite than protolith (Fig. 4.9a). Deformation bands with similar amounts of smectite in glassy nonwelded unit Qbt1g (bt45a and bt8) are higher in smectite, MgO, TiO_2, V, Cr, and Cu (Fig. 4.8).

A deformation band with >10 wt% smectite in crystallized nonwelded unit Qbt4 is also higher in smectite, Fe_2O_3, MgO, V, Cr, Ni, Y, Cu, Th, U, Sc, Sb, and As than protolith (Fig. 4.10). This deformation band is lower in quartz, feldspar, magnetite, augite, cristobalite, tridymite, SiO_2, MnO, Na_2O, K_2O, Nb, Ta, and Co than protolith (Fig. 4.10). In glassy nonwelded unit Qbt1g, deformation bands with >10 wt% smectite are variably higher or lower in feldspar and quartz relative to protolith (Fig. 4.8a). These deformation bands are higher in Al_2O_3, TiO_2, Fe_2O_3, MgO, CaO, V, Cr, Ni, Sr, Cu, Ta, Sc, and Sb than protolith; they are consistently lower in SiO_2, Na_2O, K_2O, U, and Co (Fig. 4.8b and c; Table 4.5).

A deformation band with >10 wt % calcite and smectite in crystallized nonwelded unit Qbt3 is higher in glass, smectite, TiO_2, Fe_2O_3, MgO, CaO, P_2O_5, V, Cr, Ni, Sr, Y, Ba,

Cu, Sc, and Sb than protolith (Fig. 4.9). This deformation band is lower in feldspar, tridymite, SiO_2, Na_2O, K_2O, Ta, and Co (Fig. 4.9). In glassy unit Qbt1g, this type of deformation band is higher in smectite, calcite, MgO, CaO, Sr, U, Cu, and As (Fig. 4.8). The deformation band is lower in quartz, feldspar, SiO_2, Al_2O_3, Fe_2O_3, Na_2O, K_2O, Rb, Zr, Nb, Th, and Pb (Fig. 4.8; Table 4.5).

The sole oxide-mineralized fault zone, found in an outcrop of crystallized nonwelded unit Qbt3, is higher in glass and cristobalite but lower in quartz than protolith (Fig. 4.9a). Chemically, it is higher in Al_2O_3, TiO_2, Fe_2O_3, P_2O_5, Zn, Sr, Zr, Ba, Pb, Cu, and As (Fig. 4.9b and c). It is lower in MnO relative to protolith (Fig. 4.9b).

Chemical Compositions of Protolith Matrix, Mafic Minerals, and Fault-Zone Smectite

Quantitative chemical analyses reveal the detailed chemical compositions of phases that may have been involved in fluid-fault reactions. Comparison of fault and protolith data can help determine whether or not material has been added to, or removed from, the fault zone during diagenesis. Chemical analyses of phases in several protolith-deformation-band fault pairs were performed with the electron microprobe (Tables 4.6 and 4.7). Fault zones ranging from 1.4 wt% to 93.5 wt% smectite were chosen to evaluate mechanisms of smectite enrichment (Table 4.8).

Fe is relatively scarce in rhyolitic ignimbrite deposits, but is more abundant in fault-zone smectites (Tables 4.3 and 4.4). The Fe content of each sample tracks several Fe-bearing phases in the Bandelier Tuff, such as glass, feldspar, augite, magnetite, and smectite. We calculate the total amount of Fe (FeO and Fe_2O_3) in a given protolith or

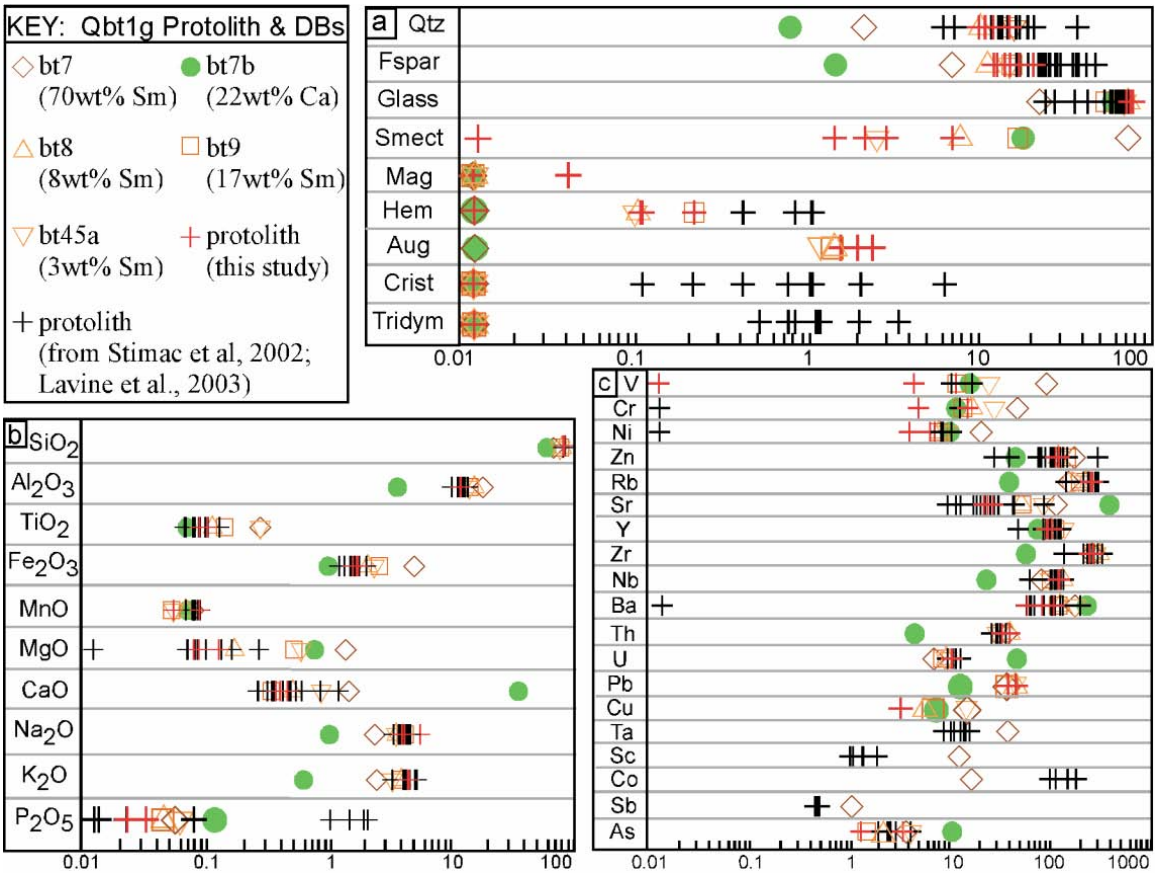

Figure 4.8. Mineralogy (a), major oxide abundances (b), and trace element concentrations (c) of variably altered deformation bands and adjacent protolith for glassy nonwelded Qbt1g (cf. Fig. 4.2b). Mineralogy and major oxide abundances given in wt%, trace element concentrations in ppm. All data are normalized to remove the effect of LOI. Sample numbers correspond to those given in Tables 4.2 and A1, Appendix A. DB = deformation band, Sm = smectite, Ca = calcite, Qtz = quartz, Fspr = plagioclase and alkali feldspar, Smect = smectite, Mag = magnetite, Hem = hematite, Aug = augite, Crist = cristobalite, Tridym = tridymite. Data from Stimac et al. [2002] from boreholes at Frijoles Mesa; those from Lavine et al. [2003] are from stratigraphic sections within Mesita de los Alamos, Sandia Canyon, and Mortandad Canyon.

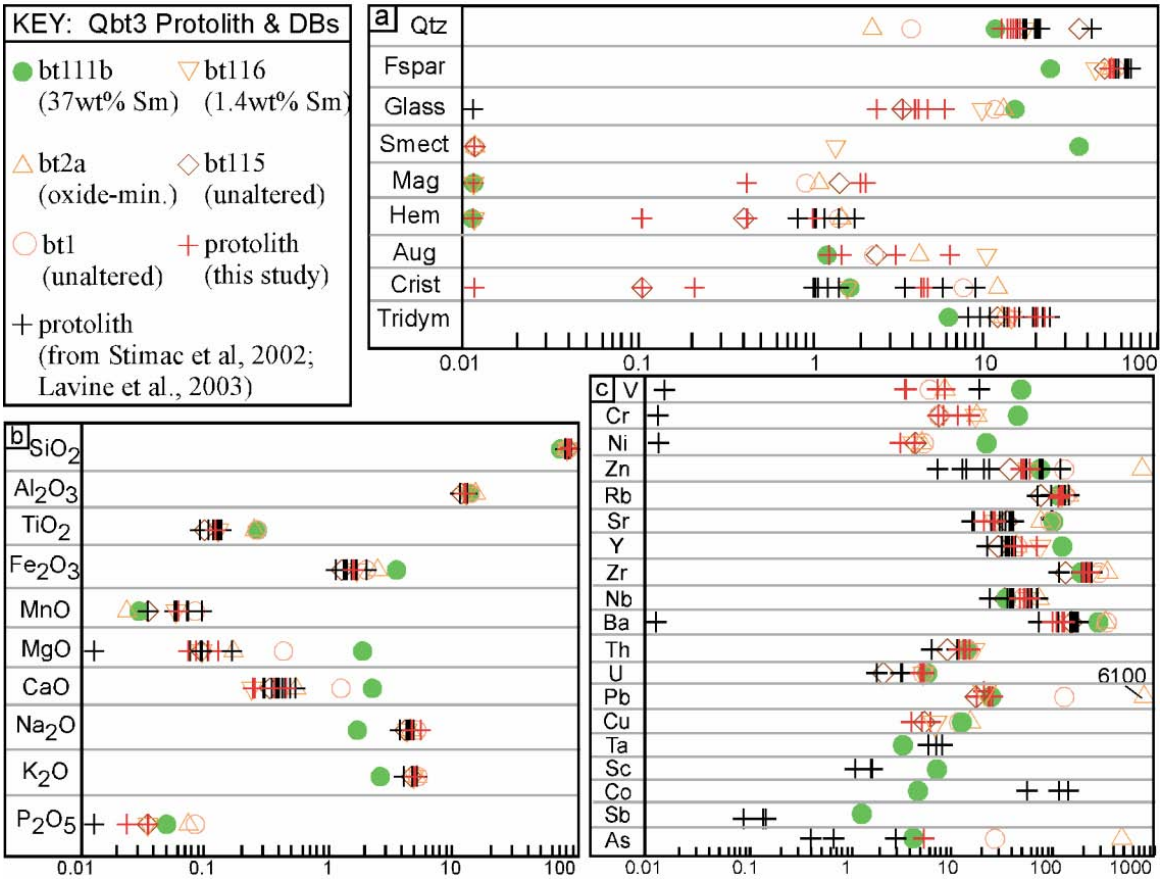

Figure 4.9. Mineralogy (a), major oxide abundances (b), and trace element concentrations (c) of variably altered deformation bands and adjacent protolith for crystallized nonwelded Qbt3 (cf. Fig. 4.2b). Mineralogy and major oxide abundances given in wt%, trace element concentrations in ppm. All data are normalized to remove the effect of LOI. Sample numbers correspond to those given in Tables 4.2 and A1, Appendix A. DB = deformation band, Sm = smectite, Qtz = quartz, Fspr = plagioclase and alkali feldspar, Smect = smectite, Mag = magnetite, Hem = hematite, Aug = augite, Crist = cristobalite, Tridym = tridymite. Data from Stimac et al. [2002] are from boreholes at Frijoles Mesa; those from Lavine et al. [2003] are from stratigraphic sections within Mesita de los Alamos, Sandia Canyon, and Mortandad Canyon.

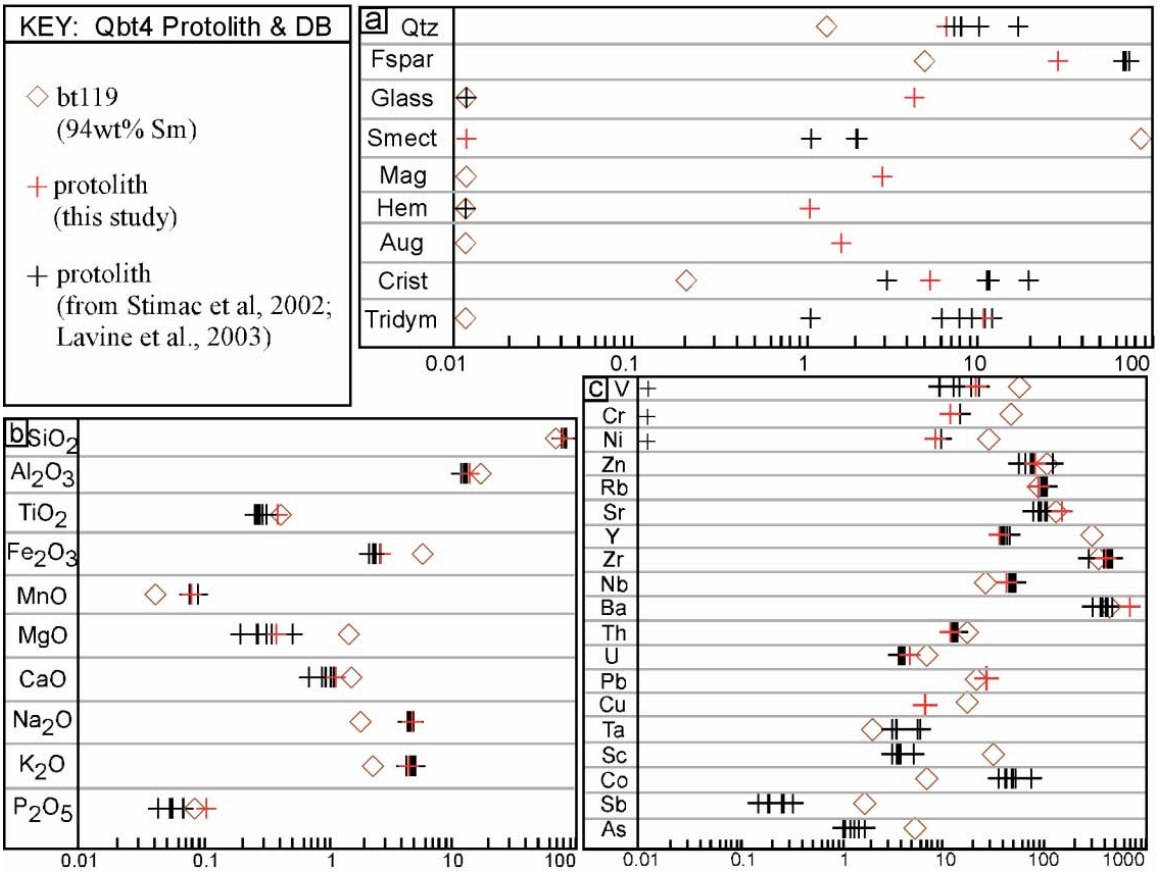

Figure 4.10. Mineralogy (a), major oxide abundances (b), and trace element concentrations (c) of variably altered deformation bands and adjacent protolith for crystallized nonwelded Qbt4 (cf. Fig. 4.2b). Mineralogy and major oxide abundances given in wt%, trace element concentrations in ppm. All data are normalized to remove the effect of LOI. Sample numbers correspond to those given in Tables 4.2 and A1, Appendix A. DB = deformation band, Sm = smectite, Qtz = quartz, Fspr = plagioclase and alkali feldspar, Smect = smectite, Mag = magnetite, Hem = hematite, Aug = augite, Crist = cristobalite, Tridym = tridymite. Data from Stimac et al. [2002] are from boreholes at Frijoles Mesa; those from Lavine et al. [2003] are from stratigraphic sections within Mesita de los Alamos, Sandia Canyon, and Mortandad Canyon.

fault-zone sample (Table 4.8) by multiplying the wt% abundance of a phase by the average wt% Fe contained within that phase (Tables 4.6 and 4.7). The wt% Fe for all phases is then summed for fault and for protolith. This mass balance calculation shows that there are variable but small Fe gains and losses in the faults analyzed relative to protolith (Table 4.8). Reductions range from 0.1 to 0.3 wt% Fe, and increases range from 0.3 to 1.9 wt% Fe. These differences are generally small relative to the standard deviation of wt% Fe determined for individual Fe-bearing phases within and outside the faults (Tables 4.6 and 4.7). These standard deviations are 0.02 wt% for feldspar, 2.4 wt% for augite, 2.7 wt% for magnetite, and 1.3 wt% for smectite.

Rare-Earth Element (REE) Distributions of Deformation Bands and Protolith

REE distributions of fault-zone smectite (determined in this study) and corresponding protolith [Stimac et al., 2002] for each nonwelded Bandelier Tuff unit are given in the chondrite-normalized plots in Figure 4.11. Normalizations were calculated according to Nakamura [1974]. Patterns of protolith are similar to those documented by Vaniman et al. [2002], with a negative Eu anomaly (due to selective alteration of mafic components) [cf. Vaniman et al., 2002] and an overall negative slope to the curves. Each of the three fault-zone smectites analyzed has higher La, Nd, Sm, Eu, and Tb concentrations than associated protolith. In the crystallized nonwelded units (Fig. 4.11b, c), the smectite-rich deformation bands have higher Yb and Lu concentrations than protolith, and exhibit negative Ce anomalies. Despite significant differences in smectite content, the similar REE patterns in these two smectites suggests that the smectite was introduced to the fault zones by similar processes.

Table 4.6. Chemical compositions* of protolith matrix and mafic minerals

Protolith Phase	Sample #	P_2O_5	SiO_2	SO_2	TiO_2	Al_2O_3	MgO	CaO	MnO	FeO	Na_2O	K_2O	F	Cl	Cr_2O_3	Fe_2O_3	Total^
Glass	ch3-4b-5	0.000	76.036	0.020	0.101	11.841	0.000	0.239	0.094	1.320	3.871	4.537	0.000	0.158	-	-	98.221
Postdepositional feldspar	ch5-11c-3	-	70.489	-	-	16.878	-	0.014	-	0.353	4.385	8.891	-	-	-	-	101.044
Postdepositional feldspar	bt119b-10	0.020	81.940	0.000	0.260	8.750	0.000	0.240	0.040	0.320	2.600	3.970	0.000	0.020	-	-	98.160
Postdepositional feldspar	bt119b-12	0.000	75.110	0.000	0.080	12.430	0.000	0.190	0.000	0.310	2.650	7.430	0.000	0.010	-	-	98.200
	Average	*0.010*	*75.846*	*0.000*	*0.170*	*12.686*	*0.000*	*0.148*	*0.020*	*0.328*	*3.212*	*6.764*	*0.000*	*0.015*			
	Std Dev	*0.014*	*5.761*	*0.000*	*0.127*	*4.070*	*0.000*	*0.119*	*0.028*	*0.023*	*1.016*	*2.527*	*0.000*	*0.007*			
Augite	bt45a-1	-	48.480	-	0.120	0.240	2.400	18.390	2.730	27.110	0.670	0.000	-	-	0.020	-	100.140
Augite	bt45a-2	-	48.600	-	0.080	0.250	2.380	18.490	2.760	27.130	0.540	0.000	-	-	0.000	-	100.230
Augite	bt8c-6	-	48.750	-	0.070	0.270	2.460	18.680	2.690	27.280	0.640	0.000	-	-	0.000	-	100.830
Augite	bt8c-7	-	48.970	-	0.110	0.250	2.510	18.460	2.850	27.280	0.660	0.010	-	-	0.000	-	101.100
Augite	bt9c-1	-	46.030	-	1.410	6.000	10.650	9.920	1.100	20.530	1.840	0.640	-	-	0.020	-	98.130
Augite	bt9c-2	-	46.690	-	1.470	5.710	10.530	9.660	1.100	20.830	1.810	0.620	-	-	0.020	-	98.430
Augite	bt115b-1	-	50.000	-	0.130	0.320	5.820	18.130	2.130	23.990	0.470	0.000	-	-	0.040	-	101.030
Augite	bt115b-2	-	49.940	-	0.110	0.330	5.530	18.000	2.190	24.360	0.500	0.010	-	-	0.020	-	100.990
Augite	bt115b-10	-	49.480	-	0.110	0.320	6.360	17.790	1.960	23.760	0.430	0.000	-	-	0.000	-	100.200
Augite	bt115b-11	-	49.850	-	0.090	0.320	6.240	18.030	2.030	23.340	0.460	0.000	-	-	0.010	-	100.360
Augite	bt119b-13	-	52.290	-	0.240	0.890	21.080	1.210	1.550	23.180	0.030	0.000	-	-	0.000	-	100.470
Augite	bt119b-14	-	52.570	-	0.250	1.030	21.220	1.310	1.450	22.640	0.020	0.000	-	-	0.020	-	100.500
	Average	-	*49.304*	-	*0.349*	*1.328*	*8.098*	*14.006*	*2.045*	*24.286*	*0.673*	*0.107*	-	-	*0.013*	-	
	Std Dev	-	*1.906*	-	*0.513*	*2.132*	*6.739*	*6.776*	*0.637*	*2.435*	*0.579*	*0.245*	-	-	*0.012*	-	
Magnetite	bt45a-3	-	0.130	-	9.500	0.440	0.080	0.050	1.240	38.630	-	-	-	-	0.030	50.300	100.390
Magnetite	bt45a-4	-	0.130	-	9.460	0.400	0.070	0.000	1.370	38.560	-	-	-	-	0.010	50.620	100.630
Magnetite	bt8c-8	-	0.130	-	9.760	0.430	0.090	0.040	1.290	38.950	-	-	-	-	0.010	50.160	100.840
Magnetite	bt8c-9	-	0.120	-	9.770	0.490	0.080	0.000	1.160	39.070	-	-	-	-	0.020	49.960	100.680
Magnetite	ch71Aa-3	-	0.110	-	9.610	0.460	0.110	0.000	1.180	38.890	-	-	-	-	-	50.380	100.730
Magnetite	ch71Aa-4	-	0.120	-	9.530	0.440	0.100	0.010	1.220	38.880	-	-	-	-	-	50.770	101.100
Magnetite	bt115b-6	-	0.130	-	3.520	0.400	0.160	0.050	2.800	31.460	-	-	-	-	0.030	62.130	100.670
Magnetite	bt115b-7	-	0.120	-	4.480	0.600	0.150	0.030	2.420	32.620	-	-	-	-	0.030	59.670	100.110
Magnetite	bt116a-1	-	0.130	-	5.380	0.790	0.070	0.000	0.880	35.200	-	-	-	-	0.010	57.790	100.260
Magnetite	bt108c-5	-	1.130	-	7.530	0.170	0.210	0.000	1.640	35.250	-	-	-	-	0.010	52.510	98.440
Magnetite	bt108c-16	-	0.200	-	9.240	0.450	0.110	0.030	1.340	37.960	-	-	-	-	0.020	50.190	99.530
Magnetite	bt108c-17	-	0.100	-	10.330	0.620	0.150	0.010	1.590	38.790	-	-	-	-	0.000	48.110	99.700
	Average	-	*0.213*	-	*8.176*	*0.474*	*0.115*	*0.018*	*1.511*	*37.022*	-	-	-	-	*0.017*	*52.716*	
	Std Dev	-	*0.290*	-	*2.368*	*0.149*	*0.044*	*0.020*	*0.556*	*2.707*	-	-	-	-	*0.011*	*4.512*	

Sample numbers correspond to those given in Appendix A.

*Given in wt% and determined by quantitative chemical analysis with electron microprobe.

- = no data.

^Analyses with totals < 98 wt% and > 102 wt% are excluded.

Table 4.7. Chemical compositions* of fault-zone smectite.

Sample #	P_2O_5	SiO_2	SO_2	TiO_2	Al_2O_3	MgO	CaO	MnO	FeO	Na_2O	K_2O	F	Cl	Total^
bt6b-3	0.030	56.390	0.040	0.490	19.350	2.260	1.540	0.020	4.490	0.590	1.910	0.210	0.130	87.430
bt6b-4	0.000	56.170	0.020	0.390	19.250	2.170	1.390	0.020	4.570	0.820	1.850	0.000	0.150	86.780
bt6b-5	0.050	51.350	0.030	17.580	17.580	2.420	1.470	0.010	4.400	0.270	1.250	0.700	0.450	80.240
bt45a-15	0.040	52.530	0.040	0.290	21.740	1.800	1.030	0.000	4.120	0.470	1.510	0.000	0.220	83.780
bt8c-12	0.070	46.760	0.060	0.110	29.960	0.610	1.070	0.000	3.340	0.720	0.610	0.220	0.290	83.810
bt8c-13	0.130	45.360	0.050	0.150	29.270	0.560	1.330	0.000	3.080	0.670	0.510	0.230	0.370	81.720
bt9c-5	0.040	52.720	0.010	0.230	18.950	1.690	0.870	0.000	4.730	1.120	1.970	0.230	0.440	82.980
ch71Aa-1	0.100	50.850	0.020	0.300	21.900	2.180	1.360	0.040	5.110	0.000	1.550	0.000	0.460	83.870
ch71Aa-2	0.090	51.520	0.030	0.380	22.300	2.060	1.380	0.030	5.180	0.220	1.610	0.000	0.440	85.240
ch71Aa-5	0.070	51.200	0.040	0.320	23.000	2.020	1.060	0.000	4.850	0.110	1.400	0.040	0.290	84.400
ch71Aa-6	0.100	50.120	0.020	0.350	22.630	2.010	1.010	0.030	4.690	0.140	1.490	0.520	0.290	83.390
ch70b-1	0.020	51.890	0.030	0.390	20.680	2.690	1.290	0.010	5.720	0.190	2.290	0.160	0.290	85.630
ch70b-2	0.100	51.890	0.030	0.330	20.040	2.250	1.400	0.020	5.820	0.150	1.780	0.110	0.330	84.240
ch70b-3	0.010	83.140	0.020	0.050	3.010	0.280	0.440	0.000	0.650	0.170	0.290	0.020	0.170	88.250
ch70b-4	0.070	73.220	0.030	0.160	7.890	0.730	0.830	0.030	2.230	0.240	0.740	0.050	0.150	86.380
ch70b-5	0.020	50.030	0.040	0.290	19.240	2.020	1.310	0.010	5.190	0.180	1.740	0.000	0.350	80.420
ch70b-6	0.060	64.260	0.020	0.310	15.870	1.510	1.200	0.000	4.110	0.410	1.470	0.070	0.320	89.600
ch102a-1	0.100	33.840	0.030	0.290	15.080	1.930	2.460	22.740	4.320	0.150	1.510	0.090	0.030	82.560
ch102a-4	0.130	48.020	0.040	0.320	21.610	1.960	1.640	1.840	5.580	0.130	1.460	0.040	0.240	83.000
bt111b-3	0.050	52.610	0.020	0.350	16.340	5.260	1.660	0.040	5.190	0.440	1.740	0.330	0.420	84.440
bt119b-2	0.090	51.300	0.040	0.300	17.960	1.890	1.370	0.000	6.210	0.280	1.670	0.170	0.350	81.630
bt119b-3	0.030	52.940	0.030	0.270	18.360	1.910	1.380	0.010	6.250	0.150	1.430	0.120	0.330	83.200
bt119b-4	0.020	53.430	0.030	0.210	18.580	1.990	1.400	0.020	6.300	0.250	1.510	0.240	0.330	84.300
Average	*0.062*	*53.545*	*0.031*	*1.037*	*19.156*	*1.922*	*1.300*	*1.081*	*4.614*	*0.342*	*1.447*	*0.154*	*0.297*	
Std Dev	*0.038*	*9.496*	*0.011*	*3.608*	*5.669*	*0.961*	*0.378*	*4.737*	*1.331*	*0.275*	*0.486*	*0.175*	*0.115*	

Sample numbers correspond to those given in Appendix A.

*Given in wt% and determined by quantitative chemical analysis with electron microprobe.

^Analyses with totals < 80 wt% are excluded.

Table 4.8. Mass balance calculations of FeO in Fe-bearing phases of protolith-deformation band pairs.

Protolith/Fault Sample	Phase	wt% phase in protolith*	wt% phase in fault*	wt% Fe in phase[#]	Calculated wt% Fe in protolith[˜]	Calculated wt% Fe in fault[˜]	**Difference in wt% Fe^**
bt116b/bt116	glass	4.7	9.6	1.3	0.1	0.1	
	feldspar	53.8	45.0	0.3	0.2	0.1	
	magnetite	0.0	0.0	89.7	0.0	0.0	
	pyroxene	6.0	10.4	24.3	1.5	2.5	
	smectite	0.0	1.4	4.6	0.0	0.1	
				Totals:	*1.7*	*2.9*	***+ 1.2***
bt45c/bt45a	glass	70.0	64.0	1.3	0.9	0.8	
	feldspar	17.0	16.0	0.3	0.1	0.0	
	magnetite	0.0	0.0	89.7	0.0	0.0	
	pyroxene	2.0	1.0	24.3	0.5	0.2	
	smectite	0.0	3.0	4.6	0.0	0.1	
				Totals:	*1.4*	*1.3*	***-0.1***
bt8/9b/bt9	glass	69.3	50.5	1.3	0.9	0.7	
	feldspar	12.5	16.2	0.3	0.0	0.0	
	magnetite	0.0	0.1	89.7	0.0	0.1	
	pyroxene	2.4	1.3	24.3	0.6	0.3	
	smectite	2.2	17.4	4.6	0.1	0.8	
				Totals:	*1.6*	*1.9*	***+ 0.3***
bt68/bt111b	glass	4.0	16.0	1.3	0.1	0.2	
	feldspar	55.1	24.1	0.3	0.2	0.1	
	magnetite	2.3	0.0	89.7	2.1	0.0	
	pyroxene	1.2	1.2	24.3	0.3	0.3	
	smectite	0.0	36.5	4.6	0.0	1.7	
				Totals:	*2.6*	*2.3*	***- 0.3***
bt7c/bt7	glass	71.9	21.2	1.3	0.9	0.3	
	feldspar	13.0	6.6	0.3	0.0	0.0	
	magnetite	0.1	0.0	89.7	0.1	0.0	
	pyroxene	1.9	0.0	24.3	0.5	0.0	
	smectite	1.5	70.2	4.6	0.1	3.2	
				Totals:	*1.6*	*3.5*	***+ 1.9***
bt120/bt119	glass	4.2	0.0	1.3	0.1	0.0	
	feldspar	29.9	4.8	0.3	0.1	0.0	
	magnetite	4.2	0.0	89.7	3.8	0.0	
	pyroxene	1.6	0.0	24.3	0.4	0.0	
	smectite	0.0	88.8	4.6	0.0	4.1	
	montmorillonite	0.0	4.7	0.8	0.0	0.0	
				Totals:	*4.3*	*4.1*	***- 0.2***

Sample numbers correspond to those given in Table 4.2.

*Determined from XRD analysis. Analytical error = 2 wt%.

[#]Total Fe (FeO + Fe_2O_3) determined by quantitative chemical analyses of phases using electron microprobe (Tables 4.5 and 4.6).

˜Calculated as the product of the wt% phase in sample and the wt% FeO contributed by that phase divided by 100.

^Positive difference (indicated by + number) indicates an increase in FeO from protolith to fault.

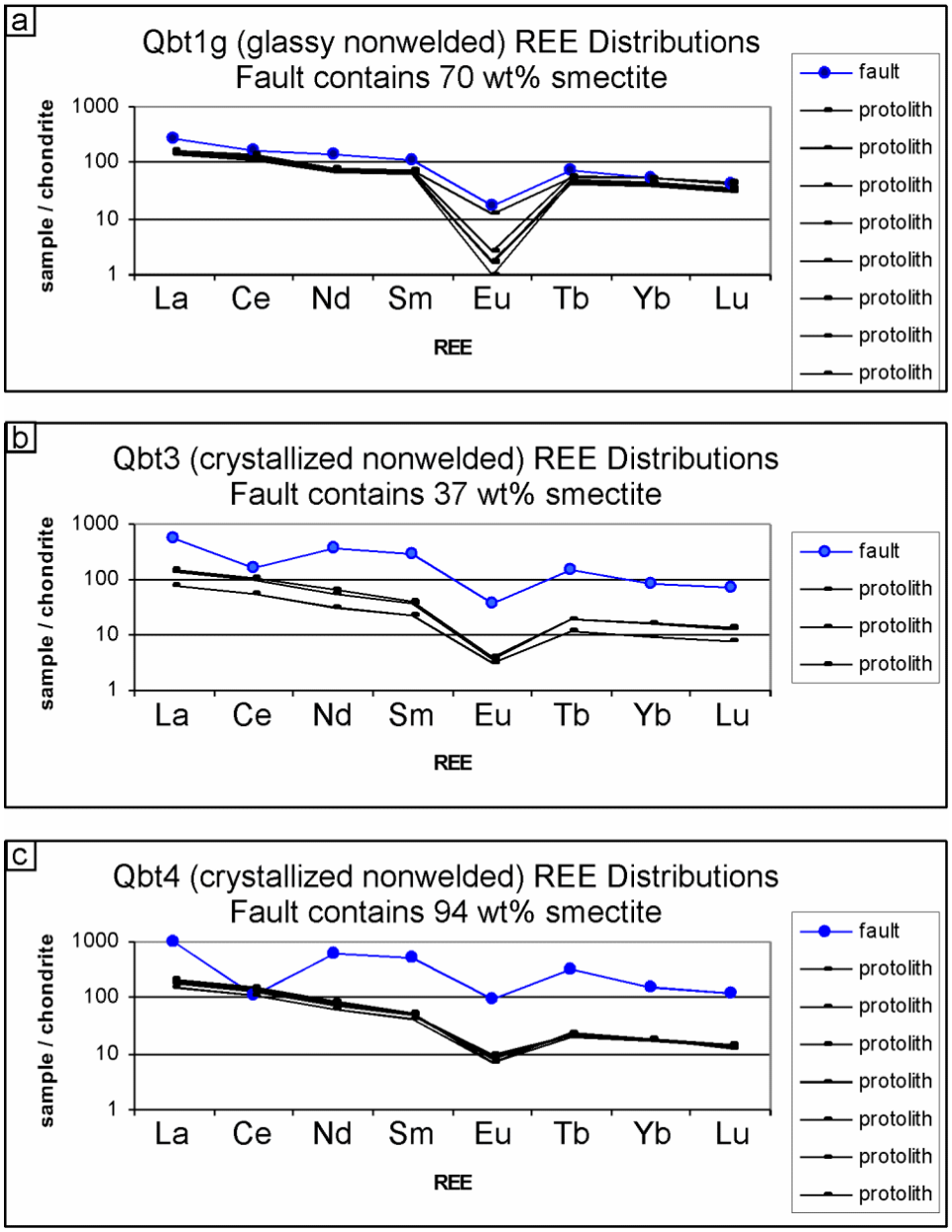

Figure 4.11. REE distributions for clay-rich (>10 wt% smectite) deformation bands and adjacent protolith, given by Bandelier Tuff unit (cf. Fig 4.2b). Protolith values from Stimac et al. [2002]; fault values determined in this study. Note the similarity of fault-zone smectite patterns in (b) and (c), both of which are generally elevated relative to protolith.

Stable Isotope Characterization of Deformation Bands and Adjacent Protolith

Four representative protolith-fault sets were analyzed for stable isotope composition (Tables 4.2 and 4.9). Protolith silicate $\delta^{18}O$ analyses range from 6.1 to 6.8 per mil (Table 4.9), values that are typical of igneous rocks and fluids [Campbell and Larsen, 1998]. In most of the fault zones analyzed, $\delta^{18}O$ values are higher than those of protolith (samples >50 cm from fault-zone boundary), especially at the fault-zone margins (<5 mm from fault zone). One notable exception is in the oxide-mineralized deformation-band fault zone in crystallized nonwelded ignimbrite shown in Fig. 4.7. Both a single unaltered deformation band (bt1) in the eastern portion of this fault zone (Fig. 4.1) and the footwall margin have lower $\delta^{18}O$ values than the protolith. The latter differences fall within analytical error (approximately 1.0 per mil), and therefore may not

Table 4.9. Stable isotope data and glass and smectite content for protolith-deformation band sets.

Sample description	□^{18}O	□^{13}C	Wt% glass	Wt% Smectite
crystallized protolith (bt37)	6.3	-26.0	5.8	0
footwall boundary (bt36)	6.2	-25.9	-	-
unaltered deformation band (bt1)	5.8	-25.9	11.7	0
oxide-mineralized deformation band (bt2a)	6.8	-25.9	13.5	0
hanging wall boundary (bt34)	7.0	-25.7	-	-
crystallized protolith (bt29)	6.1	-25.9	-	-
footwall boundary (bt116c)	8.9	-25.8	4	0
deformation band with clay (bt116)	6.7	-25.9	9.6	1.4
hanging wall boundary (bt116b)	7.1	-25.8	4.7	0
glassy protolith (bt64)	6.2	-25.7	-	-
footwall boundary (bt8/9a)	11.1	-25.3	70.3	2.9
deformation band with clay (bt9)	8.5	-25.8	50.5	17.4
deformation band with clay (bt8)	8.8	-26.0	69.6	7.8
hanging wall boundary (bt8/9b)	9.3	-26.1	69.3	2.2
crystallized protolith (bt73)	6.8	-25.8	-	-
footwall boundary (bt74)	7.2	-25.9	3.4	0
deformation band with carbonate & clay (bt111a)	20.8	-4.9	16	36.5
hanging wall boundary (bt75)	7.7	-25.8	4	0

- = not analyzed.

be statistically significant. Analysis of one calcite-cemented deformation band similar to that shown in Fig. 4.6 gives a $\delta^{13}C$ value of –4.9 per mil and a $\delta^{18}O$ value of 20.8 per mil.

Discussion

Oxygen Isotope Enrichment

Oxygen isotope ratios give information about the spatial extent of fluid-rock interaction and potential fluid sources [e.g., Campbell and Larsen, 1998]. Our data for fault-zone material, fault-zone boundaries, and distant protolith indicate a general increase in $\delta^{18}O$ for most fault zones, especially at the boundaries, compared to protolith (Table 4.9; Fig. 4.12). The increase in $\delta^{18}O$ is seen only in deformation bands that contain smectite, although there is no consistent relationship between wt% smectite and $\delta^{18}O$ value (Fig. 4.12). These data indicate meteoric fluid-rock interaction within and directly adjacent to deformation bands, which is consistent with low temperature alteration of the initially high temperature ignimbrite. The higher $\delta^{18}O$ values of fault-zone margins (e.g., bt116c; Fig. 4.12) that lack diagenetic minerals suggest that low temperature alteration is not the only process that influences the stable isotopic signature in these rocks. These elevated values could result from oxygen isotope exchange between the fault and fluids that has not led to diagenesis (e.g., evaporation into high porosity protolith). Lower $\delta^{18}O$ values in fault cores relative to fault-zone margins may indicate alteration facilitated by longer residence times of fluids rather than extensive isotopic exchange via fluid flow.

In the calcite-cemented deformation band, the $\delta^{18}O$ value of 20.8 per mil reflects a meteoric fluid source [cf. Campbell and Larsen, 1998]. The -4.9 per mil $\delta^{13}C$ value falls

within the range of values exhibited by magmatic carbon, which at first consideration suggests that the carbon in this fault is derived from ignimbrite during alteration

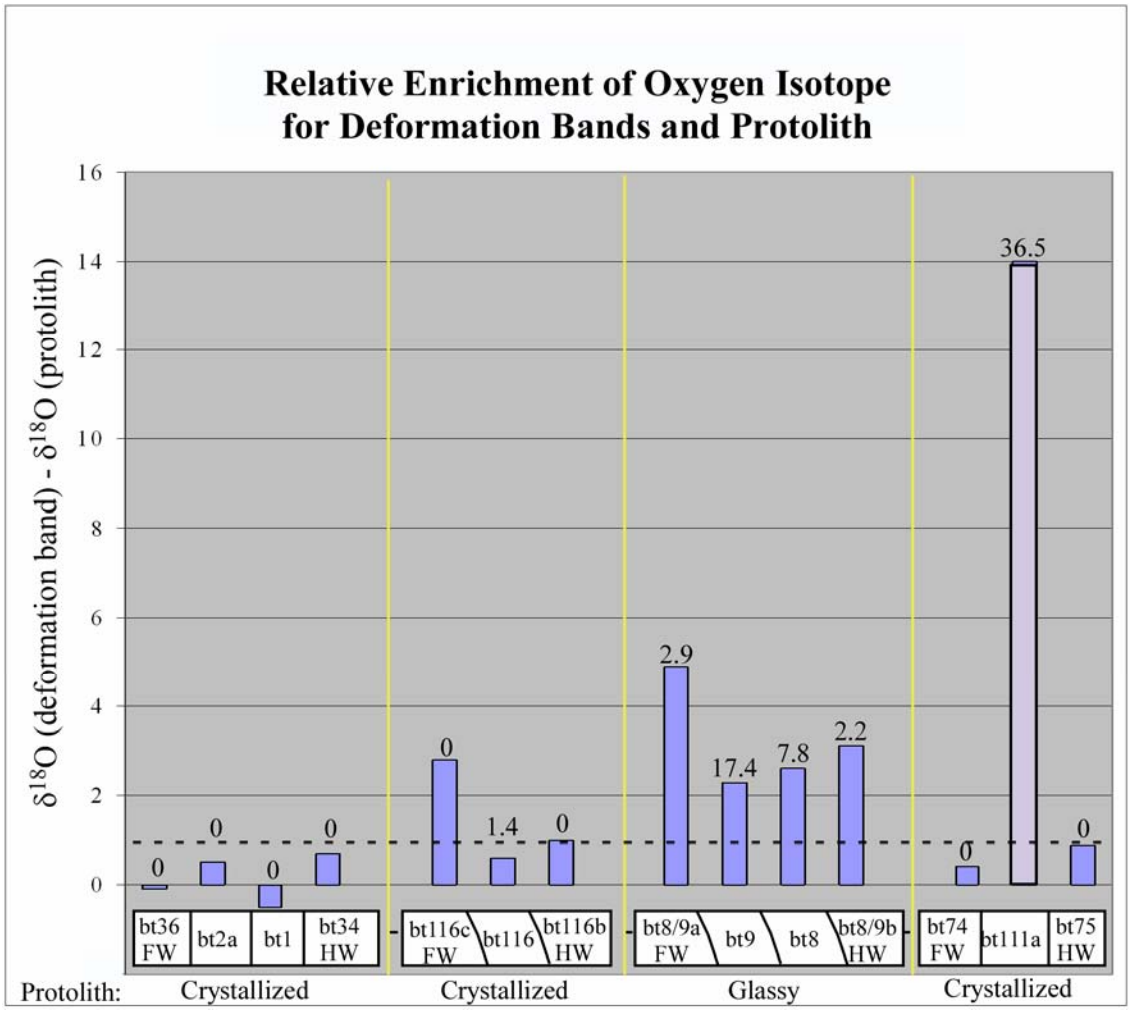

Figure 4.12. Graph of relative differences in $\delta^{18}O$ between portions of deformation-band fault zones. $\delta^{18}O$ value for protolith has been subtracted from that of deformation band such that enrichments are shown as values > 0. Wt% smectite for fault-zone sample is given above each $\delta^{18}O$ value (vertical bar). Dashed lines represent the limit of precision for determining significant differences between protolith and fault-zone $\delta^{18}O$ value. Representation of fault-zone components and approximate fault dips are given below graphed data. FW = footwall, HW = hanging wall. Sample numbers correspond to those given in Tables 4.2, 4.3, 4.4. Note the large difference in $\delta^{18}O$ between deformation band and protolith for sample bt111a, resulting from presence of calcite (all other samples are dominated by silicates and represent whole-rock analysis).

[cf. Barnes et al., 1978]. However, the amount of magmatic carbon available in rhyolitic ignimbrite like the Bandelier Tuff is very small, and therefore is insufficient for the precipitation of calcite (N. Dunbar, personal communication, 2004). Further, this $\delta^{13}C$ value is similar to that reported by Newman (1996). Newman (1996) called on local plant roots as the primary source for carbon in the precipitation of calcite in fractures of the Bandelier Tuff; a similar interpretation for calcite in the faults we have studied would be consistent with widespread observations of preferential plant root growth in deformation bands. Atmospheric CO_2 input, through dust and rain, may also affect the $\delta^{13}C$ signature within these faults since they are zones of increased translocation and fluid flow (cf. Ehleringer, 1988; cf. Newman, 1996). With any of these potential sources of carbon, the stable carbon isotope composition we have measured is consistent with low temperature, pedogenic precipitation from meteoric fluids.

The Origin of Smectite in Deformation Bands

Microstructural observations suggest two possible mechanisms by which deformation-band fault zones could be enriched in smectite: *in situ* alteration and translocation of smectite. Localized *in situ* alteration is evidenced by smectite surrounding some shards (glassy or devitrified) and mafic lithic fragments that exhibit very diffuse grain boundaries. In these cases, smectite appears to be replacing the glass and mafic grains (Fig. 4.4c). This texture is more common around mafic lithic fragments. Unaltered grains are also commonly surrounded by large accumulations of smectite, similar to textures found in desert soils (Fig. 4.4b) [cf. Gile et al., 1995]. These

microstructures suggest the introduction of smectite by transport from an external source (translocation), likely in colloidal form.

Evidence for both *in situ* formation and translocation of smectite can also be found in the mineralogical and geochemical differences between fault-zone smectite and protolith. Deformation bands that contain smectite show differences in glass and feldspar content relative to protolith that suggest *in situ* alteration of ignimbrite matrix. In glassy nonwelded unit Qbt1g and crystallized nonwelded unit Qbt4, deformation bands with increasing amounts of smectite have correspondingly lower amounts of glass and feldspar relative to protolith (Figs. 4.8a and 4.10a). In crystallized nonwelded unit Qbt3, deformation bands with increasing amounts of smectite have correspondingly lower feldspar contents, but higher glass contents relative to protolith. The consistent inverse relationship between smectite and feldspar contents suggests that smectite in these deformation bands is produced in part by alteration of feldspar grains. Glass is also altering in Qbt1g and Qbt4. The cause of higher glass content in deformation bands found in Qbt3 is explored later in this discussion.

The alteration of glass and feldspar alone is insufficient to produce smectite (Tables 4.1 and 4.8). The low Fe and Mg contents of glass and feldspar suggest that the higher bulk MgO and Fe_2O_3 contents of smectite-rich deformation bands (Tables 4.3 and 4.4; Figs. 4.8b, 4.9b, and 4.10b) record a combination of *in situ* alteration of mafic minerals and translocation of more Fe-rich soil-derived smectite (Tables 4.6, 4.7, and 4.8). This smectite is an impure montmorillonite characterized in XRD analyses by a diffuse peak [Vaniman et al., 2002; S. Chipera, personal communication, 2002]. Geochemically, soil-derived smectite analyzed by Vaniman et al. [2002] has higher bulk

Fe_2O_3 contents than protolith [Vaniman et al., 2002]. This is similar to the smectite analyzed in this study (Tables 4.3 and 4.4). REE signatures of soil-derived smectites from Vaniman et al. [2002] are also similar to the fault-zone smectites observed in Qbt3 and Qbt4 (Fig. 4.11b, c). Both soil-derived and fault-zone smectites have elevated REE patterns relative to protolith, a pronounced negative Ce anomaly, and an Eu anomaly that is similar to that of protolith. Fault-zone smectite from a deformation band in Qbt1g (Fig. 4.11a) does not show these characteristics, and therefore may be more dominated by smectite derived *in situ*. In fact, for deformation bands similar to this one (Fig 4.11a), in which the amount of smectite exceeds the porosity of the unaltered rock, *in situ* alteration of glass, feldspar, and mafic phases must be a significant process of smectite production. This is because accumulation of smectite by translocation alone is limited to the amount of pre-existing pore space in the rock. We therefore propose that both *in situ* alteration of protolith matrix and translocation of soil-derived smectite are responsible for large amounts of smectite in deformation-band faults. The extent to which one process dominates over the other is unclear, but evidence of both indicates preferential water retention and fluid flow through deformation bands. *In situ* alteration of glass, feldspar and mafic minerals to form smectite requires higher amounts or longer residence times of fluid in the deformation band relative to protolith in order to facilitate alteration of ignimbrite matrix to smectite. Fault-zone smectite with higher bulk Fe_2O_3 and MgO than protolith matrix requires that material be added to the deformation bands.

Calcite Cementation in Deformation Bands

Two distinguishing features of calcite-cemented deformation bands are 1) rod-shaped calcite micromorphology (Fig. 4.5c) and 2) high levels of CaO and MgO relative to protolith (Figs. 4.8b and 4.9b). Calcite morphology suggests two possible mechanisms of cementation in these deformation bands: physicochemical and microbially mediated precipitation [Verrecchia and Verrecchia, 1994]. Physicochemical processes reflect long dry spells alternating with brief wet periods. During dry periods, intense evaporation results in supersaturation of solutions and the rapid precipitation of crystals. Inhibition of lateral crystalline growth by adsorbed ions or clays is a common explanation for the acicular shape typical of crystals formed in this way [Verrecchia and Verrecchia, 1994]. The spatial association between smectite and calcite in these deformation bands suggests that desiccation of this swelling clay may play a key role in determining the rod-shaped morphology of these calcite crystallites. Downward transport of eolian dust and soil-derived smectite by dissolution/precipitation and colloidal transport, respectively, during transient precipitation events can also facilitate addition of CaO and MgO to deformation bands. Such pedogenic mobilization of eolian dust has been suggested to cause increases in CaO for soils in arid environments [Gile et al., 1981; Quade and Cerling, 1990], including the Pajarito Plateau [Eberly et al., 1996]. Increases in smectite that consistently accompany calcite cementation (Table 4.5) may explain the higher MgO contents relative to protolith.

Widespread observations of preferential root growth in these deformation bands suggest that organic material could also participate in the production of calcite in these zones. Microbially mediated precipitation requires organic molecules in the soil solution,

which are adsorbed onto the crystal. This adsorption inhibits crystal growth, promoting an acicular morphology [Verrecchia and Verrecchia, 1994]. Either mechanism of calcite precipitation (desiccation or microbially mediated precipitation) requires preferential fluid flow through deformation bands relative to protolith.

Oxide Mineralization within a Unique Deformation-Band Fault Zone

Only one of the more than 100 faults studied shows extensive oxide mineralization (Fig. 4.7). Given the uniqueness of this fault, it does not serve as a basis for characterizing fluid-fault interaction on the Pajarito Plateau. However, it does give insight to the processes of fluid-fault interaction in the absence of diagenetic alteration (i.e., smectite enrichment and calcite cementation).

The zone of oxide-mineralized deformation bands shown in Fig. 4.7 has higher Al_2O_3, TiO_2, Fe_2O_3, and P_2O_5 than crystallized nonwelded ignimbrite protolith (Qbt3), probably recording the higher glass and slightly higher augite content of the fault zone (Tables 4.4 and 4.5). Although mineralogical data do not show, within uncertainties, higher abundances of magnetite and ilmenite in the fault zone than in the protolith, BSE imaging reveals that these minerals are visibly more abundant in the fault zone, and therefore may account for higher Fe_2O_3 and TiO_2 relative to protolith. At the western edge of the fault zone, BSE images show textures that suggest Fe- and Sn-oxide mineral growth outward from the zone of deformation bands toward an open slip surface (Fig. 4.7c, d) [cf. Means and Li, 2001]. The euhedral form of these oxide minerals suggests that they formed after the last stage of faulting. Relatively constant $\delta^{18}O$ values (Table 4.9; Fig. 4.12), lack of low-temperature alteration (suggested by absence of smectite or calcite; Table 4.4), and high levels of trace elements associated with high-temperature

hydrothermal fluids (e.g., Pb, As, Zn) suggest that this oxide mineralization is not the result of pedogenic, meteoric fluid flow and precipitation [cf. Skinner, 1997]. Instead, mineralization is more likely to have occurred from hydrothermal fluid. We infer that Fe- and Sn-rich fluid moved upward from depth through the deformation bands, providing a source of solutes for precipitation outward from the slip surface. Crystallization resulted from supersaturation of the fluid at the slip surface, which could have been facilitated by processes of evaporation, rapid cooling, or pressure decreases between the deformation bands and the slip surface [cf. Means and Li, 2001].

The following sequence of fluid-fault interaction is proposed for this fault zone: (1) deposition of the nonwelded ignimbrite unit, (2) devitrification and vapor-phase alteration of volcanic glass, (3) post-cooling fault-zone deformation via grain crushing and pore collapse, (4) continued deformation band development in response to progressive deformation (i.e., increase in spatial density of deformation bands), (5) strain hardening of the fault zone, leading to slip surface development [cf. Aydin and Johnson, 1983; Shipton and Cowie, 2001], (6) preferential, upward flow of hydrothermal fluids through the zone of deformation bands, resulting in disseminated magnetite and ilmenite and (7) Fe- and Sn-oxide mineralization on the slip surface.

Mineralogical Differences Between Deformation Bands and Protolith Attributed to Protolith Variations: Implications for Deformation-Band Propagation and Origin in Ignimbrites

Mineralogical differences between deformation bands and protolith may offer insight into fault propagation. Microstructural observations indicate that deformation bands weave around stronger grains, apparently propagating along the interface between

strong grains and weaker matrix in the rock (Fig. 4.1b). Stronger grains include quartz and feldspar phenocrysts, unaltered lithic fragments, and tightly intergrown postdepositional crystals of tridymite and cristobalite. Weaker grains include singular glassy or devitrified shards, fine-grained ash, altered lithic clasts, and weakly connected postdepositional crystals of tridymite and cristobalite. Mineralogical differences between unaltered deformation bands and protolith in crystallized nonwelded unit Qbt3 support this observation (Table 4.5). In these faults, there are lower amounts of strong minerals (quartz, alkali feldspar, cristobalite, and tridymite) and higher amounts of weak glass relative to protolith. These differences are difficult to explain in terms of local variations in the degree and nature of postdepositional crystallization since deformation bands are typically subvertical whereas localized variations in crystallization are typically subhorizontal [Stimac et al., 1996; Freundt et al., 2000]. However, it is mechanically feasible that these deformation bands are locally deflected around larger, more competent grains because of the high mechanical contrast at grain/matrix margins. Because phenocrysts and lithic clasts are neither numerous nor large (Table B1, Appendix B), these grain-scale deflections – generally visible only at the microscopic scale - do not result in a mesoscopically wavy structure.

Mineralogical differences may also offer insight into the origin of the enigmatic features discussed earlier (sample bt115), which may be either primary or secondary structures. This type of structure was found in three locations (sample bt115, location 16, Table 4.2; Table A1, Appendix A; locations 2 and 12, Table A1, Appendix A). It is characterized by abundant phenocrysts and lithic clasts relative to pumice, pore space, and matrix ash. This particular distribution of grains may reflect an origin that is not

structural, but is instead a primary feature of ignimbrite deposits—elutriation, or lapilli, pipes. These are typically subvertical, tabular structures with locally sigmoidal geometries, and are marked by an abundance of phenocrysts and lithic clasts. They originate just after ignimbrite emplacement as conduits for volcanic gases to escape from the cooling deposit, blowing out fine vitric ash (Freundt et al., 2000; N. Dunbar, personal communication, 2004). Since there is no evidence of displacement on these structures (which can be hard to find in cases of dominantly strike-slip deformation, or more massive portions of the ignimbrite sequence), it is unclear from outcrop characterization whether these structures are primary, secondary, or primary structures reactivated during later faulting. Petrographic observations of slight strike-parallel alignment of phenocrysts could be explained by either fault-zone shearing or the vertical escape of volcanic gas and fine particles.

Geochemical Differences between Deformation Bands and Protolith Attributed to Preferential Solute Transport

Major oxide abundances and trace element concentrations of some deformation bands vary substantially relative to protolith (Table 4.5). Given the evidence for enhanced vadose-zone fluid flow and diagenetic alteration in deformation bands on the Pajarito Plateau, potential explanations for these differences are explored in terms of solute transport or deposition in the presence of fluids.

Almost all deformation bands with smectite have higher Fe_2O_3, MgO, and TiO_2 than protolith, which is consistent with smectite composition (Tables 4.5 and 4.7) [cf. Lander and Hay, 1993]. Higher V, Cr, Cu, and Ni concentrations in these deformation bands can be attributed to the presence of soil-derived smectite [Bhumbla and Keefer,

1994; McDonald et al., 1996] and, in one deformation band (bt111b; Table 4.5), calcite. Higher Ba, As, Th, and U concentrations, found in only a few of these deformation bands (Table 4.5), can also be linked to calcite and translocated smectite. The concentrations of these trace elements are higher due to their high affinity for adsorbtion onto the surfaces of fine-grained smectite and calcite crystals [cf. Bhumbla and Keefer, 1994; McDonald et al., 1996]. Other processes, such as dissolution and precipitation, could facilitate the incorporation of trace elements into the crystal structures of these diagenetic minerals. Two notable exceptions to the discussed trends include a deformation band with very low smectite (bt116, 1.4 wt% smectite) and another with relatively high calcite content (bt7b, 21.7 wt% calcite, 18.1 wt% smectite). For sample bt116, the anomalous geochemical signature is potentially due to its nearly identical major element composition relative to protolith and relatively low smectite content. For sample bt7b, the lack of higher major oxide and trace element concentrations may be due to the large amount of calcite found in this fault, which swamps the chemical signature.

The most significant difference between fault-zone and protolith trace-element geochemistry occurs in the oxide-mineralized deformation band shown in Fig. 4.7. In addition to higher Ba, Sr, Cu, and Zr, there are much higher concentrations (one to two orders of magnitude) of Pb, As, and Zn in this fault relative to protolith. These latter differences may be attributed to hydrothermal influences [cf. Skinner, 1997]. An unaltered deformation band (bt1) in this same outcrop shows similar, but less pronounced, geochemical differences.

Proposed Model of Structural and Diagenetic Evolution of Deformation Bands in Nonwelded Bandelier Tuff

The results of this work can be expressed in the form of a conceptual model of the structural and diagenetic evolution of deformation-band faults on the Pajarito Plateau. In this model, deformation bands begin as zones in which grains, especially thin and weak glass shards, are crushed, and pores collapse by shear-enhanced compaction, grain-boundary sliding, and/or shearing (Figs. 4.1b and 4.13a). Glass shards are preferentially deformed as deformation bands propagate through the weakest portions of the rock. As a result, deformation bands may have slightly more glass and lower quartz, feldspar, tridymite, cristobalite, or trace minerals than protolith. Other than this difference, which is more pronounced in crystallized nonwelded ignimbrite, deformation bands are initially composed of the same material as the protolith, but have lower porosity, smaller grains, and smaller pore sizes [Wilson et al., 2003]. In dry vadose zones, these petrophysical properties cause similar faults in sand to be zones of preferential water retention (Fig. 4.13b) [Stephens, 1996; Sigda et al., 1999; Sigda and Wilson, 2003]. This preferential water retention may lead to enhanced alteration of unstable and grain-size-reduced feldspar, mafic lithic clasts, and volcanic glass by hydrolysis [cf. Starkey and Blackman, 1979; cf. Hay and Guldman, 1987; cf. Lander and Hay, 1993], providing a portion of the constituents necessary for formation of smectite (Figs. 4.3, 4.4, and 4.13c). Preferential water retention in faulted nonwelded ignimbrites can also lead to enhanced fluid flow during infiltration events, allowing colloidal transport of soil-derived smectite from the surface [cf. Wan and Wilson, 1994], eventually leading to higher TiO_2, MgO, and Fe_2O_3 in the fault. *In situ* alteration allows for extensive accumulation of smectite within deformation bands (Figs. 4.4 and 4.13b, c). Preferentially wet zones in arid environments

are also observed to be zones of preferential root growth. The presence of retained fluids, plant roots, and soil-derived smectite within a deformation band can lead to precipitation of calcite by microbial or episodic desiccation activity (Figs. 4.6 and 4.13d) [cf. Boquet et al., 1973; Verrecchia and Verrecchia, 1994; Newman et al., 1997].

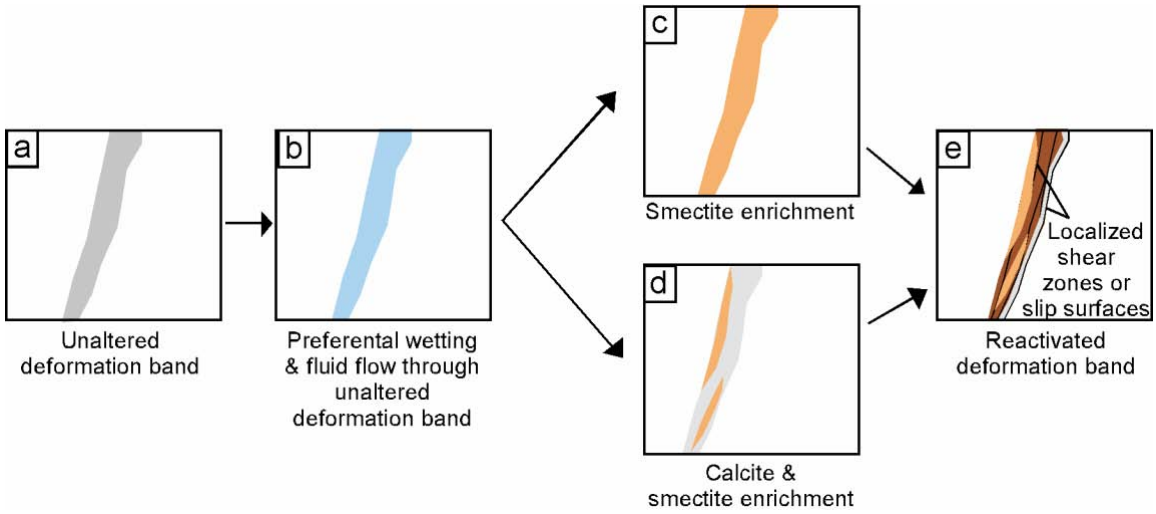

Figure 4.13. Schematic diagram of proposed evolution of a deformation band through preferential water retention, fluid flow, and subsequent diagenetic alteration and/or mineralization. (a) Unaltered deformation band is subjected to an infiltration event and preferentially retains water (b) due to pore-size reduction in a dry vadose-zone environment. Preferential water retention may lead to preferential fluid flow during infiltration events in arid vadose zones [cf. Stephens, 1996; Sigda and Wilson, 2003]. Preferential water retention and fluid flow may lead to clay enrichment (c) with variable degrees of calcite cementation (d). These diagenetic modifications further reduce pore size, destroying pore connectivity and eventually closing the pathway for fluid flow. Reactivation within or along the boundaries of modified deformation bands by additional cataclasis, root growth, and/or fracture may result in renewed pore connectivity within localized shear zones or distinct slip surfaces (e).

Continued alteration of, and precipitation within, deformation bands can further reduce pore size, eventually closing pore throats [cf. Mok et al., 2002], at which point the diagenetically modified deformation band would become a barrier to vadose-zone fluid flow (Fig. 4.13c, d). However, further structural modification of the deformation band

(e.g., additional shear within deformation bands or slip on discrete surfaces, opening of desiccation cracks in smectite, etc.), may again lead to localized pathways for fluids (Fig. 4.13e).

Implications for Vadose-Zone Fluid Flow and Transport in the Bandelier Tuff

Bandelier Tuff ignimbrite units are composed of highly heterogeneous grains and pore spaces. These include macropores (mm-scale) in undeformed matrix, micropores (μm-scale) in deformation bands in nonwelded units, and fractures (mm to cm-scale) in welded and crystallized nonwelded units. Fluid flow and transport through these features are of great concern due to the potential for movement of contaminated fluids into the water supply beneath the Pajarito Plateau. Yet the movement of water and contaminants through preferential flow pathways is difficult to characterize. This study of geochemical differences between deformation bands and adjacent protolith helps to constrain the role of these structures in vadose-zone fluid flow in the Bandelier Tuff.

At most of the locations studied, the Bandelier Tuff has been above the water table since deposition [Purtymun and Johansen, 1974]. Locations in the southern portion of the Pajarito Plateau that are at lower elevations and near canyon bottoms may have been below the water table during some period subsequent to deposition [Purtymun and Johansen, 1974] (i.e., location 6 from which samples bt7, bt8, and bt9 were collected, Fig. A1 and Table A1, Appendix A). However, structures in all of these areas exhibit similar features, suggesting that diagenesis in the faults studied did occur under similar conditions.

Because reduction of porosity in deformation bands reduces saturated permeability (Chapter 5) we do not expect these structures to act as preferential flow paths below the water table. In addition, we expect diagenetic processes and microstructures to be distinct in the phreatic versus the vadose zone. We therefore infer that preferential alteration and mineralization of all fault zones studied record enhanced vadose-zone fluid transport through deformation bands. The large surface area and small grain sizes in deformation bands facilitate these diagenetic processes in the presence of water. The extent of preferential fluid transport is restricted by the connectivity of pores in deformation bands. Capillary rise is higher in smaller pores, but irregularly shaped pores, like those in ignimbrites, make poor capillary tubes [Birkeland, 1999]. Rode [1962] suggests such a rise may be 1 m or less in sands and 3 to 4 m more in regularly shaped pores in clays. In ignimbrite deposits, capillary rise in macropores can be very small due to large pore sizes and variable pore shape, but reduction in grain size and subsequent diagenetic modification (i.e., smectite enrichment) results in smaller, more regularly shaped pores in deformation bands. In these deformation bands, preferential fluid flow still may extend only 3 to 4 m from the source of water (e.g., rainfall from the surface or perched water table at shallow depths), depending on the residual water content of the adjacent protolith [Sigda and Wilson, 2003]. In arid and semiarid climates, the residual water content of the protolith is low. This creates a fluid flow regime that is dominated by the deformation band rather than the protolith [Sigda and Wilson, 2003]. This may cause preferential fluid flow through diagenetically altered deformation bands in excess of 4 m from the surface. In fact, deformation-band faults containing large amounts of smectite and calcite were observed along the Guaje Mountain fault trace near

Chupaderos Canyon to depths of 5 to 6 m from the surface (Table 4.2). The presence of live roots and calcite in these faults suggests present-day preferential fluid flow at these depths.

Many hydrologic models of fluid flow and solute transport through ignimbrite deposits consider focused flow and transport through fractures in welded units only (Fig. 4.14) [e.g., Winograd, 1971; Turin and Rosenberg, 1996]. Deformation bands have only recently been documented in nonwelded units [Wilson et al., 2003], so matrix flow is generally assumed to dominate these ignimbrites. Accordingly, these models predict slow, diffusional flow through nonwelded ignimbrites, and focused, fast fluid flow through fractures in welded ignimbrites [e.g., Wolfsberg et al., 2000]. Data presented here, however, indicate that deformation bands are also zones of focused fluid flow.

Results from XRD, XRF, INAA (REE) and SEM chemical analyses of deformation-band material suggest that, in addition to being flow pathways in the vadose zone, these structures allow preferential *in situ* alteration of protolith matrix as well as transport of smectite and calcite into the subsurface. Higher amounts of V, Cr, and Cu may reflect the trapping of some constituents in the fault zone due to their affinity for fine-grained diagenetic minerals. These solutes may originate from the surface, traveling vertically through the deformation band. Transport could occur up to several meters through a deformation band in a nonwelded ignimbrite unit and then through connecting fractures in a welded ignimbrite unit [cf. Vaniman and Chipera, 1995], potentially arriving at the regional water table at depth. Potential vertical communication between deformation bands and fractures requires continuity of a given fault through successive

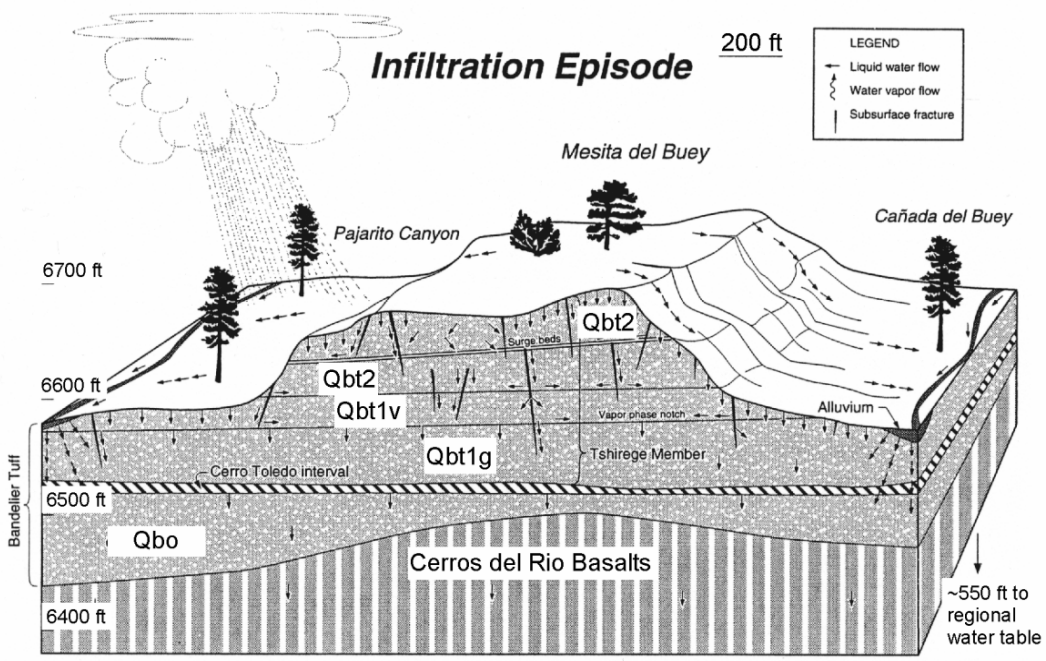

Figure 4.14. Conceptual model of vadose-zone fluid flow through the Bandelier Tuff on the Pajarito Plateau. Arrows show focused flow in fractures in the welded Qbt2 unit and crystallized nonwelded unit Qbt1v; deformation bands in nonwelded units Qbt1v, Qbt1g, and Qbo are not included in this conceptual model. Modified from Turin and Rosenberg [1996].

units of the Bandelier Tuff. This spatial continuity of a fault in variably welded units is observed only locally on the Pajarito Plateau due to the differential erosion of welded versus nonwelded units. However, a vertically continuous fault cutting variably welded ignimbrite has been documented at Busted Butte, NV [Wilson et al., 2003]. Given that such vertical continuity is also likely within the Bandelier Tuff, these faults could potentially result in fast paths for fluid flow and mineral/solute transport to far greater depths than previously considered (Figs. 4.2b and 4.14).

Conclusions

Deformation bands in both glassy and crystallized nonwelded units of the Bandelier Tuff are zones of preferential smectite enrichment and calcite cementation. Preferential vadose-zone fluid flow through these bands of pore- and grain-size reduction is recorded by these diagenetic phases, by microstructures, and by differences in chemistry between deformation bands and protolith.

Smectite enrichment in deformation bands is the result of a combination of *in situ* alteration of unstable volcanic glass, feldspar, and mafic minerals in the presence of water and colloidal transport of soil-derived smectite from the surface. Alteration is enhanced by the heightened reactivity of grain-size-reduced ignimbrite. The combination of processes requires both greater fluid retention and preferential flow through deformation bands relative to adjacent, smectite-poor protolith. Calcite cement in deformation bands consists of rod-shaped microcrystallites that form by microbially mediated precipitation and physicochemical processes associated with repeated desiccation of clay. Preferential root growth through faults and calcite micromorphology consistent with biologic activity collectively suggest that water is preferentially retained in these structures. The observed increase in CaO and smectite in these deformation bands relative to protolith via pedogenic dissolution/precipitation-mediated transport of Ca-rich eolian dust and/or colloidal transport of soil-derived smectite requires enhanced fluid flow.

The geochemistry of deformation bands changes with diagenesis. V, Cr, Cu, Sr, TiO_2, CaO, Fe_2O_3, and MgO are most consistently found in higher amounts in diagenetically modified deformation bands relative to protolith. Na_2O and K_2O are

consistently found in lower amounts in deformation bands containing smectite and calcite. Addition and removal of these constituents is evidence of higher fluid flux in these deformation bands relative to protolith.

In some localities, these deformation bands are spaced about 1 meter apart along transects hundreds of feet long (Lavine et al., 2002). Across the Pajarito Plateau, small-displacement faults may number in the thousands over a km^2 area (Carter and Winter, 1995). Although the nature of these faults has not been fully characterized, many of them occur in nonwelded ignimbrite, and therefore may be deformation bands rather than fractures. Given the evidence of the effect of deformation bands on vadose-zone fluid flow and transport, we suggest that where they are sufficiently continuous and densely spaced, these recently documented structures may be significant pathways for recharge and contaminant transport.

Acknowledgments

This research has been funded by a grant through the Institute of Geophysics and Planetary Physics (IGPP) at Los Alamos National Laboratory. Additional funding was provided by the Wyoming Geological Association (J. David Love Field Scholarship) and the New Mexico Geological Society (Grant-in-Aid). Thanks to Nelia Dunbar and Lynn Heizler for assistance on the electron microprobe, Steve Chipera for XRD analyses, Chris McKee for XRF analyses, Randy Korotev for INA analyses, and members of the Faults and Fluids group at New Mexico Tech for useful discussions.

References

Aldrich, M. (1986), Tectonics of the Jemez Lineament in the Jemez Mountains and Rio Grande rift, *J. Geophys. Res.*, *91*(B2), 1753-1762.

Antonellini, M., and A. Aydin (1994), Effect of faulting on fluid flow in porous sandstones: petrophysical properties, *AAPG Bull.*, *78*, 355-377.

Aronson, E. C., (1999), Modeling investigations on gas permeameters: spatial weighting functions and layered systems, M.S. Thesis, 91 pp., New Mexico Tech, Socorro.

Aubert, D., P. Stille, and A. Probst (2001), REE fractionation during granite weathering and removal by waters and suspended loads: Sr & Nd isotopic evidence, *Geochim. Cosmochim. Acta*, *65*(3), 387-406.

Aydin, A., and A. Johnson (1978), Development of faults as zones of deformation bands and as slip surfaces in sandstones, *PAGEOPH*, *116*, 931-942.

Aydin, A., and A. Johnson (1983), Analysis of faulting in porous sandstones, *J. Struct. Geol.*, *5*(1), 19-31.

Barnes, I., J. R. O'Neil, and J. J. Trescases (1978), Present day serpentinization in New Caledoniia, Oman, and Yugoslavia, *Geochim. Cosmochim. Acta*, *42*, 144-145.

Bhumbla, D. K., and R. F. Keefer (1994), Arsenic mobilization and bioavailability in soils, in *Arsenic in the Environment, Part I: Cycling and Characterization*, edited by J.O. Nrlagu, pp. 51-82, Wiley Series in Advances in Environmental Science and Technology, John Wiley & Sons, Inc., New York.

Birkeland, P. W. (1999), *Soils and Geomorphology*, 3rd ed., 430 pp., Oxford University Press, New York.

Boquet, E., A. Boronat, and A. Ramos-Cormenzana (1973), Production of Calcite (Calcium Carbonate) Crystals by Soil Bacteria is a General Phenomenon, *Nature*, *246*, 527-529.

Broxton, D., G. Heiken, S. J. Chipera, and F. M. Byers (1995), Stratigraphy, petrography, and mineralogy of Bandelier Tuff and Cerro Toledo deposits, in *Earth Science Investigations for Environmental Restoration—Los Alamos National Laboratory Technical Area 21*, edited by D.E. Broxton and P.G. Eller, Los Alamos National Laboratory Report LA-12934-MS, p. 33-64.

Caine, J. S., J. P. Evans, and C. B. Forster (1996), Fault zone architecture and permeability structure, *Geology*, *24*(11), 1025-1028.

Campbell, A. R., and P. Larsen (1998), Introduction to stable isotope applications in

hydrothermal Systems, in *Techniques in Hydrothermal Ore Deposit Geology, Reviews in Economic Geology, 10,* edited by J. Richardson, and P. Larsen, pp. 173-193.

Carter, K. E., and J. N. Gardner (1995), Quaternary Fault Kinematics in the Northwestern Espanola Basin, Rio Grande Rift, New Mexico, *New Mexico Geological Society Guidebook, 46th Field Conference, Geology of the Santa Fe Region*, p. 97-102.

Carter, K. E., and C. L. Winter (1995), Fractal nature and scaling of normal faults in the Espanola Basin, Rio Grande rift, New Mexico: implications for fault growth and brittle strain, *J. of Struct, Geol., 17*(6), 863-873.

Cashman, S., and K. Cashman (2000), Cataclasis and deformation-band formation in unconsolidated marine terrace sand, Humboldt County, California, *Geology, 28(*2), 111-114.

Chipera, S. J., and D. L. Bish (2001), FULLPAT: An Improved Full-Pattern Quantitative X-ray Diffraction Method, in Proceedings of the 38th Annual Clay Minerals Society Meeting, Madison, WI, p. 105.

Chipera, S. J., G. D. Guthrie, Jr., and D. L. Bish (1993), Preparation and Purification of Mineral Dusts, in *Reviews in Mineralogy 28, Health Effects of Mineral Dusts,* edited by G. D. Guthrie, Jr., and B. T. Mossman, pp. 235-249, Mineralogical Society of America.

Davenport, D. W., B. P. Wilcox, and B. L. Allen (1995), Micromorphology of Pedogenically Derived Fracture Fills in Bandelier Tuff, New Mexico, *Soil Sci. Soc. of Am. Journ., 59,* 1672-1683.

Dinwiddie, C. L., R. W. Fedors, D. A. Ferrill, and K. Keighley-Bradbury (2002), Matrix permeabilities of faulted nonwelded tuffs, *Geol. Soc. Amer .Annual Meeting Program with Abstracts*, Denver, CO.

Eberly, P., L. D. McFadden, and P. M. Watt (1996), Eolian Dust as a Factor in Soil Development on the Pajarito Plateau, Los Alamos Area, Northern New Mexico, in The Jemez Mountains Region, *New Mexico Geological Society 47th Annual Field Conference*, edited by F. Goff et al., pp. 383-389.

Ehleringer, J. R. (1988), Carbon isotope ratios and physiological processes in aridland plants, in Rundel, P. W., Ehleringer, J. R., and Nagy, K. A., eds., Applications of stable isotope ratios to ecological research, New York, Springer-Verlag, p. 41-54.

Evans, J.P. and F.M. Chester, 1995, Fluid-rock interaction in faults of the San Andreas system: Inferences from San Gabriel fault rock geochemistry and microstructures, *J. Geophys. Res., 100*(B7), 13007-13020.

Gile, L. H., J. W. Hawley, and R. Grossman (1981), Soils and geomorphology in the Basin and Range area of southern New Mexico, Guidebook to the Desert project, *New Mexico Bureau of Mines and Mineral Resources Memoir 39*, 222 pp.

Gile, L. H., J. W. Hawley, R. Grossman, H. C. Monger, C. E. Montoya, and G. H. Mack (1995), Supplement to the Desert Project Guidebook, with Emphasis on Soil Micromorphology, *New Mexico Bureau of Mines and Mineral Resources Bulletin 142*, 96 pp.

Götze, J., and R. Lewis (1994), Distribution of REE and trace elements in size and mineral fractions of high-purity quartz sands, *Chem. Geol., 114*, 43-57.

Hallet, R. B. and P. R. Kyle (1993), XRF and INAA Determinations of Major and Trace Elements in Geological Survey of Japan Igneous and Sedimentary Rock Standards, *Geostandards Newsletter, 17*, 127-134.

Hay, R.L., and S. G. Guldman (1987), Diagenetic Alteration of Silicic Ash in Searles Lake, CA, *Clays and Clay Minerals, 35*(6), 449-457.

Heiken, G., F. Goff, J. Gardner, W. Baldridge, J. Hulen, D. Nielson, and D. Vaniman (1990), The Valles/Toledo Caldera Complex, Jemez Volcanic Field, New Mexico, *Ann. Rev. Earth Plan. Sci., 18*, 27-53.

Izett, G. A., and J. D. Obradovich (1994), $^{40}Ar/^{39}Ar$ age constraints on the Jaramillo Normal Subchron and the Matuyama-Bruhnes geomagnetic boundary, *J. Geophys. Res., 99*(B2), 2925-2934.

Knipe, R. J. (1993), The influence of fault zone processes and diagenesis on fluid flow, in Diagenesis and Basin Development, *AAPG, Studies in Geology #36*, edited by A. D. Horbury and A. G. Robinson, eds., pp. 135-148.

Korotev R. L. (1991), Geochemical stratigraphy of two regolith cores from the central highlands of the Moon, in Proceedings of Lunar Planetary Sciences, 21, edited by V. L. Sharpton and G. Ryder, pp. 229-289, Lunar and Planetary Institute, Houston.

Lander, R. H., and R. L. Hay (1993), Hydrogeologic control on zeolitic diagenesis of the White River Sequence, *Geol. Soc. Amer. Bull., 105*, 361-376.

Lavine, A., C. J. Lewis, D. K. Katcher, J. N. Gardner, and J. E. Wilson (2003), Geology of the North-central to Northeastern portion of Los Alamos National Laboratory, New Mexico, *Los Alamos National Laboratory Report LA-14043-MS*, 44 pp.

Lewis, C. J., A. Lavine, S. L. Reneau, J. N. Gardner, R. Channell, and C. W. Criswell (2002), Geology of the Western Part of Los Alamos National Laboratory (TA-3 to TA-16), Rio Grande Rift, New Mexico, *Los Alamos National Laboratory Report*

LA-13960-MS, 97 pp.

McCrea, J. M. (1950), The isotopic chemistry of carbonates and a paleotemperature scale, *J. Chem. Phys. 18*, 849-857.

McDonald, E. V., P. A. Longmire, P. M. Watt, R. T. Ryti, and S. L. Reneau (1996), Natural and major trace element background geochemistry of selected soil profiles, Los Alamos, New Mexico, in The Jemez Mountains Region: *New Mexico Geological Society 47th Annual Field Conference*, edited by F. Goff et al., pp. 375-382.

McLellan, S.M., 1989, Rare earth elements in sedimentary rocks: Influence of provenance and sedimentary processes, in Geochemistry and Mineralogy of REE. Mineral. Soc. Am. Rev. Min, v. 21, edited by B. R. Lipin and G. A. McKay, pp. 169-200.

Mok, U., Y. Bernabe, and B. Evans (2002), Permeability, porosity, and pore geometry of chemically altered porous silica glass, *J. Geophys. Res., 107*(B1), JB000247.

Mozley, P. S., and L. B. Goodwin (1995), Patterns of cementation along a Cenozoic normal fault: A record of paleoflow orientations, *Geology, 23*, 539-542.

Nakamura, N. (1974), Determination of REE, Ba, Fe, Mg, Na, and K in carbonaceous and ordinary chondrites, *Geochim. Cosmochim. Acta, 38*, 757-775.

Nelson, C. S., and A. H. Smith (1996), Stable oxygen and carbon isotope compositional fields for skeletal and diagenetic components in New Zealand Cenozoic nontropical carbonate sediments and limestones: a synthesis and review, *New Zealand J. Geol. Geophys., 39*, 93-107.

Newman, B. D. (1996), Geochemical investigations of calcite fracture fills and mesa-top water dynamics on the Pajarito Plateau, New Mexico, Ph.D. Thesis, New Mexico Tech, Socorro, New Mexico, 254 p.

Newman, B. D., A. R. Campbell, D. I. Norman, and D. B. Ringelberg (1997), A model for microbially induced precipitation of vadose-zone calcites in fractures at Los Alamos,New Mexico, USA, *Geochim. Cosmochim. Acta, 61*(9), 1783-1792.

Purtymun, W. (1995), Geologic and hydrologic records of observation wells, test holes, test wells, supply wells, springs, and surface water stations in the Los Alamos area, *Los Alamos National Laboratory Miscellaneous Report LA-12883-MS*, 339 pp.

Purtymun, W. D., and S. Johansen (1974), General geohydrology of the Pajarito Plateau, in *New Mexico Geological Society guidebook, 25th Field Conference, Ghost Ranch*, 347-349.

Quade, J., and T. E. Cerling (1990), Stable Isotopic Evidence for a Pedogenic Origin of Carbonates in Trench 14 near Yucca Mountain, Nevada, *Science*, *250*, 1549-1552.

Rawling, G., L. B. Goodwin, and J. Wilson (2001), Internal architecture, permeability structure, and hydrologic significance of contrasting fault zone types, *Geology*, *29*(1), 43-46.

Rode, A. A. (1962), *Soil science*, Israel Program for Scientific Translations, Jerusalem, 517 pp.

Shipton, Z.K., Cowie, P.A., 2001, Damage zone and slip surface evolution over mm to km scales in high-porosity Navajo sandstone, Utah, *J. Struct. Geol., 23,* 1825-1844.

Sigda, J. M., L. B. Goodwin, P. S. Mozley, and J. L. Wilson (1999), Permeability alteration in small-displacement faults in poorly consolidated sediments: Rio Grande Rift, central New Mexico, in *Faults and Subsurface Fluid Flow in the Shallow Crust, AGU Monograph* 113, edited by W.C. Haneberg et al., pp. 51-68.

Sigda, J. M., and J. L. Wilson (2003), Are faults preferential flow paths through semi-arid and arid vadose zones?, *Water Res. Res., 39,* doi:10.1029/2002WR001406.

Skinner, B. J. (1997), Hydrothermal mineral deposits: what we do and don't know, in *Geochemistry of Hydrothermal Ore Deposits*, 3rd ed, edited by H. L. Barnes, John Wiley & Sons, Inc., New York, pp. 1-29.

Smith, R. L., and R. A. Bailey (1966), The Bandelier Tuff-A study of ash-flow eruption cycles from zoned magma chambers, *Bull.Volc., 29*, 83-104.

Starkey, H. C., and P. D. Blackmon (1979), Clay mineralogy of Pleistocene Lake Tecopa, Inyo County, California, *USGS Prof. Pap. 1061,* 34 pp.

Stephens, D. B. (1996), *Vadose Zone Hydrology*, Lewis Publishers, Inc.: Boca Raton, 347 pp.

Stimac, J., D. Hickmott, R. Abell, A. C. L. Larocque, D. Broxton, J. Gardner, S. Chipera, J. Wolff, and E. Gauerke (1996), Redistribution of Pb and other volatile trace metals during eruption, devitrification, and vapor-phase crystallization of the Bandelier Tuff, New Mexico, *J. Volc. Geoth. Res., 73*, 245-266.

Stimac, J. A., D. E. Broxton, E. C. Kluk, S. J. Chipera, and J. R. Budahn (2002), Stratigraphy of the Tuffs from Borehole 49-2-700-1 at Technical Area 49, Los Alamos National Laboratory, New Mexico, *Los Alamos National Laboratory Report LA-13969,* 14 pp.

Thompson, M., Potts, P.J., Kane, J.S., Chappell, B.W., 1999, GeoPT3. International Proficiency Test for Analytical Geochemistry Laboratories—Report on Round 3, *Geostandards Newsletter, 23*, 87-121.

Thompson, M., Potts, P.J., Kane, J.S., Webb, P.C., Watson, J.S., 2000, GeoPT4. An International Proficiency Test for Analytical Geochemistry Laboratories—Report on Round 4, *Geostandards Newsletter, 24*, E1-E37.

Tidwell, V. C., and J. L. Wilson (2000), Heterogeneity, permeability patterns, and permeability upscaling: physical characterization of a block of Massillon sandstone exhibiting nested scales of heterogeneity, *SPE Res. Eval. Eng.*, *3*(4), 283-291.

Tobin, H., P. Vannucchi, and M. Meschede (2001), Structure, inferred mechanical properties, and implications for fluid transport in the decollement zone, Costa Rica convergent margin, *Geology, 29*(10), 907-910.

Turin, H. J., and N. D. Rosenberg (1996), A conceptual model for flow in the vadose zone beneath the finger mesas of the Pajarito Plateau, in The Jemez Mountains Region: *New Mexico Geological Society 47th Annual Field Conference*, edited by F. Goff et al., pp. 74-76.

Vaniman, D. T., and S. J. Chipera (1995), Mesa-penetrating fractures, fracture mineralogy, and projected fault traces at Pajarito Mesa, in *Geological Site Characterization for the Proposed Mixed Waste Disposal Facility, Los Alamos National Laboratory*, edited by S. L. Reneau and R. Raymond, Jr., Los Alamos National Laboratory Report, LA-13089-MS.

Vaniman, D. T., S. J. Chipera, D. L. Bish, M. C. Duff, and D. B. Hunter (2002), Crystal Chemistry of clay-Mn oxide associations in soils, fractures, and matrix of the Bandelier Tuff, Pajarito Mesa, New Mexico, *Geochim. Cosmochim. Acta, 66*(8), 1349-1374.

Verrecchia, E. P., and K. E. Verrecchia (1994), Needle-fiber calcite: a critical review and a proposed classification, *J. Sed. Res., A64*(3), 650-664.

Wan, J., and J. L. Wilson (1994), Colloid transport in unsaturated porous media, *Water Res. Res., 30*(4), 857-864.

Wilson, J. E., L. B. Goodwin, and C. J. Lewis (2003). Deformation bands in nonwelded ignimbrites: Petrophysical controls on fault-zone deformation and evidence of preferential fluid flow, *Geology, 31*(10), 837-840.

Winograd, I. J. (1971), Hydrogeology of Ash Flow Tuff: A Preliminary Statement, *Water Res. Res., 7*(4), 994-1006.

Wohletz, K., 1996, Fracture Characterization of the Bandelier Tuff in OU-1098 (TA-2 and TA-41), *Los Alamos National Laboratory Miscellaneous Report LA-13194-MS*.

Wolfsberg, A., K. Campbell, and Fabryka-Martin (2000), Use of chlorine-36 to evaluate fracture flow and transport models at Yucca Mountain, Nevada, in *Dynamics of Fluids in Fractured Rock, AGU Monograph* 122, edited by B. Faybishenko et al., pp. 346-362.

CHAPTER 5

SATURATED PERMEABILITY OF DEFORMATION-BAND FAULT ZONES IN NONWELDED IGNIMBRITES OF THE BANDELIER TUFF[1]

Abstract

Faults can impact recharge, groundwater flow, and solute transport by modifying fluid pathways in the subsurface. Both isolated, major fault zones and more numerous small-displacement faults may affect these hydrologic processes. However, most models of groundwater flow incorporate only large fault zones. Our study focuses on much more common, small-displacement faults across the Pajarito Plateau of northern New Mexico, in the ash-dominated nonwelded ignimbrites of the Bandelier Tuff. These faulted ignimbrites contain perched aquifers, one of the primary groundwater flow regimes beneath the Pajarito Plateau. In contrast to low porosity and crystalline rocks, which fail along shear fractures, nonwelded ignimbrites can deform by grain crushing and pore collapse within deformation bands. Unlike fractures, which increase saturated permeability through welded ignimbrites by at least two orders of magnitude, we show that deformation bands reduce nonwelded ignimbrite saturated permeability by at least an order of magnitude.

Because deformation bands are very narrow, the volume interrogated by our air-minipermeameter includes protolith. In addition, measurements made with an air-

[1]To be submitted to Water Resources Research.

minipermeameter cannot take into account the impact of swelling clays like smectite, which is common in these faults, on permeability. Thus, our permeability values represent maximum estimates, and the permeability reduction associated with faults is likely to be greater than we report. If these differences exceed the range in permeability exhibited by unfaulted ignimbrite, deformation bands may affect saturated flow by introducing effective permeability heterogeneity and/or anisotropy into permeable nonwelded units. These permeability variations, even if relatively small, may be important at production time scales, possibly impacting recovery rates from perched aquifers in stratigraphically lower units of the Bandelier Tuff.

Introduction

Saturated flow is affected by the hydrologic properties of subsurface geologic features. Where subsurface lithologic units are faulted, fluid flow pathways can be modified by either juxtaposition of units with different hydrologic properties and/or processes that change the permeability of the fault zone itself, such as deformation, alteration, and cementation [e.g., Knipe, 1993; Caine et al., 1996; Rawling et al., 2001]. For faults in which displacement is less than bed thickness, the only significant impact on flow will be produced by structural and diagenetic modification of the fault zone. Such faults are the focus of this study of ash-dominated ignimbrite deposits.

Ignimbrites are spatially heterogeneous pyroclastic flow deposits consisting of poorly sorted assemblages of phenocrysts, pumice, and lithic fragments in a matrix of glass shards and ash. Individual cooling units within these deposits show a range in degree of welding (compaction and fusion of matrix glass and pumice) and postdepositional crystallization, including devitrification of volcanic glass to cristobalite

and feldspar, and/or vapor-phase crystallization of minerals such as tridymite and feldspar from vapors in pore spaces. This range reflects variations in eruption temperature, the mechanics of deposition, entrainment of volatiles, distance from caldera source, and composition [e.g., Smith and Bailey, 1966].

For hydrologic purposes, three categories of ignimbrite unit are considered, each of which has distinct ranges of porosity and permeability. Welded ignimbrites have low porosities (10-13%) [Wilson et al., 2003] and permeabilities (10^{-19} to 10^{-15} m^2) [Tidwell and Wilson, 1999; Wohletz, 1999]. Crystallized nonwelded ignimbrites have intermediate porosities relative to the other two categories (21-51%) [Wilson et al., 2003] and variable permeabilities (10^{-16} to 10^{-12} m^2) [Rogers and Gallaher, 1995; Springer and Schofield, 2002]. Glassy nonwelded ignimbrites have high porosities (32-56%) [Wilson et al., 2003] and variable permeabilities (10^{-16} to 10^{-12} m^2) [Winograd and Thordarson, 1975; Istok et al., 1994; Rogers and Gallaher, 1995; LeCain, 1997; Springer and Schofield, 2002]. Undeformed and uncompacted pumice and matrix glass shards are responsible for the high porosities observed in nonwelded ignimbrite units. The heterogeneity of clast contacts and the resulting variability of pore throat geometries is the likely cause of the highly variable saturated permeabilities documented in nonwelded units.

Hydrologic properties can be linked to controls on deformation in these different ignimbrite units. Wilson et al. [2003] have shown that for ash-dominated ignimbrites of Los Alamos, New Mexico, and Busted Butte, Nevada, welded units deform by fracture, glassy nonwelded units deform by cataclasis within deformation bands (Fig. 5.1), and crystallized nonwelded units deform by either of these mechanisms, depending on the

degree and nature of postdepositional crystallization. High porosity and permeability are generally correlated to low grain-contact area and strength, which facilitate fault-zone failure by cataclasis within deformation bands. These narrow zones in which grain crushing, grain-boundary sliding, and pore collapse accommodate mm-cm displacement are only found in nonwelded units. Low porosity and permeability typically reflect high

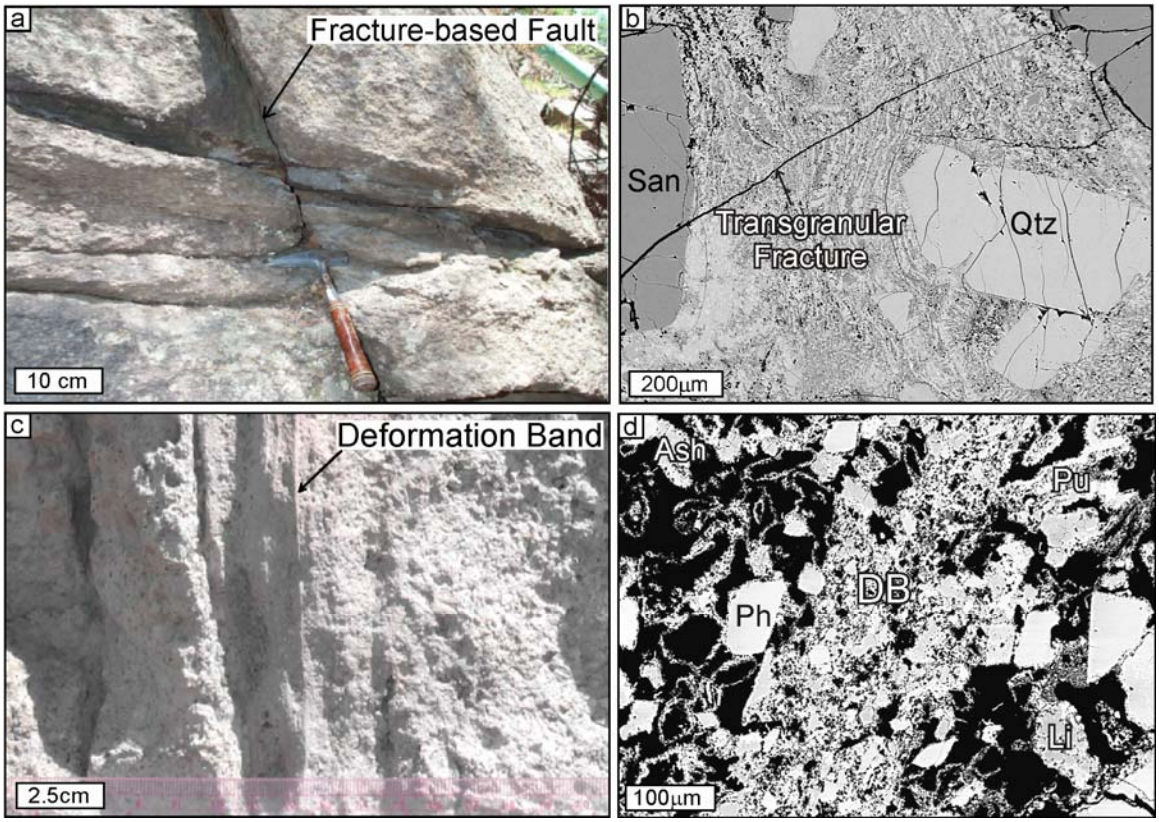

Figure 5.1. (a) Photo of a fracture-based fault in welded ignimbrite. (b) Back-scattered electron (BSE) image of a transgranular fracture in welded ignimbrite. Phenocrysts of sanidine (San) and quartz (Qtz) in a welded fabric of flattened pumice are crosscut by an open transgranular fracture. The fracture can be considered a plane of increased porosity (black) and pore connectivity. (c) Outcrop photo of 1 mm-wide deformation bands in nonwelded ignimbrite. (d) BSE image of a deformation band (DB), characterized by reduced pore- and grain-size relative to protolith. Ph = phenocryst, Pu = pumice, and Li = lithic clast.

grain-contact area and strength, which lead to fault-zone failure by fracture in welded and some crystallized nonwelded ignimbrites [Wilson et al., 2003].

Similar material controls on deformation are demonstrated by other field-based studies in different lithologies. Low porosity sedimentary and crystalline rocks deform by fracture [e.g., Chester and Logan, 1986; Reches and Locker, 1994]. In contrast, high porosity sandstone [Aydin and Johnson, 1978; Antonellini and Aydin, 1994] and poorly lithified sands [Mozley and Goodwin, 1995; Sigda et al., 1999; Cashman and Cashman, 2000] deform by cataclasis within deformation bands. Experimental studies have also demonstrated the dependence of mode of deformation on porosity [e.g., Dunn et al., 1973; Wong et al., 1997].

Fractures and deformation bands are hydrologically distinct. In contrast to fractures, deformation bands reduce porosity and saturated permeability with respect to protolith [Antonellini and Aydin, 1994; Sigda et al., 1999; Rawling et al., 2001] and are likely to increase fault unsaturated permeability in the vadose zone of arid desert environments [Sigda and Wilson, 2003].

Previous work in ignimbrite sequences shows that fractures can significantly increase the saturated permeabilities of welded units [Winograd, 1971; Wohletz, 1996; LeCain, 1997]. In this paper, we document a minimum reduction in saturated permeability of deformation bands relative to nonwelded protolith ignimbrite (Bandelier Tuff) using an air-minipermeameter. Backscattered-electron imaging shows that ignimbrite grains are crushed within deformation bands, reducing porosity, pore size, and saturated permeability both normal and parallel to the deformation band. Porosity is reduced by as much as 21% within an unaltered deformation band and up to 43% in

deformation bands containing smectite. Variable pore-size reduction leads to air permeability reduction in the range of one half to one order of magnitude. We note that our measurements likely overestimate fault-zone permeabilities. Hong [1999] demonstrated that water-saturated deformation-band faults in sand that contain smectite, a swelling clay, exhibit an order of magnitude lower permeability than that measured dry. The even smaller decreases in permeability exhibited by the other faults in our study are likely minima also, since most of the deformation-band faults studied were so thin that measurements were influenced by surrounding higher permeability protolith. Other geologic factors influencing the magnitude of permeability reduction in a given fault include local variations in protolith permeability and degree of cataclasis, diagenetic alteration and/or cementation. An unexpected increase in permeability from protolith to deformation band in some cases is attributed to the presence of desiccation cracks and post-cementation fractures in deformation bands containing smectite and calcite, respectively. This effect would not be evident with standard falling-head permeability measurements of smectite-rich faults, as hydration would cause desiccation cracks to close [e.g., Hong, 1999].

Within perched aquifers in the Bandelier Tuff, these lower permeability structures introduce effective permeability heterogeneity and/or anisotropy into the flow field and may affect production of groundwater [e.g., Yobbi, 1997]. If further study shows that the permeability reduction is greater than we have estimated from air-minipermeameter analyses, their impact on saturated flow may be greater. Deformation-band faults may, however, exert the greatest impact on unsaturated flow. Preferential diagenetic

modification of deformation bands is evidence that they have served as preferential fluid flow pathways in the unsaturated vadose zone [Wilson et al., 2003].

Geologic Setting

Our study of pore structure, porosity, and saturated permeability modification within deformation bands was focused on Bandelier Tuff ignimbrite deposits, which are located on the flanks of the Jemez Mountains of northern New Mexico (Fig. 5.2a). The Bandelier Tuff is composed of the lower, 1.6 Ma Otowi Member and the upper, 1.2 Ma Tshirege Member, both of which were deposited from violent pyroclastic eruptions of the Valles/Toledo caldera complex [Smith and Bailey, 1966; Izett and Obradovich, 1994]. Both members are dominated by silicic ash with lesser amounts of pumice, lithic fragments, and phenocrysts of quartz, sanidine, and plagioclase feldspar [Broxton et al., 1995]. The Otowi Member (Qbo) is a single, nonwelded, glassy cooling unit (Fig. 5.2b). The Tshirege Member (Qbt) comprises a sequence of cooling units, which vary in degree of welding and postdepositional crystallization (Fig 5.2b).

These welding and crystallization characteristics are the main petrophysical controls on deformation in ignimbrites, and therefore influence the mode of deformation in each unit [Wilson et al., 2003]. The differentiation among units according to response to fault-zone deformation defines a mechanical stratigraphy for the Bandelier Tuff (Fig. 5.2b), in which the stratigraphic section is dominated by nonwelded ignimbrites that fail by the formation of deformation bands.

On the Pajarito Plateau, the Bandelier Tuff is cut by the Pajarito fault system, a 41-km-long, rift-related, normal fault system consisting of four large faults, each dipping

steeply west or east and striking approximately north (Fig. 5.2a). Displacement is characteristically dip-slip, up to 180 m on the Pajarito fault with local evidence of strike-slip movement [Carter and Gardner, 1995]. Conceptual models of groundwater flow focus on how topography and this large-displacement fault zone affect regional flow paths [e.g., Rogers et al., 1996]. However, many small-displacement faults (mm-m throw) are also present, and may number in the thousands over a km^2 area on the Pajarito Plateau [e.g., Carter and Winter, 1995]. Although rarely mapped because of their size, the spatial distribution and character of these faults are important to understanding both regional deformation and subsurface fluid flow [cf. Sigda et al., 1999].

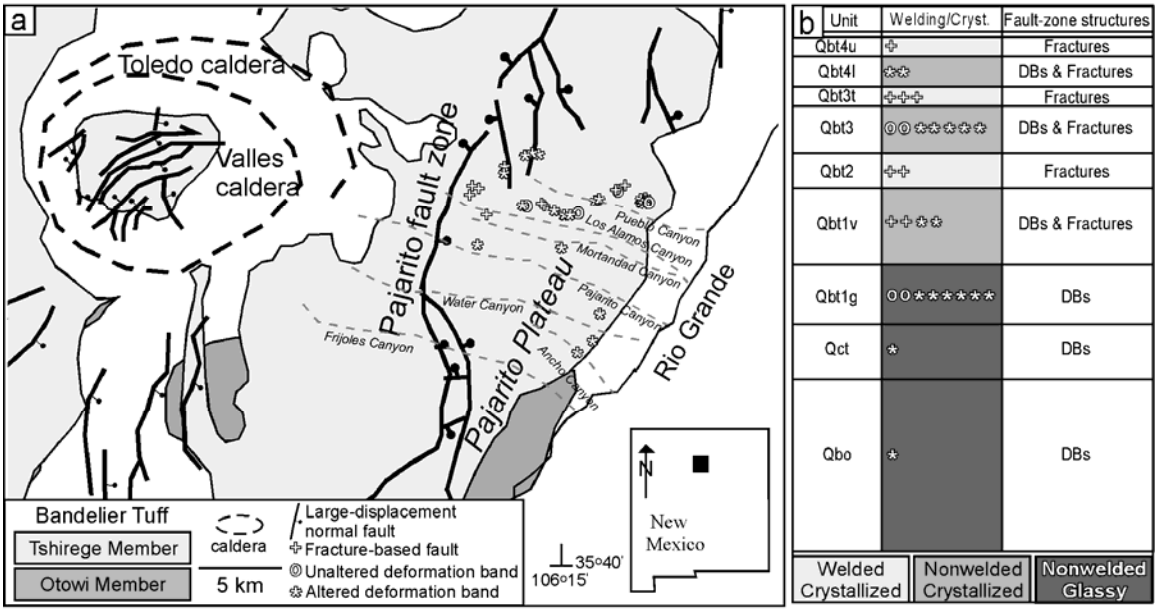

Figure 5.2. (a) Location map modified from Aldrich [1986], Heiken et al. [1990], Purtymun [1995], and Stimac [1996]. Shading shows extent of Bandelier Tuff. Dashed lines give approximate locations and trends of major canyons. (b) Bandelier Tuff stratigraphy of Lewis et al. [2002] modified to highlight mechanical behavior of stratigraphic units [cf. Wilson et al., 2003]. Thicknesses are schematic. Not all units are present in all locations. Symbols show the distribution of different fault types that were studied in detail in map view (a) and stratigraphic position (b). DB's = deformation bands, Qbo = Otowi Member, Bandelier Tuff, Qbt = Tshirege Member, Bandelier Tuff.

The Bandelier Tuff is largely above the water table, and, for the most part has been since deposition [Purtymun and Johansen, 1974]. In the semiarid climate of the Pajarito Plateau, deeply incised canyons trending roughly E-W from higher to lower elevations create two distinct hydrologic regimes: mesa tops and canyon bottoms (Fig. 5.2a) [Rogers et al., 1996]. Canyon bottoms are the dominant sources of recharge to the groundwater regimes beneath the Pajarito Plateau. These groundwater regimes include: (1) the main aquifer within the Puye Conglomerate and Santa Fe Group sediments , (2) shallow alluvium deposited in some large canyons near the Rio Grande River, and (3) discontinuous intermediate layers within the lower, nonwelded portions of the Bandelier Tuff and underlying basalts and sediments (Fig. 5.3) [McLin, 1996]. We focus on how deformation bands may affect saturated flow in the latter of these groundwater regimes.

Saturated flow in the perched aquifers is dominantly eastward toward the Rio Grande. However, small-displacement faults may alter flow paths by either inhibiting or enhancing fluid flow and transport. Fractures, widely recognized as conduits under saturated conditions, are prevalent in the welded units of the Bandelier Tuff and underlying basalts, and therefore fracture-based faults may enhance hydraulic connectivity in these perched aquifers [e.g., Wohletz, 1999]. On the other hand, small-displacement faults in nonwelded ignimbrites and poorly consolidated rift sediments are dominated by deformation bands [e.g., Sigda et al., 1999; Rawling et al., 2001; Wilson et al., 2003]. Studies of deformation bands in sands show that pore size, porosity, and saturated permeability can be drastically reduced relative to protolith, likely inhibiting saturated flow [Sigda et al., 1999]. In this paper, we document modifications in pore size, porosity, and saturated permeability within deformation bands in nonwelded

ignimbrites in order to determine whether these structures could also impact saturated flow and water recovery in the perched aquifers of the Bandelier Tuff [e.g., Rogers et al., 1996; Yobbi, 1997].

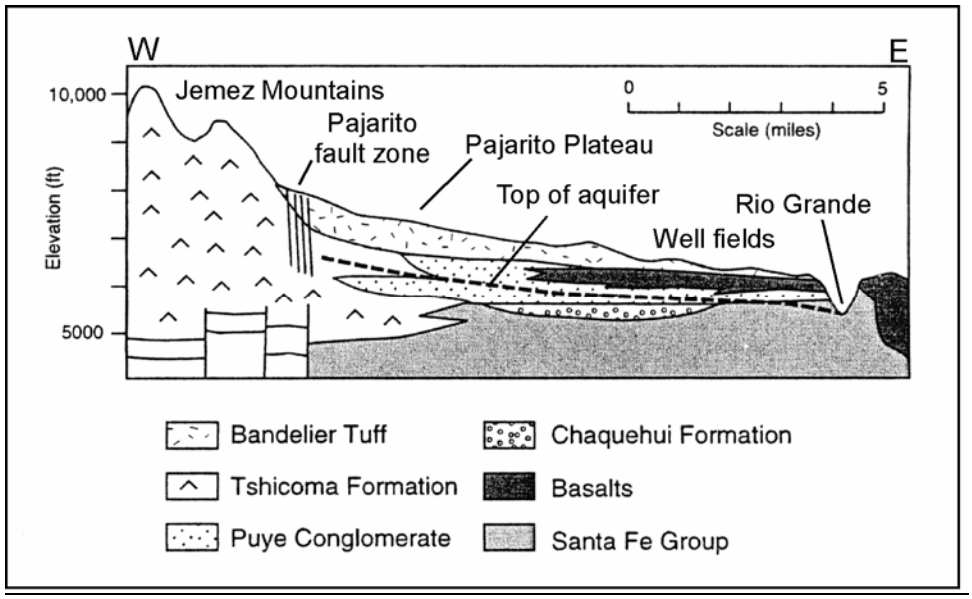

Figure 5.3. Geologic cross section through the Pajarito Plateau showing conceptual sketch of hydrogeologic units and aquifer levels. After Purtymun [1995] and Rogers et al. [1996].

Characteristics of Deformation-Band Faults on the Pajarito Plateau

High porosity and heterogeneous pore structure in poorly sorted, nonwelded ignimbrites are modified by pore collapse and grain-size reduction within deformation bands (Fig 5.1c, d; Fig. 5.4a, b) [Wilson et al., 2003]. Porosity is reduced, pore structure is variably homogenized, and pore connectivity is variably increased by destruction of glass walls that had previously isolated pore spaces (i.e., pumice vesicles).

In the nonwelded ignimbrites of the Bandelier Tuff, zones of deformation bands range in thickness from 1 mm to 15 cm, and contain variable amounts of diagenetic

smectite and calcite cement [Wilson et al., 2003]. These minerals are not abundant in surrounding protolith (Chapter 4) and result in significant porosity reduction (Fig. 5.4c,

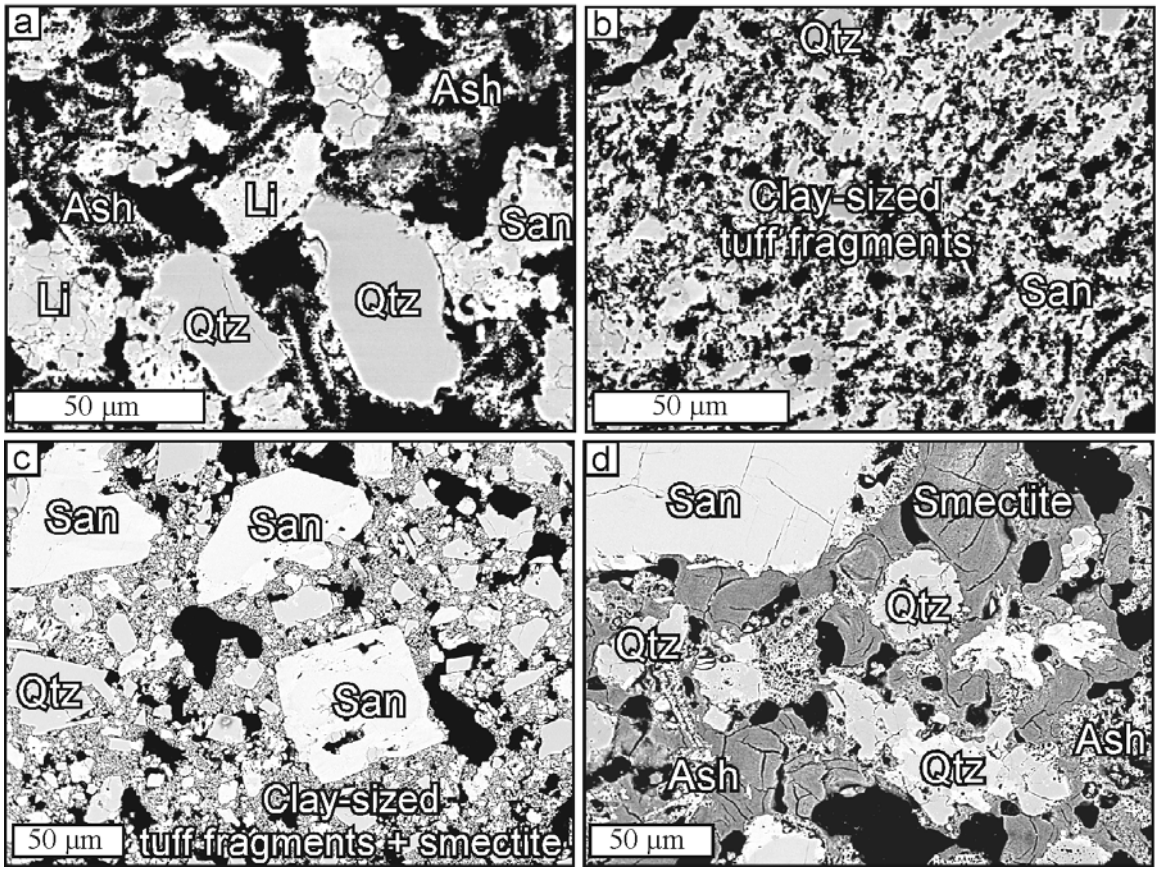

Figure 5.4. BSE images of (a) nonwelded crystallized ignimbrite, (b) unaltered deformation band in which grains are reduced to predominantly clay-sized fragments with highly irregular edges, (c) deformation band with 1.4 wt% smectite, and (d) deformation band with 94 wt% smectite. Qtz = quartz phenocryst, San = sanidine phenocryst. Note that both relative sizes and area of pore spaces (black) decrease from (a) to (c). Sizes of pore spaces appear similar in (c) and (d) due to desiccation cracking and plucking of pure smectite in more clay-rich deformation band (d).

d). Most deformation bands exhibit foliation defined by compositional layering or alignment of grains and/or diagenetic minerals parallel to fault boundaries.

The reduction in pore space and variable increase in pore connectivity within deformation bands in the vadose zone of arid environments results in preferential water

retention [Sigda and Wilson, 2003]. In the Bandelier Tuff, this leads to (1) preferential *in situ* alteration of ignimbrite matrix (volcanic glass, feldspar, and mafic lithic clasts) to smectite, (2) increased infiltration leading to both preferential colloidal transport of smectite (Fig. 5.4c, d) and fault-zone dissolution and/or precipitation, and (3) increased volume of plant roots, playing a key role in calcite cementation in these deformation bands (Chapter 4).

Methods

More than 100 faults in welded and nonwelded ignimbrite units of the Bandelier Tuff were characterized at the outcrop scale (Fig. 5.2; Appendix A). A representative subset of these faults and corresponding protolith was identified for additional detailed study (Table 4.2; Table A3, Appendix A). This subset of faults includes unaltered deformation bands, deformation bands with 1.4 to 93.5 wt% smectite, calcite-cemented deformation bands, and fractured ignimbrite. The relative amounts of pumice, matrix glass, phenocrysts, and lithic fragments were determined for each protolith-fault pair by point counting on a petrographic microscope (Table B1, Appendix B). Porosity was determined in two dimensions by pixel counts of black (porosity) versus gray (grain) within back-scattered electron microprobe images using Matlab (Appendix B). An alternate method of determining three-dimensional, effective porosity was also employed for a subset of protolith samples. The volume, dry mass, and water-saturated mass of ignimbrite protolith were measured, and effective porosity was calculated from these data.

Protolith, fault-parallel and fault-normal saturated permeabilities were measured for protolith-fault pairs in order to determine the hydrologic impact of deformation bands in ignimbrites in perched saturated zones. Sets of permeability data were collected and organized by date (Appendix C) in order to constrain such conditions as temperature, atmospheric pressure, etc., for a given set of measurements. These measurements were made on samples collected for lab analysis and at outcrop sites with a portable air-minipermeameter based on a design by J. Matt Davis at the University of New Hampshire. This design was chosen because it is ideal for obtaining rapid measurements in both a lab and field (outcrop) setting. In the air-minipermeameter design, air from a compressed air tank enters the air-minipermeameter at a constant pressure, travels through a mass flow meter (rotameter) and a pressure gauge, and then out of the air-minipermeameter through flexible tygon tubing to the tip seal (Fig. C1, Appendix C). Gas is directed into the rock via this tip seal, which consists of a rigid brass housing to which a molded silicone rubber ring is affixed. This soft, durable silicone rubber establishes the seal between the injection nozzle and the rock surface. The tip seal size used for all measurements has a 0.31 cm inner radius and a 0.62 cm outer radius. Similar to Davis et al. [1997], we use the approximation that the radius of influence for this 2:1 outer to inner tip seal radius ratio is 4 times the inner tip seal diameter (Fig. 5.5) [Goggin et al., 1988], and that the permeability measurements represent a hemispherical volume of interrogation with a radius of 2.48 cm. As opposed to a tip seal with a 4:1 ratio, the 2:1 tip seal ratio has a smaller sample volume and can be used to minimize effects of sample boundaries. Since most deformation bands are narrower (typically 1 mm) than the radius of influence (Fig. 5.5), the 2:1 tip seal was chosen to minimize the impact of

adjacent protolith on fault permeability measurements; however, we were not able to measure the permeability of deformation bands alone. All permeabilities were calculated from Darcy's law using the applied pressure, measured flow rate, and the geometry of the tip seal [e.g., Suboor and Heller, 1995].

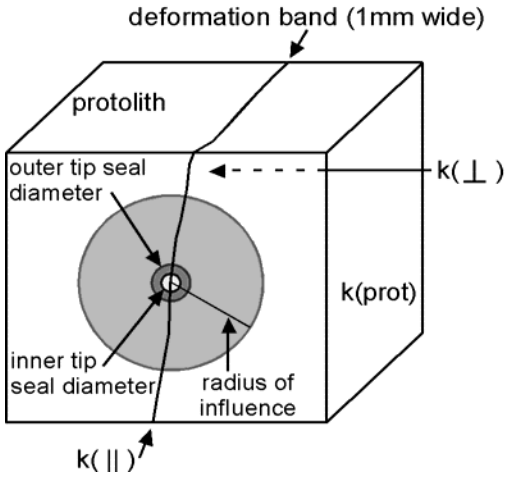

Figure 5.5. Schematic diagram showing measurement location and tip seal coverage for fault-parallel, k (||), permeability measurement. Inner tip seal diameter is 0.62 cm, outer tip seal diameter is 1.24 cm. Radius of influence is 4 times the diameter of inner tip seal (2.48 cm). Fault-normal, k (⊥), and protolith, k (prot), permeability measurement locations are also shown. Fault-normal measurements were taken by removing protolith material to reveal the deformation band.

Standardization

Instrument drift and measurement error were documented by comparing lab or outcrop permeability measurements of standards from one data-collection period to the next. Standards included a suite of ignimbrite and sandstone samples provided by Vince Tidwell at Sandia National Laboratory (SNL). Prior to use in this study, these samples were measured for air permeability with a multisupport permeameter (MSP) at SNL.

This MSP is equipped with a pneumatic piston to compress the tip seal to the prepared surface [Tidwell and Wilson, 1997; 1999]. Measurements of standards in this study were performed periodically before or after a set of protolith-fault measurements in order to document instrument drift and measurement error. Instrument drift refers to the steady increase or decrease in measurement values for a standard with continued minipermeameter use. Measurement error is the standard deviation from the mean of permeability measurements taken for a standard over several dates. These errors were minimized by (1) having a consistent operator for all experiments, (2) shielding the minipermeameter and gas source from extreme cold and heat, and (3) carefully choosing measurement locations on a sample or outcrop that do not lie on major visible heterogeneities.

Results

Evaluation of Approaches to Determining Porosity

Effective porosity determined from sample volume and dry versus saturated mass was found to be consistently higher, averaging approximately 9% greater, than the BSE-image derived, two-dimensional porosity values (Table 5.1). However, poorly lithified protolith and fault samples typically disaggregated upon saturation with water. We therefore rely on BSE image analysis to compare the porosities of faults with protolith. Thus, the porosity values given in this study (discussed in a later section) should be considered minimum values.

Standardization of Saturated Permeability Measurements

Samples of ignimbrite and sandstone were used as standards to check the accuracy of protolith-fault permeability values obtained from the air-minipermeameter. Permeabilities obtained with the MSP were compared to the minipermeameter measurements of each standard for a given set of protolith-fault data (Table 5.2).

Table 5.1. Comparison of effective porosity determinations for selected ignimbrite protoliths.

Sample[#]	Volume of dry sample* (cm^3)	Mass of dry sample (g)	Mass of wet sample (g)	Mass of water ^(g)	**Effective porosity˜ (%)**	**Porosity from BSE images (%)**	**Difference (%)**
bb3	12.66	30.90	41.27	10.37	47.0	41.0	6.0
bt37	16.10	40.91	56.13	15.22	50.6	46.9	3.7
bt73	14.25	37.66	50.36	12.70	49.1	40.6	8.5
bt109	8.49	22.46	24.97	2.51	24.3	13.1	11.2
bt120	6.02	15.95	23.98	8.03	59.1	42.4	16.7
						Mean difference:	9.2

[#]Sample numbers correspond to those in Tables 4.2, A1, A3, and A5)

*Volume of sample determined by pichnometer.

^Density of water: $9.23g/10cm^3 = 0.923\ g/cm^3$

˜Effective porosity = [(mass of wet sample - mass of dry sample) / density of water] / volume of dry sample

Table 5.2. Air-saturated permeabilities for standards--comparison of MSP versus air-minipermeameter values.

Sample	MSP measurement (m^2)	Minipermeameter measurement (m^2)	Date of minipermeameter measurement
Pink ignimbrite	**4.64E-15**	**6.12E-14**	Mean permeability for dates below
		1.40E-14	Standard Deviation
		5.49E-14	23-Jul-03
		5.39E-14	6-Aug-03
		5.73E-14	6-Aug-03
		5.21E-14	12-Aug-03
		5.98E-14	18-Sep-03
		8.92E-14	18-Sep-03
Orange ignimbrite	**1.90E-14**	**9.35E-14**	Mean permeability for dates below
		4.39E-14	Standard Deviation
		4.98E-14	23-Jul-03
		7.45E-14	6-Aug-03
		6.88E-14	6-Aug-03
		1.46E-13	12-Aug-03
		6.98E-14	18-Sep-03
		1.52E-13	18-Sep-03
Gray ignimbrite	**8.16E-14**	**8.85E-14**	Mean permeability for dates below
		1.44E-14	Standard Deviation
		7.17E-14	23-Jul-03
		1.11E-13	6-Aug-03
		8.14E-14	6-Aug-03
		8.55E-14	12-Aug-03
		8.12E-14	18-Sep-03
		1.00E-13	18-Sep-03
Brown sandstone	**1.04E-12**	**1.37E-13**	Mean permeability for dates below
		2.03E-14	Standard Deviation
		1.19E-13	23-Jul-03
		1.34E-13	6-Aug-03
		1.41E-13	6-Aug-03
		1.10E-13	12-Aug-03
		1.49E-13	18-Sep-03
		1.66E-13	18-Sep-03
Massillon sandstone	**8.45E-12**	**2.38E-12**	Mean permeability for dates below
		2.85E-13	Standard Deviation
		2.28E-12	23-Jul-03
		2.76E-12	6-Aug-03
		2.24E-12	6-Aug-03
		1.99E-12	12-Aug-03
		2.34E-12	18-Sep-03
		2.66E-12	18-Sep-03

Minipermeameter measurements for the ignimbrite standards varied by relatively large amounts, and were variably higher or lower than the MSP permeability values. In contrast, permeability measurements for the sandstone standards were relatively constant and were consistently lower than MSP permeability values. Based on these trends and visual inspection of the standards, the ignimbrite samples were considered too heterogeneous to serve as standards to document instrument drift or measurement error. The more homogeneous brown and Massillon sandstones were more suitable for these purposes. Due to the availability of published permeability data on Massillon sandstone

[Tidwell and Wilson, 2000; Lechler, 2002], it was chosen to document instrument drift and measurement error.

The Massillon sandstone dataset obtained with the minipermeameter does not show an overall increasing or decreasing trend (Table 5.2), suggesting that no instrument drift occurred with continued minipermeameter use. However, the average minipermeameter measurement for Massillon sandstone was low, 2.38×10^{-12} m^2 with a standard deviation (measurement error) of 2.84×10^{-13}, compared to the MSP measurement of 8.45×10^{-12} m^2. A correction for the low average permeability measurement for Massillon sandstone was not performed since the primary objective of this study is to document the permeability differences between fault and protolith samples. Thus, relative differences are more important than absolute values. As detailed below, our permeability measurements of Massillon sandstone standard are fairly consistent from one measurement date to the next. This documents the consistency of conditions by which fault and protolith permeability measurements were taken, thus ensuring that permeability differences between protolith and fault are recognized.

Porosity and Permeability Differences for Protolith-Fault Pairs

Porosity is increased by fractures (Fig. 5.1b). As a result, fractures are by far the greatest influence on saturated permeability in welded ignimbrites, increasing permeability by at least two orders of magnitude (Table 5.3; Fig. 5.6). In contrast, deformation bands in nonwelded ignimbrite units are variably diagenetically modified zones of grain crushing and pore collapse (Fig. 5.4). Not surprisingly, they result in porosity and permeability reduction (Table 5.3).

Table 5.3. Porosity & permeability differences between protolith-fault pairs.							
Protolith-fault pair	Fault thickness (mm)	Porosity (%)	Normalized* difference in porosity	Fault-parallel k_{sat} (m^2)	Normalized* difference in fault-parallel k_{sat}	Fault-normal ksat (m^2)	Normalized* difference in fault-normal k_{sat}
Crystallized welded ignimbrite (Qbt3t)		10		5.2E-14		5.2E-14	
Fracture	1	100^	10.00	5.4E-12	103.85	NA	NA
Glassy NW ignimbrite (Qbt1g)		56		1.1E-12		1.1E-12	
Unaltered deformation band	1	44	0.79	NA	NA	1.9E-13	0.17
Crystallized NW ignimbrite (Qbt3)		47		6.0E-13		6.0E-13	
Unaltered deformation band	80	26	0.55	1.1E-13	0.18	1.7E-13	0.28
Crystallized NW ignimbrite (Qbt3)		37		1.2E-12		1.2E-12	
Deformation band (1.4 wt% smectite)	10	0.2	0.01	1.6E-12	1.33	8.9E-13	0.74
Glassy NW ignimbrite (Qbt1g)		49		1.1E-12		1.1E-12	
Deformation band (7.8 wt% smectite)	30	19	0.39	NA	NA	3.0E-13	0.27
Glassy NW ignimbrite (Qbt1g)		49		1.1E-12		1.1E-12	
Deformation band (17.4 wt% smectite)	30	13	0.27	6.2E-13	0.56	4.0E-13	0.36
Crystallized NW ignimbrite (Qbt4)		42		4.0E-13		4.0E-13	
Deformation band (93.5 wt% smectite)	1	14	0.33	NA	NA	1.9E-13	0.48
Glassy NW ignimbrite (Qbt1g)		54		4.7E-13		4.7E-13	
Calcite-cemented deformation band	2	11	0.20	7.1E-13	1.51	8.3E-14	0.18
*Normalizations were calculated as average fault value / average protolith value (normalized protolith values = 1; decreases from protolith <1, increases from protolith							
^Porosity of fracture only considered, spatial density and aperture of fractures not considered.							
NA = not analyzed, NW = nonwelded.							

Unaltered deformation bands show moderate reductions in porosity and permeability (Figs. 5.1d and 5.4b; Table 5.3). These deformation bands also have variable thickness, ranging from 1 to 80 mm. Due to the volume of interrogation imposed by our tip seal, permeability measurements of deformation bands thinner than 49.6 mm are likely affected by surrounding, higher permeability protolith, and thus are overestimates of permeability.

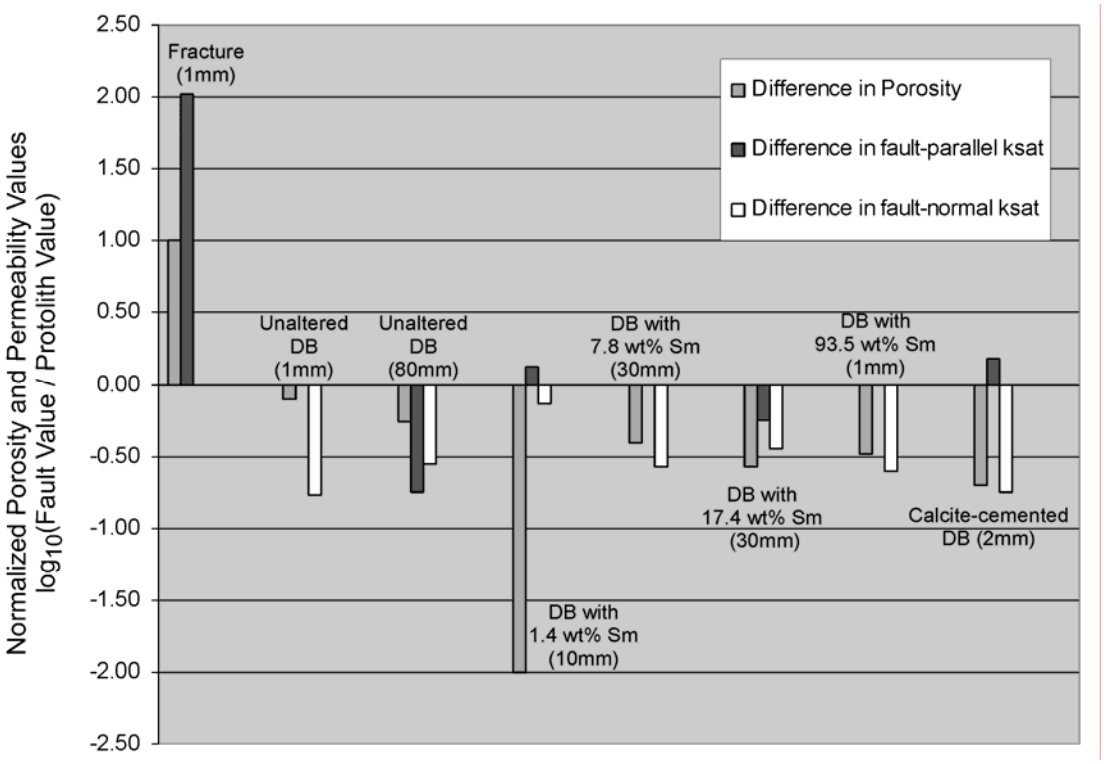

Figure 5.6. Normalized differences in porosity, fault-parallel saturated permeability, and fault-normal saturated permeability for fractures and variably altered deformation bands (DB). Sm = smectite. Thickness of fault is given below each fault description.

Deformation bands containing diagenetic minerals generally show larger reductions in porosity, but variable decreases in saturated permeability (Fig. 5.6). Among the protolith-fault pairs, the largest decreases in permeability are not associated with the highest porosity reductions (Table 5.3; Fig. 5.6). In fact, the largest porosity reductions result in surprisingly small reductions in fault-normal and fault-parallel saturated permeabilities of less than one order of magnitude (Table 5.3; Fig. 5.6). This smaller than expected reduction in permeability is in part due to the thickness of all deformation bands that contain smectite or calcite. All are narrower than 49.6 mm, which allows higher permeability protolith to be incorporated into the fault-permeability measurement.

Two exceptions to the reduction in saturated permeability from protolith to fault include fault-parallel permeability values of a calcite-cemented deformation band and a deformation band containing 1.4 wt% smectite. These two measurements are up to one half order of magnitude higher than protolith. These increases in air-saturated permeability are likely due to the presence of desiccation cracks and post-cementation fractures, respectively. These structures were not evident in outcrop, but were observed under the petrographic microscope and with BSE imaging.

Permeability Ranges for All Protoliths and Faults

Additional protolith and fault permeability measurements were made on samples that were not analyzed for porosity or diagenetic mineral content. These permeability data (Table C3, Appendix C) are combined with data from Table 5.3 to show the overall ranges in permeability for different types of protolith and fault (Fig. 5.7).

Measured permeabilities of glassy nonwelded protolith range from $10^{-12.4}$ to $10^{-11.9}$ m^2. Crystallized nonwelded protolith permeabilities have a wide range of $10^{-12.9}$ to $10^{-11.3}$ m^2. Permeabilities measured parallel to deformation bands are generally reduced compared to protolith but are typically higher than those measured normal to the deformation band. Fault-normal permeabilities for unaltered deformation bands range from $10^{-13.0}$ to $10^{-12.2}$ m^2 (Fig. 5.7). Fault-parallel permeabilities for unaltered deformation bands show more variability, from $10^{-13.2}$ to $10^{-11.3}$ m^2. Deformation bands containing smectite have permeability ranges similar to both protolith and unaltered deformation bands. Fault-normal permeabilities range from $10^{-12.9}$ to $10^{-11.9}$ m^2, and fault-parallel permeabilities range from $10^{-12.2}$ to $10^{-11.7}$ m^2. The calcite-cemented deformation band has

the lowest fault-normal permeability of $10^{-13.2}$ m^2, and a moderate fault-parallel permeability of $10^{-12.2}$ m^2. Welded ignimbrite is less permeable than nonwelded ignimbrite, ranging in permeability from $10^{-13.3}$ to $10^{-12.3}$ m^2, with fracture-parallel permeabilities ranging from $10^{-11.5}$ to $10^{-11.1}$ m^2.

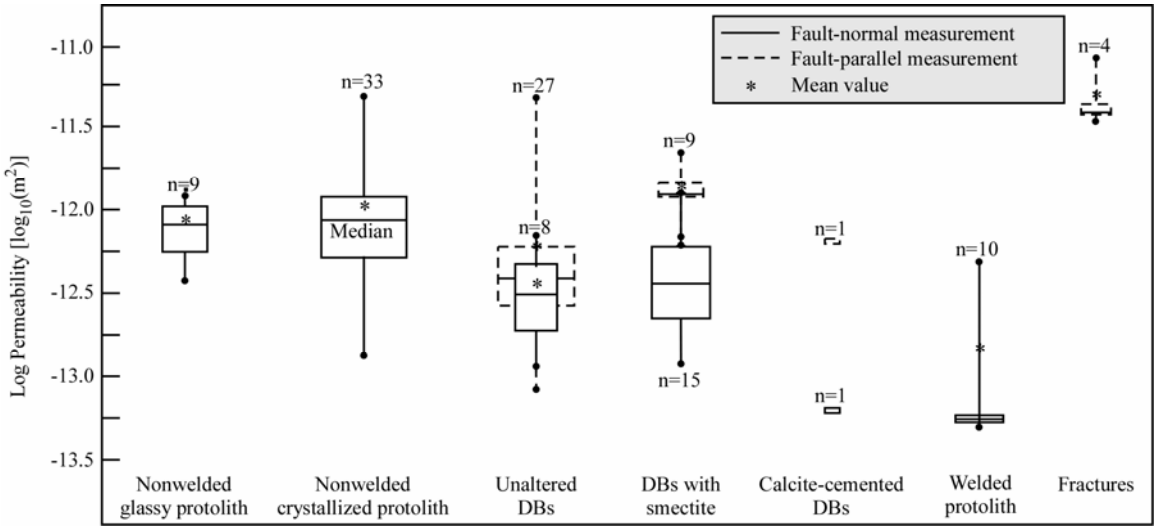

Figure 5.7. Box plots of log saturated permeabilities of protoliths with variable welding and crystallization characteristics, and different fault types (fractures, deformation bands (DBs), and altered and/or mineralized deformation-band fault zones). Data collected *in situ* and on hand samples using an air–minipermeameter. Boxes encompass 50% of data, vertical lines bounded by filled circles show full range of data, horizontal line within each box is the median permeability, asterisks indicate mean permeability, and box widths are proportional to the square root of n for each group.

Discussion

Measurement error

Permeability measurement of Massillon sandstone standard yields a mean permeability of 2.38 x 10^{-12} m^2 with a standard deviation, or measurement error, of 2.85 x 10^{-13}. This is a significant error, potentially caused by biases or small uncertainties in input parameters in permeability calculations, spatial variability of the standard, any

miniscule tilt on the tip seal that could alter the radius of influence (Fig. 5.5), and/or differences in mode of measurement (manual versus automated). However, this error is fairly consistent from one measurement date to the next (Table 5.2). This documents the consistency of conditions by which fault and protolith permeability measurements were taken, thus ensuring that permeability differences between protolith and fault are recognized. Therefore, measurement error does not affect our objective of identifying significant permeability modifications (i.e., contrasts of at least two orders of magnitude).

Non-Darcian Flow Effects

Our measurements of permeability for Massillon sandstone were consistently lower than, but within one order of magnitude of, the automated measurement provided by V. Tidwell. This difference in permeability values may be due to sample heterogeneity. Measurement of air permeability on the Massillon sandstone standard with the MSP may have been made in a different location on the sample than that consistently measured with the minipermeameter. Since Massillon sandstone is actually fairly heterogeneous (although less so than ignimbrite), different values in permeability from one location to another in the same sample may cause the small difference in permeability measurement from the MSP to our minipermeameter.

Alternatively, high velocity (inertial) non-Darcian flow effects, which result in pressure losses and an underestimate of permeability [Davis et al., 1994], may be causing the consistently lower permeability measurements. These effects may be accentuated by the 2:1 tip seal which forces air through a smaller sample volume than a 4:1 tip seal [Lechler, 2002]. Also, at higher gauge pressures, measured flow rates are less than

expected for Darcian behavior. A lower flow rate and non-linear deviation from Darcy's law is due to inertial effects resulting from the transition to turbulent gas flow. Deviation from Darcy's law occurs at a gauge pressure of 0.029 to 0.363 psi for Massillon sandstone [Lechler, 2002]. Measurements below these pressures reflect Darcian flow; measurements above these pressures reflect non-Darcian flow and are biased toward lower permeabilities. All measurements in this study were made at gauge pressures that ranged from 0.5 to 15 psi, within the range of non-Darcian flow. Gauge pressures for deformation-band permeability measurements range from 3.4 to 10.6 psi and for protolith from 1.0 to 6.6 psi. Given the similarities in the ranges of these gauge pressures, this effect may be fairly consistent for all measurements. Therefore, our objective of identifying the effect that deformation-band faulting has on permeability may not be significantly affected.

Effect of Deformation-Band Thickness on Fault-Normal Permeability Measurements

For permeability calculations, the material through which air flows is assumed to be relatively homogeneous. However, because fault zones are thin (Fig. 5.6), fault measurements typically encompass two materials with different hydrologic properties. Flow through a wide deformation band fault zone (greater than 4 times the inner tip seal diameter) may be considered homogeneous; flow through a narrow deformation band incorporates the hydrologic properties of surrounding protolith into the permeability calculation.

Deformation-band fault zones analyzed in this study range in width from 1 to 80 mm. The volume of interrogation for narrow deformation-band fault zones (those that are < 49.6 mm wide for a tip seal with an inner diameter of 0.62 cm) can be considered a

two-layer system consisting of the deformation-band fault zone and surrounding protolith. Corrections to remove the effect of the surrounding protolith can better isolate the hydrologic properties of the deformation-band fault zone. This involves calculation of a dual versus single layer geometric factor (G_d versus G_o) [Aronson, 1999]. We were not able to evaluate the magnitude of the effect that deformation-band fault zone thickness would have on fault-normal permeability since there were not enough permeability data for wide versus narrow deformation-band fault zones in this study. Additional data collection to document this relationship and constrain data corrections is anticipated.

Uncertainties in Saturated Permeabilities Associated with Smectite and Calcite in Deformation Bands

The small reduction and even local increase in fault permeability for diagenetically modified deformation bands relative to protolith reflects not only the influence of surrounding undeformed protolith, but also: (1) post-cementation fractures in calcite-cemented deformation bands, (2) open desiccation cracks in deformation bands containing smectite, and (3) the use of air instead of water for the saturating medium in an investigation of materials containing swelling clays (e.g., smectite) [Sigda et al., 1999; Hong, 1999]. These effects result in measured fault air-permeabilities that are considered maximum values. Hong [1999], for example, shows an order of magnitude smaller permeability of deformation-band faults in sand measured with a flexible-wall permeameter than with an air-minipermeameter. Since the faults he examined have far less smectite than some of the faults studied here [Sigda et al., 1999; Wilson et al., 2003], this effect may be more pronounced in this study. Although the magnitude of

permeability reduction is not well characterized in this study, we propose that deformation bands containing smectite or calcite are likely to have the largest impact on saturated permeability of the faults examined in this study.

Heterogeneity of Saturated Permeabilities of Protolith Versus Deformation Bands

Given the effects of deformation band thickness and the presence of diagenetic minerals, we use only data from the widest unaltered deformation-band fault zones to evaluate the effect that deformation bands may have on saturated permeability in nonwelded ignimbrites. One fault in this study meets these criteria, with a thickness of 80 mm and absence of smectite or calcite (Fig. 5.4b). This fault exhibits a one half to one order of magnitude decrease in fault-parallel and fault-normal permeability. However, comparison of this permeability modification to the wide range in values for unfaulted ignimbrite (just over two orders of magnitude; Fig. 5.7) reveals that the impact of unaltered deformation bands on saturated flow may be minimal.

Implications for Saturated Flow Through Nonwelded Ignimbrites

The reduction in saturated permeability of unaltered deformation bands relative to protolith is similar, at least in process, to the porosity and permeability reductions observed in high porosity sandstones and sands [Antonellini and Aydin, 1994; Sigda et al., 1999]. Porosity within sandstone may decrease from a value of 25% down to 1%, and permeability from more than 10^{-13} to less than 10^{-15} m^2 [Antonellini and Aydin, 1994]. Reductions of up to three orders of magnitude in air-saturated permeability for deformation bands containing relatively small amounts of clay (< 30 %) have also been documented in poorly lithified sands [Sigda et al., 1999]. Additional water-saturated

permeability measurements performed on these same faults demonstrated that faults containing swelling clay (smectite) exhibited permeabilities up to four orders of magnitude lower than adjacent sand [Hong, 1999]. In these faults, adding water caused the clays to swell, further blocking porosity and reducing permeability [Hong, 1999]. This suggests that deformation bands in sands and sandstones, in sufficient numbers, can inhibit cross-fault saturated flow, especially where the faults contain even small amounts of smectite.

In ignimbrites, deformation bands show similar reductions in porosity, but air-saturated permeability is reduced by only one order of magnitude at most. The reduction in saturated permeability for unaltered deformation bands relative to protolith is small, and may only have the effect of creating small permeability heterogeneities in the perched aquifers beneath the Pajarito Plateau. However, the number of unmapped, small-displacement faults can be very large in this tectonically active area of rift extension, on the order of 3000 within a roughly 400-km^2 area [Carter and Winter, 1995]. Although a systematic study of deformation-band fault spatial densities on the Pajarito Plateau has not yet been done, direct observations of deformation bands in nonwelded portions of the Bandelier Tuff suggest that deformation-band faults are likely to be distributed in these deposits at a regional scale. Of these deformation-band faults, the majority contain some amount of smectite, ranging from 1.4 to 93.5 wt%. Given the size of the volume of interrogation relative to the size of the deformation bands during permeability measurements, and the potential effect of smectite on air- versus water-saturated permeability measurements on dry fault material, smectite-rich deformation band permeabilities are likely to be two orders of magnitude or more lower than the protolith.

Therefore, they are likely to have the largest impact on saturated permeability of the faults examined.

The differences between the fault-normal and fault-parallel saturated permeabilities of deformation bands documented in this study suggest permeability anisotropy within the faults themselves (i.e., at the mm scale). At the scale of a perched aquifer (m to km scale), an accurate characterization of permeability anisotropy would have to take into account these direction-dependent permeability variations of deformation bands as well as their thicknesses, spatial density, distribution, and orientations [cf. Antonellini and Aydin, 1994; cf. Yobbi, 1997]. Although the petrophysical properties of deformation-band faults have been documented [Wilson et al., 2003], refinement of permeability values and a comprehensive geometric characterization of deformation-band faults across the Pajarito Plateau must be performed in order to evaluate the effect that these faults may have on saturated flow and water production at the aquifer scale.

Ultimately, deformation-band faults in the Bandelier Tuff may have the most effect on unsaturated, vadose-zone flow since these deposits lie mostly above the regional groundwater table and are saturated only within discontinuous perched aquifers [cf. Purtymun and Johansen, 1974; cf. McLin, 1996]. Current models of vadose-zone fluid flow through ignimbrites only consider fractures in welded units as significant flow pathways [e.g., Turin and Rosenberg, 1996; Wolfsberg et al., 2000] (cf. Fig. 4.19, Chapter 4). However, the diagenetic record of preferential fault-zone alteration and cementation suggests that deformation bands in nonwelded units may also be fluid flow conduits above the water table [Wilson et al., 2003]. The indirect result on saturated flow

is that the preferential vadose-zone fluid flow through these deformation bands and the potential for enhanced transport may affect the amount and chemistry of fluids that end up in both the regional and perched aquifers that underlie the Pajarito Plateau.

Conclusions

In the ash-dominated ignimbrites of the Bandelier Tuff, New Mexico, welded units deform by fracture, and nonwelded glassy units deform by cataclasis within deformation bands [Wilson et al., 2003]. Analysis of BSE images from protolith and deformation-band fault material shows that cataclasis within deformation bands reduces porosity via grain- and pore-size reduction by up to 21%. In the vadose zone of dry environments, this porosity reduction leads to preferential fluid flow and diagenesis [Wilson et al., 2003; Chapter 4), further reducing porosity and pore sizes. Therefore, deformation bands have very different hydrologic properties than fractures. Fracturing within welded units significantly increases porosity and pore connectivity, resulting in an increase in saturated permeability of at least two orders of magnitude. In contrast, we show that deformation bands are zones of reduced saturated permeability. The reduction in saturated permeability compared to protolith, in some cases up to one order of magnitude, could result in permeability heterogeneity and/or anisotropy in nonwelded ignimbrites. Consideration of the limitations in measuring air-saturated permeabilities of dry, thin deformation bands containing variable amounts of desiccated smectite and fractured calcite cement leads us to propose that the permeability reduction for these faults is likely to be greater by at least an order of magnitude than measured in this study. Therefore, deformation bands, if sufficiently numerous and continuous, may impact fluid

flow associated with water recovery [cf. Yobbi, 1997] in perched aquifers across the Pajarito Plateau.

Acknowledgments

This research has been funded by a grant through the Institute of Geophysics and Planetary Physics (IGPP) at Los Alamos National Laboratory. Additional funding was provided by the New Mexico Geological Society. Special thanks to J. Matt Davis for allowing us to replicate his air-minipermeameter and to Floyd Hewitt for construction of the minipermeameter. Thanks to Mark Cal and Justin Prien for assistance in calibrating flow meters, Bob Svec for assistance in calibrating pressure gauges, Vince Tidwell for the use of tuff and sandstone standards, and the New Mexico Firefighter Training Academy for use of compressed air tanks. Also, thanks to Nelia Dunbar and Lynn Heizler for assistance on the electron microprobe, Emily Schultz and Teryn Ebert for assistance in the field, and members of the Faults and Fluids group at New Mexico Tech for many useful discussions.

References

Aldrich, M. (1986), Tectonics of the Jemez Lineament in the Jemez Mountains and Rio Grande rift, *J. Geophys. Res.*, *91*(B2), 1753-1762.

Antonellini, M., and A. Aydin (1994), Effect of faulting on fluid flow in porous sandstones: petrophysical properties, *AAPG Bull.*, *78*, 355-377.

Aronson, E. C., (1999), Modeling investigations on gas permeameters: spatial weighting functions and layered systems, M.S. Thesis, 91 pp., New Mexico Tech, Socorro.

Aydin, A., and A. Johnson (1978), Development of faults as zones of deformation bands and as slip surfaces in sandstones, *PAGEOPH, 116,* 931-942.

Broxton, D., G. Heiken, S. J. Chipera, and F. M. Byers (1995), Stratigraphy, petrography, and mineralogy of Bandelier Tuff and Cerro Toledo deposits, in *Earth Science Investigations for Environmental Restoration—Los Alamos National Laboratory Technical Area 21*, edited by D.E. Broxton and P.G. Eller, Los Alamos National Laboratory Report LA-12934-MS, p. 33-64.

Caine, J. S., J. P. Evans, and C. B. Forster (1996), Fault zone architecture and permeability structure, *Geology, 24*(11), 1025-1028.

Carter, K. E., and J. N. Gardner (1995), Quaternary Fault Kinematics in the Northwestern Espanola Basin, Rio Grande Rift, New Mexico, *NMGS Guidebook, 46th Field Conference, Geology of the Santa Fe Region*, p. 97-102.

Carter, K. E., and C. L. Winter (1995), Fractal nature and scaling of normal faults in the Espanola Basin, Rio Grande rift, New Mexico: implications for fault growth and brittle strain, *J. of Struct, Geol., 17*(6), 863-873.

Cashman, S., and K. Cashman (2000), Cataclasis and deformation-band formation in unconsolidated marine terrace sand, Humboldt County, California, *Geology, 28(*2), 111-114.

Chester, F. and J. Logan (1986), Implications for mechanical properties of brittle faults from observations of the Punchbowl fault zone, California, *PAGEOPH, 124*, 79–106.

Davis, J. M., J. L. Wilson, and F. M. Phillips (1994), A portable air-minipermeameter for rapid i*n situ* field measurements, *Ground Water, 32*(2), 258-266.

Davis, J. M., J. L. Wilson, F. M. Phillips, and M. B. Gotkowitz (1997), Relationship between fluvial bounding surfaces and the permeability correlation structure, *Water Res. Res., 33*(8), 1843-1854.

Dunn, D. E., L. J. LaFountain, and R .E. Jackson (1973), Porosity dependence and mechanism of brittle fracture in sandstones, *J.Geophys. Res., 78*(14), 2403-2417.

Goggin, D. J., R. L. Thrasher, and L. W. Lake (1988), A theoretical and experimental analysis of minipermeameter response including gas slippage and high velocity flow effects, *In Situ, 12*, 79-116.

Heiken, G., F. Goff, J. Gardner, W. Baldridge, J. Hulen, D. Nielson, and D. Vaniman (1990), The Valles/Toledo Caldera Complex, Jemez Volcanic Field, New Mexico, *Ann. Rev. Earth Plan. Sci., 18*, 27-53.

Hong, S. -H. (1999) Anisotropic hydraulic conductivity of faulted poorly consolidated eolian sands: Bosque, New Mexico, M.S. Thesis, 70 pp. New Mexico Tech, Socorro, New Mexico.

Istok, J. D., C. A. Rautman, L. E. Flint, and A. L. Flint (1994), Spatial variability in hydrologic properties of a volcanic tuff, *Ground Water, 32*(5), 751-760.

Izett, G. A., and J. D. Obradovich (1994), $^{40}Ar/^{39}Ar$ age constraints on the Jaramillo Normal Subchron and the Matuyama-Bruhnes geomagnetic boundary, *J. Geophys. Res., 99*(B2), 2925-2934.

Knipe, R. J. (1993), The influence of fault zone processes and diagenesis on fluid flow, in *Diagenesis and Basin Development, AAPG, Studies in Geology #36*, edited by A. D. Horbury and A. G. Robinson, eds., pp. 135-148.

LeCain, G. D. (1997), Air-injection testing in vertical boreholes in welded and nonwelded tuff, Yucca Mountain, Nevada, *U.S.G.S. Wat. Res. Inv. Rep. 96-4262*, 33 pp.

Lechler, B.J., 2002, Gas Permeameters: Operation, Modification, and Design, M.S. Thesis, 119 pp., New Mexico Tech, Socorro, New Mexico.

Lewis, C. J., A. Lavine, S. L. Reneau, J. N. Gardner, R. Channell, and C. W. Criswell (2002), Geology of the Western Part of Los Alamos National Laboratory (TA-3 to TA-16), Rio Grande Rift, New Mexico, *Los Alamos National Laboratory Report LA-13960-MS*, 97 pp.

McLin, S. G. (1996), Analysis of water level fluctuation in Pajarito Plateau wells, in, *The Jemez Mountains Region: New Mexico Geological Society 47th Annual Field Conference Guidebook*, edited by F. Goff et al., pp. 421-426.

Mozley, P. S., and L. B. Goodwin (1995), Patterns of cementation along a Cenozoic normal fault: A record of paleoflow orientations, *Geology*, *23*, 539-542.

Neeper, D.A., Gilkeson, R.H., 1996, The influence of topography, stratigraphy, and barometric venting on the hydrology of unsaturated Bandelier Tuff, in *The Jemez Mountains Region, New Mexico Geological Society 47th Annual Field Conference Guidebook*, edited by F. Goff et al., pp. 427-432.

Purtymun, W. D. (1995), Geologic and hydrologic records of observation wells, test holes, test wells, supply wells, springs, and surface water stations in the Los Alamos area, *Los Alamos National Laboratory Report LA-12883-MS*, 339 pp.

Purtymun, W. D., and S. Johansen (1974), General geohydrology of the Pajarito Plateau, in *New Mexico Geological Society guidebook, 25th Field Conference, Ghost Ranch*, pp. 347-349.

Rawling, G. C., L. B. Goodwin, and J. L. Wilson (2001), Internal architecture, permeability structure, and hydrologic significance of contrasting fault-zone

types, *Geology*, *29*(1), 43-46.

Reches, Z., and D. A. Lockner (1994). Nucleation and growth of faults in brittle rock. *J. Geophys. Res. 99*, 18159-18173.

Rogers, D., and B. M. Gallaher (1995), The unsaturated hydraulic characteristics of the Bandelier Tuff, *Los Alamos National Laboratory Report LA-12968-MS*, 76 pp.

Rogers, D. B., A. K. Stoker, S. G. McLin, and B. M. Gallaher (1996), Recharge to the Pajarito Plateau regional aquifer system, in *The Jemez Mountains Region: New Mexico Geological Society 47th Annual Field Conference Guidebook*, edited by F. Goff et al., pp. 407-412.

Sigda, J. M., L. B. Goodwin, P. S. Mozley, and J. L. Wilson (1999), Permeability alteration in small-displacement faults in poorly consolidated sediments: Rio Grande Rift, central New Mexico, in *Faults and Subsurface Fluid Flow in the Shallow Crust, AGU Monograph 113*, edited by W.C. Haneberg et al., pp. 51-68.

Sigda, J. M., and J. L. Wilson (2003), Are faults preferential flow paths through semi-arid and arid vadose zones?, *Water Res. Res., 39*, doi:10.1029/2002WR001406.

Smith, R. L., and R. A. Bailey (1966), The Bandelier Tuff-A study of ash-flow eruption cycles from zoned magma chambers, *Bull.Volc., 29*, 83-104.

Springer, E. P., and T. G. Schofield (2002), Unsaturated zone hydrologic properties for TA-49, *Los Alamos National Laboratory Report LA-UR-02-6321*, 42 pp.

Stimac, J. A. (1996), Hornbelnde-dacite pumice in the Tshirege Member of the Bandelier Tuff: implications for magma chamber and eruptive processes, in *The Jemez Mountains Region: New Mexico Geological Society 47th Annual Field Conference Guidebook*, edited by F. Goff et al., pp. 269-274.

Suboor, M. A., and J. P. Heller (1995), Minipermeameter characteristics critical to its use, *In Situ*, *19*(3), 225-248.

Tidwell, V. C., and J. L. Wilson (2000), Heterogeneity, permeability patterns, and permeability upscaling: physical characterization of a block of Massillon sandstone exhibiting nested scales of heterogeneity, *SPE Res. Eval. Eng., 3*(4), 283-291.

Tidwell, V. C., and J. L. Wilson (1999), Upscaling experiments conducted on a block of volcanic tuff: Results for a bimodal permeability distribution, *Water Res. Res., 35*(11), 3375-3387.

Tidwell, V. C., and J. L. Wilson (1997), Laboratory method for investigation permeability upscaling, *Water Res. Res., 33*(7), 1607-1616.

Turin, H. J., and N. D. Rosenberg (1996), A conceptual model for flow in the vadose zone beneath the finger mesas of the Pajarito Plateau, in *The Jemez Mountains Region: New Mexico Geological Society 47th Annual Field Conference*, edited by F. Goff et al., pp. 74-76.

Wilson, J. E., L. B. Goodwin, and C. J. Lewis (2003). Deformation bands in nonwelded ignimbrites: Petrophysical controls on fault-zone deformation and evidence of preferential fluid flow, *Geology*, *31*(10), 837-840.

Winograd, I. J. (1971), Hydrogeology of Ash Flow Tuff: A Preliminary Statement, *Water Res. Res.*, *7*(4), 994-1006.

Winograd, I. J., and W. Thordarson (1975), Hydrogeologic and hydrochemical framework, south-central Great Basin, Nevada-California, with special reference to the Nevada Test Site, *USGS Prof. Pap. 712-C*, 126 pp.

Wohletz, K., 1996, Fracture Characterization of the Bandelier Tuff in OU-1098 (TA-2 and TA-41), *Los Alamos National Laboratory Report LA-13194-MS*.

Wohletz, K. (1999), Fractures in welded tuff, *Los Alamos National Laboratory Report, LA-UR-99-6556*, 27 pp.

Wolfsberg, A., K. Campbell, and J. Fabryka-Martin (2000), Use of chlorine-36 to evaluate fracture flow and transport models at Yucca Mountain, Nevada, in *Dynamics of Fluids in Fractured Rock*, AGU Monograph 122, edited by B. Faybishenko et al., pp. 346-362.

Wong, T.-F., C. David, and W. Zhu (1997), The transition from brittle faulting to cataclastic flow in porous sandstones: Mechanical deformation, *J. Geophys. Res., 102*, 3009–3025.

Yobbi, D. K. (1997), Simulation of Subsurface Storage and Recovery of Effluent Using Multiple Wells, St. Petersburg, Florida, *USGS Water Res. Inv. Rep. 97-4024*, 30 pp.

CHAPTER 6

CONCLUSION

Shallow crustal faults are of interest for a variety of reasons, including their potential impact on vadose-zone and groundwater flow. In this study, I have identified two classes of small-displacement faults in the near-surface Bandelier Tuff deposits of the Pajarito Plateau: fractures and deformation bands. Not only do these two fault types occur in stratigraphically distinct zones within the ignimbrite sequence, they also have very different effects on fluid flow above and below the water table.

Degree of welding and postdepositional crystallization determine whether a given ash-dominated ignimbrite unit deforms by formation of fractures or deformation bands. These characteristics are qualitatively inversely proportional to porosity and directly related to grain-contact area and strength. Welded units deform by fracture, and glassy nonwelded units deform by cataclasis within deformation bands. Nonwelded units that have undergone postdepositional crystallization deform by development of either fractures or deformation bands, depending on the nature and extent of crystallization (e.g., glass and cristobalite contents, degree of grain connectivity, etc.). These relationships between fault-zone structure and protolith petrophysical properties provide a basis for predicting fault-zone character from rock type, which is useful for fluid flow and transport models.

Deformation bands in both glassy and crystallized nonwelded units of the

Bandelier Tuff are zones of preferential fault-zone diagenesis. Diagenetic modification includes smectite enrichment and calcite cementation. The presence of these minerals, which occur in only trace amounts in the protolith, records preferential vadose-zone fluid transport. Smectite enrichment is associated with a combination of increased *in situ* alteration of ignimbrite matrix (unstable volcanic glass, feldspar, and mafic components) and enhanced infiltration of soil smectite from the surface via colloidal transport. *In situ* alteration and infiltration require a combination of enhanced fluid retention and fluid flow through deformation bands relative to adjacent smectite-poor protolith. Calcite cement in deformation bands consists of rod-shaped microcrystallites that form as a result of repeated desiccation events and microbially mediated precipitation. Preferential root growth through faults and calcite micromorphology consistent with biologic activity collectively suggest that water is preferentially retained in these structures. An increase in CaO relative to protolith also requires enhanced infiltration via fluid-flow-assisted dissolution/precipitation of Ca-rich eolian dust from the surface.

Detailed geochemical analyses indicate that these mineralogic changes in deformation bands are consistent with major oxide and trace element concentrations. Higher amounts of Fe_2O_3, MgO, CaO, TiO_2, V, Cu, and Cr are consistent with increased smectite and calcite in deformation bands. Lower amounts of Na_2O and K_2O indicate removal of these constituents from the deformation band. Addition and removal of any constituents is evidence of higher fluid flux in deformation bands relative to protolith. This increased fluid flux ultimately results in smectite enrichment by translocation of soil-derived smectite from the surface as well as localized *in situ* alteration of ignimbrite matrix and mafic minerals. Given that these deformation bands in the Bandelier Tuff

record enhanced fluid-fault interaction, in sufficient numbers they may play an important role in vadose-zone fluid flow and transport through these and other ash-dominated ignimbrite deposits.

Fractures and deformation bands in variably welded and crystallized ignimbrite sequences have very different saturated hydrologic properties. Fracturing within welded units significantly increases porosity, pore connectivity, and saturated permeability by at least two orders of magnitude. In contrast, deformation bands are zones of reduced porosity, pore size, and saturated permeability. The reduction in saturated permeability compared to protolith, in some cases measuring up to an order of magnitude, can result in zones of lower permeability in a given ignimbrite unit. Deformation bands are typically subparallel in a given outcrop. The resulting permeability anisotropy may affect flow in perched saturated zones such that water recovery is affected. Given the limitations of current data, the reduction of saturated permeability in deformation bands relative to protolith can be considered a minimum. Thus, although our measurements suggest that regional flow patterns are probably not affected by deformation bands in nonwelded ignimbrites, additional data collection and corrections may reveal larger impacts of these subvertical zones of reduced permeability in these permeable units.

Suggestions for Future Work

Image Analysis

More sophisticated analysis of the size and arrangement of pore spaces and grain sizes with a program such as NIH will be performed on BSE images obtained in this study. This characterization will allow quantification of grain-size and pore-size

distributions within and outside deformation bands. Thus, a better characterization of the modification of pore-fluid pathways in deformation bands relative to ignimbrite protolith will be achieved.

Detailed Petrographic and Geochemical Characterization of Nonwelded Ignimbrite Units

The primary controls on fault-zone deformation in ignimbrites have been identified in this study as degree of welding and postdepositional crystallization. Among variably welded units, porosity is a proxy for degree of welding. Welded units, which have porosities less than 13%, deform by fracture. Nonwelded units that have porosities ranging from 21-56% deform by development either fractures or deformation bands, depending on the degree and nature of postdepositional crystallization. I have qualitatively identified lower glass and higher cristobalite contents as the control on this transitional behavior in nonwelded ignimbrites. Quantification of this mineralogical control on fault-zone deformation needs to be explored further.

Grain connectivity and grain-contact strength are also properties that have been identified qualitatively as a control on mode of failure in these deposits. A field-based investigation involving experimental deformation of cores with known distributions of postdepositional crystals (determined by SEM and/or TEM) may reveal the mineralogical and textural characteristics associated with these petrophysical controls on deformation.

Another property of ignimbrites that affects mode of failure is the relative content of phenocrysts, lithic clasts, and pumice. The effect that these properties have on the transition from deformation-band faulting to fracture-based faulting should be explored

with detailed field-based petrographic investigations of Bandlier Tuff and other near-surface ignimbrite deposits (e.g., Bishop Tuff in California, Calico Hills Tuff in Nevada).

3-D Imaging of Pore Space and Flow (Unsaturated and Saturated)

In addition to 2-D imaging of pore-size and pore-shape distribution through image analysis programs like NIH, 3-D imaging of these properties to evaluate pore connectivity will be performed. This work is part of a proposed second-year renewal of an IGPP-funded project involving laser scanning confocal microscopy (LSCM) at Sandia National Laboratory. This technique will initially be used to image the pore connectivity in dry samples of deformation bands. Subsequent imaging will focus on visualization and modeling of fluids moving through the previously imaged 3-D pore network under both saturated and unsaturated conditions. These experiments will provide hydrologic context for the inferred vadose-zone (Chapter 4) and saturated-zone (Chapter 5) properties of deformation bands in ignimbrites presented in this dissertation.

Additional Saturated Permeability Measurements of Fault-Protolith Pairs

Saturated permeability measurements presented in Chapter 5 require additional corrections in order to provide a quantitatively sound value of permeability for deformation bands and protolith. First, the calculation of a dual-layer geometric factor will be performed in order to remove the effect of surrounding protolith from fault-normal permeability measurements of thin deformation bands (e.g., Aronson, 1999). Second, additional permeability measurements of calcite-cemented deformation bands are necessary to statistically constrain the permeability of this type of deformation band.

Third, permeability measurements for smectite-rich faults should be performed with water- rather than air-saturation. As these faults are rich in swelling clay, this will remove the effects of desiccation cracks and will more accurately measure the permeability of these faults under water-saturated conditions.

Determine Spatial Distribution of Deformation Bands by Detailed Mapping of the Bandelier Tuff

Deformation bands have been identified in the nonwelded ignimbrites of the Bandelier Tuff at several locations across the Pajarito Plateau (Fig. A1, Table A1, Appendix A). However, systematic mapping of these deformation bands is necessary to determine the spatial density, lateral distribution, and connectivity of these faults. This information will be a key aspect in evaluating the impact of these small-displacement faults on regional deformation and vadose-zone flow on the Pajarito Plateau.

Similar Investigations in Other Ash-Dominated Ignimbrite Deposits

Several deformation-band faults were identified at Busted Butte, Nevada. This suggests that deformation bands may be found in many other ash-dominated nonwelded ignimbrite deposits around the world. Identification of deformation bands in these other deposits would further identify this study as non-site-specific, and may provide insight into the potential impact that these undiscovered faults may have on fluid flow in their respective regions.

Deformation Experiments and Subsequent Investigation of Fault-Zone Structures in Nonwelded Ignimbrites

Controlled deformation experiments on nonwelded ignimbrite samples with sufficient homogeneity could be used to constrain some of the non-petrophysical controls on ignimbrite deformation (i.e., confining pressure, fluid pressure, strain rate, etc.). These and other experiments that would simulate near-surface deformation (i.e., low confining pressure) could be taken a step further by observing the microstructural characteristics of fault-zone structures developed during these experiments.

APPENDIX A

OUTCROP CHARACTERIZATION OF SMALL-DISPLACEMENT FAULTS AND CORRESPONDING PROTOLITH IN THE BANDELIER TUFF (NM) AND CALICO HILLS TUFF (NV)

Location and Description of Small-Displacement Faults Investigated in the Bandelier Tuff, Pajarito Plateau, New Mexico

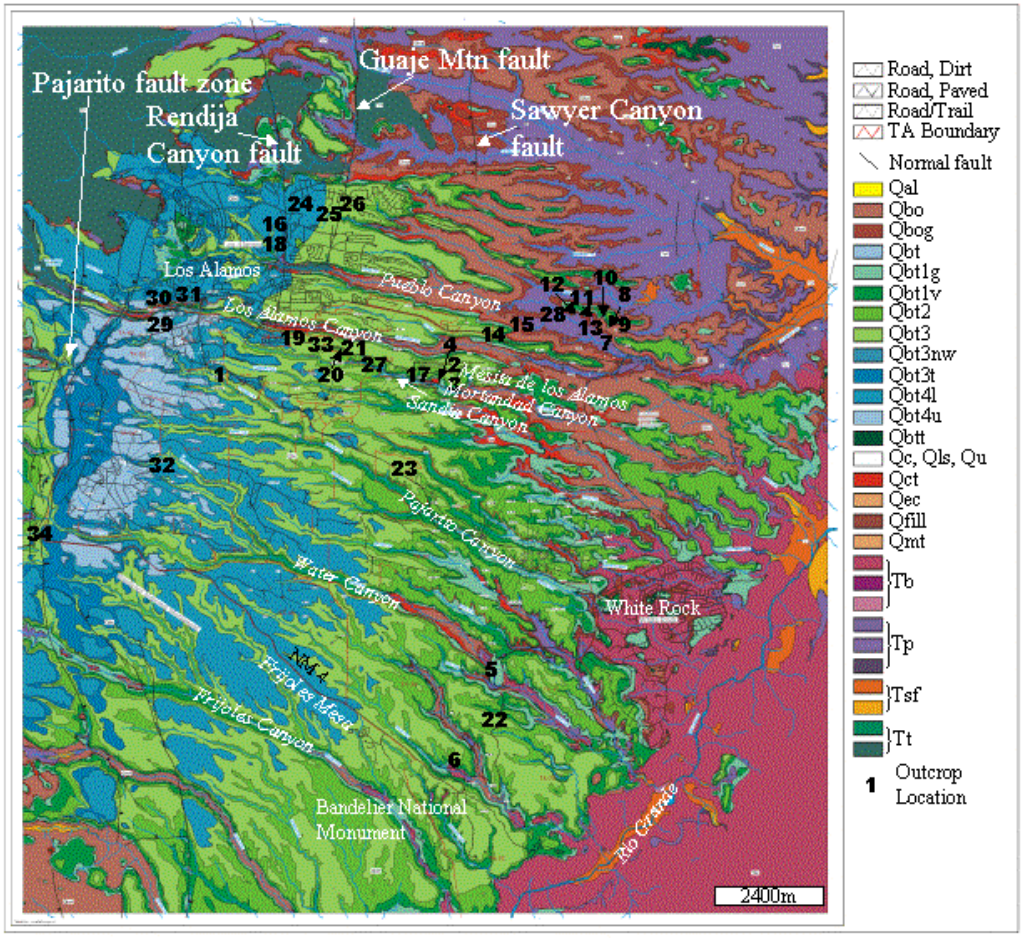

Figure A1. Geologic map of the Pajarito Plateau showing numbered outcrop locations at which small-displacement faults were identified and described in this study. Outcrop location numbers correspond to those in Table A1. Geologic map modified from Stone et al. (1999).

Table A1 (continued). Descriptions of small-displacement faults at each outcrop location on the Pajarito Plateau.

Location	GPS Reading	Elevation	Unit	Protolith[#]	Fault Orientation	Fault Type*	Fault Description	Fault Thickness	Samples Collected
					N30W 45SW	3	white cement, offset increases toward bottom of outcrop, 9cm to 17cm	1-3mm	
					N20W 75NE	3	white cement, 2cm normal offset	1-3mm	
					N80W 80NE	3	white cement, 13cm normal offset	2-10mm	
					N45E 50NW	2	no cement or clay, 9cm normal offset	1mm	
					N45E 50NW	2	no cement or clay, 4cm normal offset	1mm	
			Qbt1g	G, NW	N79E 82SE	3	cemented fault surface stands out in positive relief, no observable offset	1mm	
					N11E 85SE	3	cemented fault surface stands out in positive relief, no observable offset	1mm	
	N35°53.431' W106°18.138'	7112 +/- 25ft	Qbt1g	G, NW	N80W 85NE	4	compositional foliation (thinly anastomosing clay gouge and white cement), no observable offset	6mm	
19	N35°52.395' W106°17.585'	7309 +/- 30ft	Qbt3	C, NW	N17E 43NW	4	tan/brown zone, no fractures, no foliation or observable offset	10mm	bt61 (fault)
20	N35°52.285' W106°17.088'	7120 +/- 25ft	Qbt2	C, W	N47E 48NW	1 / 5	abundant fractures with isolated clay-rich faults (anastomosing white cement with dark brown and orange clay), no observable offset	25mm	
21	N35°52.194' W106°16.366'	7058 +/- 32ft	Qbt2	C, W	N18E 90	1 / 5	abundant fractures with isolated clay-rich faults (anastomosing white cement with dark brown and orange clay), no observable offset	70mm	
22	N35°47.818' W106°14.843'	6572 +/- 16ft	Qbt3	C, NW	N11E 90	5	compositional foliation (anastomosing orange clay gouge and white cement), no observable offset	6-10mm	bt74, bt111 (fault)
23	N35°50.406' W106°15.815'	6748 +/- 28ft	Qbt1v	C, NW	N56E 90	1/ 5	abundant fractures with isolated clay-rich faults (anastomosing orange and dark brown clay), no observable offset	3mm	
					N54W 90	5	abundant fractures with isolated clay-rich faults (anastomosing orange and dark brown clay), no observable offset	2mm	
					N53E 79SE	5	abundant fractures with isolated clay-rich faults (dark brown clay), no observable offset	3mm	
					N85E 90	5	abundant fractures with isolated clay-rich faults (anastomosing orange and dark brown clay), no observable offset	10mm	
					N30E 84NW	5	abundant fractures with isolated clay-rich faults (anastomosing orange and dark brown clay), no observable offset	5mm	
					N35W 90	5	abundant fractures with isolated clay-rich faults (anastomosing orange and dark brown clay), no observable offset	10mm	
24	Bayo Canyon	?	Qbt3	C, NW	N85E 86NW	5	orange and brown clay gouge with white cement patches, no observable offset	6mm	bt77, bt78 (fault surface)
25	Bayo Canyon	?	Qbt3	C, NW	N04E 86NW	3	white cement, no observable offset	3mm	
26	Bayo Canyon	?	Qbt3	C, NW	N49E 88SE	5	foliated orange clay with splays normal to main fault that decrease in width away from fault	30-100mm	
27	N35°52.134' W106°683'	6915 +/- 20ft	Qbt1v	C, NW	N49E 88SE	4	dark brown clay gouge with pervasize fine roots	2-10mm	bt80 (fault surface)
28	Pueblo Canyon	?	Qbt1v	C, NW	N38W 65SW	3	white cement, no observable offset	1mm	bt86, bt87 (fault surface)
					N47W 65 SW	3	white cement, no observable offset	1mm	bt89 (fault surface)
				C, W	N51E 90	1	fracture with no cement or clay, no observable offset	1-2mm	bt90
					N20W 90	1	fracture with no cement or clay, no observable offset	1-2mm	bt94, bt95 (fault surface)
					N59E 90	1	fracture with no cement or clay, no observable offset	1-2mm	
			Qbt2	C, W	N65E 86NW	1	fracture with no cement or clay, no observable offset	1-2mm	bt97, bt98 (fault surface)
29	N35°52.771' W106°19.669'	7376 +/- 16ft	Qbt4u	C, W	N15E 83NW	1	fracture filled partially with dirt (gray, incohesive), no observable offset	1mm	bt100, bt101 (fault surface)
					N68E 84SE	1	fracture with no cement or clay, no observable offset	1-2mm	bt100 (fault surface)
					N81W 90	1	fracture with no cement or clay, no observable offset	1-2mm	
					N81E 76NW	1	fracture with no cement or clay, no observable offset	1-2mm	
					N37E 85SE	1	fracture with no cement or clay, no observable offset	1-2mm	
	N35°52.780' W106°19.674'	7375 +/- 46ft	Qbt4u	C, W	N77W 84SW	1	fracture with no cement or clay, no observable offset	1-2mm	
	N35°52.783' W106°19.705'	7358 +/- 27ft	Qbt4u	C, W	N75E 83SE	1	fracture with no cement or clay, no observable offset	1-2mm	
					N77W 84SW	1	fracture with no cement or clay, no observable offset	1-2mm	
30	N35°52.855' W106°19.892'	7368 +/- 30ft	Qbt3t	C, W	N10E 86NW	1	fracture with no cement or clay, no observable offset	1-2mm	
	N35°52.827' W106°19.850	7376 +/- 30ft	Qbt3t	C, W	N15E 87NW	1	fracture with no cement or clay, no observable offset	1-2mm	
					N21W 74NE	1	fracture with no cement or clay, no observable offset	1-2mm	bt105 (fault surface)
31	N35°52.860' W106°19.795'	7269 +/- 31ft	Qbt3t	C, W	N50E 77SE	1	fracture with no cement or clay, no observable offset	1-2mm	bt107, bt108 (fault surface)
	N35°52.866' W106°19.800'	7266 +/- 40ft	Qbt3t	C, W	N56E 82NW	1	fracture with no cement or clay, no observable offset	1-2mm	
	N35°52.855' W106°19.767'	7262 +/- 28 ft	Qbt3t	C, W	N18E 53NW	1	fracture with no cement or clay, no observable offset	1-2mm	
	N35°52.845' W106°19.730'	7365 +/- 31ft	Qbt3t	C, W	N14W 61NE	1	fracture with no cement or clay, no observable offset	1-2mm	

Table A1 (continued). Descriptions of small-displacement faults at each outcrop location on the Pajarito Plateau.

Location	GPS Reading	Elevation	Unit	Protolith[#]	Fault Orientation	Fault Type*	Fault Description	Fault Thickness	Samples Collected
	N35°52.862' W106°19.732'	7229 +/- 36ft	Qbt3t	C, W	N15W 88NE	1	fracture with no cement or clay, no observable offset	1-2mm	
	N35°52.773' W106°18.680'	7109 +/- 26ft	Qbt3	C, W	N23W 82NE	1	fracture with no cement or clay, no observable offset	1-2mm	
	N35°52.773' W106°18.653'	7082 +/- 20ft	Qbt3	C, W	N58W 9NE	1	fracture with no cement or clay, no observable offset	1-2mm	
	N35°52.808' W106°18.790'	7110 +/- 20ft	Qbt3t	C, W	N16W 83NE	1	fracture with no cement or clay, no observable offset	1-2mm	
	N35°52.813' W106°18.915'	7168 +/- 19ft	Qbt3t	C, W	N42E 90	1	fracture with no cement or clay, no observable offset	1-2mm	
32	MDAP S-Site	?	Qbt4l	C, NW	N41E 87NW	5	orange clay gouge with very weak foliation, no observable offset	1-5mm	bt117 (fault surface)
					N23E 90	5	orange clay gouge with very weak foliation and white cement, no internal zonation, no observable offset	5-15mm	
					N57E 90	5	orange clay gouge with very weak foliation and white cement, no internal zonation, no observable offset	5-15mm	
					N75E 90	5	orange clay gouge with very weak foliation and white cement, no internal zonation, no observable offset	5-15mm	
					N25E 90	5	orange clay gouge with very weak foliation and white cement, no internal zonation, no observable offset	5-15mm	
					N45E 90	5	orange clay gouge with very weak foliation and white cement, no internal zonation, no observable offset	5-15mm	
					N05E 90	5	orange clay gouge with very weak foliation, dip-parallel striations, no measurable offset	1-5mm	bt118 (fault surface)
					N70E 65NW	5	compositional foliation (thick orange clay gouge with ignimbrite fragments and bounding white cement)	up to 70mm	bt119 (fault)
33			Qbt3	C, NW		2	no alteration, shear zones with no fractures, displaced pumice clasts, preferential wetting of db's observed		
34	W of fault escarpment, NM4		Qbt3t	C, W	vert. and horiz.	1	1mm wide fractures in strongly welded ignimbrite	1-2mm	bt121, bt122, bt123 (fault/fracture surfaces)

#Protolith is described as glassy nonwelded (G, NW), crystallized nonwelded (C, NW), or crystallized welded (C, W)

*Fault Types: 1 = fracture-based fault, 2 = unaltered deformation band, 3 = cemented deformation band, 4 = deformation band with clay but not foliation or internal zonation, 5 = deformation band with clay (+/- calcium carbonate cement) and foliation and/or internal zonation, 6 = unaltered zone of multiple deformation bands.

Table A2. Orientations of small-displacement faults on the Pajarito Plateau, organized by fault type.

Fracture-based fault		Deformation-band fault		Unaltered deformation-band fault		Cemented deformation-band fault		Deformation-band fault with clay but no foliation		Deformation-band fault with foliation (clay and/or carbonate)	
strike	dip	strike	dip	strike	dip	strike	dip	strike	dip	strike	dip
N35E	85NW	N85E	60SE	N05W	85NE	N16E	72NW	N85E	60SE	N06W	77SW
N20E	49SE	N05W	85NE	N06W	86NE	N56E	35NW	N10W	80NE	N44E	83SE
N85W	41SW	N06W	86NE	N46E	82NW	N06W	83NE	N35W	58NE	N85W	88SW
N45E	80NW	N10W	80NE	N27E	90	N37E	84SE	N63E	30SE	N21W	75NE
N47E	48NW	N06W	77SW	N45E	50NW	N26E	89NW	N26E	53SE	N10W	90
N18E	90	N16E	72NW	N45E	50NW	N22E	79NW	N17E	43NW	N69W	90
N11E	90	N56E	35NW			N29E	90	N49E	88SE	N61W	88NE
N56E	90	N44E	83SE			N81W	89SW			N49E	8SE
N54W	90	N85W	88SW			N20E	83NW			N41E	87NW
N53E	79SE	N21W	75NE			N10E	72SE			N05E	90
N85E	90	N06W	83NE			N51W	82SW			N70E	65NW
N30E	84NW	N37E	83SE			N30W	45SW			N05E	90
N35W	90	N26E	89NW			N20W	75NE			N45E	90
N51E	90	N22E	79NW			N80W	80NE			N25E	90
N20W	90	N29E	90			N45E	50NW			N75E	90
N59E	90	N81W	89SW			N45E	50NW			N23E	90
N65E	86NW	N20E	83NW			N79E	82SE			N57E	90
N15E	83NW	N10E	72SE			N11E	85SE				
N68E	83SE	N46E	82NW			N85E	86NW				
N81W	90	N51W	82SW			N04E	86NW				
N81E	76NW	N10W	90			N38W	65SW				
N37E	85SE	N69W	90			N47W	65SW				
N77W	74SW	N35W	58NE								
N75E	83SE	N63E	30SE								
N77W	84SW	N26E	53SE								
N10E	86NW	N27E	90								
N15E	87NW	N72W	85SE								
N21W	74NE	N61W	88NE								
N50E	77SE	N30W	45SW								
N56E	82NW	N20W	75NE								
N18E	53NW	N80W	80NE								
N14W	61NE	N45E	50NW								
N15W	88NE	N45E	50NW								
N23W	82NE	N79E	82SE								
N58W	9NE	N11E	85SE								
N16W	83NE	N17E	43NW								
N42E	90	N85E	86NW								
		N04E	86NW								
		N49E	88SE								
		N49E	88SE								
		N38W	65SW								
		N47W	65SW								
		N41E	87NW								
		N05E	90								
		N70E	65NW								
		N05E	90								
		N45E	90								
		N25E	90								
		N75E	90								
		N23E	90								
		N57E	90								

Table A1. Descriptions of small-displacement faults at each outcrop location on the Pajarito Plateau.

Location	GPS Reading	Elevation	Unit	Protolith[#]	Fault Orientation	Fault Type*	Fault Description	Fault Thickness	Samples Collected
1	N35°52.105' W106°19.124'	7379 +/- 24ft	Qbt4	C, NW	N35E 85NW	1	no gouge or clay, no observable offset	1mm	bt20 & bt21 (fracture walls)
					N20E 49SE	1	no gouge or clay, no observable offset	1mm	bt26 (fracture wall)
					N85W 41SW	1	no gouge or clay, no observable offset	1mm	bt27 (fracture wall)
					N85E 60SE	4	orange/brown gouge, no fractures, no observable offset	2-3mm	bt110 (fault)
2	N35°52.154' W106°15.661'	7110 +/- 20ft	Qbt3	C, NW	N05W 85NE	6	zone of gray to pink deformation bands bounded by fractures, no observable offset	150mm	bt1, bt2, bt33 (faults)
					N06W 86NE	2	dark, crystal-rich gouge, very poorly lithified, no observable offset	12-40mm	
					N10W 80NE	4	brown zone, no fractures, no foliation or observable offset	25-40mm	bt130 (fault)
3	1/3 mi. W of Ta-72, E. Jemez Rd.	~ 7100 ft	Qbt1g	G, NW	n/a	n/a	fissures (no fracture-based faults or deformation bands)		
4	N35°51.981' W106°16.134'	6856 +/- 14ft	Qbt1g	G, NW	N06W 77SW	5	compositional foliation (clay gouge),10cm normal down-to-west displacement	30-40mm	bt45 (fault)
5	N35°48.658' W106°13.655'	6522 +/- 17ft	Qbt1g	G, NW	N16E 72NW	3	white calcium carbonate with striations or slickenlines, cohesive, no measurable offset	1mm	bt65, bt66 (fault)
					N56E 35NW	3	white calcium carbonate with striations or slickenlines, cohesive, no measurable offset	1mm	
6	N35°47.243' W106°15.226'	6325 +/- 18ft	Qbt1g	G, NW	N44E 83SE	5	compositional foliation (incohesive brown gouge, cohesive orange gouge, white/gray resistant material with white cement patches), positive relief, no measurable offset	60mm	bt8 (resistant zone) & bt9 (orange gouge)
					N85W 88SW	5	compositional foliation (brown clay gouge, orange gouge), no measurable offset	30mm	bt6 & bt7 (orange gouge)
					N21W 75NE	5	compositional foliation (white cement, black strongly foliated clay, orange clay gouge), no measurable offset	60mm	bt5 (fault)
					?	5	compositional foliation (white cement bounded by brown clay gouge), no measurable offset	60mm	
					?	5	compositional foliation (white cement, brown clay gouge, orange clay gouge), no measurable offset	50mm	
7	N35°52.452' W106°13.073'	6455 +/- 31ft	Otowi	G, NW	N06W 83NE	3	non-carbonate, gray cement, slip surface, no measurable offset	1mm	bt10, bt12 (fault)
8	N35°52.600' W106°13.119'	6581 +/- 17ft	Qbt1g	G, NW	N37E 84SE	3	white cement or very fine-grained gouge, no measurable offset, no striations or slicks	1mm	bt18, bt19 (fault)
					N26E 89NW	3	white cement or very fine-grained gouge, no measurable offset, no striations or slicks	1mm	bt18, bt19 (fault)
					N22E 79NW	3	white cement or very fine-grained gouge, no measurable offset, no striations or slicks	1mm	bt18, bt19 (fault)
					N29E 90	3	white cement or very fine-grained gouge, no measurable offset, no striations or slicks	1mm	bt18, bt19 (fault)
					N81W 89SW	3	white cement or very fine-grained gouge, no measurable offset, no striations or slicks	1mm	bt18, bt19 (fault)
9	Pueblo Canyon, E of Loc. 8	~ 6600 ft	Qbt1g	G, NW	N20E 83NW	3	dip-slip slicks on case-hardened or cemented fault surface, no observable offset	1mm	
					N10E 72SE	3	dip-slip slicks on case-hardened or cemented fault surface, fibrous mats from roots on fault surface, no observable offset	1mm	bt13 (fault)
10	N35°52.643' W106°13.161'	6611 +/- 31ft	Cerro Toledo	G, NW	n/a	n/a	cemented fine-grained zones 1-5mm thick parallel (horizontal), subhorizontal, and cross-bedded with respect to strata, no observable offset	1-5mm	
11	Pueblo Canyon, W of Loc. 10	~ 6600 ft	Qbt1g	G, NW	N45E 80NW	1	en echelon fractures, no offset observed	1mm	
12	N35°52.710', W106°13.267'	6668 +/- 22ft	Qbt1g	G, NW	N46E 82NW	2	crystal-rich gouge, fault extends into overlying oxidized 1g as an open fracture/fault, no observable offset	15-20mm	
13	N35°52.583', W106°13.191'	6504 +/- 17ft	Otowi	G, NW	N51W 82SW	3	en echelon faults with orange/brown cement, slickenlines evident	1mm	bt14, bt15 (fault surface)
14	N35°52.215', W106°14.475'	7008 +/- 13ft	Cerro Toledo	G, NW	N10W 90	5	compositional foliation (anastomosing lenses of clay gouge and sediments), no measurable offset	60-80mm	bt22
15	Pueblo Canyon, E of Loc. 14	~ 7000 ft	Cerro Toledo	G, NW	N69W 90	5	compositional foliation (foliated clay gouge; mixed zones of phenocrysts, orange clay gouge, and brown clay gouge; phenocrysts and lithics; brown foliated clay gouge), < 1cm offset	150-200mm	bt24, bt25 (fault)
16	N35°53.727', W106°14.475'	7213 +/- 40ft	Qbt3	C, NW	N35W 58NE	4	tan/brown zone, no fractures, no foliation or observable offset	7-35mm	bt28 (fault)
					N63E 30SE	4	tan/brown zone, no fractures, no foliation or observable offset	10mm	bt30, bt31 (fault)
					N26E 53SE	4	tan/brown zone, no fractures, pumice cut by fault, no measurable offset	10mm	bt116 (fault)
					N27E 90	2	crystal-rich gouge, no observable offset	15mm	bt114, bt115 (fault)
17	N35°52.026' W106°16.268'	6863 +/- 19ft	Qbt1g	G, NW	N72W 85SE	3	white cement or very fine-grained gouge, no measurable offset, no striations or slicks	1mm	bt47 (fault)
18	N35°53.376' W106°18.106'	7120 +/- 18ft	Cerro Toledo	G, NW	N61W 88NE	4	clay gouge with strong foliation, roots and white cement, offset increases from 5cm to 16cm (bottom to top of outcrop)	5mm	bt49, bt50, bt51 (fault)

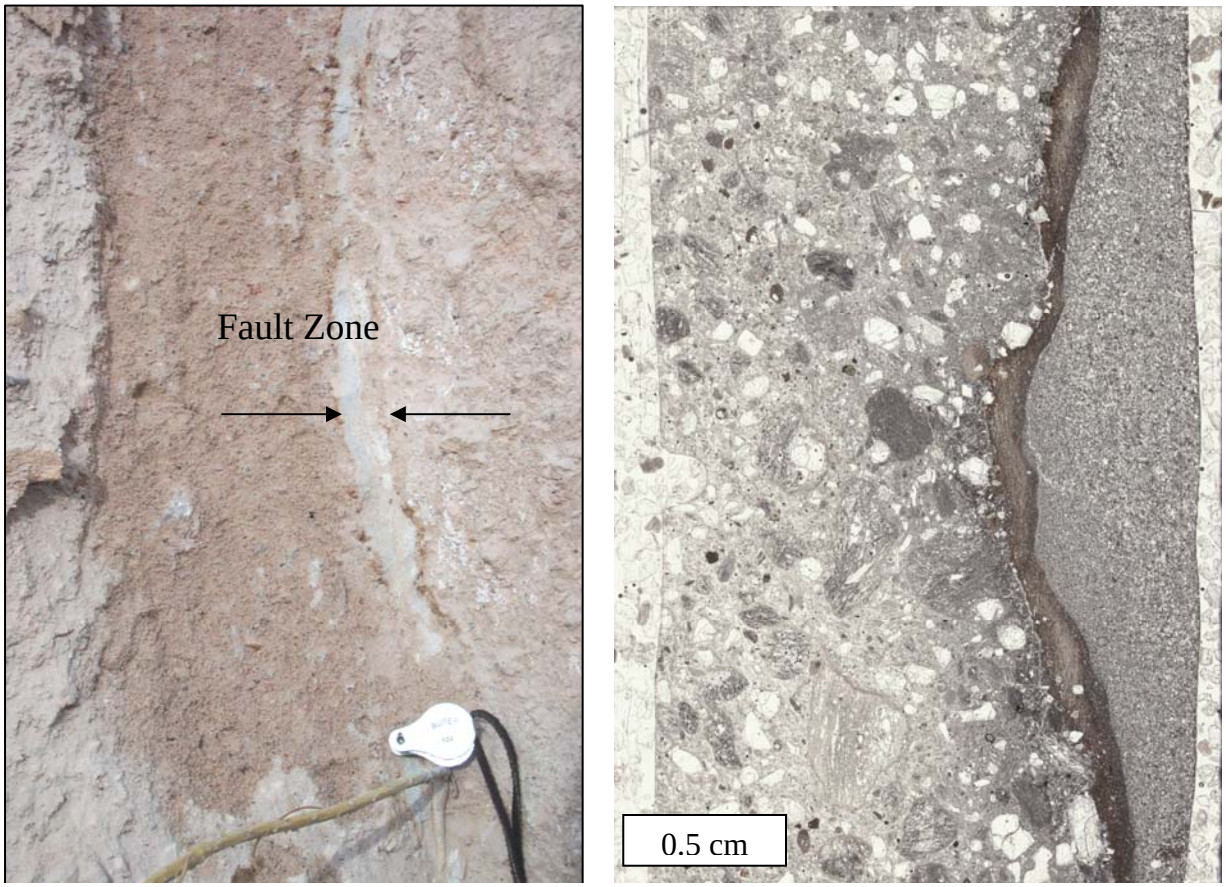

Figure A2. Outcrop (a) and thin section photo (b) of a deformation-band fault zone containing a zonal structure of clay-enrichment and ash-enrichment. Outcrop location 4, samples bt45a (clay portion of fault), bt45b (ash portion of fault), and bt45c & bt46 (protolith). Thin section shows view perpendicular to fault strike and parallel to dip direction.

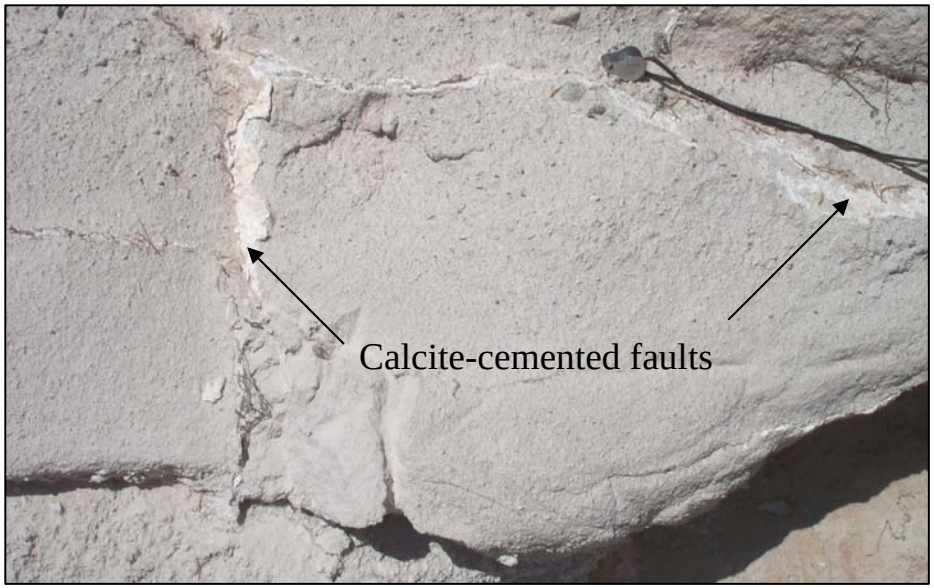

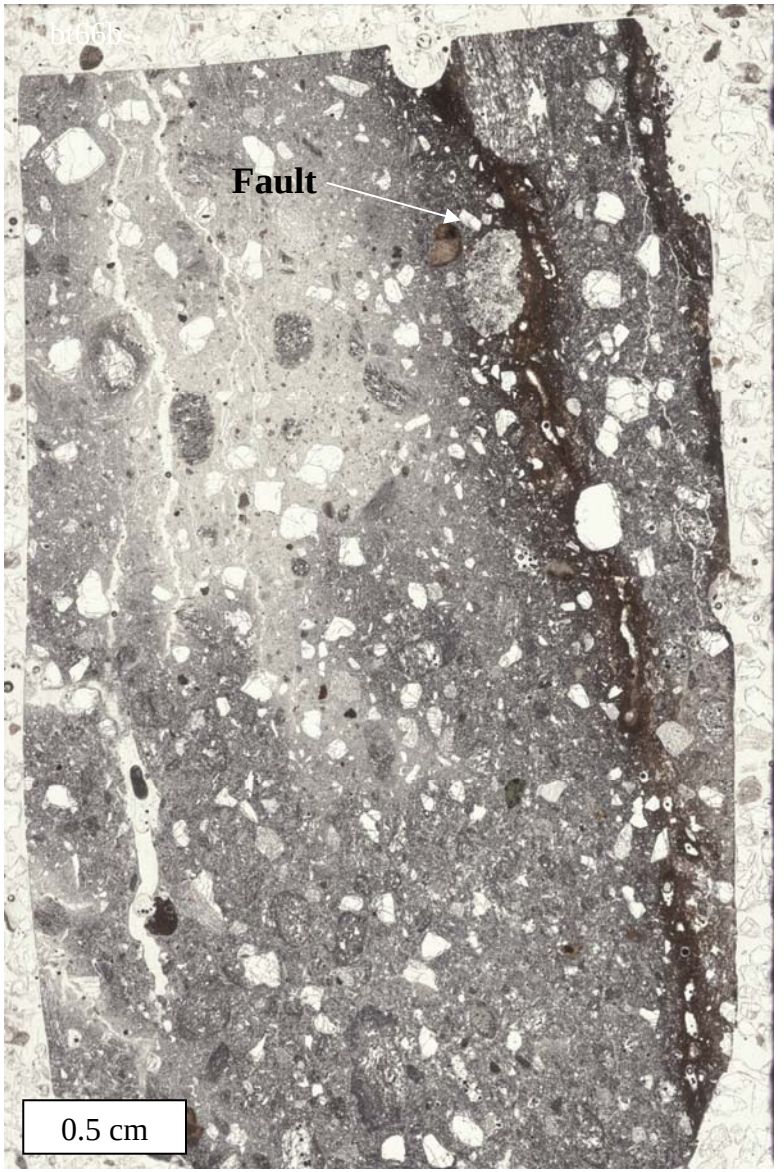

Figure A3. Outcrop (a) and thin section photo (b) of calcite-cemented deformation bands. Outcrop location 5, samples bt66 (fault) and bt67 (protolith). Thin section shows view perpendicular to fault strike and parallel to dip direction.

Figure A4. Outcrop (a) and thin section photo (b) of a deformation-band fault zone with 70 wt% smectite. Outcrop location 6, samples bt7 (clay portion of fault), bt7b (clay and calcite portion of fault), and bt7c (protolith). Thin section shows view perpendicular to fault strike and perpendicular to dip direction.

Table A3. Protolith-fault (fracture-based) set from welded Bandelier Tuff, classified by sample number and analyses performed.

Sample Number	Fault	Protolith	Fault Type	Protolith Description	Alteration Minerals	Analyses Performed					
						Outcrop	Petrography	XRD	XRF	INAA	Stable Isotope
bt107	x		fracture wall		n/a	x					x
bt108	x		fracture wall			x	x				x
bt109		x		welded crystallized (Qbt3t)		x	x				x

Sample numbers correspond to those given in Table A1.

Location and Description of Small-Displacement Faults Investigated in the Calico Hills Tuff, Busted Butte, NV

Small-displacement faults were investigated in August 2001 in the main adit and alcove of the Busted Butte Unsaturated Zone Transport Test facility (Turin et al., 2002; Fig. A5). Initial investigation of one fault in the main adit (Location BB1, Fig. A5b) revealed a slickensided fault surface with an orientation of N32E 69NW and about 0.5m normal separation. Protolith samples were collected from this location. Three samples of another small-displacement fault were also collected, sectioned for petrographic description, and analyzed for geochemistry. These samples were from the final (8^{th}) mine-back face of the test block (Location BB2, Fig. A5b). The fault that was sampled, shown schematically in Fig. A5b, traversed both the Topopah Spring and Calico Hills Tuffs (Fig. A6). The fault changes in character from a fracture-based fault in the moderately welded Topopah Spring Tuff to a deformation band in the nonwelded Calico Hills Tuff. Fluid from tracer tests reached this final mine-back face, as evidenced by preferential wetting of part of the Calico Hills Tuff. Although tracers did not reach this part of the test block, hydrologic information can be obtained from the change in height of the moisture front in the vicinity of the deformation band relative to adjacent protolith. A rise in the wetting front along the deformation band suggests that this zone of grain crushing and pore collapse has different hydrologic properties than the surrounding undeformed ignimbrite, and therefore may affect fluid flow.

Table A4. Descriptions of small-displacement faults at each location at Busted Butte.

Location	Ignimbrite Unit	Protolith#	Fault Orientation	Fault Type*	Fault Description	Fault Thickness	Samples Collected
BB1	Calico Hills Tuff	NW, G	N32E 69NW	3	cement or very fine-grained material slickenside surface and 50cm normal offset	1-3mm	bb1 (fault) bb2 (protolith)
BB2	Topopah Spring Tuff	MW, G		1	fracture-based fault with opal/chalcedony cementation	10-70mm	
	Base surge, Topopah Spring Tuff	NW, G		2	no cement, clay, or fractures	2-7mm	bb5
	Calico Hills Tuff	NW, G		2	no cement or fractures some clay (protolith also has clay)	1-3mm	bb6
	Calico Hills Tuff	NW, G		2	no cement or fractures some clay (protolith also has clay)	1-5mm	bb7

#Protolith is described as glassy nonwelded (G, NW), crystallized nonwelded (C, NW), or crystallized welded (C, W)

*Fault Types: 1 = fracture-based fault, 2 = unaltered deformation band, 3 = cemented deformation band.

Table A5. Protolith-deformation band set from Busted Butte (NV), classified by sample number and analyses performed.

Sample Number	Fault	Protolith	Fault Type	Protolith Description	Alteration Minerals	Analyses Performed				
						Outcrop	Petrography	XRD	XRF	INAA
BB5	x		DB (altered?)		smectite	x	x	x	x	
BB6	x		DB (altered?)		smectite	x	x	x	x	
BB7	x		DB (altered?)		smectite	x	x	x	x	x
BB2		x		Calico Hills Tuff (NV)	smectite	x	x			
Chn		x		Calico Hills Tuff (NV)	smectite	x		x		
Tpt/Tptpv1		x		Topopah Spring Tuff (NV)	smectite	x		x		

BB = Busted Butte, Chn = nonwelded Calico Hills Tuff, Tpt/Tptpv1 = partially welded Topopah Spring Tuff

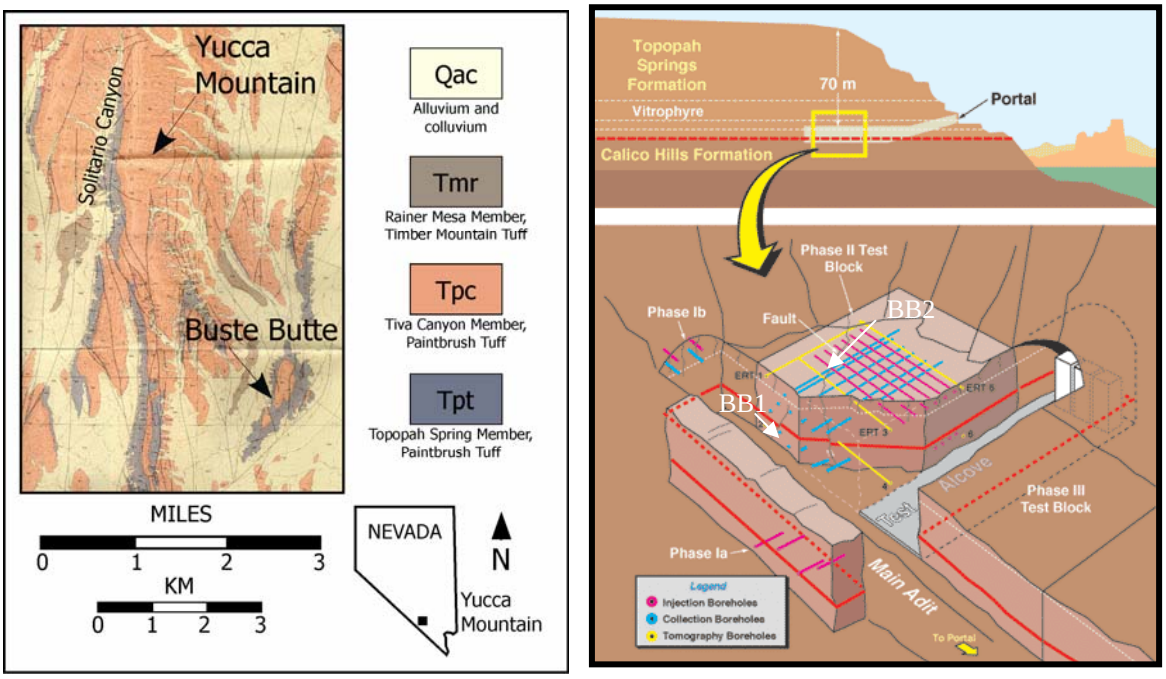

Figure A5. (a) Location map showing location and surface geology in the vicinity of Busted Butte, NV. Geology from Lipman and McKay (1965). (b) Schematic diagram of the Busted Butte Unsaturated Zone Transport test facility, showing the stratigraphy, portal, main adit, and alcove. From http://www.ees.lanl.gov/EES5/bbutte/southern.html.

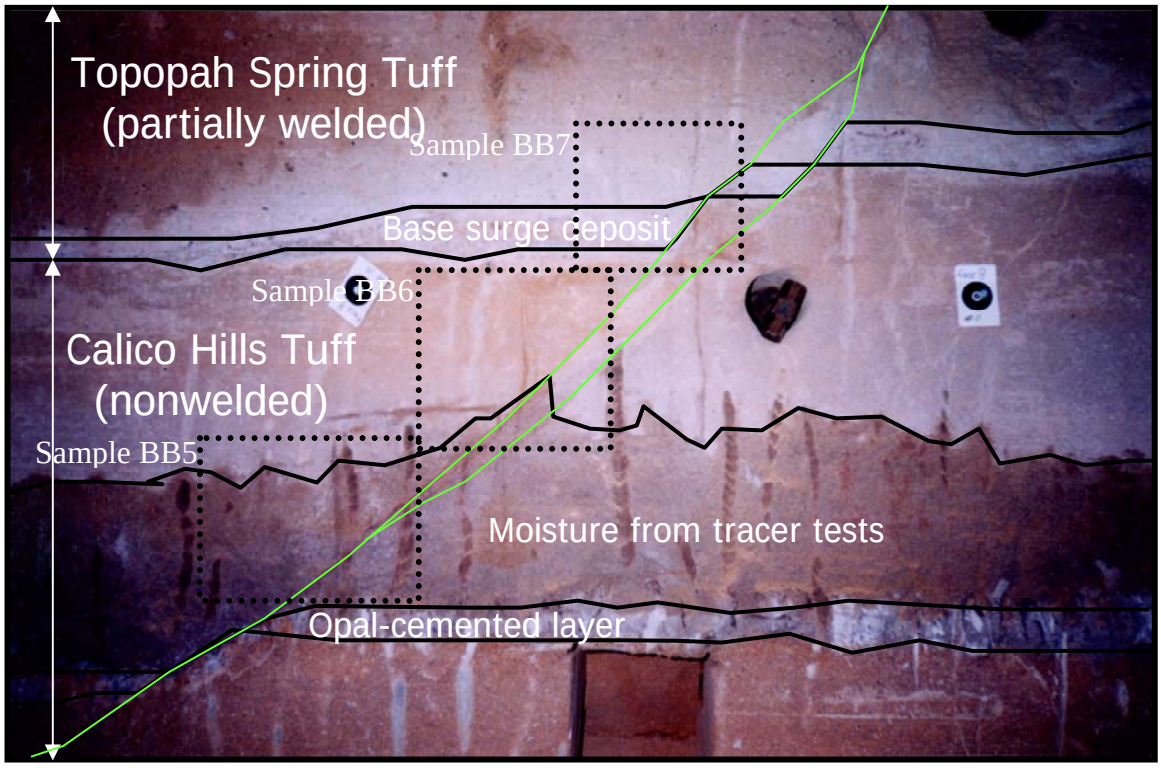

Figure A6. Photo of final mine-back face (face 8; location BB2 in Fig. A5b), showing a small-displacement fault that displaces the Topopah Spring/Calico Hills Tuff sequence. Fault is highlighted in green, lithologic contacts in black. The character of the fault changes from a discrete slip surface in the partially welded Topopah Spring Tuff to a zone of deformation bands in the nonwelded base surge deposit and Calico Hills Tuff. Note the rise in the moisture front in the vicinity of the deformation band relative to surrounding protolith. Distance between grid markers is 1 meter. Locations of samples collected from this mine-back face (BB5, BB6, and BB7) are shown by dashed boxes.

(a)

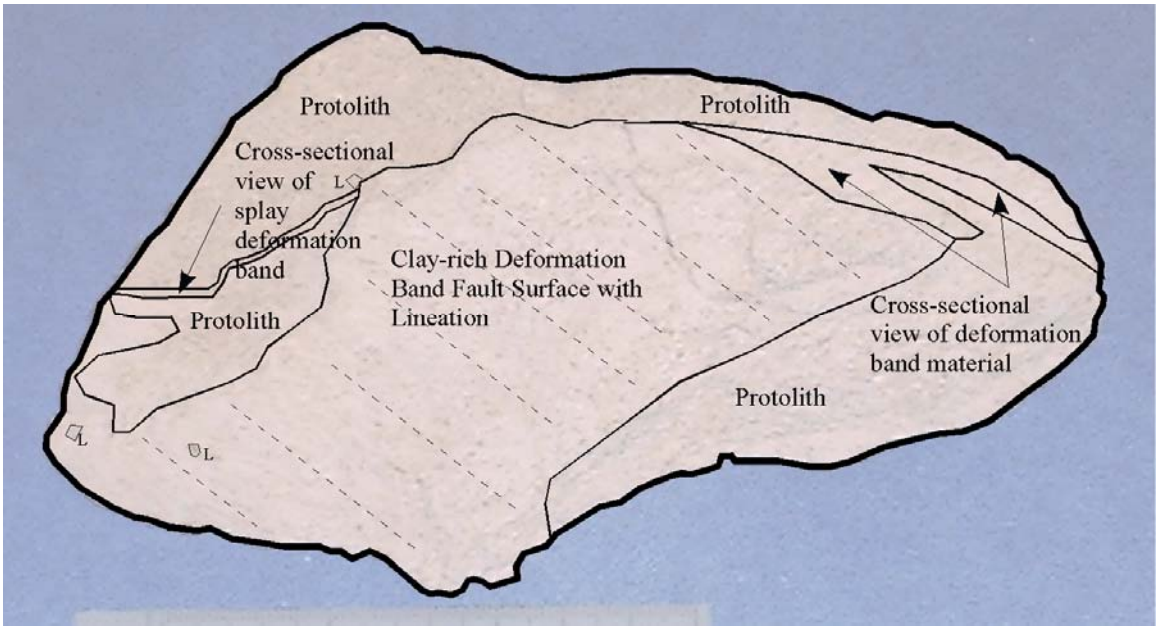

(b)

Figure A7. (a) Photograph of sample BB5. (b) Annotated photograph of sample BB5 showing deformation-band fault surface in Calico Hills Tuff. L = lithic clast. Sample is approximately 15 cm in length.

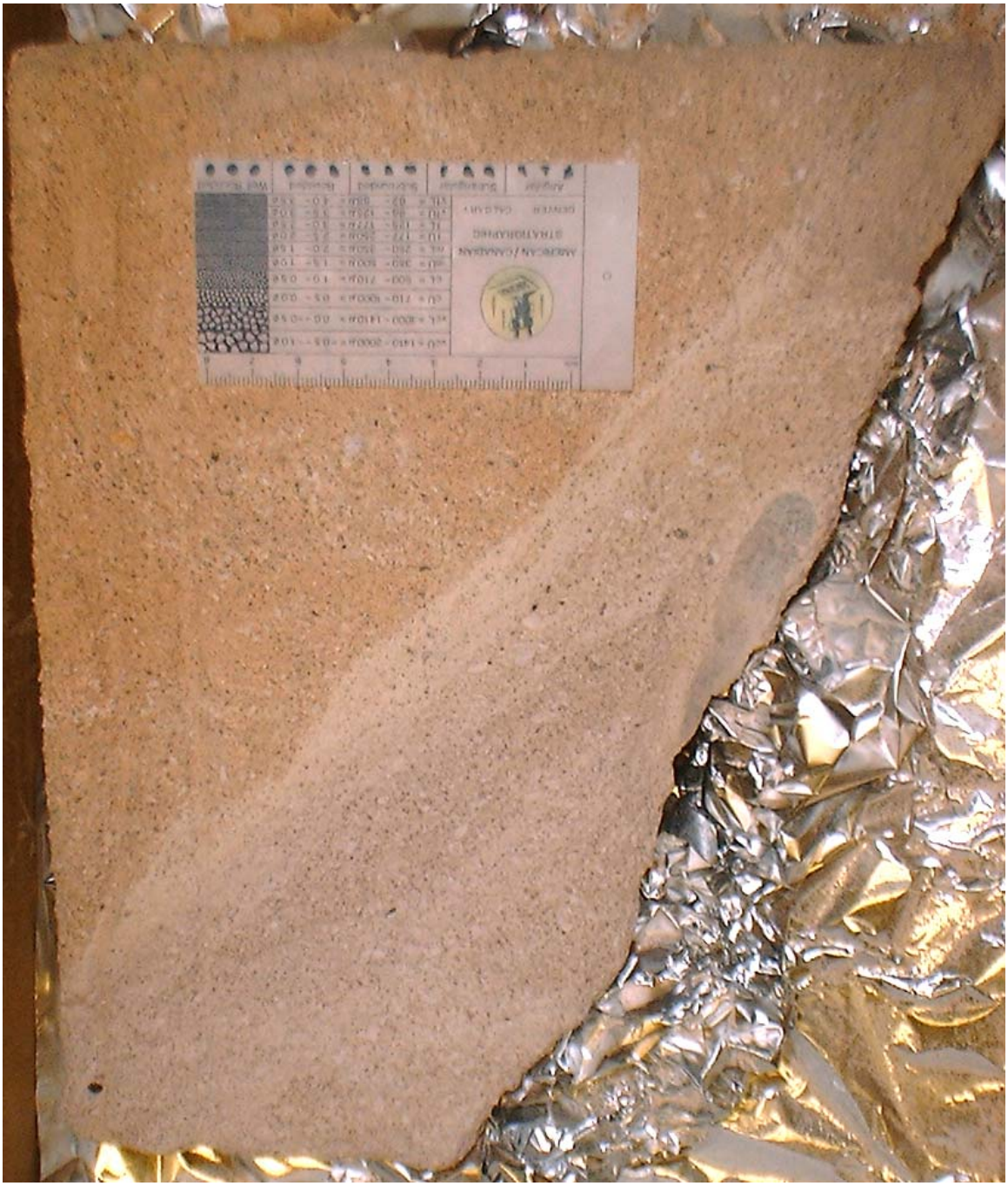

(a)

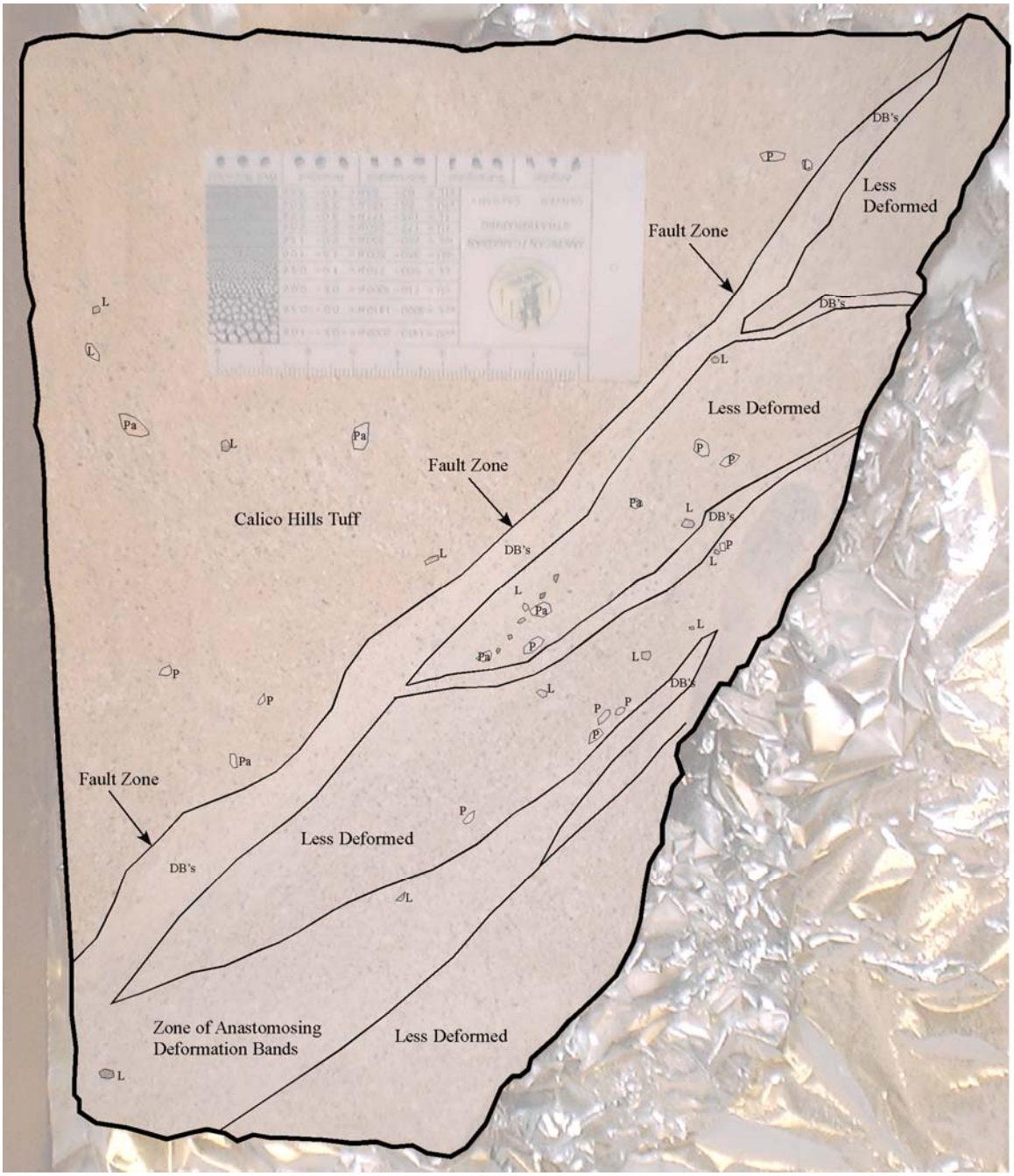

(b)

Figure A8. (a) Photograph of sample BB6. (b) Annotated photograph of sample BB6 showing zones of anastomosing and branching deformation bands in Calico Hills Tuff. P = pumice, Pa = altered pumice, L = lithic clast. Sample is approximately 25 cm in height.

(a)

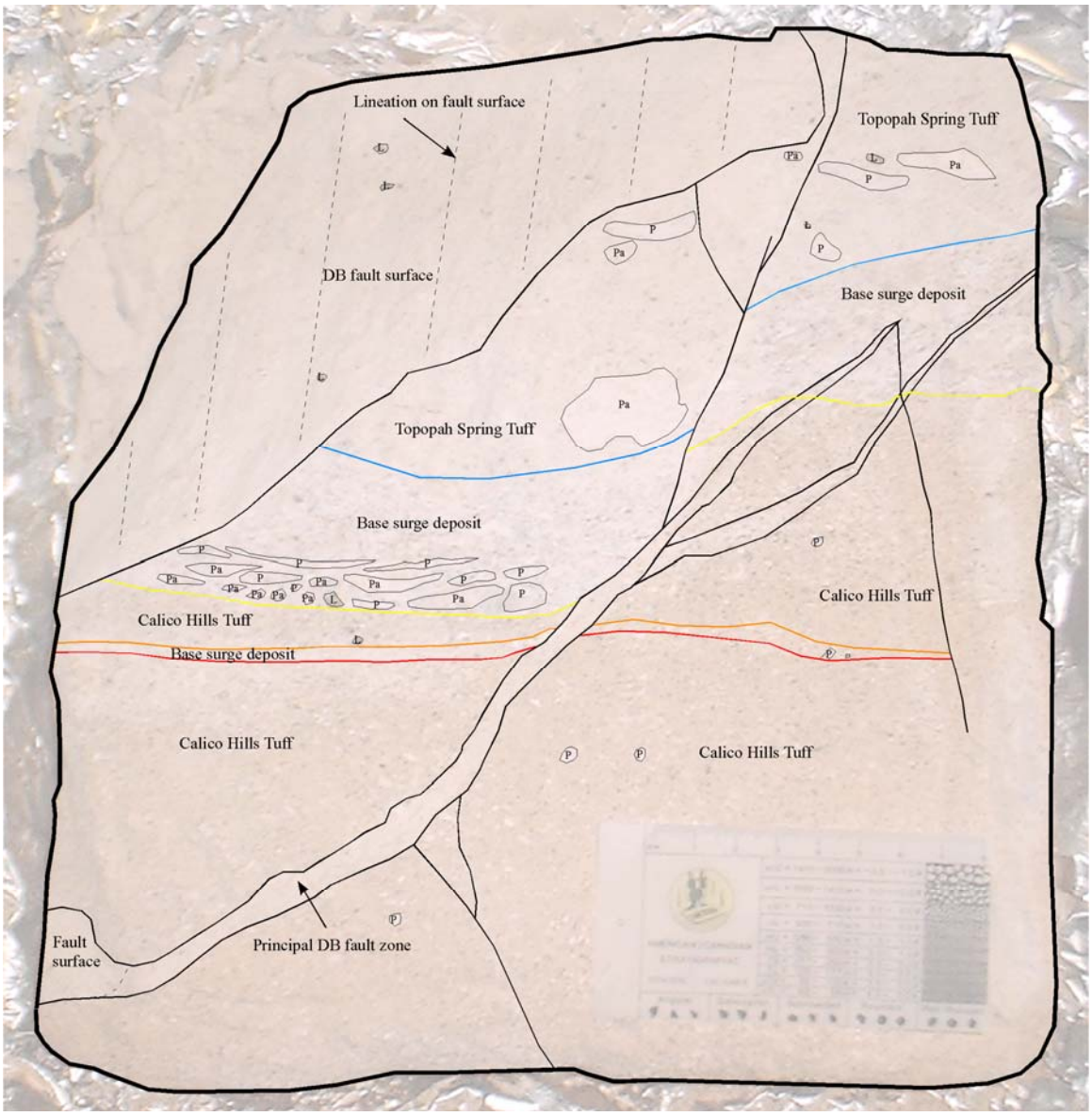

(b)

Figure A9. (a) Photograph of sample BB7. (b) Annotated photograph of sample BB7 showing deformation-band offset of Calico Hills and Topopah Spring Tuffs. P = pumice, Pa = altered pumice, and L = lithic clast. Sample is approximately 25 cm in height.

Table A6. Mineralogy, major oxides, and trace elements for deformation-band samples from Busted Butte, NV.

	BB5	BB6	BB7
Quartz (wt%)	3	3	2
Alkali Feldspar	3	4	3
Plag Feldspar	7	8	6
Glass	78	73	73
Smectite	8	12	14
Cristobalite	0	0	0
Tridymite	0	0	0
Hematite	0	0	0
Magnetite	0	0	1
Augite	0	0	0
Calcite	0	0	0
Other^	1	1	1
Total	100	100	100
SiO_2 (wt%)	76.38 *(0.53)*	76.07 *(0.53)*	75.67 *(0.53)*
TiO_2	0.14 *(0.00)*	0.14 *(0.00)*	0.15 *(0.00)*
Al_2O_3	13.41 *(0.03)*	13.64 *(0.03)*	14.01 *(0.03)*
Fe_2O_3	1.24 *(0.00)*	1.27 *(0.00)*	1.34 *(0.00)*
MnO	0.07 *(0.00)*	0.08 *(0.00)*	0.07 *(0.00)*
MgO	0.51 *(0.00)*	0.67 *(0.00)*	0.85 *(0.00)*
CaO	0.8 *(0.00)*	0.88 *(0.00)*	0.98 *(0.00)*
Na_2O	2.87 *(0.04)*	2.78 *(0.04)*	2.71 *(0.04)*
K_2O	4.56 *(0.03)*	4.45 *(0.03)*	4.19 *(0.03)*
P_2O_5	0.02 *(0.00)*	0.02 *(0.00)*	0.02 *(0.00)*
Total~	100.00	100.00	100.00
LOI	5.01	5.77	6.09
V (ppm)	nd	14	nd
Cr	17	24	19
Ni	4	9	5
Zn	147	157	151
Rb	174	171	172
Sr	97	115	138
Y	31	33	34
Zr	134	140	150
Nb	25	25	25
Ba	117	133	150
Th	29	30	32
U	6	7	6
Pb	33	31	44
Cu	4	5	6
La*	-	-	60.7 *(0.6)*
Ce*	-	-	131.1 *(1.3)*
Nd*	-	-	45 *(3)*
Sm*	-	-	7.63 *(0.08)*
Eu*	-	-	0.465 *(0.017)*
Tb*	-	-	0.71 *(0.03)*
Yb*	-	-	2.96 *(0.03)*
Lu*	-	-	0.53 *(0.03)*
Hf*	-	-	5.57 *(0.06)*
Ta*	-	-	7.98 *(0.14)*
Sc*	-	-	4.92 *(0.05)*
Co*	-	-	228 *(2)*
As	3	3	3
Sb*	-	-	0.62 *(0.03)*

DB = deformation band, Sm = smectite, Ca = calcite, Plag = plagioclase, - = not analyzed, nd = below detection limits.

^Other minerals include biotite, halite, dolomite, and fluorite. ~Major oxide wt% normalized to 0 wt% LOI. *INAA data uncertainties given in parantheses are one-standard-deviation estimates of analytical precision. Mineralogic data analytical error = 2 wt%. Major oxide analytical error from XRF analyses given in parantheses are calculated according to Hallet and Kyle (1993). Precision (in %) for trace elements determined by XRF are 5 (V), 5 (Cr), 3 (Ni), 2 (Zn), 1 (Rb), 1 (Sr), 1 (Y), 2 (Zr), 1 (Nb), 5 (Ba), 2 (Th), 3 (U), 2 (Pb), 3 (Cu), and 3 (As). Detection limits (in ppm) for XRF analyses are 3 (V), 4 (Cr), 3 (Ni), 2 (Zn), 2 (Rb), 2 (Sr), 1 (Y), 2 (Zr), 2 (Nb), 15 (Ba), 2 (Th), 2 (U), 2 (Pb), 3 (Cu), and 2 (As).

APPENDIX B

SAMPLE PREPARATION AND PETROGRAPHIC DATA COLLECTION

Epoxy-Impregnation Procedure

1. Removed water from samples by performing either a or b below:

    a. Samples containing non-swelling clays were immersed in acetone for 1-3 days, changing the acetone bath every 24 hours and checking for water content (using copper II sulfate). Acetone was drained into approved disposal container.
    b. Friable samples containing swelling clays were not immersed in acetone since test samples fell apart. These samples were dried at room temperature for 24 hours, followed by $\geq$ 24 hours in a 100^{o}C oven.

2. Samples were placed into sample boats (pre-formed aluminum pans). The style and size of pan (muffin, miniloaf, loaf, potpie) were chosen to reduce the volume of empty space around sample. This saves epoxy and provides support for the sample if it starts to disaggregate. For samples that were particularly friable or very clay-rich, the lower half of the sample was wrapped with aluminum foil, then placed into the sample boat to add more support.

3. Spurr epoxy was mixed in a sturdy but light container (mid-size aluminum loaf or potpie pan), a balance, gloves, a stirrer (a plastic pipet), four plastic pipets (one for each component) and a working fume hood. All chemicals used in the Spurr epoxy are very toxic, especially the DMAE, so gloves were worn at all times, and the room was well ventilated using the fume hood. The basic "recipe" is:

ERL 4206 (epoxy resin)	10g
DER 736 (flexibilizer)	5g
NSA (epoxy hardener)	26g
DMAE (accelerator)	0.1g (2-4 small pipet drops)

    These amounts were increased proportionally to yield more Spurr epoxy. For a full load of small to mid-size samples, 5x the amounts above gives enough epoxy for full impregnation (this is also the maximum volume that an aluminum potpie pan can hold).

The balance was placed in the fume hood, where each component was added to the container. A pipet was used for small amounts.

4. Once the epoxy was mixed, it was placed carefully on the counter. The balance was removed from the fume hood, and replaced with the bell jar. The samples were placed in the bell jar and evacuated for ~ 5 minutes to pull any air from the samples and the epoxy.

5. Once evacuated, the samples and epoxy were removed from the vacuum chamber. Epoxy was added to each sample boat to cover each sample about halfway, keeping the top surface clear.

6. The vacuum chamber was closed and the samples evacuated for about half an hour. The turet was turned to lock in the vacuum, which was maintained for 3 to 4 days. Samples were checked at least once a day to ensure that samples were still under vacuum.

7. After samples imbibed enough epoxy, they were removed from the vacuum chamber and placed in a 40^{o}C oven. The following heating schedule was used to cure the samples:

    24 hours at 40^{o}C (104^{o}F)
    24 hours at 50^{o}C (122^{o}F)
    24 hours at 60^{o}C (140^{o}F)
    24 hours at 70^{o}C (158^{o}F)
    Remove samples and cool under fume hood

Petrographic Point Count Determinations

Petrography of ignimbrite protolith was determined by point count on a petrographic microscope at 10x magnification on a minimum of 50x35 point grid for each thin section. Ash/glass shards, pumice, phenocrysts, and lithic clasts were identified (Table B1). Since BSE imaging was used to quantify porosity, pore spaces were not included in the petrographic point counts.

Table B1. Petrographic point-count data for all ignimbrite protolith samples.								
Sample #	Unit	Location*	Fault type(s)[+]	% Matrix Ash/Shards	% Pumice	% Phenocrysts	% Lithic clasts	% Epoxy (Porosity)
				(pt.ct. / normalized^)	(pt.ct. / normalized)	(pt.ct. / normalized)	(pt.ct. / normalized)	(pt.ct. / BSE)
bt120	Qbt4	32	1, 4, 5	46.1 / 32.4	10.9 / 7.7	20.6 / 14.5	4.3 / 3	na / 42.4
				incipiently & locally altered	almost completely	fine sand to 4mm	devitrified, heavily altered tuff	many pores filled w/ clay
				vfg matrix w/larger shards	devitrified			
49-2-53.0[#]	Qbt4	TA-49	na	66.5 / 46.8	8.8 / 6.2	21.7 / 15.3	3.0 / 2.1	na / 29.6
				incipiently & locally altered	almost completely	fine sand to 4mm	devitrified tuff	
				vfg matrix w/larger shards	devitrified			
49-2-73.0	Qbt4	TA-49	na	70.4 / 55.7	10.4 / 8.2	18.1 / 14.3	1.1 / 0.9	na / 20.9
				incipiently & locally altered	almost completely	fine sand to 4mm	devitrified tuff	
				vfg matrix w/larger shards	devitrified			
bt109	Qbt3t	31	1	51.7 / 47.1	7.7 / 7.0	36 / 32.8	2.3 / 2.1	na / 13.1
				devitrified, welded	completely devitrified	mm's to cm's	devitrified, heavily altered tuff	extensive compaction & fracs
bt108	Qbt3t	31	1	45.8	19.5	32.8	1.5	na / 12.9
				devitrified, welded	completely devitrified	mm's to cm's	devitrified, heavily altered tuff	extensive compaction & fracs
bt73	Qbt3	22	1, 3, 5	36.8 / 25.2	24.5 / 16.8	22.6 / 15.5	2.9 / 1.9	na / 40.6
				devitrified, slightly compacted	partially devitrified	fine sand to 4mm	devitrified &/or altered tuff	localized compaction
				vfg matrix w/larger shards				
bt29	Qbt3	16	1, 2, 4	26.4 / 20.6	25.3 / 19.7	28.6 / 22.3	0.7 / 0.5	na / 37
				devitrified, nonwelded, long &	partially devitrified	fine sand to 4mm	devitrified, heavily altered tuff	relatively dense packing
				thin shards				
bt37	Qbt3	2	1, 2, 6	32.6 / 23.4	20.0 / 14.4	20.2 / 14.5	1.11 / 0.8	na / 46.9
				devitrified, nonwelded, fg	partially to almost	fine sand to 4mm	devitrified &/or altered tuff	relatively dense packing
				matrix w/ long & thin shards	completely devitrified	crystallization at edges		
49-2-197.6	Qbt2	TA-49	na	58.8 / 46.9	8.0 / 6.4	33.0 / 26.3	0.2 / 0.2	na / 20.2
				devitrified with vp crystallization	completely crystallized,	fine sand to 3mm	devitrified tuff	dense packing
				moderately compacted	moderately flattened			
49-2-257.0	Qbt2	TA-49	na	60.0 / 48.0	15.8 / 12.6	21.9 / 17.5	2.4 / 1.9	na / 20.0
				devitrified with vp crystallization	completely crystallized,	fine sand to 3mm	devitrified tuff and mafic	dense packing
				moderately compacted	moderately flattened		clasts	
49-2-297.0	Qbt2	TA-49	na	50.3 / 40.4	15.9 / 12.8	31.9 / 25.6	2.0 / 1.6	na / 19.7
				devitrified with vp crystallization	completely crystallized,	fine sand to 3mm	devitrified tuff and mafic	dense packing
				moderately compacted	moderately flattened		clasts	
*Outcrop location numbers correspond to those in Figure A1.								
[+]Fault-type designations correspond to those in Tables A1 and A2.								
^Point count data normalized according to the porosity value determined by BSE imaging (i.e., point count % represents percentage of non-pore volume of component, normalized % represents								
percentage of total volume of component).								
[#]49-2-xxxx sample numbers refer to thin sections provided by D. Broxton (LANL) and analyzed for geochemistry by Stimac et al. (1996).								

Table B1. (continued)								
Sample #	Unit	Location*	Fault type(s)[+]	% Matrix Ash/Shards	% Pumice	% Phenocrysts	% Lithic clasts	% Epoxy (Porosity)
				(pt.ct. / normalized^)	(pt.ct. / normalized)	(pt.ct. / normalized)	(pt.ct. / normalized)	(pt.ct. / BSE)
49-2-342.0	Qbt1vu	TA-49	na	43.9 / 33.1	23.9 / 18.0	27.7 / 20.9	4.5 / 3.4	na / 24.7
				devitrified, nonwelded,	devitrified edges, vfg	medium sand to 3mm	devitrified tuff and mafic	loose packing
				fg matrix w/larger shards	vp crystals in pores		clasts	
49-2-364.5	Qbt1v	TA-49	na	42.7 / 32.8	30.5 / 23.4	22.8 / 17.5	3.9 / 3.0	na / 23.2
				devitrified, nonwelded, vfg matrix	devitrified edges, vp	medium sand to 3mm	devitrified tuff and mafic	relatively dense packing
				w/larger shards	crystals within pores		clasts	
49-2-380.35	Qbt1vc	TA-49	na	49.2 / 37.7	21.6 / 16.6	25.8 / 19.8	3.5 / 2.7	na / 23.3
				devitrified, nonwelded, fg matrix	fine-grained devit.of	medium sand to 3mm	devitrified tuff and mafic	relatively dense packing
				w/ orange (Fe) alteration	edges, vp crystals in		clasts	
					pores, some coherent			
bt63	Qbt1g	6	3, 5	22.7 / 16.2	31.3 / 22.4	15.3 / 10.9	2.0 / 1.4	na / 49
				glassy, low relief	glassy	fine sand to 3mm	devitrified &/or altered tuff	low relief, loose packing
bt46	Qbt1g	4	5	19.4 / 10.7	44.7 / 24.6	12.2 / 6.7	4.1 / 2.3	na / 55.7
				glassy, low relief	glassy	fine sand to 3mm	devitrified &/or altered tuff	low relief, loose packing
bt67	Qbt1g	5	3	19.8 / 13.8	22.5 / 15.6	21.0 / 14.6	2.9 / 2.0	na / 54.0
				glassy, low relief	glassy	fine sand to 3mm	devitrified &/or altered tuff	low relief, loose packing
49-2-596.0	Qct	TA-49	na	33.3 / 26.7	13.8 / 11.1	21.1 / 16.9	10.9 / 8.7	na / 40.8
				glassy, fg matrix	glassy	fine sand to cm's	devitrified tuff & mafic clasts	loose packing
49-2-615.2	Qbo	TA-49	na	49.3 / 33.6	27.6 / 18.8	14.4 / 9.8	8.6 / 5.9	na / 31.8
				glassy, vfg matrix	glassy	fine sand to cm's	devitrified tuff & mafic clasts	loose packing
49-2-656.5	Qbo	TA-49	na	51.0 / 33.4	28.1 / 18.4	13.2 / 8.6	7.8 / 5.1	na / 34.6
				glassy, vfg matrix	glassy	fine sand to cm's	devitrified tuff & mafic clasts	loose packing
49-2-676.5	Qbo	TA-49	na	49.8 / 37.4	27.9 / 20.9	13.7 / 10.3	8.6 / 6.5	na / 25.0
				glassy, vfg matrix	glassy	fine sand to cm's	devitrified tuff & mafic clasts	loose packing
ch3	Qbt1g	Chupaderos	5	34.1 / 28.5	12.5 / 10.5	9.3 / 7.8	0.6 / 0.5	na / 50.5
		Canyon		glassy, fg matrix w/larger shards	glassy	fine sand to 3mm	devitrified & altered tuff	low relief, loose packing
ch5	Qbt1v	Chupaderos	5	43.2 / 27.8	12.1 / 7.8	20.0 / 12.9	0.4 / 0.3	na / 50.5
		Canyon		devitrified	devitrification & vp	medium sand to 3mm	devitrified & altered tuff	low relief, loose packing
					alteration			
bb3	Calico	Busted	2	17.3 / 13.1	37.7 / 28.6	7.2 / 5.5	15.5 / 11.8	na / 41.0
	Hills	Butte		fine matrix of glass & altered glass	very abundant, glassy	fine sand to 3mm	devitrified, altered tuff	moderate packing
*Outcrop location numbers correspond to those in Figure A1.								
[+]Fault-type designations correspond to those in Tables A1 and A2.								
^Point count data normalized according to the porosity value determined by BSE imaging (i.e., point count % represents percentage of non-pore volume of component, normalized % represents								
percentage of total volume of component).								
[#]49-2-xxxx sample numbers refer to thin sections provided by D. Broxton (LANL) and analyzed for geochemistry by Stimac et al. (1996).								

Porosity Determinations

Initially, blue-dyed epoxy was used to impregnate samples to aid in the identification of pore space under a petrographic microscope. However, the transparency of volcanic glass in these materials made it difficult to distinguish blue pore space from pale blue glass shards (Fig. B1). This created significant overestimations of porosity when using an automated image analysis program (Scion Image, NIH). In order to distinguish pore space from grains in these samples, BSE imaging was employed. Under BSE, epoxy is black and any grain in the thin section is a shade of gray (brighter = higher atomic number, like Fe-oxide minerals; darker = lower atomic number, like quartz). Pore spaces readily stand out in this imaging technique.

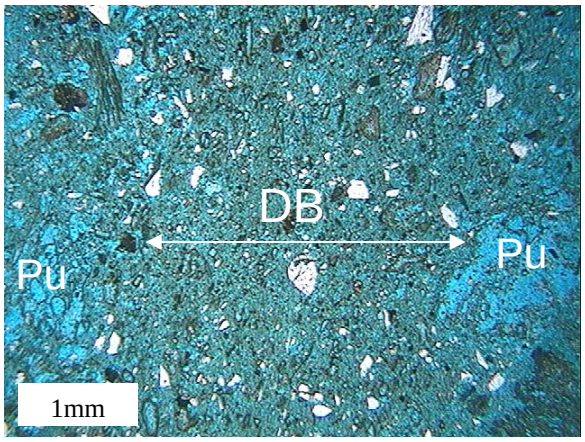

Figure B1. Photomicrograph of a deformation band (DB) in crystallized nonwelded Bandelier Tuff. Extent of deformation band is given by double-arrow, and is characterized by reduced grain- and pore-sizes. Blue-dyed epoxy represents porosity. Pu = undeformed pumice.

Three randomly oriented (mutually perpendicular if possible) thin sections were probe-polished at the NM Bureau of Geology and Mineral Resources. Each thin section was imaged in mosaic-fashion, with a total of 100 images covering the majority of the section. This set of 100 images excludes portions of the thin section in which

phenocrysts, lithic clasts, or pumice fragments have been artificially plucked or polished away.

For each image, the number of black versus gray pixels were counted using Matlab code (Fig. B2). Each pixel has a value from 0 to 256, with lower values approaching black. A pixel value of 10 was used to represent the cutoff between black and gray pixels. From an image with 768x1024 pixels, the percentage of black pixels was used as the estimate of two-dimensional porosity. Possible limitations of this approach include: (1) overestimation of porosity by low contrast images masking very small, low atomic number grains, (2) over- or underestimation of porosity due to an inappropriate cutoff value chosen for pixels representing grains versus pore space, (3) underestimation of porosity if pores are smaller than the resolution of the image, (4) over- or underestimation of porosity since a two-dimensional surface is being used to estimate a three-dimensional quantity (i.e., pore space or grains below the polished surface are not incorporated), and (5) this method does not identify connected (effective) porosity. Effective porosity is an important property in hydrologic characterization.

Limitation (1) was minimized by creating high contrast BSE images for each thin section. In order to address limitation (2), different cutoff values were tested as a means of determining how much porosity could be affected by this parameter. A lower cutoff value counts only the darkest pixels, resulting in a lower porosity value that more accurately counts pore spaces rather than dark grains. In order to determine the cutoff value that is most appropriate for distinguishing pores from dark grains, pixel values ranging from 0 to 30 were entered into the Matlab code, and a value of porosity was

```
**************************************************************************
clear
pixelcutoff=10;

listname = 'imagefiles.list';
fida=fopen(listname,'r');
n=0;
while 1
filename = fgetl(fida);
if ~isstr(filename), break, end
n=n+1;
[X,map] = imread(filename,'tiff');

X2 = X(1:768,1:1024);
RGB2 = ind2rgb(X2,map);
rgbsum = floor(256*(RGB2(:,:,1) + RGB2(:,:,2) + RGB2(:,:,3))/3);
total(n) = length(X2(:,1))*length(X2(1,:));
[h]=hist(reshape(rgbsum,uint32(total(n)),1),0:255);
npix(n)=sum(h(1:pixelcutoff+1));
percnt = 100*npix(n)/total(n);
disp(sprintf('%s %6.2f%s',filename(1:length(filename)-4),percnt,'%'))

end
fclose(fida);

final_percent = 100*sum(npix)/sum(total);

disp(sprintf('%s %6.2f%s','BSE mosaic',final_percent,'% porosity'))

percnts = 100*npix./total;
median_porosity = median(percnts);
standard_deviation = std(percnts);
disp(sprintf('%s %6.2f%s','BSE mosaic standard deviation ',standard_deviation,'%'))

figure(1); clf
for n = 1:20,
randnums=rand(1,length(total));
[Y,I]=sort(randnums);
final_percent2(n,:) = 100.*cumsum(npix(I))./cumsum(total(I));
end

plot(mean(final_percent2),'b')
hold on
plot(mean(final_percent2)+std(final_percent2),'b--')
plot(mean(final_percent2)-std(final_percent2),'b--')

ylabel('porosity (%)')
xlabel('number of images')
title('Porosity values for 20 random subsets')
legend('mean','standard deviation')
**************************************************************************
```

Figure B2. Matlab code for calculating porosity.

determined for each cutoff value. For values greater than 10, porosity values were highly variable and generally larger than for values less than 10. This is probably due to the incorporation of grains that are thin or have very low atomic number. In order to limit the incorporation of these grains in to the porosity determinations, a pixel cutoff value of 10 was chosen.

Limitation (3) was tested by obtaining images of relatively homogeneous fault-zone material at two microscales (500μm versus 100μm; Table B2). Measurement of fault-zone porosity for this test was similar to that of protolith, except that porosity was calculated with a limited number of images. Determination of porosity with higher magnification images generally, though not always, results in higher values than in lower magnification images. Differences between porosity estimated at these two magnifications are small, averaging 4% (Table B2). This indicates that the resolution of the commonly obtained images for all protolith samples results in a slight averaging, and thus lowering, of the porosity value. On the other hand, lower magnification images cover a larger area, and therefore may better represent average porosity in these highly heterogeneous materials. Porosity values for protolith thin sections had already been approximated using BSE images at the lower (500μm-scale) magnification. For consistency, and to give a better estimate of average values, the fault-zone porosity values given in the Chapters 3, 4, and 5 are from the lower magnification images.

Minimizing limitation (4) was attempted by using three mutually perpendicular thin sections whenever possible. With this approach, a pseudo-three-dimensional value of porosity can be estimated. An alternate method of determining three-dimensional porosity was also employed for a subset of protolith samples (Table 5.1). This method also addresses limitation (5), the connectivity of pore spaces in three dimensions (i.e., effective porosity). In order to evaluate these limitations, the volume, dry mass, and water-saturated mass of ignimbrite protolith were measured. Effective porosity was determined from these data, and was found to be consistently higher than the lower magnification BSE-derived porosity values. The increase in effective porosity values,

averaging 9%, is greater than that found for low versus high magnification BSE-derived porosity values (Table B2). This suggests that effective porosity is higher than that being measured in any of the BSE images, especially when those BSE images are taken at lower magnification. Thus, the porosity values given in this study may be considered minimum values.

Table B2. Porosity determinations for deformation-band faults using BSE imaging--comparison of two microscales of measurement

Location	Unit	Fault Type*	Protolith Sample	Protolith Porosity (%)	Fault-Zone Sample	Number of images used for fault-zone porosity 500mm	100mm	Fault-Zone Porosity (%) 500µm	100µm	Difference (%)
31	Qbt3t	1	bt108	12.9	n/a	0	0	n/a	n/a	n/a
31	Qbt3t	1	bt109	13.1	n/a	0	0	n/a	n/a	n/a
16	Qbt3	4	bt29	36.5	bt116	6	4	0.2	2.7	2.5
16	Qbt3	2	bt29	36.5	bt115	6	5	18.7	36.9	18.2
22	Qbt3	5	bt73	40.6	bt111	4	13	19.4	26.9	7.5
Busted Butte	ChT	3	bb3	41.0	bb2a	4	3	16.4	19.3	2.9
Busted Butte	ChT	2	bb3	41.0	bb6	14	24	5.6	10.6	5.0
32	Qbt4l	5	bt120	42.4	bt119	5	5	14.3	15.4	1.1
2	Qbt3	2	bt37	46.9	bt1	4	6	22.5	29.0	6.5
2	Qbt3	2	bt37	46.9	bt2	4	2	17.7	24.5	6.8
6	Qbt1g	5	bt63	48.6	bt6	5	4	2.5	6.4	3.9
6	Qbt1g	5	bt63	48.6	bt8	6	2	18.8	18.1	-0.7
6	Qbt1g	5	bt63	48.6	bt9	7	8	12.6	14.0	1.4
Guaje Mtn	Qbt1g	5	ch3 & ch5	50.5	ch71A	11	8	6.4	13.1	6.7
Guaje Mtn	Qbt1g	5	ch3 & ch5	50.5	ch102	5	5	5.7	13.6	7.9
Guaje Mtn	Qbt1g	5	ch3 & ch5	50.5	ch70	4	7	14.2	10.9	-3.3
5	Qbt1g	3	bt67	54.0	bt66	9	13	12.0	10.8	-1.2
4	Qbt1g	5	bt46	55.7	bt45 (clay zone)	5	8	14.7	10.4	-4.3
4	Qbt1g	5	bt46	55.7	bt45 (vfg zone)	1	2	36.2	44.0	7.8

*Fault-type designation given in Table A1. Sample locations are given in Figure A1.

ChT = Calico Hills Tuff, Guaje Mtn = Guaje Mountain fault zone, vfg = very fine-grained. Mean difference: 4.0

Textures of Fault-Zone Material and Corresponding Protolith Observed in Back-Scattered Electron and Secondary Electron Microprobe Imaging

Table B3. Summary of BSE imaging observations of selected protolith-fault pairs.

Unit	Protolith	Fault Zone
Qbt4 crystallized nonwelded	bt120: very fine-grained matrix (10-25mm) moderate grain connectivity	bt119: some grain-size reduction, no mineral alignment
Qbt3t crystallized welded	bt109: very fine-grained welded shards (10-50mm) high grain connectivity	bt108: no damage zone, very few & randomly oriented microfractures cut across welded fabric and phenocrysts
Qbt3 crystallized nonwelded	bt29: fine-grained matrix of shards with some larger shards (100mm) low to moderate grain connectivity	bt115: smaller glass shards, more large phenocrysts alignment of phenocrysts parallel to strike (seen in section a)
	bt29: fine-grained matrix of shards with some larger shards (100mm) low to moderate grain connectivity	bt116: fine-grained ignimbrite fragments and smectite in pores weak alignment of small grains parallel to strike (seen in section b) weak alignment of small grains 40^{o} from strike (seen in section c)
	bt73: fine-grained matrix of shards with some larger shards (100mm) moderate grain connectivity	bt111: small ignimbrite fragments, smectite, and carbonate fill pores, clay accumulations at boundaries and within fault zone lineation on fault surface parallel to dip, weak grain alignment parallel (seen in section a) and perpendicular (seen in section b) to dip direction
Qbt2 crystallized welded	49-2-197.6: fine-grained matrix (50-100mm) and larger shards, some blocky crystallization minerals, compacted high grain connectivity	fractures observed in field, no BSE images
Qbt1vu crystallized nonwelded	49-2-342.0: very fine-grained matrix (<10mm) with larger shards, more extensive crystallization at grain boundaries than Qbt1v and Qbt1vc low to moderate grain connectivity	fractures and deformation bands observed in field, no BSE images
Qbt1v crystallized nonwelded	49-2-364.5: very fine-grained matrix (10-50mm) with larger shards moderate grain connectivity	fractures and deformation bands observed in field, no BSE images
Qbt1vc crystallized nonwelded	49-2-380.35: very fine-grained matrix (10-50mm) with larger shards, crystallization has resulted in high grain connectivity and pumice appearing as coherent clasts	fractures and deformation bands observed in field, no BSE images
Qbt1g glassy nonwelded	bt46: fine-grained matrix (100-150mm) with long, thin glassy shards low grain connectivity	bt45: pores infilled with clay and ignimbrite fragments, discontinuous grain-size foliation lineation on fault surface parallel to dip alignment of grains parallel to dip (seen in section a) alignment of grains parallel to strike (seen in section b)
	bt63: fine-grained matrix (100-150mm) with long, thin glassy shards low grain connectivity	bt6: pores infilled with clay an clay accumulations that define a compositional foliation with fine-grained and aligned ignimbrite fragments alignment of ignimbrite fragments and clay 80^{o} from strike (seen in section c)
	bt63: fine-grained matrix (100-150mm) with long, thin glassy shards low grain connectivity	bt8: pores infilled with clay and ignimbrite fragments lineation on fault surface 45^{o} from strike alignment of grains 40^{o} from fault surface (seen in section a)
	bt63: fine-grained matrix (100-150mm) with long, thin glassy shards low grain connectivity	bt9: pores infilled with larger clay minerals and small ignimbrite fragments, glass shards observed to alter to smectite, pheno/glass globules in smectite weak mineral lineation parallel to fault (seen in section a) clay and compositional foliation perpendicular to weak mineral lineation
	bt67: fine-grained matrix (100-150mm) with long, thin glassy shards low grain connectivity	bt66: pores infilled with clay-sized clay minerals, calcium carbonate, and ignimbrite fragments, lining of grains and complete infilling alignment of grains parallel to fault (seen in section a) alignment of grains perpendicular to fault (seen in section b)
	ch3: fine-grained matrix (100-150mm) with long, thin glassy shards low grain connectivity	ch71Aa/ch102a/ch70b: strong alignment of grains with variable clay amounts of clay accumulation and ignimbrite fragments, some clay books alignment of grains parallel to dip direction (seen in section a) alignment of grains parallel to strike (seen in section b)
Calico Hills glassy nonwelded	bb2: fine matrix with large amounts of pumice and lithic clasts, moderate grain connectivity due to high abundance of pumice, moderate packing, alteration minerals in pores	bb5: weak alignment of minerals parallel to strike (seen in section b)

Table B4. Summary of secondary electron imaging of selected protolith-fault pairs.

Unit	Protolith	Fault Zone
Qbt4 crystallized nonwelded	stubby postdepositional crystals among rounded post-depositional crystals, shard texture still evident, post-depositional crystals of relict shards are finer than interstitial matrix, pumice is crystallized but there is little to no growth into vesicles	[fractures and clay/carbonate-rich faults observed, no SE images]
Qbt3t crystallized welded	welded contacts between postdepositional crystals that are mostly rounded and 5-10 microns in size, many postdepositional crystals and phenos are fractured, phenocrysts are large (>100 microns), pumice is flattened but long vesicles are still apparent, recrystallized pumice walls are welded like matrix	[fractures observed, no SE images]
Qbt3 crystallized nonwelded	fibrous and dense feldspar (?) > 20 microns long and less than 5 microns wide with variable amounts of rounded postdepositional crystals that are 5-10 microns in size, large pores, shard texture still present large phenocrysts lined with fine-grained (2 to 5 microns) tridymite and possibly a small amount of cristobalite, large pores [mineralogy very similar to first Qbt3 protolith, no SE images]	bt1: unaltered zone of deformation bands shorter (< 10 microns) fibrous and still dense feldspar with fractured phenocrysts and fine-grained postdepositional crystals (10 microns), roots in pores common bt116: deformation bands with smectite small phenocrysts and pores, matrix is fine-grained (2 to 5 microns) tridymite, smectite, and possibly a small amount of cristobalite bt111: deformation band with smectite and calcium carbonate fractured phenocrysts in matrix of clay (~ 1 micron) and carbonate crystallites (10-20 microns long, ~ 1 micron wide) that appear to be mixed together and then coated (clay?), clasts of carbonate crystallites present that have less clay intermixed, unaltered pumice observed with coating and crystallites growing in vesicles, fractures on surface of fault, roots in pores spaces with carbonate crystallites entwined at ends
Qbt2 crystallized welded	matrix consists of postdepositional crystals that are stubby but fibrous and others that are more rounded, pumice fragments have long fibers, but postdepositional crystals are not radial but are more aligned (an expression of welding?) and have larger rounded postdepositional crystals "adhered" to their surfaces	[fractures observed, no SE images]
Qbt1v (upper) crystallized nonwelded	matrix consists of postdepositional crystals that are stubby but fibrous and others that are more rounded, pumice fragments have long fibers (> 100 microns long and 1-5 microns wide) that are densely spaced and radial	[fractures observed, no SE images]
Qbt1v (middle) crystallized nonwelded	matrix consists of postdepostional crystals that are stubbier than in Qbt2 and Qbt1v (upper), but still fibrous, with others that are more rounded, pumice similar too, but fibrous post-depositional crystals have small (~ 1 micron) particles are other postdepositional crystals near ends, some pumice only has shorter postdepositional crystals (5 to 10 microns) replacing glass only (no growth into vesicles)	[fractures observed, no SE images]
Qbt1v (colonnade) crystallized nonwelded	matrix consists of postdepositional crystals that are similar to those in Qbt1v (middle), but the fibrous postdepositional crystals are narrower (~ 1 micron), pumice is also similar but some particles or postdepositional crystals that are near fibrous postdepositional crystal ends are more platey, fewer rounded postdepositional crystals in matrix (more fibrous postdepositional crystals and jagged postdepositional crystals)	[fractures observed, no SE images yet]
Qbt1g glassy nonwelded	large glass particles and phenocrysts (> 10 microns) with some fine-grained particles (<~ 1 micron) adhered to surfaces, pumice fragments evident and many have fragmental ash in vesicles	bt66: deformation band with calcium carbonate and some smectite inside fault: fine-grained glass and pumice fragments with fragmental ash on surface, no carbonate crystallites observed, just very fine-grained fragments (< 5 microns)

APPENDIX C

HYDROLOGIC DATA COLLECTION

Construction and Use of Air-Minipermeameter

An air-minipermeameter with the greatest versatility (compact and portable, able to provide accurate measurements under varying temperature conditions, etc.) and measurement range (at least three orders of magnitude) was replicated from the design of J. Matt Davis at the University of New Hampshire. In this design, a set of flow gauges (rotameters) and pressure gauges in a metal housing provide the tools and data to calculate the air permeability of a rock (Fig. C1). Air flows from a compressed gas cylinder (A in Fig. C1) equipped with a pressure regulator (B in Fig. C1), through tygon tubing and to a control valve (C in Fig. C1). This first control valve is set to either the high (1-15 psi) or low (0-1 psi) pressure setting, and air flows through the corresponding flow gauge (D in Fig. C1). Flow rate is measured by displacement of the float in the rotameter. Air then passes through another control valve (E in Fig. C1) that is set to direct air to either the high (Fa in Fig. C1) or low (Fb2 in Fig. C1) pressure gauge. If air is directed to the low pressure gauge, it first passes through a low-pressure regulator (Fb1 in Fig. C1) to ensure that the very low pressures (<1 psi) necessary for this gauge are not exceeded. The pressure of the gas as it moves through the minipermeameter and into the

rock is measured in one of these pressure gauges. Air leaves the minipermeameter (G in Fig. C1) via tygon tubing connected to the tip seal and an optional tip seal housing (a gun apparatus is used here; H in Fig. C1). The tip seal, when firmly placed against a clean and smooth rock surface, establishes a seal for airflow through the air-minipermeameter, and allows measurement of flow rate and pressure required for permeability calculations.

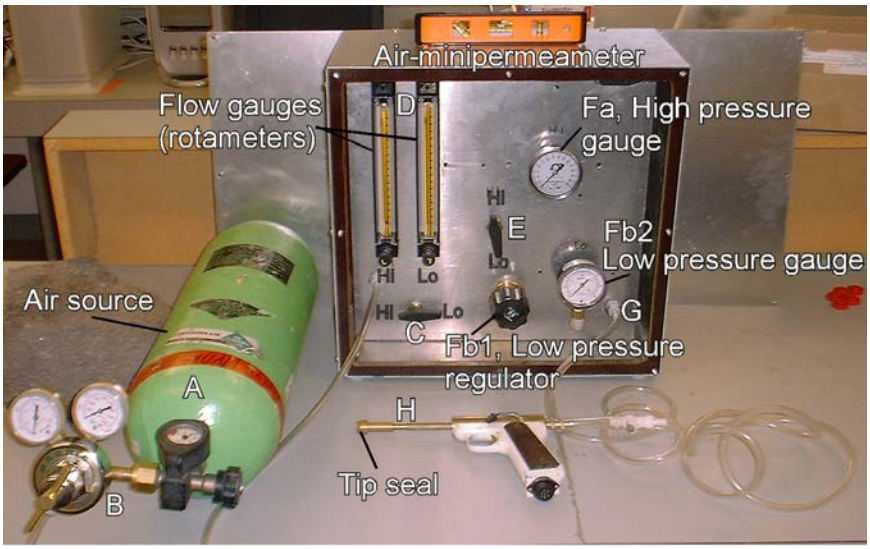

Figure C1. Photo of air-minipermeameter used for saturated permeability measurements.

Procedure Followed for Field and Laboratory Measurement of Air Permeability

1. Removed ≥2 mm of rock surface to expose fresh, unweathered material. Removed loose debris with a compressed air can.

2. Positioned minipermeameter and air tank on stable ground close to sample or outcrop. Leveled the minipermeameter using adjustable legs and level/compass.

3. Connected pressure regulator to air tank (use wrench to tighten fittings), regulator to minipermeameter via tygon tubing, and minipermeameter to tip seal attachment via tygon tubing.

4. Noted time, temperature, atmospheric pressure, and location/outcrop/sample details.

5. Measured permeability of standards

    a. opened air tank valve and set pressure regulator to ≤15 psi (if using high pressures) or <1 psi (if using low pressures)

b. tested air flow by applying tip seal to metal casing of minipermeameter or hand (pressure gauge should indicate the same pressure that is set on air tank regulator)
c. pressed tip seal firmly against the standard
d. allowed float in rotameter (flow gauge) to stabilize; [note: if float did not stabilize or could not be adjusted to give a reading, the controls valves were switched to the alternate pressure system (i.e., high or low)]
e. read flow rate (mm) and pressure (psi for high pressures, inches water for low pressures)

6. Measured permeability of sample or outcrop following steps 5c-e.

Calculation of Permeability

The following data must be obtained at the time of measurement in order to calculate permeability:

1. flow rate (mm)
2. gauge pressure (psi)
3. atmospheric pressure (Pa)
4. air temperature
5. inner and outer radius of tip seal

From the flow rate, gauge pressure, and atmospheric pressure data, flow (m^3/s) and pressure (Pa) are computed in an excel spreadsheet according to equations (1) and (2) in Fig. C2 (e.g., Suboor and Heller, 1995). Temperature is used to calculate air viscosity (mu; Fig. C3). Tip seal geometry is used to derive the geometric factor (G_o, e.g., Tidwell and Wilson, 1997). From these quantities, permeability is calculated according to equation (3) in Fig. C2.

Permeability measurements with Davis-clone permeameter

Date, Location:

Measurements by:

Protolith: Fault:

Constants, parameters for calculating permeability

μ=	viscosity of air (Pa*s)	*for __ C*
p0=	atmospheric pressure {Pa}	*Pa*
bd=	dimensionless tip seal radius (b/a)	4.1667 *large tip seal* 2.0833 *small tip seal*
Go(bd)=	geometric factor *(from Tidwell & Wilson, 1997)*	5.099 *small tip seal* 4.432 *large tip seal*
a=	radius of tip seal orifice {m}	0.003 *small tip seal* 0.006 *large tip seal*

Time	Temp (ºC)	Tip seal 0=small 1=large	Sample	Sample point or description	Flow (mm)	Fgauge 0=Lo 1=Hi	Pressure (psi)	Pgauge 0=Lo 1=Hi	Calculated flow (m^3/s)	Calculated pressure (Pa)	k(m^2)	k(darcy)

(1) Calculated flow eqn: IF(F70 = 1, (0.0195*E70 + 0.000003*(E70^2) - 0.0000003*(E70^3) + 0.0000000009*(E70^4))* 0.00001667, (0.0011*E70-0.000005*(E70^2) + 0.0000001*(E70^3) - 0.0000000003*(E70^4)) * 0.00001667)

(2) Calculated pressure eqn: IF(H70=1, p0 + (0.9402*G70+0.022*(G70^2)-0.002*(G70^3)-0.00005*(G70^4))*6895, p0 + (1.1725*G70-0.0384*(G70^2)+0.0035*(G70^3) - 0.0001*(G70^4)+0.000002*(G70^5))*249.089)

(3) Calculated k (m^2) =IF(C20=1,2*$J20*mu*$K20/(a*g0*($K20^2-p0^2)),2*$J20*mu*$K20/(asmall*g0small*($K20^2-p0^2)))

(4) Calculated k (darcy) =M20/0.000000000001

Figure C2. Example spreadsheet showing constants, parameters, and equations used for calculating permeability using an air-minipermeameter. Equation (1) is calculated flow equation, where F70 is the flow meter index and E70 is the flow measured in mm. Equation (2) is the calculated pressure equation, where H70 is the pressure gauge index and G70 is the pressure measured in psi. Equations (1) and (2) are polynomial fits to calibration data given in Tables C1 and C2, respectively. Equation (3) is the calculated permeability equation, after Goggin et al. (1988), where C20 is the tip seal index, J20 is the calculated flow in m^3/s, mu is air viscosity in Pa·s, K20 is the calculated pressure in Pa, a is the inner tip seal radius, g0 is the geometric factor, and p0 is atmospheric pressure in Pa. Equation (4) is the calculated permeability equation to convert permeability in m^2 to darcies.

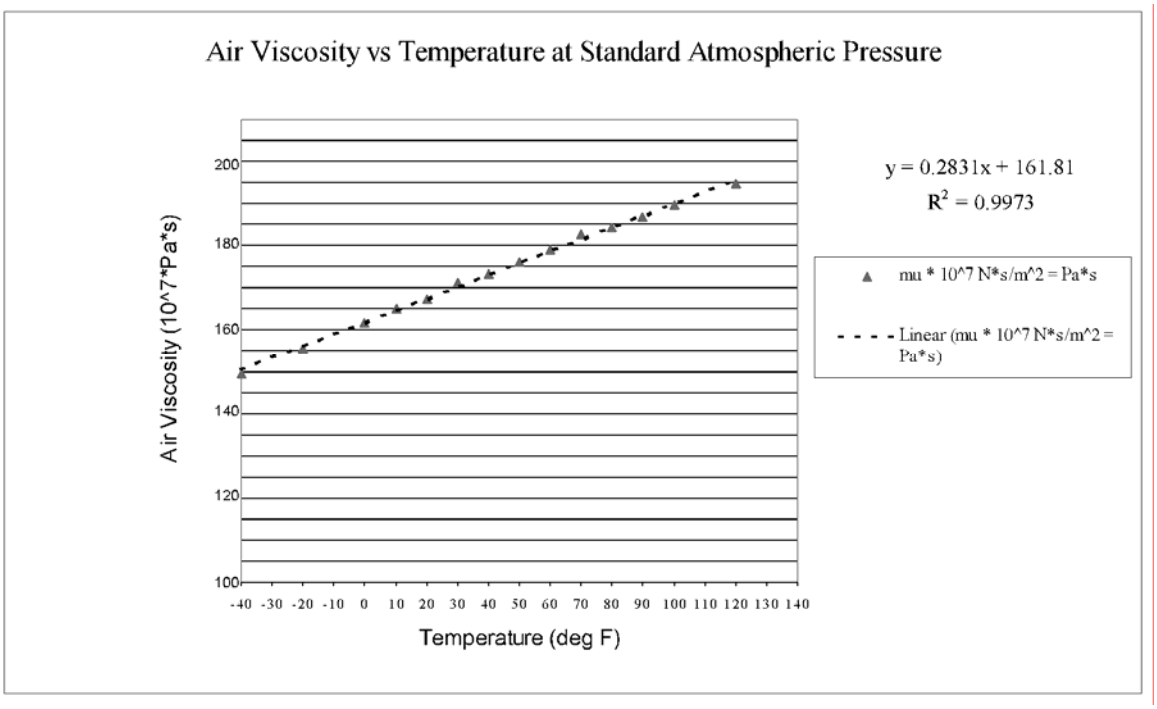

Figure C3. Relationship between temperature and air viscosity at standard atmospheric pressure. After Daugherty et al. (1985).

Source of Input Variables

Temperature: Casio alti-thermo watch readings (lab and field) and Los Alamos National Weather records (field only).

Atmospheric pressure: Casio alti-thermo watch readings (lab and field) and Los Alamos National Weather records (field only).

Tip seal radius: measurement in mm by ruler with silicone rubber in place and not compressed against a rock surface.

Flow rate: measured as the height of the center of float in the rotameter (flow gauge) in the air-minipermeameter during airflow.

Gauge pressure: measured from pressure gauge in air-minipermeameter during air flow.

Corrections to Input Variables

Temperature and atmospheric pressure data both from watch readings and from Los Alamos National Laboratory weather reports were within expected ranges, and

therefore were not corrected. The tip seal orifice is smaller when compressed against the rock surface (0.25cm) than when uncompressed (0.31 cm). This difference of 0.06 cm was not incorporated as a correction since it biases all samples the same. Flow and gauge pressure measurements required calibration of each gauge.

Calibration of Flow Gauges

Two Omega flow gauges were used in the design of the air-minipermeameter in order to measure airflow through materials with a wide range in permeability (i.e., at least three orders of magnitude). A low flow gauge was used in the high-pressure system (labeled hi, serial # 092-04-N, on minipermeameter), and a high flow gauge was used in the low-pressure system (labeled lo, serial # N062-01). Calibration of both flow gauges was performed against a Bios DryCal DC Lite Primary Flow Meter (Model #DCL-M) under the direction of Mark Cal and Justin Prien of the Environmental Engineering Department at New Mexico Tech. Airflow accuracy on an average of >3 readings, as performed for this calibration, was $\pm$ 1%. Calibration data for each flow meter and polynomial fits to these data are shown in Table C1 and Fig. C4, respectively. Polynomial fits to the curves were used in the calculation of the flow equation (equation (1) in Fig. C2).

Table C1. Data used in flow gauge (rotameter) calibrations.

Flow reading (mm)	Hi flow rate (L/min)	Lo flow rate (L/min)
150	2.306	0.2834
120	1.978	0.1969
90	1.599	0.1257
60	1.11	0.0716
30	0.5841	0.033

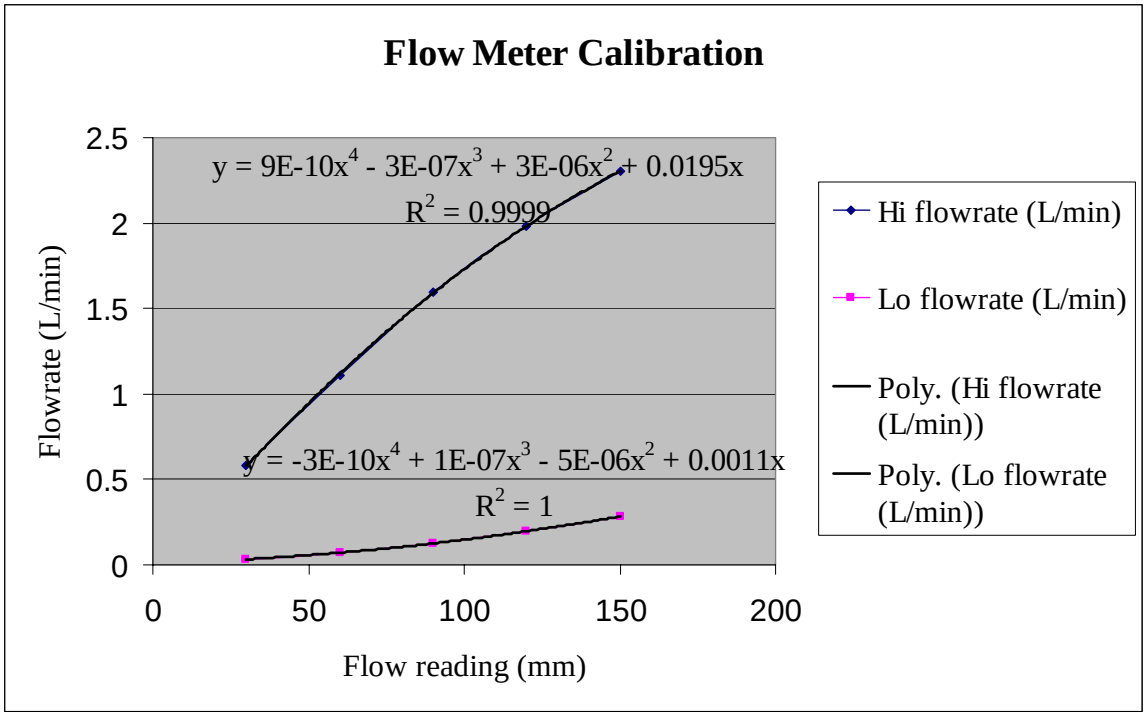

Figure C4. Polynomial fit to calibration curves for high and low flow gauges.

Calibration of Pressure Gauges

Calibration of both pressure gauges was performed against an ISCO Pump Controller (Series D Model 500D) Syringe Pump equipped with a Honeywell Transducer, (Model STD120-E1H) under the direction of Bob Svec at the Petroleum Research and Recovery Center at New Mexico Tech. Nitrogen gas was used in these calibrations. Calibration data and polynomial fits to curves for each gauge are given in Table C2 and Fig. C5, respectively. The equations describing this polynomial fit were used as a calibration factor for calculating pressure (equation (2) in Fig. C2).

Table C2. Data used in calibration of pressure gauges.

Reading #	Lo pressure gauge reading (psi)	Transducer reading (psi)	Hi pressure gauge reading (inches H_2O)	Transducer reading (inches H_2O)
1	2.1	2.06	5.25	5.49
2	4	3.99	10.5	10.78
3	6	6.09	15.5	15.8
4	8	8.15	20	20.5
5	10.1	10.27	25.5	25.7
6	12.2	12.38	30.25	30.4
7	14	14.15		

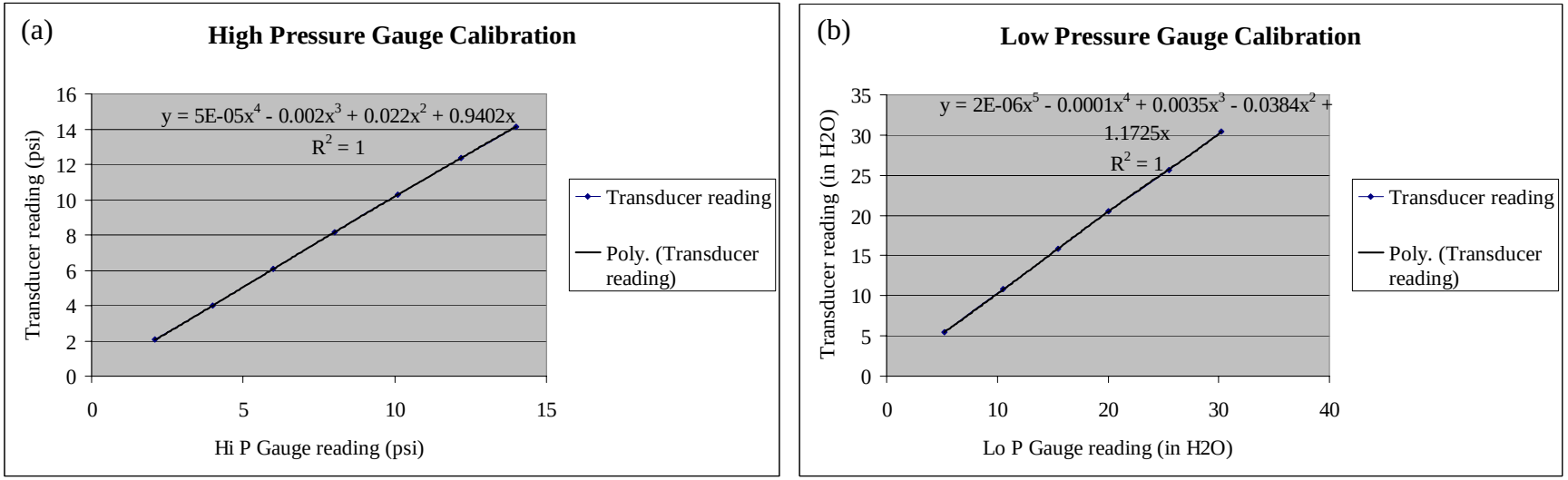

Figure C5. Calibration curves for (a) high pressure gauge and (b) low pressure gauge.

Permeability Data for all Samples/Outcrop Locations

Air permeability was measured for a suite of samples in the lab (Figs. C6, C7 and C10) and at selected outcrop sites (Figs. C8, C9, C11, and C12). All data collected for a given date and location are given in the following figures. Lab or outcrop location is given in the header of each figure, along with constants and parameters used for calculating permeability. Sample numbers or outcrop descriptions are given within the datasheet of each figure. A summary of permeability data, organized by ignimbrite protolith and fault type, is given in Table C3. Table C4 contains the values of permeability used to calculate log(k) in the box plots of Fig. 5.7.

Permeability measurements with Davis-clone permeameter

July 10, 2003, Location: msec220 lab ,NMT, Socorro, NM

Measurements by: Jen Wilson

Protolith: Fault:

Constants, parameters for calculating permeability

μ=	viscosity of air (Pa*s)	1.82E-05	*for 22.2 C*
p0=	atmospheric pressure {Pa}	102482.897	*Pa*
bd=	dimensionless tip seal radius (b/a)	4.1667	*large tip seal*
		2.08333	*small tip seal*
Go(bd)=	geometric factor *(from Tidwell & Wilson, 1997)*	5.099	*small tip seal*
		4.432	*large tip seal*
a=	radius of tip seal orifice {m}	0.003	*small tip seal*
		0.006	*large tip seal*

Time	Temp (oC)	Tip seal 0=sml, 1=larg	Sample	Sample point or description	flow (mm)	Fgauge 0=L,1=H	pressure (psi)	Pgauge 0=L,1=H	calculated flow (m^3/s)	calculated pressure (Pa)		k(m^2)	k(darcy)
355pm	23.8	0	standard1	(pink ignimbrite)	15.5	1	7.4	1	5.03277E-06	152139.4401		1.44102E-13	0.14410
355pm	23.8	0	standard2	(orange ignimbrite)	17	1	7.3	1	5.51724E-06	151546.4402		1.59632E-13	0.15963
355pm	23.8	0	standard3	(gray ignimbrite)	19	1	7.2	1	6.16194E-06	150948.2295		1.80198E-13	0.18020
355pm	23.8	0	standard4	(brown sandstone)	23	1	7	1	7.4463E-06	149736.7455		2.22612E-13	0.22261
355pm	23.8	0	standard5	(Massilon sandstone)	97	1	2.6	1	2.87658E-05	120105.1597		2.09589E-12	2.09589
405pm	23.8	1	BB7	HW-Calico Hills	94	1	1.8	1	2.80156E-05	114559.1527		1.67612E-12	1.67612
405pm	23.8	1	BB7	HW-Base Surge	64	1	3.9	1	1.99497E-05	129174.7853		5.70478E-13	0.57048
405pm	23.8	1	BB7	HW-Topopah Spring	13.5	1	6.1	1	4.38569E-06	144064.2207		8.43618E-14	0.08436
405pm	23.8	1	BB7	DB-normal	36	1	5.4	1	1.1559E-05	139448.0728		2.46717E-13	0.24672
405pm	23.8	1	BB7	DB-parallel (CH/CH)	50	1	4.6	1	1.58469E-05	134016.3573		3.89809E-13	0.38981
405pm	23.8	1	BB7	DB-parallel (BS/CH)	70	1	3.4	1	2.16445E-05	125689.4699		7.0327E-13	0.70327
405pm	23.8	1	BB7	FW-Calico Hills	66	1	3.6	1	2.0519E-05	127085.153		6.31998E-13	0.63200
405pm	23.8	1	BB7	FW-Base Surge	64	1	3.8	1	1.99497E-05	128478.9111		5.84349E-13	0.58435
405pm	23.8	1	BB7	FW-Topopah Spring	49	1	4.6	1	1.55464E-05	134016.3573		3.82416E-13	0.38242
415pm	23.8	0	BB7	HW-Calico Hills	62	1	2	1	1.93761E-05	115939.1792		1.81874E-12	1.81874
415pm	23.8	0	BB7	HW-Base Surge	34	1	4.6	1	1.09335E-05	134016.3573		4.67532E-13	0.46753
415pm	23.8	0	BB7	HW-Topopah Spring	13	1	5.3	1	4.22374E-06	138777.0299		1.5929E-13	0.15929
415pm	23.8	0	BB7	DB-normal	28	1	4.8	1	9.04047E-06	135386.6227		3.72116E-13	0.37212
415pm	23.8	0	BB7	DB-parallel (CH/CH)	16	1	5.2	1	5.19434E-06	138103.4734		1.99186E-13	0.19919
415pm	23.8	0	BB7	DB-parallel (BS/CH)	21	1	5.1	1	6.80502E-06	137427.5294		2.65442E-13	0.26544
415pm	23.8	0	BB7	FW-Calico Hills	68	1	3	1	2.1084E-05	122895.8895		1.34019E-12	1.34019
415pm	23.8	0	BB7	FW-Base Surge	60	1	3.4	1	1.87982E-05	125689.4699		1.06178E-12	1.06178
415pm	23.8	0	BB7	FW-Topopah Spring	36	1	4.7	1	1.1559E-05	134702.3745		4.84825E-13	0.48483

Figure C6. Permeability datasheet for samples measured in the lab, July 10, 2003. BB7 from Busted Butte, NV (Appendix A). HW = hanging wall, DB = deformation band, CH = Calico Hills Tuff, BS = base surge deposit (see Appendix A), FW = footwall.

Permeability measurements with Davis-clone permeameter

July 23, 2003, Location: msec220 lab ,NMT, Socorro, NM

Measurements by: Jen Wilson

Protolith: Fault:

Constants, parameters for calculating permeability

μ=	viscosity of air (Pa*s)	1.82E-05	for 22.2 C
p0=	atmospheric pressure {Pa}	85844.9	*Pa*
bd=	dimensionless tip seal radius (b/a)	4.1667	*large tip seal*
		2.08333	*small tip seal*
Go(bd)=	geometric factor *(from Tidwell & Wilson, 1997)*	5.099	*small tip seal*
		4.432	*large tip seal*
a=	radius of tip seal orifice {m}	0.003	*small tip seal*
		0.006	*large tip seal*

Time	Temp (oC)	Tip seal 0=small, 1=large	Sample	Sample point or description	flow (mm)	flow gauge 0=Lo,1=Hi	pressure (psi)	pressure gauge 0=Lo,1=Hi	calculated flow (m^3/s)	calculated pressure (Pa)		k(m^2)
206pm	32.3	0	standard1	(pink ignimbrite)	5	1	6.2	1	1.62596E-06	128072.5519		5.48552E-14
	32.3	0	standard2	(orange ignimbrite)	5	1	7.0	1	1.62596E-06	133098.7841		4.97748E-14
	32.3	0	standard3	(gray ignimbrite)	6	1	5.6	1	1.95113E-06	124144.1477		7.16673E-14
	32.3	0	standard4	(brown sandstone)	10	1	5.6	1	3.2508E-06	124144.1477		1.19406E-13
	32.3	0	standard5	(Massilon sandstone)	106	1	2.6	1	3.09566E-05	103467.1983		2.28461E-12
	32.3	0	bt48	Qbt1g protolith (Loc. 17)	75	1	4.0	1	2.30261E-05	113231.8758		1.13794E-12
	32.3	0	bt18	Qbt1g ashy protolith (Loc. 8)	82	1	3.5	1	2.49125E-05	109749.5345		1.39148E-12
	32.3	0	bt83	Qbt1v protolith (Loc. 27)	11	1	5.6	1	3.57533E-06	124144.1477		1.31326E-13
	32.3	0	bt98	Qbt2 protolith (Loc. 28)	36	1	5.0	1	1.1559E-05	120111.3621		4.68119E-13
	32.3	0	bt126	Qbt3 protolith (Loc. 2)	40	1	5.0	1	1.2801E-05	120111.3621		5.18415E-13
	32.3	0	bt71	Qbt3 protolith (Loc. 22)	53	1	4.6	1	1.67428E-05	117378.3959		7.29735E-13
	32.3	0	bt116	Qbt3 protolith (Loc. 16)	71	1	3.0	1	2.19231E-05	106257.9281		1.41357E-12
	32.3	0	bt116	Qbt3 protolith (Loc. 16)	71	1	3.0	1	2.19231E-05	106257.9281		1.41357E-12
	32.3	0	bt116	Qbt3 protolith (Loc. 16)	83	1	1.0	1	2.51774E-05	92465.17005		4.69283E-12
	32.3	0	bt116	Qbt3 protolith (Loc. 16)	80	1	1.6	1	2.43793E-05	96546.80541		2.86939E-12
	32.3	0	bt123	Qbt3t protolith (Loc. 34)	4	1	5.8	1	1.30074E-06	125466.5949		4.6383E-14
	32.3	0	bt118	Qbt4 protolith (Loc. 32)	25	1	5.4	1	8.0856E-06	122810.1114		3.06351E-13
	32.3	0	bt9	db w/clay (db-normal; Qbt1g; Loc. 6)	59	1	7.4	1	1.85076E-05	135501.4786		5.42926E-13
	32.3	0	bt9	db w/clay (db-||; Qbt1g; Loc. 6)	63	1	6.8	1	1.96634E-05	131868.1584		6.15791E-13
	32.3	0	bt8	db w/clay (db-normal; Qbt1g; Loc. 6)	15	1	10.6	1	4.87111E-06	150828.7216		1.13672E-13
	32.3	0	bt5	db w/clay (db-normal; Qbt1g; Loc. 6)	21	1	10.0	1	6.80502E-06	148603.2258		1.63544E-13
	32.3	0	bt5	db w/clay (db-normal; Qbt1g; Loc. 6)	37	1	8.0	1	1.18707E-05	138941.9518		3.28823E-13
	32.3	0	bt125	porous db zone (db-||, vert.; Qbt3; Loc. 2)	40	1	7.5	1	1.2801E-05	136089.124		3.7175E-13
	32.3	0	bt125	vfg db zone (db-||, vert.; Qbt3; Loc. 2)	17	1	10.2	1	5.51724E-06	149384.346		1.31216E-13
	32.3	0	bt125	vfg db zone (db-normal, horiz.; Qbt3; Loc. 2)	28	1	9.0	1	9.04047E-06	144161.1221		2.3121E-13
	32.3	0	bt125	vfg db zone (db-||, horiz.; Qbt3; Loc. 2)	17	1	10.2	1	5.51724E-06	149384.346		1.31216E-13
	32.3	0	bt116	db w/clay (db-||; Qbt3; Loc. 16)	65	1	4.0	1	2.02349E-05	113231.8758		1E-12
	32.3	0	bt123	fracture (<1mm wide; Qbt3t; Loc. 34)	96	1	2.8	1	2.85168E-05	104861.7783		1.96205E-12
	32.3	0	bt123	fracture (1mm wide; Qbt3t, Loc. 34)	127	1	1.6	1	3.57489E-05	96546.80541		4.20756E-12
	32.3	0	bt123	fracture (1mm wide; Qbt3t; Loc. 34)	122	1	1.9	1	3.46449E-05	98610.54837		3.45243E-12
	32.3	0	bt123	fracture (>1mm wide; Qbt3t; Loc. 34)	114	1	0.5	1	3.28321E-05	89122.4525		1.21417E-11
	32.3	0	bt117	db w/clay (db-normal; Qbt4; Loc. 32)	13	1	5.6	1	4.22374E-06	124144.1477		1.55143E-13

Figure C7. Permeability datasheet for samples measured in the lab, July 23, 2003. Qbt = Bandelier Tuff, unit designations given in Figure 16b; location numbers refer to outcrop locations given in Table A1; db = deformation band; db-|| = parallel to deformation band; vert. = vertical, horiz. = horizontal.

Permeability measurements with Davis-clone permeameter

August 6, 2003, Location: NM4, just S of Pajarito Acres, White Rock (Location 5)

Measurements by: Jen Wilson / Emily Schultz

Protolith: Qbt1g (nonwelded, glassy, ash-rich)

Fault: carbonate-cemented deformation bands

Constants, parameters for calculating permeability

μ=	viscosity of air (Pa*s)	1.83E-05	for 22.9 C
p0=	atmospheric pressure {Pa}	82246.5	*Pa*
bd=	dimensionless tip seal radius (b/a)	4.1667	*large tip seal*
		2.08333	*small tip seal*
Go(bd)=	geometric factor	5.099	*small tip seal*
	(from Tidwell & Wilson, 1997)	4.432	*large tip seal*
a=	radius of tip seal orifice {m}	0.003	*small tip seal*
		0.006	*large tip seal*

Time	Temp (oC)	Tip seal 0=small, 1=large	Sample	Sample point or description	flow (mm)	flow gauge 0=Lo,1=Hi	pressure (psi)	pressure gauge 0=Lo,1=Hi	calculated flow (m^3/s)	calculated pressure (Pa)		k(m^2)
930am	31.1	0	standard1	(pink ignimbrite)	5	1	6.4	1	1.62596E-06	125755.5077		5.39109E-14
	31.1	0	standard2	(orange ignimbrite)	7	1	6.5	1	2.27623E-06	126390.337		7.45341E-14
	31.1	0	standard3	(gray ignimbrite)	10	1	6.2	1	3.2508E-06	124474.1161		1.10605E-13
	31.1	0	standard4	(brown sandstone)	12	1	6.1	1	3.89965E-06	123827.8234		1.34465E-13
	31.1	0	standard5	(Massilon sandstone)	66	1	1.4	1	2.0519E-05	91580.39885		2.76354E-12
9am	28.7	0		HW protolith (30cm from fault)	30	1	5.4	1	9.67408E-06	119211.6756		3.6952E-13
	28.7	0		HW protolith (13cm from fault)	30	1	5.2	1	9.67408E-06	117867.0761		3.81691E-13
	28.7	0		carbonate-cemented db (normal)	8	1	6.7	1	2.60122E-06	127647.5817		8.314E-14
	28.7	0		carbonate-cemented db (parallel)	45	1	4.0	1	1.4335E-05	109633.44		7.13599E-13
	28.7	0		FW protolith (22cm from fault)	38	1	4.4	1	1.21816E-05	112403.103		5.56585E-13
	28.7	0		FW protolith (38cm from fault)	40	1	4.4	1	1.2801E-05	112403.103		5.84886E-13

Figure C8. Permeability datasheet for carbonate-cemented deformation bands measured at outcrop location 5, August 6, 2003. HW = hanging wall, db = deformation band, FW = footwall.

Permeability measurements with Davis-clone permeameter

August 6, 2003, Location: LANSCE, TA-53 (Location 2)

Measurements by: Jen Wilson / Laurel Goodwin

Protolith: Qbt3 (nonwelded, devitrified & vapor-phase crystallized)

Fault: deformation band zone & fractures

Constants, parameters for calculating permeability

μ=	viscosity of air (Pa*s)	1.84E-05	for 27.1 C
p0=	atmospheric pressure {Pa}	82183.5	*Pa*
bd=	dimensionless tip seal radius (b/a)	4.1667	*large tip seal*
		2.08333	*small tip seal*
Go(bd)=	geometric factor	5.099	*small tip seal*
	(from Tidwell & Wilson, 1997)	4.432	*large tip seal*
a=	radius of tip seal orifice {m}	0.003	*small tip seal*
		0.006	*large tip seal*

Time	Temp (oC)	Tip seal 0=small, 1=large	Sample	Sample point or description	flow (mm)	flow gauge 0=Lo,1=Hi	pressure (psi)	pressure gauge 0=Lo,1=Hi	calculated flow (m^3/s)	calculated pressure (Pa)		k(m^2)
1115am	37.7	0	standard1	(pink ignimbrite)	5	1	6.0	1	1.62596E-06	123114.978		5.73085E-14
	37.7	0	standard2	(orange ignimbrite)	6	1	6.0	1	1.95113E-06	123114.978		6.87694E-14
	37.7	0	standard3	(gray ignimbrite)	7	1	5.9	1	2.27623E-06	122461.7126		8.13552E-14
	37.7	0	standard4	(brown sandstone)	12	1	5.8	1	3.89965E-06	121805.1591		1.41382E-13
	37.7	0	standard5	(Massilon sandstone)	60	1	1.6	1	1.87982E-05	92885.36961		2.242E-12
1045am	35.1	0	db fault	1, undeformed zone in fault	37	1	4.5	1	1.18707E-05	113029.2952		5.36048E-13
	35.1	0	db fault	2, undeformed zone in fault	34	1	4.6	1	1.09335E-05	113716.9601		4.84194E-13
	35.1	0	db fault	3a, W side of db zone	34	1	5.0	1	1.09335E-05	116449.9263		4.50007E-13
	35.1	0	db fault	3b, W side of db zone	40.5	1	4.0	1	1.29553E-05	109570.44		6.50272E-13
	35.1	0	db fault	4, W side of db zone	37.5	1	4.2	1	1.20262E-05	110957.6142		5.77631E-13
	35.1	0	db fault	5, porous zone in fault	29	1	5.0	1	9.35759E-06	116449.9263		3.85144E-13
	35.1	0	db fault	6, porous zone in fault	70	1	1.0	1	2.16445E-05	88803.73425		4.08491E-12
	35.1	0	db fault	7, porous zone in fault	37	1	4.2	1	1.18707E-05	110957.6142		5.70161E-13
	35.1	0	db fault	8, porous zone in fault	27.5	1	5.0	1	8.88168E-06	116449.9263		3.65557E-13
	35.1	0	not taken	9, porous zone in fault (pumice)								
	35.1	0	db fault	10, porous zone in fault	46	1	3.2	1	1.46392E-05	103993.358		9.01958E-13
	35.1	0	db fault	11, E side of db zone (vfg)	8	1	6.6	1	2.60122E-06	126958.0739		8.48413E-14
	35.1	0	db fault	12, E side of db zone (vfg)	17.5	1	6.0	1	5.67856E-06	122788.7645		2.0154E-13
	35.1	0	db fault	13, protolith (E side)	36.5	1	4.4	1	1.17149E-05	112340.103		5.39712E-13
	35.1	0	db fault	14, protolith (E side)	30.5	1	4.9	1	9.8321E-06	115769.5828		4.1187E-13
	35.1	0	db fault	15, protolith (W side)	41.5	1	3.8	1	1.32634E-05	108179.5139		6.97512E-13
	35.1	0	db fault	16, protolith (W side)	41.5	1	3.8	1	1.32634E-05	108179.5139		6.97512E-13
	35.1	0	db fault	17, db zone (vfg, normal to fault)	9.5	1	6.4	1	3.08847E-06	125692.5077		1.03255E-13
	35.1	0	db fault	18, db zone (vfg, parallel to fault)	10.5	1	6.3	1	3.41309E-06	125053.7223		1.15575E-13
	35.1	0	not taken	19, protolith (at fault edge, normal)								
	35.1	0	db fault	20, lichen & weathered protolith	18	1	5.4	1	5.83978E-06	119148.6756		2.24917E-13
	35.1	0	db fault	21, fracture surface, weath. Only	23	1	5.0	1	7.4463E-06	116449.9263		3.06479E-13
	35.1	0	db fault	22, fresh surface protolith	30	1	4.4	1	9.67408E-06	112340.103		4.45689E-13
	35.1	0	db fault	23, db zone (oblique)	6.5	1	6.2	1	2.11369E-06	124411.1161		7.25147E-14
	35.1	0	db fault	24, db zone (oblique)	5	1	6.4	1	1.62596E-06	125692.5077		5.43597E-14
	35.1	0	db fault	25, protolith (W flt edge, normal)	42.5	1	3.2	1	1.35706E-05	103993.358		8.3612E-13

Figure C9. Permeability datasheet for unaltered deformation bands measured at outcrop location 2, August 6, 2003. db = deformation band, vfg = very fine-grained (dominated by clay-sized or smaller ignimbrite fragments).

Permeability measurements with Davis-clone permeameter

August12, 2003, Location: msec220 lab ,NMT, Socorro, NM

Measurements by: Jen Wilson

Protolith: Fault:

Constants, parameters for calculating permeability

μ=	viscosity of air (Pa*s)	1.82E-05 for 22.2 C
p0=	atmospheric pressure {Pa}	86183.57 *Pa*
bd=	dimensionless tip seal radius (b/a)	4.1667 *large tip seal* 2.08333 *small tip seal*
Go(bd)=	geometric factor *(from Tidwell & Wilson, 1997)*	5.099 *small tip seal* 4.432 *large tip seal*
a=	radius of tip seal orifice {m}	0.003 *small tip seal* 0.006 *large tip seal*

Time	Temp (oC)	Tip seal 0=small, 1=large	Sample	Sample point or description	flow (mm)	flow gauge 0=Lo,1=Hi	pressure (psi)	pressure gauge 0=Lo,1=Hi	calculated flow (m^3/s)	calculated pressure (Pa)		k(m^2)
748am	22.2	0	standard1	(pink ignimbrite)	5	1	6.6	1	1.62596E-06	130958.1485		5.2115E-14
	22.2	0	standard2	(orange ignimbrite)	13	1	6.0	1	4.22374E-06	127115.0526		1.46333E-13
	22.2	0	standard3	(gray ignimbrite)	8	1	6.4	1	2.60122E-06	129692.5823		8.5468E-14
	22.2	0	standard4	(brown sandstone)	10	1	6.2	1	3.2508E-06	128411.1907		1.09616E-13
	22.2	0	standard5	(Massilon sandstone)	64	1	1.9	1	1.99497E-05	98949.18717		1.98756E-12
	22.2	0	bt125	db zone (II, vert.; Qbt3; Loc. 2)	7	1	6.4	1	2.27623E-06	129692.5823		7.47897E-14
	22.2	0	bt125	db zone (II, vert.; Qbt3; Loc. 2)	6.5	1	6.4	1	2.11369E-06	129692.5823		6.94492E-14
	22.2	0	bt125	porous db zone (II, vert.; Qbt3; Loc. 2)	21	1	5.6	1	6.80502E-06	124482.7865		2.49833E-13
	22.2	0	bt125	porous db zone (II, vert.; Qbt3; Loc. 2)	18	1	5.7	1	5.83978E-06	125145.5234		2.11206E-13
	22.2	0	bt125	porous db zone (II, vert.; Qbt3; Loc. 2)	46	1	3.5	1	1.46392E-05	110088.1733		8.17361E-13
	22.2	0	bt125	db zone (II, horiz.; Qbt3; Loc. 2)	10	1	6.2	1	3.2508E-06	128411.1907		1.09616E-13
	22.2	0	bt125	db zone near edge (II, horiz.; Qbt3; Loc. 2)	47	1	3.4	1	1.49425E-05	109390.1473		8.5699E-13
	22.2	0	bt125	porous db zone (nml, horiz.; Qbt3; Loc. 2)	42	1	3.8	1	1.34171E-05	112179.5885		6.94545E-13
	22.2	0	bt125	porous db zone (nml, horiz.; Qbt3; Loc. 2)	36	1	4.3	1	1.1559E-05	115649.5777		5.34868E-13
	22.2	0	bt125	1mm wide db (nml, horiz.; Qbt3; Loc. 2)	30	1	4.8	1	9.67408E-06	119087.3001		4.0588E-13
	22.2	0	bt125	1mm wide db (nml, horiz.; Qbt3; Loc. 2)	32	1	4.8	1	1.03051E-05	119087.3001		4.32357E-13
	22.2	0	bt123	strongly welded (Qbt3t; Loc. 34)	5	1	6.4	1	1.62596E-06	129692.5823		5.3424E-14
	22.2	0	bt123	strongly welded (Qbt3t; Loc. 34)	5	1	6.5	1	1.62596E-06	130327.4116		5.27583E-14
	22.2	0	bt123	fracture (<1mm wide; Qbt3t; Loc. 34)	65	1	1.6	1	2.02349E-05	96885.44421		2.38112E-12
	22.2	0	bt123	fracture (1mm wide; Qbt3t; Loc. 34)	75	1	0.5	1	2.30261E-05	89461.0913		8.5147E-12
	22.2	0	bt118	cryst, nonw, fg protolith (Qbt4l; Loc. 32)	30	1	4.9	1	9.67408E-06	119769.6574		3.98588E-13
	22.2	0	bt118	cryst, nonw, fg protolith (Qbt4l; Loc. 32)	35	1	4.5	1	1.12466E-05	117029.3698		4.99649E-13
	22.2	0	bt117	db w/clay (db-normal; Qbt4l; Loc. 32)	18	1	5.8	1	5.83978E-06	125805.2337		2.08135E-13
	22.2	0	bt117	db w/clay (db-normal; Qbt4l; Loc. 32)	18	1	5.8	1	5.83978E-06	125475.765		2.09656E-13
	22.2	0	bt71	cryst, nonw protolith (Qbt3; Loc. 22)	35	1	4.5	1	1.12466E-05	117029.3698		4.99649E-13
	22.2	0	bt71	cryst, nonw protolith (Qbt3; Loc. 22)	43	1	3.8	1	1.37239E-05	112179.5885		7.10428E-13
	22.2	0	bt98	cryst, moderately welded (Qbt2; Loc. 28)	32	1	4.7	1	1.03051E-05	118403.0518		4.4047E-13
	22.2	0	bt98	cryst, moderately welded (Qbt2; Loc. 28)	18	1	5.4	1	5.83978E-06	123148.7502		2.21153E-13
	22.2	0	bt83	cryst, nonw (Qbt1v; Loc. 27)	14	1	6.0	1	4.54757E-06	127115.0526		1.57553E-13
	22.2	0	bt83	cryst, nonw (Qbt1v; Loc. 27)	17	1	5.8	1	5.51724E-06	125805.2337		1.96639E-13
	22.2	0	bt8	db w/clay (db-nml; Qbt1g; Loc. 6)	31	1	4.7	1	9.98995E-06	118403.0518		4.26998E-13
	22.2	0	bt8	db w/clay (db-nml; Qbt1g; Loc. 6)	27	1	5.0	1	8.72275E-06	120450.0009		3.5309E-13
	22.2	0	bt9	db w/clay (db-nml; Qbt1g; Loc. 6)	38	1	4.1	1	1.21816E-05	114264.6287		5.88429E-13
	22.2	0	bt9	db w/clay (db-nml; Qbt1g; Loc. 6)	27	1	5.0	1	8.72275E-06	120450.0009		3.5309E-13
	22.2	0	bt135	strongly welded (Qbt3t; Loc. 34)	5	1	6.4	1	1.62596E-06	129692.5823		5.3424E-14
	22.2	0	bt135	strongly welded (Qbt3t; Loc. 34)	5	1	6.4	1	1.62596E-06	129692.5823		5.3424E-14
	22.2	0	bt135	strongly welded (Qbt3t; Loc. 34)	5	1	6.4	1	1.62596E-06	129692.5823		5.3424E-14
	22.2	0	bt135	strongly welded (Qbt3t; Loc. 34)	5	1	6.4	1	1.62596E-06	129692.5823		5.3424E-14
	22.2	0	bt135	fracture (<1mm wide; Qbt3t; Loc. 34)	17	1	5.8	1	5.51724E-06	125805.2337		1.96639E-13
	22.2	0	bt135	fracture (1mm wide; Qbt3t; Loc. 34)	69	1	1.2	1	2.13648E-05	94156.67901		3.32908E-12
	22.2	0	bt18	glassy, nonw, ashy protolith (Qbt1g, Loc. 8)	51	1	3.0	1	1.61465E-05	106596.5669		1.04075E-12
	22.2	0	bt18	glassy, nonw, ashy protolith (Qbt1g, Loc. 8)	56	1	2.5	1	1.76298E-05	103109.3991		1.35007E-12
	22.2	0	bt18	glassy, nonw, wthrd protolith (Qbt1g, Loc. 8)	47	1	3.8	1	1.49425E-05	112179.5885		7.73508E-13
	22.2	0	bt18	unaltered db (db-nml; Qbt1g; Loc. 8)	16	1	5.9	1	5.19434E-06	126133.9132		1.83802E-13
	22.2	0	bt18	unaltered db (db-nml; Qbt1g; Loc. 8)	16	1	5.8	1	5.19434E-06	125805.2337		1.85131E-13
	22.2	0	bt18	wthrd db (db-nml; Qbt1g; Loc. 8)	39	1	4.0	1	1.24917E-05	113570.5146		6.1708E-13
	22.2	0	bt18	wthrd db (db-nml; Qbt1g; Loc. 8)	53	1	2.6	1	1.67428E-05	103805.8371		1.23525E-12

Figure C10. Permeability datasheet for samples measured in the lab, August 12, 2003. db = deformation band, || = parallel, vert = vertical, horiz = horizontal, nml = normal, adj. prot. = adjacent protolith, fg = fine-grained, cryst = crystallized, nonw = nonwelded, wthrd = weathered.

Permeability measurements with Davis-clone permeameter

September 18, 2003, Location: LANSCE, E of beamline

Measurements by: Jen Wilson

Protolith: Qbt3 (nonwelded, crystallized)

Fault: clay-enriched & carbonate-cemented deformation bands (or fractures?)

Constants, parameters for calculating permeability

μ=	viscosity of air (Pa*s)	1.78E-05 for 16.0 C
p0=	atmospheric pressure {Pa}	81784.5 *Pa*
bd=	dimensionless tip seal radius (b/a)	4.1667 *large tip seal*
		2.08333 *small tip seal*
Go(bd)=	geometric factor	5.099 *small tip seal*
	(from Tidwell & Wilson, 1997)	4.432 *large tip seal*
a=	radius of tip seal orifice {m}	0.003 *small tip seal*
		0.006 *large tip seal*

Time	Temp (oC)	Tip seal 0=small, 1=large	Sample	Sample point or description	flow (mm)	flow gauge 0=Lo,1=Hi	pressure (psi)	pressure gauge 0=Lo,1=Hi	calculated flow (m^3/s)	calculated pressure (Pa)		k(m^2)
1035am	32.3	0	standard1	(pink ignimbrite)	6	1	6.9	1	1.95113E-06	128117.1121		5.98183E-14
	32.3	0	standard2	(orange ignimbrite)	7	1	6.9	1	2.27623E-06	128117.1121		6.97853E-14
	32.3	0	standard3	(gray ignimbrite)	8	1	6.7	1	2.60122E-06	127185.5817		8.11538E-14
	32.3	0	standard4	(brown sandstone)	14	1	6.3	1	4.54757E-06	124654.7223		1.49068E-13
	32.3	0	standard5	(Massilon sandstone)	65	1	1.6	1	2.02349E-05	92486.36961		2.33528E-12
1015am	32.3	0		db w/clay (strike ||, horiz.)	55	1	2.6	1	1.73351E-05	99406.76251		1.25599E-12
	32.3	0		db w/clay (strike ||, horiz.)	55	1	2.8	1	1.73351E-05	100801.3425		1.1712E-12
	32.3	0		db w/clay (strike ||, horiz.)	61	1	1.6	1	1.90876E-05	92486.36961		2.20287E-12
	32.3	0		db w/clay (strike ||, horiz.)	60	1	2.1	1	1.87982E-05	95932.66488		1.66915E-12
	32.3	0		db w/clay (db-normal, horiz.)	42	1	4.0	1	1.34171E-05	109171.44		6.51831E-13
	32.3	0		db w/clay (db-normal, horiz.)	53	1	2.8	1	1.67428E-05	100801.3425		1.13118E-12
	32.3	0		protolith (E of db, db-normal)	48	1	3.2	1	1.52449E-05	103594.358		9.09058E-13
	32.3	0		protolith (E of db, db-normal)	48	1	3.0	1	1.52449E-05	102197.4923		9.65444E-13
	32.3	0		protolith (W of db, db-normal)	52	1	2.0	1	1.64451E-05	95240.782		1.53018E-12
	32.3	0		protolith (W of db, db-normal)	49	1	3.0	1	1.55464E-05	102197.4923		9.84536E-13
	32.3	0		protolith (E of db, db-||, S-facing wall)	58	1	2.2	1	1.8216E-05	96625.6615		1.54704E-12
	32.3	0		protolith (E of db, db-||, S-facing wall)	52	1	2.6	1	1.64451E-05	99406.76251		1.19151E-12

Figure C11. Permeability datasheet for clay-rich deformation band fault measured at outcrop location 2, September 18, 2003. db = deformation band, strike || = strike-parallel, horiz = horizontal, db-|| = parallel to deformation band.

Permeability measurements with Davis-clone permeameter

September 18, 2003, Location: Golf Course trail, Los Alamos, near canyon bottom

Measurements by: Jen Wilson / Teryn Ebert

Protolith: Qbt3 (nonwelded, crystallized, no cristobalite)

Fault: clay-enriched (~ 2wt.% smectite) & phenocryst-rich deformation bands

Constants, parameters for calculating permeability

μ=	viscosity of air (Pa*s)	1.80E-05 for 18.4 C
p0=	atmospheric pressure {Pa}	81721.5 *Pa*
bd=	dimensionless tip seal radius (b/a)	4.1667 *large tip seal* 2.08333 *small tip seal*
Go(bd)=	geometric factor *(from Tidwell & Wilson, 1997)*	5.099 *small tip seal* 4.432 *large tip seal*
a=	radius of tip seal orifice {m}	0.003 *small tip seal* 0.006 *large tip seal*

Time	Temp (oC)	Tip seal 0=small, 1=large	Sample	Sample point or description	flow (mm)	flow gauge 0=Lo,1=Hi	pressure (psi)	pressure gauge 0=Lo,1=Hi	calculated flow (m^3/s)	calculated pressure (Pa)		k(m^2)
1pm	27.3	0	standard1	(pink ignimbrite)	9	1	7.0	1	2.92609E-06	128975.3483		8.92062E-14
	27.3	0	standard2	(orange ignimbrite)	15	1	6.8	1	4.87111E-06	127744.7226		1.51906E-13
	27.3	0	standard3	(gray ignimbrite)	10	1	6.9	1	3.2508E-06	128362.3579		1.00222E-13
	27.3	0	standard4	(brown sandstone)	16	1	6.6	1	5.19434E-06	126496.0739		1.65865E-13
	27.3	0	standard5	(Massilon sandstone)	74	1	1.6	1	2.2752E-05	92423.36961		2.65539E-12
1215pm	27.3	0		db w/clay (db-||)	64	1	2.6	1	1.99497E-05	99343.76251		1.46176E-12
	27.3	0		db w/clay (db-||)	64	1	2.6	1	1.99497E-05	99343.76251		1.46176E-12
	27.3	0		protolith (db-||)	55	1	3.4	1	1.73351E-05	104928.0727		9.88272E-13
	27.3	0		protolith (db-||)	72	1	1.6	1	2.22005E-05	92423.36961		2.59102E-12
	27.3	0		intersection of dbs w/clay (db-||)	59	1	3.0	1	1.85076E-05	102134.4923		1.18532E-12
	27.3	0		pheno-rich db (db-||), horizontal	78	1	1.0	1	2.38414E-05	88341.73425		4.40262E-12
	27.3	0		pheno-rich db (db-||), horizontal	64	1	2.4	1	1.99497E-05	97951.59306		1.57703E-12
	27.3	0		pheno-rich db (db-||), subvertical	62	1	2.6	1	1.93761E-05	99343.76251		1.41973E-12
	27.3	0		protolith (db-||)	62	1	2.4	1	1.93761E-05	97951.59306		1.53169E-12
	27.3	0		protolith (db-||)	63	1	2.4	1	1.96634E-05	97951.59306		1.5544E-12
	27.3	0		protolith (db-normal)	62	1	2.4	1	1.93761E-05	97951.59306		1.53169E-12
	27.3	0		protolith (db-normal)	67	1	1.8	1	2.08021E-05	93797.75547		2.1664E-12

Figure C12. Permeability datasheet for variably clay-rich deformation band faults measured at outcrop location 16, September 18, 2003. db = deformation band, db-|| = parallel to deformation band, pheno = phenocryst.

Table C3. Summary of permeability measurements organized by protolith and fault type.			
Protolith	Fault	k (m2)	Lab or Field
NW, G (Qbt1g), ash- & pumice-rich		1.13E-12	lab
	clay-rich db (flt-normal)	5.42E-13	lab
	clay-rich db (flt-normal)	5.88E-13	lab
	clay-rich db (flt-normal)	3.53E-13	lab
	clay-rich db (flt-parallel)	6.16E-13	lab
	clay-poor db (flt-normal)	1.14E-13	lab
	clay-poor db (flt-normal)	4.27E-13	lab
	clay-poor db (flt-normal)	3.53E-13	lab
	foliated clay db (flt-normal)	1.64E-13	lab
	foliated clay-rich gouge (flt-normal)	3.29E-13	lab
NW, G (Qbt1g), vfg ashy base		1.39E-12	lab
NW, G (Qbt1g), vfg ashy base		1.04E-12	lab
NW, G (Qbt1g), vfg ashy base		1.35E-12	lab
NW, G (Qbt1g), vfg ashy base, weathered		7.74E-13	lab
	unaltered db (flt-normal)	1.84E-13	lab
	unaltered db (flt-normal)	1.85E-13	lab
	altered portion of db (flt-normal)	6.17E-13	lab
	altered portion of db (flt-normal)	1.24E-12	lab
NW, G (Qbt1g), ashy base		3.70E-13	field
NW, G (Qbt1g), ashy base		3.82E-13	field
NW, G (Qbt1g), ashy base		5.57E-13	field
NW, G (Qbt1g), ashy base		5.85E-13	field
	carbonate-cemented (flt-normal)	8.31E-14	field
	carbonate-cemented (flt-parallel)	7.14E-13	field
NW, DV (Qbt1v)		1.31E-13	lab
NW, DV (Qbt1v)		1.58E-13	lab
NW, DV (Qbt1v)		1.97E-13	lab
welded, DV (Qbt2)		4.68E-13	lab
welded, DV (Qbt2)		4.40E-13	lab
welded, DV (Qbt2)		2.21E-13	lab
NW, DV- & VP (Qbt3), w/crist. & trid.		5.18E-13	lab
NW, DV- & VP (Qbt3), w/crist. & trid.		5.00E-13	lab
NW, DV- & VP (Qbt3), w/crist. & trid.		7.10E-13	lab
	porous cataclastic zone (flt-parallel), vert	3.72E-13	lab
	porous cataclastic zone (flt-parallel), vert	2.50E-13	lab
	porous cataclastic zone (flt-parallel), vert	2.11E-13	lab
	porous cataclastic zone (flt-parallel), vert	8.17E-13	lab
	porous cataclastic zone (flt-nrml), horiz	6.95E-13	lab
	porous cataclastic zone (flt-nrml), horiz	5.35E-13	lab
	vfg zone of dbs (flt-parallel), vert	1.31E-13	lab
	vfg zone of dbs (flt-parallel), vert	7.48E-14	lab
	vfg zone of dbs (flt-parallel), vert	6.94E-14	lab
	vfg zone of dbs (flt-normal), horiz	2.31E-13	lab
	vfg zone of dbs (flt-parallel), horiz	1.31E-13	lab
	vfg zone of dbs (flt-parallel), horiz	1.10E-13	lab
	vfg zone of dbs (flt-parallel), horiz, edge	8.57E-13	lab
	1mm thick prot to fault (flt-nrml)	4.06E-13	lab
	1mm thick prot to fault (flt-nrml)	4.32E-13	lab
NW, DV- & VP (Qbt3), w/crist. & trid.		5.40E-13	field
NW, DV- & VP (Qbt3), w/crist. & trid.		4.12E-13	field
NW, DV- & VP (Qbt3), w/crist. & trid.		6.98E-13	field
NW, DV- & VP (Qbt3), w/crist. & trid.		6.98E-13	field
NW, DV- & VP (Qbt3), w/crist. & trid.		4.45E-13	field
NW, DV- & VP (Qbt3), w/crist. & trid.		8.36E-13	field
same except lichen-covered & weathered surface		2.25E-13	field
	fracture surface (weathered), horiz	3.07E-13	field
	undfmd zone in fault (flt-parallel), horiz	5.36E-13	field
	undfmd zone in fault (flt-parallel), horiz	4.84E-13	field
	cataclastic zone, horiz	4.50E-13	field
	cataclastic zone, horiz	6.50E-13	field
	cataclastic zone, horiz	5.78E-13	field
	porous cataclastic zone, horiz	3.85E-13	field
	porous cataclastic zone, horiz	4.09E-13	field
	porous cataclastic zone, horiz	5.70E-13	field
	porous cataclastic zone, horiz	3.66E-13	field
	porous cataclastic zone, horiz	9.02E-13	field
	vfg zone of dbs (flt-parallel), horiz	8.48E-14	field
	vfg zone of dbs (flt-parallel), horiz	2.02E-13	field
	vfg zone of dbs (flt-normal), horiz	1.03E-13	field
	vfg zone of dbs (flt-parallel), horiz	1.16E-13	field
	vfg zone of dbs (flt-oblique), horiz	7.25E-14	field
	vfg zone of dbs (flt-oblique), horiz	5.43E-14	field

Table C3 (continued).			
Protolith	Fault	k (m2)	Lab or Field
NW, DV- & VP (Qbt3), w/crist. & trid.		9.09E-13	field
NW, DV- & VP (Qbt3), w/crist. & trid.		9.65E-13	field
NW, DV- & VP (Qbt3), w/crist. & trid.		1.53E-12	field
NW, DV- & VP (Qbt3), w/crist. & trid.		9.85E-13	field
NW, DV- & VP (Qbt3), w/crist. & trid.		1.55E-12	field
NW, DV- & VP (Qbt3), w/crist. & trid.		1.19E-12	field
	clay-rich fault (strike-parallel), horiz	1.26E-12	field
	clay-rich fault (strike-parallel), horiz	1.17E-12	field
	clay-rich fault (strike-parallel), horiz	2.20E-12	field
	clay-rich fault (strike-parallel), horiz	1.67E-12	field
	clay-rich fault (flt-normal), horiz	6.52E-13	field
	clay-rich fault (flt-normal), horiz	1.13E-12	field
NW, DV- & VP (Qbt3), w/trid., no crist.		1.41E-12	lab
NW, DV- & VP (Qbt3), w/trid., no crist.		1.41E-12	lab
NW, DV- & VP (Qbt3), w/trid., no crist.		4.69E-12	lab
NW, DV- & VP (Qbt3), w/trid., no crist.		2.87E-12	lab
NW, DV- & VP (Qbt3), w/trid., no crist.		9.88E-13	field
NW, DV- & VP (Qbt3), w/trid., no crist.		2.59E-12	field
	clay-poor zone of dbs (flt-parallel)	1.00E-12	lab
	clay-poor zone of dbs (flt-parallel)	1.46E-12	field
	clay-poor zone of dbs (flt-parallel)	1.46E-12	field
	intersection of clay-poor dbs (flt-parallel)	1.19E-12	field
NW, DV- & VP (Qbt3), w/trid., no crist.		1.53E-12	field
NW, DV- & VP (Qbt3), w/trid., no crist.		1.55E-12	field
NW, DV- & VP (Qbt3), w/trid., no crist.		1.53E-12	field
NW, DV- & VP (Qbt3), w/trid., no crist.		2.17E-12	field
	phenocryst-rich db (flt-parallel), horiz	4.40E-12	field
	phenocryst-rich db (flt-parallel), horiz	1.58E-12	field
	phenocryst-rich db (flt-parallel), subvert	1.42E-12	field
welded, DV- & VP (Qbt3t)		4.63E-14	lab
welded, DV- & VP (Qbt3t)		5.34E-14	lab
welded, DV- & VP (Qbt3t)		5.34E-14	lab
welded, DV- & VP (Qbt3t)		5.34E-14	lab
welded, DV- & VP (Qbt3t)		5.34E-14	lab
welded, DV- & VP (Qbt3t)		5.34E-14	lab
welded, DV- & VP (Qbt3t)		5.27E-14	lab
	fracture, <1mm wide (flt-parallel)	1.96E-12	lab
	fracture, <1mm wide (flt-parallel)	1.97E-12	lab
	fracture, <1mm wide (flt-parallel)	2.38E-12	lab
	fracture, 1mm wide (flt-parallel)	4.21E-12	lab
	fracture, 1mm wide (flt-parallel)	8.51E-12	lab
	fracture, 1mm wide (flt-parallel)	3.33E-12	lab
	fracture, 1-2mm wide (flt-parallel)	3.45E-12	lab
	fracture, 2mm wide (flt-parallel)	1.21E-11	lab
NW, DV- & VP (Qbt4), w/crist. & trid.		3.06E-13	lab
NW, DV- & VP (Qbt4), w/crist. & trid.		3.99E-13	lab
NW, DV- & VP (Qbt4), w/crist. & trid.		5.00E-13	lab
	clay-rich fault/fracture (flt-normal)	1.55E-13	lab
	clay-rich fault/fracture (flt-normal)	2.08E-13	lab
	clay-rich fault/fracture (flt-normal)	2.10E-13	lab
vfg = very fine-grained, db = deformation band, flt = fault, NW = nonwelded, W = welded, G = glassy, DV = devitrified,			
VP = vapor-phase crystallized, crist. = cristobalite, trid. = tridymite, horiz. = horizontal, vert. = vertical, subvert. = subvertical			

Table C4. Summary of air-saturated permeability values for all protolith and faults.

	Glassy Nonwelded Protolith	Crystallized Nonwelded Protolith	Unaltered DBs (fault-normal)	Unaltered DBs (fault-parallel)	DBs with clay (fault-normal)	DBs with clay (fault-parallel)	DBs with carbonate (fault-normal)	DBs with carbonate (fault-parallel)	Welded Protolith	Fracture (fault-parallel)
	3.70E-13	1.31E-13	1.03E-13	6.94E-14	1.14E-13	6.16E-13	8.31E-14	7.14E-13	4.63E-14	3.33E-12
	3.82E-13	1.58E-13	1.84E-13	7.48E-14	1.55E-13	1.00E-12			5.27E-14	3.45E-12
	5.57E-13	1.97E-13	1.85E-13	8.48E-14	1.64E-13	1.17E-12			5.34E-14	4.21E-12
	5.85E-13	2.25E-13	2.31E-13	1.10E-13	2.08E-13	1.19E-12			5.34E-14	8.51E-12
	7.74E-13	3.06E-13	4.06E-13	1.16E-13	2.10E-13	1.26E-12			5.34E-14	
	1.04E-12	3.99E-13	4.32E-13	1.31E-13	3.29E-13	1.46E-12			5.34E-14	
	1.13E-12	4.12E-13	5.35E-13	1.31E-13	3.53E-13	1.46E-12			5.34E-14	
	1.35E-12	4.45E-13	6.95E-13	2.02E-13	3.53E-13	1.67E-12			2.21E-13	
	1.39E-12	5.00E-13		2.11E-13	4.27E-13	2.20E-12			4.40E-13	
		5.00E-13		2.50E-13	5.42E-13				4.68E-13	
		5.09E-13		3.66E-13	5.88E-13					
		5.18E-13		3.72E-13	6.17E-13					
		5.40E-13		3.85E-13	6.52E-13					
		6.98E-13		4.09E-13	1.13E-12					
		6.98E-13		4.50E-13	1.24E-12					
		7.10E-13		4.84E-13						
		8.36E-13		5.36E-13						
		9.09E-13		5.70E-13						
		9.65E-13		5.78E-13						
		9.85E-13		6.50E-13						
		9.88E-13		8.17E-13						
		1.19E-12		8.57E-13						
		1.41E-12		9.02E-13						
		1.41E-12		1.42E-12						
		1.53E-12		1.58E-12						
		1.53E-12		4.40E-12						
		1.53E-12								
		1.55E-12								
		1.55E-12								
		2.17E-12								
		2.59E-12								
		2.87E-12								
		4.69E-12								
n	9	33	8	27	15	9	1	1	10	4
Mean	8.42E-13	1.08027E-12	3.46375E-13	5.9837E-13	4.72133E-13	1.33622E-12	8.31E-14	7.14E-13	1.495E-13	4.875E-12
Median	7.74E-13	8.36E-13	3.19E-13	3.97E-13	3.53E-13	1.26E-12	8.31E-14	7.14E-13	5.34E-14	3.83E-12

n = number of measurements. All permeability values are in m^2.

Table C5. Summary of air-saturated log permeability values for all faults and protolith from the Bandelier Tuff.

	Glassy Nonwelded Protolith	Crystallized Nonwelded Protolith	Unaltered DBs (fault-normal)	Unaltered DBs (fault-parallel)	DBs with clay (fault-normal)	DBs with clay (fault-parallel)	DBs with carbonate (fault-normal)	DBs with carbonate (fault-parallel)	Welded Protolith	Fracture (fault-parallel)
	-12.43	-12.88	-12.99	-13.16	-12.94	-12.21	-13.08	-12.15	-13.33	-11.48
	-12.42	-12.80	-12.74	-13.13	-12.81	-12.00			-13.28	-11.46
	-12.25	-12.71	-12.73	-13.07	-12.79	-11.93			-13.27	-11.38
	-12.23	-12.65	-12.64	-12.96	-12.68	-11.92			-13.27	-11.07
	-12.11	-12.51	-12.39	-12.94	-12.68	-11.90			-13.27	
	-11.98	-12.40	-12.36	-12.88	-12.48	-11.84			-13.27	
	-11.95	-12.39	-12.27	-12.88	-12.45	-11.84			-13.27	
	-11.87	-12.35	-12.16	-12.69	-12.45	-11.78			-12.66	
	-11.86	-12.30		-12.68	-12.37	-11.66			-12.36	
		-12.30		-12.60	-12.27				-12.33	
		-12.29		-12.44	-12.23					
		-12.29		-12.43	-12.21					
		-12.27		-12.41	-12.19					
		-12.16		-12.39	-11.95					
		-12.16		-12.35	-11.91					
		-12.15		-12.32						
		-12.08		-12.27						
		-12.04		-12.24						
		-12.02		-12.24						
		-12.01		-12.19						
		-12.01		-12.09						
		-11.92		-12.07						
		-11.85		-12.04						
		-11.85		-11.85						
		-11.82		-11.80						
		-11.82		-11.36						
		-11.82								
		-11.81								
		-11.81								
		-11.66								
		-11.59								
		-11.54								
		-11.33								
n	9	33	8	27	15	9	1	1	10	4
mean	-12.07	-11.97	-12.46	-12.22	-12.33	-11.87	-13.08	-12.15	-12.83	-11.31
median	-12.11	-12.08	-12.50	-12.40	-12.45	-11.90	-13.08	-12.15	-13.27	-11.42

n = number of measurements. All permeability values are log(m^2). Shaded boxes denote measurements that constitute 50% of data.

REFERENCES CITED

Aldrich, M., 1986, Tectonics of the Jemez lineament in the Jemez Mountains and Rio Grande Rift: Journal of Geophysical Research, v. 91, p. 1753–1762.

Antonellini, M., Aydin, A., 1994, Effect of faulting on fluid flow in porous sandstones: Petrophysical properties: American Association of Petroleum Geologists Bulletin, v. 78, p. 355–377.

Aronson, E.C., 1999, Modeling investigations on gas permeameters: spatial weighting functions and layered systems: M.S. Thesis, New Mexico Tech, Socorro, NM, 91p.

Aubert, D., Stille, P., Probst, A., 2001, REE fractionation during granite weathering and removal by waters and suspended loads: Sr & Nd isotopic evidence: Geochimica et Cosmochimica Acta, v. 65, no. 3, p. 387-406.

Aydin, A., Johnson, A., 1978, Development of faults as zones of deformation bands and as slip surfaces in sandstones: Pure and Applied Geophysics, v. 116, p. 931–942.

Aydin, A., Johnson, A., 1983, Analysis of faulting in porous sandstones: Journal of Structural Geology, v. 5, no. 1, p. 19-31.

Barnes, I., O'Neil, J.R., Trescases, J.J., 1978, Present day serpentinization in New Caledoniia, Oman, and Yugoslavia: Geochimica et Cosmochimica Acta, v. 42, p. 144-145.

Bhumbla, D.K., Keefer, R.F., 1994, Arsenic mobilization and bioavailability in soils, in, Nrlagu, J.O. (ed.), Arsenic in the Environment, Part I: Cycling and Characterization: Wiley Series in Advances in Environmental Science and Technology, John Wiley & Sons, Inc., New York, p. 51-82.

Birkeland, P.W., 1999, Soils and Geomorphology, 3rd edition, Oxford University Press, New York, 430p.

Boquet, E., Boronat, A., Ramos-Cormenzana, A., 1973, Production of Calcite (Calcium Carbonate) Crystals by Soil Bacteria is a General Phenomenon: Nature, v. 246, p. 527-529.

Broxton, D., Bish, D., Warren, R., 1987, Distribution and chemistry of diagenetic minerals at Yucca Mountain, Nye County, Nevada: Clays and Clay Minerals, v. 35, p. 89–110.

Broxton, D., Heiken, G., Chipera, S.J., Byers, F.M., 1995, Stratigraphy, petrography, and mineralogy of Bandelier Tuff and Cerro Toledo deposits, in D.E. Broxton and P.G. Eller, eds., Earth Science Investigations for Environmental Restoration—Los Alamos National Laboratory Technical Area 21: Los Alamos National Laboratory Report LA-12934-MS, p. 33-64.

Broxton, D., Reneau, S., 1995, Stratigraphic nomenclature of the Bandelier Tuff for the Environmental Restoration Project at Los Alamos National Laboratory: Los Alamos National Laboratory Report LA-13010-MS, 20 p.

Bruhn, R. L., Yonkee, W.A., 1988. Fracture networks: Implications for fault zone permeability and mechanics: EOS 69, 484.

Caine, J.S., Evans, J.P., Forster, C.B., 1996, Fault zone architecture and permeability structure: Geology, v. 24, p. 1025–1028.

Campbell, A.R., Larsen, P., 1998, Introduction to stable isotope applications in hydrothermal Systems, in, Richardson, J., and Larsen, P., eds., Techniques in Hydrothermal Ore Deposit Geology: Reviews in Economic Geology, v. 10, p. 173-193.

Carter, K.E., Gardner, J.N., 1995, Quaternary fault kinematics in the northwestern Espanola Basin, Rio Grande rift, New Mexico, *in* Bauer, P.W., Kues, B.S., Dunbar, N.W., Karlstrom, K.E., Harrison, B., eds., Geology of the Santa Fe region: New Mexico Geological Society Guidebook, 46th Field Conference, p. 97–103.

Carter, K.E., Winter, C.L., 1995, Fractal nature and scaling of normal faults in the Espanola Basin, Rio Grande rift, New Mexico: implications for fault growth and brittle strain: Journal of Structural Geology, v. 17, no. 6, p. 863-873.

Cashman, S., Cashman, K., 2000, Cataclasis and deformation-band formation in unconsolidated marine terrace sand, Humboldt County, California: Geology, v. 28, p. 111–114.

Chester, F., Logan, J., 1986, Implications for mechanical properties of brittle faults from observations of the Punchbowl fault zone, California: Pure and Applied Geophysics, v. 124, p. 79–106.

Chester, F.M., Evans, J.P., and Biegel, R.L., 1993, Internal Structure and Weakening Mechanisms of the San Andreas Fault: Journal of Geophysical Research, v. 98, no. B1, p. 771-786.

Chipera, S.J., Bish, D.L., 2001, FULLPAT: An improved full-pattern quantitative X-ray diffraction method: Madison, Wisconsin, Clay Minerals Society: Proceedings of the 38th Annual Meeting, p. 105.

Chipera, S.J., Guthrie, Jr., G.D., Bish, D.L., 1993, Preparation and Purification of Mineral Dusts, in Guthrie, Jr., G.D., Mossman, B.T.,eds., Reviews in Mineralogy Volume 28: Health Effects of Mineral Dusts, Mineralogical Society of America, p.235-249.

Davenport, D.W., Wilcox, B.P., Allen, B.L., 1995, Micromorphology of Pedogenically Derived Fracture Fills in Bandelier Tuff, New Mexico: Soil Science Society of America Journal, v. 59, p. 1672-1683.

Davis, J.M., Wilson, J.L., Phillips, F.M., 1994, A Portable Air-Minipermeameter for Rapid In Situ Field Measurements: Ground Water, v. 32, no. 2, p. 258-266.

Davis, J.M., Wilson, J.L., Phillips, F.M., Gotkowitz, M.B., 1997, Relationship between fluvial bounding surfaces and the permeability correlation structure: Water Resources Research, v. 33, no. 8, p. 1843-1854.

Dinwiddie, C.L., Fedors, R.W., Ferrill, D.A., and Keighley-Bradbury, K., 2002, Matrix Permeabilities of Faulted Nonwelded Tuffs: GSA Annual Meeting, Denver, CO, October-November (poster).

Dunn, D.E., LaFountain, L.J., Jackson, R.E., 1973, Porosity dependence and mechanism of brittle fracture in sandstones: Journal of Geophysical Research, v. 78, no. 14, p. 2403-2417.

Eberly, P., McFadden, L.D., Watt, P.M., 1996, Eolian dust as a factor in soil development on the Pajarito Plateau, Los Alamos Area, Northern New Mexico, in Goff, F., Kues, B.S., Rogers, M.A., McFadden, L.D., Gardner, J.N., eds., The Jemez Mountains Region: New Mexico Geological Society 47th Annual Field Conference, p. 383-389.

Ehleringer, J.R., 1988, Carbon isotope ratios and physiological processes in aridland plants, in Rundel, P. W., Ehleringer, J. R., and Nagy, K. A., eds., Applications of stable isotope ratios to ecological research, New York, Springer-Verlag, p. 41-54.

Evans, J.P., Bradbury, K.K., 2004, Faulting and Fracturing of Non-Welded Bishop Tuff, Eastern California: Deformation mechanisms in very porous materials in the vadose zone: Vadose Zone Journal, v. 3, p. 602-623 .

Evans, J.P. and F.M. Chester, 1995, Fluid-rock interaction in faults of the San Andreas system: Inferences from San Gabriel fault rock geochemistry and microstructures: Journal of Geophysical Research, v. 100, no. B7, p. 13007-13020.

Flinn, D., 1977. Transcurrent faults and associated cataclasis in Shetland: Journal of the Geological Society of London 133, 231-248.

Forster, C. B., Evans, J.P., 1991. Hydrogeology of thrust faults and crystalline thrust sheets: results of combined field and modeling studies: Geophysical Research Letters 18, 979-982.

Freundt, A., Wilson, C.J.N., Carey, S.N., 2000, Ignimbrites and Block-and-Ash Flow Deposits, in Encyclopedia of Volcanoes, Academic Press, p. 581-599.

Gile, L.H., Hawley, J.W., Grossman, R., 1981, Soils and geomorphology in the Basin and Range area of southern New Mexico, Guidebook to the Desert project: New Mexico Bureau of Mines and Mineral Resources Memoir, v. 39, 222 p.

Gile, L.H., Hawley, J.W., Grossman, R., Monger, H.C., Montoya, C.E., Mack, G.H., 1995, Supplement to the Desert Project Guidebook, with Emphasis on Soil Micromorphology: New Mexico Bureau of Mines and Mineral Resources Bulletin 142, 96 p.

Goggin, D.J., Thrasher, R.L., Lake, L.W., 1988, A theoretical and experimental analysis of minipermeameter response including gas slippage and high velocity flow effects: In Situ, v. 12, p. 79-116.

Goodwin, L.B., Mozley, P.S., Moore, J.C., Haneberg, W.C., 1999. Faults and Subsurface Fluid Flow in the Shallow Crust: An Introduction, in Haneberg, W.C., Mozley, P.S., Moore, J.C., Goodwin, L.B., eds., Faults and Subsurface Fluid Flow in the Shallow Crust: American Geophysical Union Monograph 113, 1-5.

Götze, J., Lewis, R., 1994, Distribution of REE and trace elements in size and mineral fractions of high-purity quartz sands: Chemical Geology, v. 114, p. 43-57.

Hallet, R. B. P. R. Kyle, 1993, XRF and INAA Determinations of Major and Trace Elements in Geological Survey of Japan Igneous and Sedimentary Rock Standards: Geostandards Newsletter, v. 17, p. 127-134.

Hay, R.L., Guldman, S.G., 1987, Diagenetic Alteration of Silicic Ash in Searles Lake, CA: Clays and Clay Minerals, v. 35, no. 6, p. 449-457.

Heiken, G., Goff, F., Gardner, J., Baldridge, W., Hulen, J., Nielson, D., Vaniman, D., 1990, The Valles/Toledo caldera complex, Jemez volcanic field: New Mexico: Annual Review of Earth and Planetary Sciences, v. 18, p. 27–53.

Herrin, M., 2001. Outcrop and Petrographic Observations of Deformation Bands in Poorly Lithified Sand, Lower Santa Fe Group, Central New Mexico: M.S. Thesis, New Mexico Tech.

Hong, S., 1999. Anisotropic Hydraulic Conductivity of Faulted Poorly Consolidated Eolian Sands: Bosque, New Mexico: M.S. Thesis, New Mexico Tech, 70 p.

Istok, J.D., Rautman, C.A., Flint, L.E., and Flint, A.L., 1994, Spatial Variability in Hydrologic Properties of a Volcanic Tuff: Ground Water, v. 32, no. 5, p. 751-760.

Izett, G.A., Obradovich, J.D., 1994, $^{40}Ar/^{39}Ar$ age constraints on the Jaramillo Normal Subchron and the Matuyama-Brunhes geomagnetic boundary: Journal of Geophysical Research, v. 99, p. 2925–2934.

Kastning, E. H., 1977. Faults as positive and negative influences on groundwater flow and conduit enlargement, in D. R.R. and S. C. Csallany, eds., Hydrologic problems in karst regions, Bowling Green, Kentucky, West Kentucky University, p. 193-201.

Knipe, R.J., 1993, The influence of fault zone processes and diagenesis on fluid flow, *in* Horbury, A.D., and Robinson, A.G., eds., Diagenesis and basin development: American Association of Petroleum Geologists Studies in Geology no. 36, p. 135–148.

Korotev R. L., 1991, Geochemical stratigraphy of two regolith cores from the central highlands of the Moon, in Sharpton, V.L. and Ryder, G., eds., Proceedings of Lunar Planetary Sciences, vol. 21, p. 229-289, Lunar and Planetary Institute, Houston.

Lander, R.H., Hay, R.L., 1993, Hydrogeologic control on zeolitic diagenesis of the White River Sequence: GSA Bulletin, v. 105, p. 361-376.

Lavine, A., Lewis, C.J., Katcher, D.K., Gardner, J.N., Wilson, J.E., 2003, Geology of the North-central to Northeastern portion of Los Alamos National Laboratory, New Mexico: Los Alamos National Laboratory Report LA-14043-MS, 44 p.

LeCain, G.D., 1997, Air-Injection Testing in Vertical Boreholes in Welded and Nonwelded Tuff, Yucca Mountain, Nevada: U.S.G.S. Water-Resources Investigations Report 96-4262, 33 p.

Lechler, B.J., 2002, Gas Permeameters: Operation, Modification, and Design: M.S. Thesis, New Mexico Tech, 119 p.

Lewis, C.J., Lavine, A., Reneau, S.L., Gardner, J.N., Channell, R., Criswell, C.W., 2002, Geology of the Western Part of Los Alamos National Laboratory (TA-3 to TA-16), Rio Grande Rift, New Mexico: Los Alamos National Laboratory Report LA-13960-MS, 97 p.

Lloyd, G. E., Knipe, R.J., 1992. Deformation mechanisms accommodating faulting of

quartzite under upper crustal conditions: Journal of Structural Geology 14, 127-144.

McCrea, J.M., 1950, The isotopic chemistry of carbonates and a paleotemperature scale: Journal of Chemical Physics, v. 18, p. 849-857.

McDonald, E.V., Longmire, P.A., Watt, P.M., Ryti, R.T., Reneau, S.L., 1996, Natural and major trace element background geochemistry of selected soil profiles, Los Alamos, New Mexico, in, Goff, F., Kues, B.S., Rogers, M.A., McFadden, L.D., Gardner, J.N., eds., The Jemez Mountains Region: New Mexico Geological Society 47th Annual Field Conference, p. 375-382.

McLellan, S.M., 1989, Rare earth elements in sedimentary rocks: Influence of provenance and sedimentary processes, in, Lipin, B.R., and McKay, G.A., eds., Geochemistry and Mineralogy of REE: Mineral. Soc. Am. Rev. Min, v. 21, p. 169-200.

McLin, S.G., 1996, Analysis of water level fluctuation in Pajarito Plateau wells, in, Goff, F., Kues, B.S., Rogers, M.A., McFadden, L.D., Gardner, J.N., eds., The Jemez Mountains Region: New Mexico Geological Society 47th Annual Field Conference, p. 421-426.

Mok, U., Bernabe, Y., Evans, B., 2002, Permeability, porosity, and pore geometry of chemically altered porous silica glass: Journal of Geophysical Research, v. 107, no. B1, JB000247, 2002.

Moon, V., 1993a, Microstructural controls on the geomechanical behavior of ignimbrite: Engineering Geology, v. 35, p. 19–31.

Moon, V., 1993b, Geotechnical characteristics of ignimbrite: a soft pyroclastic rock Type: Engineering Geology, v. 35, p. 33-48.

Mozley, P.S., Goodwin, L.B., 1995, Patterns of cementation along a Cenozoic normal fault: A record of paleoflow orientations: Geology, v. 23, p. 539–542.

Nakamura, N., 1974, Determination of REE, Ba, Fe, Mg, Na, and K in carbonaceous and ordinary chondrites: Geochimica et Cosmochimica Acta, v. 38, p. 757-775.

Neeper, D.A., Gilkeson, R.H., 1996, The influence of topography, stratigraphy, and barometric venting on the hydrology of unsaturated Bandelier Tuff, in Goff, F., Kues, B.S., Rogers, M.A., McFadden, L.D., Gardner, J.N., eds., The Jemez Mountains Region: New Mexico Geological Society 47th Annual Field Conference Guidebook, p. 427-432.

Nelson, C.S., Smith, A.H., 1996, Stable oxygen and carbon isotope compositional fields for skeletal and diagenetic components in New Zealand Cenozoic

nontropical carbonate sediments and limestones: a synthesis and review: New Zealand Journal of Geology and Geophysics, v. 39, p. 93-107.

Newman, B.D., 1996, Geochemical investigations of calcite fracture fills and mesa-top water dynamics on the Pajarito Plateau, New Mexico, Ph.D. Thesis, New Mexico Tech, Socorro, New Mexico, 254 p.

Newman, B.D., Campbell, A.R., Norman, D.I., Ringelberg, D.B., 1997, A model for microbially induced precipitation of vadose-zone calcites in fractures at Los Alamos, New Mexico, USA: Geochimica et Cosmochimica Acta, v. 61, no. 9, p. 1783-1792.

Purtymun, W.D., 1995, Geologic and hydrologic records of observation wells, test holes, test wells, supply wells, springs, and surface water stations in the Los Alamos area: Los Alamos National Laboratory Report LA-12883-MS, 339 p.

Purtymun, W.D., Johansen, S., 1974, General geohydrology of the Pajarito Plateau, *in* Ghost Ranch: New Mexico Geological Society Guidebook, 25th Field Conference, p. 347–349.

Quade, J., Cerling, T.E., 1990, Stable Isotopic Evidence for a Pedogenic Origin of Carbonates in Trench 14 near Yucca Mountain, Nevada: Science, v. 250, p. 1549-1552.

Rawling, G., Goodwin, L., Wilson, J., 2001, Internal architecture, permeability structure, and hydrologic significance of contrasting fault zone types: Geology, v. 29, p. 43–46.

Reches, Z., Lockner, D.A., 1994, Nucleation and growth of faults in brittle rock: Journal of Geophysical Research, v. 99, p. 18,159–18,173.

Rode, A.A., 1962, Soil science, Israel Program for Scientific Translations, Jerusalem, 517p.

Rogers, D., Gallaher, B.M., Vold, E.L., 1996, Vadose zone infiltration beneath the Pajarito Plateau at Los Alamos National Laboratory, in Goff, F., Kues, B.S., Rogers, M.A., McFadden, L.D., Gardner, J.N., eds., The Jemez Mountains Region: New Mexico Geological Society 47th Annual Field Conference Guidebook, p. 413-420.

Rogers, D., Gallaher, B., 1995, The unsaturated hydraulic characteristics of the Bandelier Tuff: Los Alamos National Laboratory Report LA-12968-MS, 76 p.

Ross, C.S., Smith, R.L., 1961. Ash-flow tuffs: their origin, geologic relations, and Identification: U.S. Geological Survey Professional Paper 366, 81 p.

Schultz, R., Li, Q., 1995. Uniaxial strength testing of non-welded Calico Hills tuff, Yucca Mountain, Nevada: Engineering Geology, v. 40, p. 287-299.

Self, S., Goff, F., Gardner, J.N., Wright, J.V., Kite, W.M., 1986. Explosive rhyolitic volcanism in the Jemez Mountains: Vent locations, caldera development and relation to regional structure: Journal of Geophysical Research 91, 1779-1798.

Shipton, Z.K., Cowie, P.A., 2001, Damage zone and slip surface evolution over mm to km scales in high-porosity Navajo sandstone, Utah: Journal of Structural Geology, v. 23, p. 1825-1844.

Sigda, J., Goodwin, L., Mozley, P., Wilson, J., 1999, Permeability Alteration in Small-Displacement Faults in Poorly Lithified Sediments: Rio Grande Rift, Central New Mexico, *in* Haneberg, W., Mozley, P., Moore, J., Goodwin, L., eds., Faults and Subsurface Fluid Flow in the Shallow Crust: American Geophysical Union Monograph, v. 113, p. 51-68.

Sigda, J., Wilson, J.L., 2003, Are faults preferential flow paths through semi-arid and arid vadose zones?: Water Resources Research, v. 39, doi:10.1029/2002WR001406.

Skinner, B. J., 1997, Hydrothermal mineral deposits: what we do and don't know, in Barnes, H.L., ed., Geochemistry of Hydrothermal Ore Deposits, 3rd ed., John Wiley & Sons, Inc., New York, p. 1-29.

Smith, R.L., Bailey, R.A., 1966, The Bandelier Tuff—A study of ash-flow eruption cycles from zoned magma chambers: Bulletin of Volcanology, v. 29, p. 83–104.

Spell, T., McDougall, I., Doulgeris, A., 1996. Cerro Toledo Rhyolite, Jemez Volcanic Field, New Mexico: $^{40}Ar/^{39}Ar$ geochronology of eruptions between two caldera-forming events: Geological Society of America Bulletin 108 (12), 1549-1566.

Springer, E.P., Schofield, T.G., 2002, Unsaturated Zone Hydrologic Properties for TA-49: Los Alamos National Laboratory Report LA-UR-02-6321, 42p.

Starkey, H.C., Blackmon, P.D., 1979, Clay mineralogy of Pleistocene Lake Tecopa, Inyo County, California: U.S.G.S. Professional Paper 1061, 34p.

Stephens, D.B., 1996, Vadose Zone Hydrology: Boca Raton, Florida, CRC Press, Inc., 347 p.

Stimac, J., Hickmott, D., Abell, R., Larocque, A.C.L., Broxton, D., Gardner, J., Chipera, S., Wolff, J., Gauerke, E., 1996, Redistribution of Pb and other volatile trace metals during eruption, devitrification, and vapor-phase crystallization of the Bandelier Tuff, New Mexico: Journal of Volcanology and Geothermal Research, v. 73, p. 245-266.

Stimac, J.A., Broxton, D.E., Kluk, E.C., Chipera, S.J., Budahn, J.R., 2002, Stratigraphy of the Tuffs from Borehole 49-2-700-1 at Technical Area 49, Los Alamos National Laboratory, New Mexico: Los Alamos National Laboratory Report LA-13969, 14 p.

Stone, W., Cole, G., Carey, W., 1999, Los Alamos National Laboratory Sitewide Geologic Model.

Suboor, M.A., Heller, J.P., 1995, Minipermeameter Characteristics Critical to its Use: In Situ, v. 19, no. 3, p. 225-248.

Thompson, M., Potts, P.J., Kane, J.S., Chappell, B.W., 1999, GeoPT3. International Proficiency Test for Analytical Geochemistry Laboratories—Report on Round 3: Geostandards Newsletter, v. 23, p. 87-121.

Thompson, M., Potts, P.J., Kane, J.S., Webb, P.C., Watson, J.S., 2000, GeoPT4. An International Proficiency Test for Analytical Geochemistry Laboratories—Report on Round 4: Geostandards Newsletter, v. 24, p. E1-E37.

Tidwell, V.C., and Wilson, J.L., 2000, Heterogeneity, Permeability Patterns, and Permeability Upscaling: Physical Characterization of a Block of Massillon Sandstone Exhibiting Nested Scales of Heterogeneity: SPE Reservoir Evaluation and Engineering, v. 3, no. 4, p. 283-292.

Tidwell, V.C., Wilson, J.L., 1999, Upscaling experiments conducted on a block of volcanic tuff: Results for a bimodal permeability distribution: Water Resources Research, v. 35, no. 11, p. 3375-3387.

Tidwell, V.C., Wilson, J.L., 1997, Laboratory method for investigation permeability upscaling: Water Resources Research, v. 33, no. 7, p. 1607-1616.

Tobin, H., Vannucchi, P., and Meschede, M., 2001, Structure, inferred mechanical properties, and implications for fluid transport in the decollement zone, Costa Rica convergent margin: Geology, v. 29, no. 10, p. 907-910.

Turin, H.J., Groffman, A.R., Wolfsberg, L.E., Roach, J.L., and Strietelmeier, B.A., 2002, Tracer and radionuclide sorption to vitric tuffs of Busted Butte, Nevada: Applied Geochemistry, v. 17, no. 6, p. 825–836.

Turin, H.J., Rosenberg, N.D., 1996, A conceptual model for flow in the vadose zone beneath the finger mesas of the Pajarito Plateau, in Goff, F., Kues, B.S., Rogers, M.A., McFadden, L.D., Gardner, J.N., eds., The Jemez Mountains Region: New Mexico Geological Society 47th Annual Field Conference Guidebook, p. 74-76.

Vaniman, D.T., and Chipera, S.J., 1995, Mesa-penetrating fractures, fracture mineralogy,

and projected fault traces at Pajarito Mesa, in, Reneau, S.L., and Raymond, R., Jr., eds., Geological Site Characterization for the Proposed Mixed Waste Disposal Facility, Los Alamos National Laboratory: Los Alamos National Laboratory Report, LA-13089-MS.

Vaniman, D.T., Chipera, S.J., Bish, D.L., Duff, M.C., and Hunter, D.B., 2002, Crystal chemistry of clay-Mn oxide associations in soils, fractures, and matrix of the Bandelier Tuff, Pajarito Mesa, New Mexico: Geochimica et Cosmochimica Acta, v. 66, no. 8, p. 1349-1374.

Verrecchia, E.P., Verrecchia, K.E., 1994, Needle-fiber calcite: a critical review and a proposed classification: Journal of Sedimentary Research, v. A64, no. 3, p. 650-664.

Wan, J. and Wilson, J.L., 1994, Colloid transport in unsaturated porous media: Water Resources Research, v. 30, no. 4, pl 857-864.

Warren, R.G., McDonald, E.V., Ryti, R.T., 1997. Baseline geochemistry of soil and bedrock Tshirege Member of the Bandelier Tuff: Los Alamos National Laboratory Report LA-13330-MS, 69 p.

Wilson, J.E., Chester, J.S., Chester, F.M., 2003a, Microfracture analysis of fault growth and wear processes, Punchbowl Fault, San Andreas System, California: Journal of Structural Geology, v. 25, no. 11, p. 1855-1873.

Wilson, J.E., Goodwin, L.B., Lewis, C.J., 2003b, Deformation bands in nonwelded ignimbrites: Petrophysical controls on fault-zone deformation and evidence of preferential fluid flow: Geology, v. 31, no. 10, p. 837-840.

Wilson, C.J.N., Walker, G.P.L., 1982, Ignimbrite depositional facies: the anatomy of a pyroclastic flow: Journal of the Geological Society of London, v. 139, p. 581-92.

Winograd, I.J., 1971, Hydrogeology of Ash Flow Tuff: A Preliminary Statement: Water Resources Research, v. 7, no. 4, p. 994-1006.

Winograd, I.J., Thordarson, W., 1975, Hydrogeologic and hydrochemical framework, south-central Great Basin, Nevada-California, with special reference to the Nevada Test Site: U.S. Geological Survey Professional Paper 712-C, 126 p.

Wohletz, K., 1999, Fractures in Welded Tuff: Los Alamos National Laboratory Report LA-UR-99-6556, 27 p.

Wohletz, K., 1996, Fracture Characterization of the Bandelier Tuff in OU-1098 (TA-2 and TA-41): Los Alamos National Laboratory Report, LA-13194-MS.

Wolfsberg, A., Campbell, K., and Fabryka-Martin, 2000, Use of chlorine-36 to evaluate

fracture flow and transport models at Yucca Mountain, Nevada, in Faybishenko, B., Witherspoon, P.A., and Benson, S.M., (eds.), Dynamics of Fluids in Fractured Rock: American Geophysical Union Monograph, v. 122, p. 346-362.

Wong, T.-F., David, C., and Zhu, W., 1997, The transition from brittle faulting to cataclastic flow in porous sandstones: Mechanical deformation: Journal of Geophysical Research, v. 102, p. 3009–3025.

Wong, T.F., Zhu, W., 1999. Brittle faulting and permeability evolution: Hydromechanical measurement, microstructural observation, and network modeling, In Haneberg, W.C., Mozley, P.S., Moore, J.C., Goodwin, L.B. (eds.), Faults and Subsurface Fluid Flow in the Shallow Crust: American Geophysical Union Monograph 113, 83-100.

Yobbi, D. K., 1997, Simulation of Subsurface Storage and Recovery of Effluent Using Multiple Wells, St. Petersburg, Florida: U.S. Geological Survey Water-Resources Investigations Report 97-4024, 30 p.